

ED 609 - Sciences et Ingénierie des Matériaux, Mécanique, Énergétique (SIMME)
Institute of Research for Ceramics (IRCER) - UMR CNRS 7315

A thesis submitted to University of Limoges
in partial fulfillment of the requirements of the degree of. **Doctor of Philosophy**
Specialty: **Ceramic Materials and Surface Treatments**

Presented and defended by

Adrian-Ionut BERCEA

September 13, 2021

**Structuration périodique multi-échelle de surface par auto assemblage de
masques colloïdaux : relations forme-taille-propriétés, applications optiques.**

**Periodic multi-scale structuring of surfaces by self -assembly of colloidal masks:
shape-size effects, optical applications**

Thesis supervisors: **Cătălin-Daniel CONSTANTINESCU** and **Frédéric DUMAS-BOUCHIAT**

JURY:

President

Mohamed CHAKER, Professor, INRS, Varennes, Québec

Reporters

Florence GARRELIE, Professor, Hubert Curien Laboratory, Jean Monnet University, Saint-Etienne

David GROJO, CNRS Research Director, Lasers, Plasmas and Photonic Processes (LP3), Marseille

Examiners

Alexandre BOULLE, CNRS Research Director, IRCER, Limoges

Mohamed CHAKER, Professor, INRS, Varennes, Québec

Corinne CHAMPEAUX, Professor, IRCER, University of Limoges

Maggy COLAS, CNRS Researcher, IRCER, Limoges

Cătălin-Daniel CONSTANTINESCU, CNRS Researcher, Lasers, Plasmas and Photonic Processes (LP3), Marseille.

Frédéric DUMAS-BOUCHIAT, Professor, IRCER, University of Limoges

Invited

Julie CORNETTE, Engineer, IRCER, Limoges

Sylvain VEDRAINE, Associate Professor, XLIM, University of Limoges



Dedication
to my parents

*"L'homme ne peut découvrir de nouveaux océans tant qu'il n'a pas le courage de perdre de vue la côte."
"Man cannot discover new oceans unless he has the courage to lose sight of the shore."
André Gide.*

Acknowledgements

Ce travail a été cofinancé par la Région Limousin et le LabEx Σ -lim (50%), un projet de recherche académique entre l'Institut de Recherche XLIM (<https://www.xlim.fr>) et l'IRCER (<https://www.ircer.fr>), mutualisant des moyens financiers importants (<https://www.unilim.fr/labex-sigma-lim>). Je tiens à remercier pour l'appui technique de la plateforme CARMALIM, un équipement disponible à l'Université de Limoges qui regroupe la grande majorité des instruments et techniques d'investigation de l'IRCER, situé au Centre Européen de la Céramique.

Je voudrais commencer par exprimer ma gratitude à Corinne Champeaux, Catalin-Daniel Constantinescu et Frédéric Dumas-Bouchiat pour m'avoir accueilli dans leur équipe. Même si nous n'étions pas toujours sur la même longueur d'onde, ce fut un réel plaisir de travailler avec vous. Merci pour tout votre soutien indéfectible, votre disponibilité et surtout votre patience. J'ai beaucoup appris de vous, non seulement du point de vue scientifique, mais aussi comment développer ma personnalité et devenir une meilleure personne. Je suis vraiment reconnaissant pour cela.

J'exprime ma gratitude à M. Mohamed CHAKER, Professeur INRS, Responsable scientifique du Laboratoire de Micro et Nanofabrication (LMN) et Titulaire de la Chaire de Recherche du Canada en Plasma Appliqué aux Technologies de Micro et Nanofabrication, d'avoir accepté de présider le jury de ma thèse.

Je tiens à remercier Mme Florence Garrelie, Professeur à l'Université Jean Monnet (UJM), membre IUF et Directrice du Laboratoire Hubert Curien, France et M. David GROJO, Directeur de recherche CNRS à Lasers, Plasmas et Procédés Photoniques (LP3, UMR 6182 CNRS), Université de la Méditerranée, Campus de Luminy-case, France, pour avoir accepté d'être les rapporteurs de mes travaux.

Je remercie également Mme Maggy COLAS, Chercheuse CNRS à l'IRCER - Institut de Recherche sur la Céramique, Limoges, et M. Alexandre BOULLE, Directeur de Recherche CNRS à l'IRCER - Institut de Recherche sur la Céramique, Limoges, d'avoir accepté de juger cette thèse.

Je tiens à remercier Mme Julie CORNETTE, Ingénieur d'études à l'Université de Limoges, et M. Sylvain VEDRAINE, Maître de Conférences Université de Limoges et XLIM Research Institute, d'avoir accepté l'invitation à faire le point sur mes travaux.

Je tiens à remercier mes collègues de l'équipe de recherche dirigée par le Dr Maria DINESCU de l'Institut national de physique des lasers, plasmas et rayonnements (INFLPR), Roumanie, pour leurs encouragements.

Enfin, je tiens à remercier mes parents, ma tante et mon oncle pour leur soutien continu et indéfectible. Sans leurs efforts, je n'aurais certainement pas eu la possibilité de réaliser mes rêves et mes aspirations de terminer mon doctorat. études. Je serai toujours reconnaissant pour tout ce que vous avez fait pour moi.

Și nu în ultimul rând, aș dori să le mulțumesc părinților mei, mătușii și unchiului meu, pentru sprijinul lor continuu și neclintit. Pour eforturile lor, cu siguranță nu aș fi avut posibilitatea să-mi urmez visle și aspirațiile de a-mi finaliza studiile de doctorat. Voi fi mereu recunoscător pentru tot ceea ce ati făcut pentru mine.

This work was co-financed by the Limousin Region and the LabEx Σ -lim (50%), an academic research project between the XLIM Research Institute (<https://www.xlim.fr>) and IRCER (<https://www.ircer.fr>), pooling significant financial resources (<https://www.unilim.fr/labex-sigma-lim>). I would like to thank for the technical support from the CARMALIM platform, a facility available at the University of Limoges that regroups the vast majority of instruments and investigation techniques of IRCER, situated at the "Centre Européen de la Céramique".

I would like to start by expressing my gratitude to Corinne Champeaux, Catalin-Daniel Constantinescu, and Frédéric Dumas-Bouchiat for welcoming me into their team. Although we were not always on the same wavelength, it was a real pleasure to work with you. Thank you for all of your unwavering support, your availability,

and above all your patience. I learned a lot from you, not just from the scientific point of view, but also how to develop my personality and become a better person. I am really grateful for that.

I express my gratitude to Mr. Mohamed CHAKER, INRS Professor, Scientific leader of the Laboratory of Micro and Nanofabrication (LMN) and Chairholder of the Canada Research Chair in Plasma Applied to Micro-and Nanomanufacturing Technologies, for agreeing to chair the jury for my thesis.

I would like to thank Ms. Florence Garrelie, Professor at Jean Monnet University (UJM), IUF member and Director of the Hubert Curien Laboratory, France and Mr. David GROJO, CNRS Research Director at Lasers, Plasmas and Photonic Processes (LP3, UMR 6182 CNRS), University of the Mediterranean, Campus de Luminy-case, France, for agreeing to be the rapporteurs of my work.

I also thank Ms. Maggy COLAS, CNRS Researcher at IRCER - Institute for Research on Ceramics, Limoges, and Mr. Alexandre BOULLE, CNRS Research Director at IRCER - Institute for Research on Ceramics, Limoges, for agreeing to judge this dissertation.

I would like to thank Ms. Julie CORNETTE, Study engineer at the University of Limoges, and Mr. Sylvain VEDRAINE, Lecturer University of Limoges and XLIM Research Institute, for accepting the invitation to review my work.

I would like to thank my colleagues from the research team lead by Dr. Maria DINESCU from the National Institute for Laser, Plasma and Radiation Physics (INFLPR), Romania, for their encouragements.

And last but not least, I would like to thank my parents, my aunt, and my uncle, for their continuous and unwavering support. Without their efforts, I would definitely not have had the possibility to follow my dreams and aspirations of completing my Ph.D. studies. I will always be grateful for everything that you did for me.

Și nu în ultimul rând, aș dori să le mulțumesc părinților mei, mătușii și unchiului meu, pentru sprijinul lor continuu și neclintit. Fără eforturile lor, cu siguranță nu aș fi avut posibilitatea să-mi urmez visele și aspirațiile de a-mi finaliza studiile de doctorat. Voi fi mereu recunoscător pentru tot ceea ce ati făcut pentru mine.

Rights

This creation is available under a Creative Commons contract:

« **Attribution-Non Commercial-No Derivatives 4.0 International** »

online at <https://creativecommons.org/licenses/by-nc-nd/4.0/>



Table of Contents

Acknowledgements.....	5
Rights.....	7
Table of Contents.....	8
List of Figures.....	11
List of Tables.....	19
Introduction.....	20
Chapter I. Interaction of Electromagnetic Waves with sub-micrometer objects (metallic nanoparticles).....	24
I.1. Electromagnetic waves general framework.....	24
I.1.1. . Electromagnetic waves (light) – metal interaction.....	26
I.2. Plasmons-polaritons, definitions.....	28
I.2.1. Surface Plasmon Resonance (SPR).....	29
I.2.2. Localized surface plasmon resonance (LSPR).....	32
I.2.3. Numerical approaches used to simulate the scattering of electromagnetic radiation by metallic nanoparticles.....	37
I.2.4. LSPR theoretical spectra of nanoparticles with different shapes, obtained by implementing the plasmonic simulation techniques (Mie Theory, DDA, and FDTD).....	40
I.3. Applications of Localized Surface Plasmon Resonance: Surface-enhanced Raman scattering and Surface-Enhanced Infrared Absorption.....	43
I.4. Materials and their optical properties.....	43
I.4.1. Iridium (Ir).....	45
I.4.2. Gold (Au).....	46
I.4.3. Vanadium dioxide (VO ₂).....	51
I.5. Conclusions.....	56
Chapter II. Experimental techniques and procedures for sample preparation - Optimization of the manufacturing steps.....	59
II.1. Pulsed Laser Deposition (PLD).....	59
II.1.1. LASER system and matter interaction (target ablation).....	61
II.1.2. Laser ablation, Plasma plume dynamics.....	63
II.1.3. Deposition, thin film growth mechanisms and substrate influence on the deposition process.....	63
II.2. Colloidal lithography- Langmuir-Blodgett.....	66
II.2.1. Langmuir-Blodgett deposition system and experimental procedure.....	68
II.2.2. Langmuir-Blodgett microspheres arrangement.....	70
II.2.3. Defects in the microsphere arrangement of the Langmuir-Blodgett system.....	71
II.2.4. Langmuir-Blodgett monolayer formation and interaction between microspheres.....	72
II.3. Langmuir-Blodgett- Results.....	73
II.3.1. Surface pressure (SP) measurements.....	73
II.3.2. Langmuir-Blodgett– Fast Fourier transform (FFT).....	74
II.3.3. Temperature dependence of microsphere monolayer quality.....	76
II.3.4. Substrate dependence and barrier-sway effects.....	79
II.4. Description of the experimental techniques used in sample investigation.....	81
II.5. Sample manufacturing roadmap.....	82
II.6. Conclusions.....	84

Chapter III. Gold and Iridium nanoparticle arrays - Study of nanoparticles dewetting process by thermal treatments	86
III.1. Influence of nanoparticle size and metal composition on the LSPR maximum position	86
III.2. Tunable absorption: Influence of the nanoparticle shape on the LSPR response - Role of dewetting process	93
III.2.1. Thermal treatment effects on Au nanoparticle arrays	93
III.2.2. Investigation of solid-state dewetting of Au nanoparticle arrays by HR-XRD	100
III.2.3. Optical detection of LSPR in the visible part of the electromagnetic spectrum and the correlation to the thermal treatment of Gold nanoparticles arrays.	103
III.2.4. Influence of polystyrene microsphere diameter and nature of the metal on LSPR properties	104
III.2.5. Conclusions	106
Chapter IV. Nanocomposites: Matrix influence on the LSPR properties.	109
IV.1.1. Optical response of Gold nanoparticles arrays – Experimental and FDTD studies of the LSPR linked to the solid-state dewetting process.....	109
IV.2. Nanocomposites - Influence of dielectric environment on the optical response of the metallic nanoparticle arrays	113
IV.2.1. Gold nanoparticles arrays in an Alumina matrix.....	113
IV.2.2. Influence of a Vanadium dioxide matrix on the LSPR peak position of metallic nanoparticles arrays	115
IV.2.3. Origin of the double plasmonic resonance peaks of the metallic nanoparticle arrays embedded into VO ₂ and origin of the resonance peak redshift during VO ₂ insulator to metal transition.....	127
IV.2.4. Conclusions	130
Chapter V. Beyond plasmonic resonances; Chemical composition, optical and structural properties of metallic nanoparticle- VO ₂ system.	132
V.1. Metallic nanoparticle arrays and VO ₂ chemical composition.	132
V.2. Influence of metallic nanoparticle arrays on Vanadium dioxide optical; transmittance, optical hysteresis, transmission contrast, and optically determined temperature of transition.	135
V.3. Influence of metallic nanoparticle arrays on Vanadium dioxide crystalline structure	141
V.3.1. Assessment of crystalline structure of Vanadium dioxide by XRD	141
V.3.2. HR-XRD on Au nanoparticle arrays embedded VO ₂ , assessing the structural quality of Au nanoparticles and VO ₂	146
V.3.3. Temperature induced structural transition of VO ₂ containing metallic (Au or Ir) nanoparticles revealed by HR-XRD measurements.	147
V.4. Raman spectroscopy measurements were performed on VO ₂ thin films and VO ₂ thin films with embedded metallic nanoparticle arrays.	150
V.4.1. Raman spectroscopy point measurements.	150
V.4.2. Raman spectroscopy mapping	153
V.5. Conclusions.....	156
General conclusions and perspectives:	157
Bibliography	163
General works.....	163
Particular works.....	163
Appendices.....	177
Appendix 1. Appendix for Chapter I.....	178
Appendix 1.1. Coupling of light to a surface plasmon using a prism	178
Appendix 1.2. Techniques used to simulate the scattering of electromagnetic radiation by metallic nanoparticles.....	179

Appendix 1.3. Surface-Enhanced Raman Scattering and Surface-Enhanced Infrared Absorption.....	180
Appendix 1.4. VO ₂ metal to insulator transition debate.	188
Appendix 2. Appendix to Chapter II.....	190
Appendix 2.1. Energy level diagram of an excimer laser vs. a solid-state laser and their beam profiles...	190
Appendix 2.2. Nanosecond laser ablation vs femtosecond laser ablation	191
Appendix 2.3. Interaction forces between microspheres	192
Appendix 3. Appendix to Chapter IV	198
Appendix 3.1. Evolution of position and intensity of the resonance peaks of the Au nanoparticle arrays (2 μm polystyrene microspheres) and Ir Au nanoparticle arrays embedded in VO ₂	198

List of Figures

Figure I-1: Electromagnetic spectrum.; https://myasadata.larc.nasa.gov/basic_page/electromagnetic-spectrum-diagram	25
Figure I-2: Interface along the $x - y$ plane between a dielectric (top) and a metal (bottom) [31].	29
Figure I-3: Evanescent fields in the two half-spaces [32].	30
Figure I-4: SPP characteristics at the interface between dielectric and metal [32].	30
Figure I-5: The dispersion relation of the surface plasmons compared to light in vacuum and the dielectric medium [31], [33].	31
Figure I-6: LSPR of a spherical metallic nanoparticle in the absence (left) and presence of an external electromagnetic field [31].	32
Figure I-7: Metallic nanoparticle placed into an electrostatic field [37].	33
Figure I-8: Schematic of near-field coupling between metallic nanoparticles for the two different polarizations [37].	37
Figure I-9: Single nanoparticle absorbance spectrum in green and plasmon coupling absorbance spectrum in red (adapted from https://nanohybrids.net/pages/plasmon-coupling-explained).....	37
Figure I-10: LSPR resonance peaks of different nanoparticle shapes;(extinction- black curve, absorption – red curve and scattering- blue curve); for a) sphere, b) cube, c) tetrahedron, d) octahedron, e) triangular plate. f) Extinction spectra of rod-shaped nanoparticles with aspect ratios of 2 (the black curve), 3 (the red one), and 4 (the blue curve). These figures are taken from reference [49]; the panels a)-e) were modified by [49] from reference [50], while panel f) was also modified by reference [49] from reference [51].	40
Figure I-11: Shape and electric field distribution of a) cylindrical nanoparticle, b) triangular nanoparticle, and c) two triangular nanoparticles. Scattering cross-section for d) cylindrical nanoparticle, e) triangular nanoparticle, and f) two triangular nanoparticles; Image is taken from [53].	42
Figure I-12: a) Crystal structure of Al_2O_3 (0001), b) A hexagonal (0001) plane [59].	44
Figure I-13: Refractive index (n) and Extinction coefficient (k) of Al_2O_3 (0001). Taken from https://refractiveindex.info/	44
Figure I-14: Dielectric function for the Al_2O_3 substrate is derived from the reflectance spectrum; ϵ_1 , ϵ_2 real and imaginary part of the dielectric function, respectively [58].....	44
Figure I-15. Properties of Iridium and abundances of rare elements in Earth's crust relative to silicon [60].	45
Figure I-16: Refractive index n (left) and Extinction coefficient k (right) of Ir thin films compared to the n and k of bulk Ir [64]. The Ir-ALD represents an 20 nm Ir thin film deposited on BK7. The Ir-Thin film represents a 115 nm thin film deposited by electron beam evaporation on a fused silica substrate. And Ir-Bulk characterizes the optical characteristics measured on bulk Iridium.	46
Figure I-17:Oldest Gold treasure ever found. http://archaeologyinbulgaria.com Treasure from Europe's first human civilization, developed in the Neolithic in the Balkan Peninsula (Southeast Europe), 8,000 to 6,000 years ago. The treasure is 2000 years older than the Giza Pyramids (2504 BC). For more see info about: Varna Necropolis.	47
Figure I-18: Dielectric function of Au: real part $-\epsilon_1$ (left) and imaginary part ϵ_2 (right) in IR spectral region. Figure taken from reference [72].	48

Figure I-19: Dielectric function of Au: real part $-\epsilon_1$ (left) and imaginary part ϵ_2 (right) in UV, VIS and IR spectral regions. The figure is taken from reference [72].	49
Figure I-20: Skin depth δ_{skin} versus photon energy. Figure taken from [72].	50
Figure I-21: Experimental (solid lines) and calculated (dashed lines) of complex conductivity. The figure is taken from [72].	50
Figure I-22: a) The unit cell of R phase showing the 3d orbitals of t_{2g} symmetry for the center V atom, in a rotated xyz reference frame. b) Unit cell of monoclinic M_1 and M_2 phase. c) Lattice vector transformation matrix in real space between the monoclinic M_1 phase and R phase, and M_2 phase and R phase. d) Lattice vector relations in reciprocal space between the monoclinic M_1 , M_2 phases, and R phases, displayed together with the Brillouin zone of the R phase [74].	52
Figure I-23: A 1-D view of vanadium ions positions for the different phases (R, M_1 , M_2 and T) of VO_2 . The green lines and the green dots show the corresponding R phase characteristics in the other insulating phases [75].	53
Figure I-24: Strain-temperature phase diagram of VO_2 . ω_0 represents the photon frequency shift that characterizes the VO_2 insulating phases in Raman spectroscopy [77].	53
Figure I-25: Raman scattering in different phases of VO_2 (M_1 , M_2 , T, and R). Adapted from [76], [78]. Depending on the value of strain, the scattering of the VO_2 T can differ greatly from the spectrum presented here.	54
Figure I-26: Change of physical properties (resistivity, transmittance) of VO_2 as a temperature and phase function. Figure adapted from reference [79].	54
Figure I-27: Refractive index n (left image) and k (right image) of a 120 nm VO_2 thin film deposited on Al_2O_3 -c by magnetron sputtering. Adapted from the supplementary material of [81].	55
Figure I-28: Real part ϵ_R (left image) and imaginary part ϵ_I (right image) of complex dielectric function, depending on temperature and wavelength, for a 120 nm VO_2 thin film deposited on Al_2O_3 -c by pulsed laser deposition. Adapted from the supplementary material of reference [83].	56
Figure II-1: Standard pulsed laser deposition system.	59
Figure II-2: Versatility of pulsed laser deposition technique [84].	59
Figure II-3: Control of thin film stoichiometry and growth rate by different deposition techniques. The number close to data points shown refer to references, for more details see [87].	60
Figure II-4: Large area pulsed laser deposition system for thin films [88].	60
Figure II-5: Absorption factor of Au as a function of wavelength, compiled from multiple studies by [90].	62
Figure II-6: Target ablation profile of the excimer laser [91].	62
Figure II-7: Plasma plume dynamics of vanadium metal at different oxygen pressures. The ablation was made with a KrF excimer laser at a fluence of 3 J/cm^2 .	63
Figure II-8: Basic atomistic nucleation process. a) Thin film growth, b) Volmer–Weber (island), c) Frank–Van der Merwe (layer-by-layer), and d) Stranski–Krastanov growth, e) Interfacial tensions between the thin film, vapor, and substrate [95], Picture a) is adapted from https://www.bnl.gov/nsls2/sciOps/chemSci/growth.asp .	64
Figure II-9: Thin film under a) tensile stress and b) compressive stress. Structural changes for a thin film c) and a substrate, d) within an epitaxial over layer structure. e) Strain relaxation with a thickness (the relaxation is elastic until a critical layer thickness (t_c), after which plastic relaxation starts via the introduction of heteroepitaxy edge dislocations) [96].	65

Figure II-10: VO_2 growth modes: initially 2D, then island growth followed islands coalescence as the thickness increases [97].	66
Figure II-11: a) Langmuir-Blodgett process steps, b) Theoretical compression isotherm [99].	67
Figure II-12: Grafting of C_{18} on silica [107].	68
Figure II-13: Langmuir-Blodgett deposition system.	69
Figure II-14: Polystyrene microspheres in water suspension.	69
Figure II-15: Surface pressure isotherm.	70
Figure II-16: Langmuir-Blodgett deposition process.	70
Figure II-17: Microsphere arrangement, 2D hexagonal close-packed structure.	71
Figure II-18 Surface pressure (SP) isotherms; when the Wilhelmy plate is moving (red) or not (black).	73
Figure II-19: Surface pressure, pulling speed, and microspheres orientation [116].	73
Figure II-20: Movement of Wilhelmy plate during Langmuir-Blodgett deposition: a) Results of the deposition of Ps 3 μm microspheres in the first stages of the substrate extraction, b) Further substrate extraction of the same sample as a) affected by Wilhelmy plate movement, c) Wilhelmy plate movement.	74
Figure II-21: Fourier transforms of combinations of the 2D hexagonal close packed structure for different orientations: a) 0 degrees, b) 0 and 30 degrees, c) 0, 30 and 45 degrees, d) 0, 15, 30 and 45 degrees, e) 0 and 90 degrees, f) 0 and 60 degrees [117].	75
Figure II-22: Fourier transform of 5 μm polystyrene microspheres on Si, at low (a) 300-x) and high magnification (b) 1000-x, c) 2000-x and d) 5000-x). The FFT procedure makes the insert of each optical microscopy image.	76
Figure II-23: Optical images at a 300-x magnification of polystyrene microspheres (PS) 5 μm deposited on Al_2O_3 -c at a) 16 $^\circ\text{C}$, b) 20 $^\circ\text{C}$, c) 25 $^\circ\text{C}$, c) 30 $^\circ\text{C}$. The inserts represent the FFT (for 300 -x and 2000-x respectively).	77
Figure II-24 Optical images at 500-x and 2000-x magnification of polystyrene microspheres 3 μm deposited on Al_2O_3 -c at a) 25 $^\circ\text{C}$, b) 30 $^\circ\text{C}$. The inserts represent the FFT (for 500 -x and 2000-x respectively).	78
Figure II-25: Optical images at 500-x and 2000-x magnification of polystyrene microspheres 2 μm deposited on Al_2O_3 -c at a) 25 $^\circ\text{C}$, b) 30 $^\circ\text{C}$. The inserts represent the FFT (for 500 -x and 2000-x respectively).	79
Figure II-26: Polystyrene 3 μm microspheres deposited at 25 $^\circ\text{C}$ on a) Al_2O_3 , b) Si, c) BK7. The insert in the images corresponds to FFT.	80
Figure II-27: Polystyrene 2 μm microspheres deposited at 25 $^\circ\text{C}$ on Si: a) Conventional deposition of microspheres, b) Deposition of microspheres with an additional barrier sway process at 200 mHz for 30 min. The insert in the images corresponds to FT.	81
Figure II-28: Roadmap of all the practical steps involved in sample manufacturing and experimental results assessment.	83
Figure III-1: a) Scanning electron microscopy picture of Au nanoparticle showing the nanoparticles characteristic size a and the distance tip to tip d between two adjacent nanoparticles. b) AFM image of the global nanoparticle arrays. c) Focused ion beam scanning electron microscopy image used for nanoparticle's precise thickness quantification.	86
Figure III-2: Localized surface plasmon resonance of Gold and Iridium metallic nanoparticles arrays (deposited on an Al_2O_3 -c substrate) as a function of the diameter of the polystyrene microsphere used in the Langmuir-Blodgett process.	88

Figure III-3: Influence of metallic thickness on the Localized surface plasmon resonance Gold and Iridium metallic nanoparticles arrays; a) and b) Au nanoparticles arrays made with 2, respectively 3 μm polystyrene microsphere c) and d) Iridium nanoparticles arrays made with 2, respectively 3 μm polystyrene microspheres; "o" ($\lambda_{\text{max}1}$) corresponds to dipole resonances while "x" corresponds to the resonances ($\lambda_{\text{max}2}$) given by the thickness. All samples are made on the $\text{Al}_2\text{O}_3\text{-c}$ substrate	90
Figure III-4: Example of a sample containing Gold nanoparticles before and after a thermal treatment process (The initial factor $a=0.90\ \mu\text{m}$ becomes a final diameter of $0.40\ \mu\text{m}$).	93
Figure III-5: Conventional thermal treatment of Au nanoparticle array made with 3 μm polystyrene microspheres and initially having $a=0.90\ \mu\text{m}$ and a thickness of 50 nm. The thermal treatment starts every time with a sample made at room temperature.	95
Figure III-6: Dewetting of Au nanoparticle, with a thickness of 50 nm and initial $a=0.90\ \mu\text{m}$ on an $\text{Al}_2\text{O}_3\text{-c}$ substrate. The thermal treatment is made in furnace inside a SEM system. The starting temperature is R_T and the process stops at 1273 K or 1000 $^\circ\text{C}$. The white scale bar is 2 μm and the yellow one is 0.2 μm . The inserts are AFM and SEM-FIB analyses of samples submitted to conventional thermal treatment (see also SEM movie)....	96
Figure III-7: SEM-FIB image of Au nanoparticle arrays after thermal treatment in a conventional furnace at 1000 $^\circ\text{C}$ (1273 K).....	97
Figure III-8: a) Effects of thermal treatment on the Au nanoparticles projected area and inter- nanoparticles distance (tip-to-tip) d_{it} . (b) Evolution of inter- nanoparticles average distance between the tips of non-connected adjacent nanoparticles compared to the distance between the tips of two nanoparticles connected before the thermal treatment. (c) Shape factor of nanoparticles as a function of the thermal treatment temperature. (d) Percentage of nanoparticles projected area change and percentage of the substrate coverage as a function of temperature. The data from (a)-(d) are extracted from the step by step in-situ SEM observation using the ImageJ software. The nanoparticles projected area refers to the 2D area of the nanoparticles projected on the substrate, as seen in from the SEM images and should not be confused with the total 2D area (surface) of the nanoparticles.	99
Figure III-9: a-d: In-situ HR-XRD scan; Reciprocal space mapping of the (111) Au QTPs reflection as a function of the terminal treatment temperature, from (a)room temperature up to (c)1000 $^\circ\text{C}$ (1273 K) and back to room temperature(d). The maps are plotted as a function of the diffraction space coordinates Q_z and Q_x	100
Figure III-10: a) $\Delta\omega$ (mosaic spread) from the (111) plane of Au nanoparticles, b) Mosaicity of Au nanoparticles.	102
Figure III-11: a) Q scan of Au nanoparticles (111) plane as a function of temperature, b) Experimental and theoretical Au unit cell expansion as a function of temperature.	102
Figure III-12: LSPR resonances in the visible part of the electromagnetic spectrum. a) Absorbance spectra of thermally treated Au nanoparticle arrays (before thermal treatment " a " =0.9 μm) measured by UV-VIS spectroscopy and corroborated with the FDTD based simulation (the dotted lines). b) SEM image of Au nanoparticle array thermally treated at 1273 K and used to identify the LSPR visible resonances' origin. Note that the Au residue nanoparticles (in figure b) have an enlarged diameter due to the deposition of an additional 20 nm platinum layer that prevents electron charging effects during SEM observation.....	103
Figure III-13: Effect of the thermal treatment on Au nanoparticle arrays deposited on an $\text{Al}_2\text{O}_3\text{-c}$ substrate and made with 2 μm polystyrene microspheres. a) Absorbance spectrum pointing out the wavelength blue shift. b) Au nanoparticle array made with 2 μm polystyrene microspheres and thermally treated at 1000 $^\circ\text{C}$ (1273 K).....	105

Figure III-14: Thermal treatment of the Iridium nanoparticle arrays. a) Optical absorbance of the Ir nanoparticle arrays before and after thermal treatment at 1000 °C. b) SEM image of Iridium nanoparticle arrays thermally treated at 1000 °C.	106
Figure IV-1: Localized surface plasmon resonance of Au nanoparticle's arrays (a: measured by UV-VIS; b: measured by FTIR) as a function of the solid-state dewetting temperature. The initial "a" of Au nanoparticles is 0.9 μm , and their thickness is 50 nm. After the solid-state dewetting at 1000°C (1273 K), the nanoparticles' diameter is close to 0.4 μm , and the thickness is close to 200 nm. The continuous lines are the experimental measurements, and the dotted lines are the results from FDTD simulation.....	110
Figure IV-2: a-c: Electric field cartography, obtained by FDTD, of LSPR of Au nanoparticles arrays as a function of thermal treatment temperature a) at $\lambda = 4.45 \mu\text{m}$ for RT sample b) $\lambda = 2.58 \mu\text{m}$ for sample treated at 805 K and c) $\lambda = 1.54 \mu\text{m}$ for sample treated at 823 K d) Evolution of the LSPR position - Comparison between experimental and theoretical (FDTD) values. The FDTD calculation at 1273 K ($\lambda_{\text{LSPR}} = 1.59$) are written in the Table IV 1.	111
Figure IV-3: FTIR optical response of gold arrays in alumina surrounding. Effects of alumina thickness. a) for Au nanoparticle array made with 2 μm polystyrene microspheres. b) for Au nanoparticle array made with 3 μm polystyrene microspheres.	114
Figure IV-4: AFM image of metallic nanoparticle array embedded into a 200nm-VO ₂ matrix. a) gold nanoparticle arrays. b) Iridium nanoparticle arrays. The initial thickness of the Au and Ir made with 3 μm polystyrene microspheres nanoparticles is 50 nm.	115
Figure IV-5: Gold nanoparticle array embedded into a VO ₂ matrix. a) FIB image of gold nanoparticle arrays with 200 nm VO ₂ matrix. b) FIB image taken after removing the VO ₂ matrix (by chemical etching). The initial thickness of the Au nanoparticles, made with 3 μm polystyrene microspheres, is 50 nm. For FIB measurements, a 20 nm layer of Platinum was deposited on top of the samples by thermal evaporation.....	116
Figure IV-6: Optical absorbance spectra of Au nanoparticle arrays, before VO ₂ deposition (in blue), in different thicknesses of the VO ₂ matrix (200 and 100 nm, in orange and green resp.) and optical absorbance of the Au nanoparticle arrays after total removal of the VO ₂ matrix (in red). The optical measurements are performed by FTIR spectroscopy on Au nanoparticle arrays made with 3 μm polystyrene microspheres,.....	117
Figure IV-7: Optical absorbance spectra of metallic nanoparticle arrays embedded into VO ₂ . a) Au nanoparticles with 50, 100, and 200 nm of VO ₂ . b) Ir nanoparticles with 50, 100, 200 nm of VO ₂ . The FTIR measurements are made on metallic nanoparticles made with 2 μm polystyrene microspheres and with initial thickness of 50 nm.	118
Figure IV-8. Optical absorbance spectra of metallic nanoparticle arrays embedded into VO ₂ . a) Ir nanoparticles with 50, 100, and 200 nm of VO ₂ made with 3 μm polystyrene microspheres and an initial thickness of 50 nm. b) Optical absorbance of VO ₂ thin films with thickness 50, 100, and 200 nm and of the Al ₂ O ₃ -c substrate. These contributions were extracted to obtain the spectra in Figure IV-6, Figure IV-7and Figure IV-8.a . The measurements are made by FTIR.	119
Figure IV-9: Optical absorbance spectra of Au nanoparticle arrays embedded into a 200 nm VO ₂ , as a function of the temperature matrix. The Au nanoparticles are made using 3 μm polystyrene microspheres and have an initial thickness of 50 nm. The data are measured by FTIR spectroscopy, and the baseline was subtracted using OriginPro 2015 software.	120
Figure IV-10: Example of resonance peak position determination of the Au nanoparticle arrays, made with 3 μm polystyrene microspheres, and embedded into 200 nm of VO ₂ . In this example, the experimental data (green curve) are collected at 70 °C. The baseline is subtracted from the experimental data, and a Voigt function is used for resonance peak determination.	121

Figure IV-11: Temperature evolution of a) resonance peaks wavelength of Au nanoparticle arrays in 200 nm VO₂ matrix. b) resonance peaks wavelength of Au nanoparticle in 100 nm VO₂ matrix. c) resonance peaks intensity of Au nanoparticle arrays in 200 nm VO₂ matrix. d) resonance peaks intensity of Au nanoparticle arrays in 100 nm VO₂ matrix. Au nanoparticles are made with 3 μm polystyrene microspheres and thickness of 50 nm in both cases. 122

Figure IV-12: Optical absorbance spectra of Au nanoparticle arrays thermally treated at 532 °C and embedded in VO₂. The red curve represents Au nanoparticle arrays made with 2 μm microspheres and thermally treated at 532 °C. The green curve represents Au nanoparticle arrays made with 2 μm microspheres, thermally treated at 532 °C, then embedded in 100 nm of VO₂. The orange curve represents the Au nanoparticle arrays made with 3 μm polystyrene and thermally treated at 532 °C. The blue curve represents the Au nanoparticle arrays made with 3 μm polystyrene, thermally treated at 532 °C, then embedded in 100 nm of VO₂. The data are collected by UV-VIS spectroscopy..... 124

Figure IV-13: Temperature evolution of the plasmonic resonance peak located in the visible part of the electromagnetic spectrum of residue Au nanoparticles embedded into 100 nm of VO₂. a) Au residue nanoparticles made by thermally treating at 532 °C; the Au nanoparticle array was made with 2 μm polystyrene microspheres. b) Au residue nanoparticles made by thermally treating at 532 °C the Au nanoparticle array was made with 3 μm polystyrene microspheres. 125

Figure IV-14: Optical absorbance spectra of Au nanoparticle arrays thermally treated at 532 °C and embedded in VO₂. The red curve represents Au nanoparticle arrays made with 2 μm microspheres and thermally treated at 532 °C. The green curve represents Au nanoparticle arrays made with 2 μm microspheres, thermally treated at 532 °C, then embedded in 100 nm of VO₂. The orange curve represents the Au nanoparticle arrays made with 3 μm polystyrene and thermally treated at 532 °C. The blue curve represents the Au nanoparticle arrays made with 3 μm polystyrene, thermally treated at 532 °C, then embedded in 100 nm of VO₂. The data are collected by FTIR spectroscopy. 126

Figure IV-15: a) Temperature evolution of resonance peak of Au nanoparticle arrays made with 2 μm polystyrene microspheres thermally treated at 532 °C and then covered by 100 nm of VO₂. b) Temperature evolution of resonance peaks of Au nanoparticle arrays made with 3 μm polystyrene microspheres thermally treated at 532 °C then covered by 100 nm of VO₂. 126

Figure IV-16: Localized surface plasmon resonance of Au nanoparticles-VO₂ system: a) Absorbance spectra of Au nanoparticles embedded in 200 nm of VO₂ (top panel) at different temperatures (R_T and 338 K), vs theoretical absorbance spectra (bottom panel) obtained from FDTD calculations. b) Temperature dependence of the LSPR position measured during a heating/cooling cycle (from R_T to SMT temperature and back to R_T). The LSPR positions are extracted from a Voigt function fit of experimental data. c-d) FDTD deduced Electric field cartography for the two resonant peaks at: λ = 4.15 μm (Peak_I) and λ = 3.55 μm (Peak_{II}) (model FDTD-N₁). The Au nanoparticles are made using 3 μm polystyrene microspheres..... 128

Figure IV-17: Simulated electric field cartography of an array of Au nanoparticles covered with a shell of metallic VO₂ and embedded in a VO₂ dielectric matrix. The electric field is plotted at λ = 3.7 μm for Peak_{II} and λ = 4.7 μm for Peak_I. The thickness of the dielectric matrix is 50 nm. The simulation is performed on the actual image of the Au nanoparticle array obtained by AFM measurements made on the Au nanoparticle arrays after the chemical removal of VO₂, and the scale bar is 1 μm. 129

Figure V-1: Energy Dispersive X-Ray Spectroscopy results. a) SEM image of Au nanoparticle arrays made with 3 μm polystyrene microsphere and embedded into 200 nm of VO₂. b) Corresponding EDS elemental analyses. 132

Figure V-2: Elemental mapping of a sample consisting of Au nanoparticle arrays made with 3 μm polystyrene microsphere and embedded into 200 nm of VO ₂ . a) Elemental map of Oxygen. b) Elemental map of Vanadium. c) Elemental map of Aluminum. d) Elemental map of Iridium.	133
Figure V-3: Energy Dispersive X-Ray Spectroscopy results and Elemental mapping of a sample consisting of Ir nanoparticle arrays made with 3 μm polystyrene microsphere and embedded into 200 nm of VO ₂ . a) SEM image of Ir nanoparticle arrays made with 3 μm polystyrene microsphere and embedded into 200 nm of VO ₂ . b) EDS elemental analyses of Ir nanoparticle arrays made with 3 μm polystyrene microsphere and embedded into 200 nm of VO ₂ . c) Elemental map of Oxygen. d) Elemental map of Vanadium. e) Elemental map of Aluminum. f) Elemental map of Iridium.	134
Figure V-4: Optical transmission of VO ₂ deposited on the Al ₂ O ₃ -c substrate. a) Wavelength dependence of the optical transmission of a 200 nm VO ₂ thin film. b) Wavelength dependence of transition temperatures for a 200 nm VO ₂ thin film. c) The influence of thickness VO ₂ on the optical transmission at a wavelength $\lambda = 1.5 \mu\text{m}$. d) The influence of thickness VO ₂ on transition temperature (semiconductor to metal (heating) and metal to semiconductor (cooling)).	135
Figure V-5: Optical transmission of 50, 100, and 200 nm VO ₂ with metallic nanoparticle arrays inside, measured at a wavelength of 1.5 μm , during heating up (colored in red) and cooling down (blue points), for: a) Gold arrays made with 3 μm polystyrene microsphere, b) Iridium arrays made with 3 μm polystyrene microsphere, c) Gold arrays made with 2 μm polystyrene microsphere, d) Iridium arrays made with 2 μm polystyrene microsphere. The thickness of the metallic nanoparticles is 50 nm.....	136
Figure V-6: Derivatives of the temperature dependence of transmission of 50, 100, and 200 nm VO ₂ with metallic nanoparticle arrays inside, measured at a wavelength of 1.5 μm , during heating up (colored in red) and cooling down (blue points), for a) Gold arrays made with 3 μm polystyrene microsphere, b) Iridium arrays made with 3 μm polystyrene microsphere, c) Gold arrays made with 2 μm polystyrene microsphere, d) Iridium arrays made with 2 μm polystyrene microsphere. The thickness of the metallic nanoparticles is 50 nm.	137
Figure V-7: a) Optical transmission of 100 nm VO ₂ thin films that contain Au nanoparticles arrays made with 2 and 3 μm polystyrene microspheres and thermally treated at 532 °C before VO ₂ deposition. b) Derivatives of the temperature dependence of optical transmission of 100 nm VO ₂ thin films that contain Au nanoparticles arrays made with 2 and 3 μm polystyrene microspheres and thermally treated at 532 °C before VO ₂ deposition.	138
Figure V-8: The theta-2theta XRD pattern of 200 nm VO ₂ thin films, with and without metallic nanoparticles embedded. The black pattern corresponds to a pristine sample of 200 nm VO ₂ . The red line corresponds to the XRD pattern of Iridium nanoparticle arrays made with 2 μm polystyrene microsphere and embedded into 200 nm VO ₂ . The green line corresponds to the XRD pattern of Iridium nanoparticle arrays made with a 3 μm polystyrene microsphere and embedded into 200 nm VO ₂ . The orange line corresponds to the XRD pattern of Gold nanoparticle arrays made with 2 μm polystyrene microsphere and embedded into 200 nm VO ₂ . The blue line corresponds to the XRD pattern of Gold nanoparticle arrays made with 2 μm polystyrene microsphere and embedded into 200 nm VO ₂	141
Figure V-9: The theta-2theta XRD pattern of metallic nanoparticles arrays embedded into 50, 100, and 200 nm of VO ₂ , respectively. a) Au nanoparticle arrays made with 3 μm polystyrene. b) Au nanoparticle arrays made with 2 μm polystyrene microspheres. c) Ir nanoparticle arrays made with 3 μm polystyrene microspheres. d) Ir nanoparticle arrays made with 2 μm polystyrene microspheres. The thickness of the metallic nanoparticles is 50 nm. The dotted vertical lines correspond to the theoretical 2theta position of strain-free, Au, Ir, and VO ₂	142
Figure V-10: a) The theta-2theta XRD patterns of 50, 100, and 200 nm VO ₂ thin films free of metallic nanoparticles. b) Comparison of the VO ₂ crystallites size of as a function of VO ₂ thickness and the presence of metallic nanoparticles. c) The strain in the z direction of the b component of the VO ₂ unit cell and strain of a	

component of Au nanoparticle unit cell relative to their respective theoretical counterparts. c) The strain in the z direction of the b component of the VO ₂ unit cell and strain of a component of Ir nanoparticle unit cell.	143
Figure V-11: Example of Gaussian (a), Lorentzian (b), and Voigt (c) fit of the XRD pattern of Au nanoparticle arrays made with 3 μm polystyrene microspheres and embedded into 200 nm of VO ₂	145
Figure V-12: HR-XRD measurement performed on Au nanoparticle arrays embedded into different samples of different VO ₂ thicknesses. a) φ-scan recorded from the (220) planes of VO ₂ , the red lines indicate the positions of the (104) peaks of the Al ₂ O ₃ -c substrate, the thickness of VO ₂ is 200 nm. b) The theta-2 theta scan of Au nanoparticles embedded into 25 and 200 nm of VO ₂ , respectively. c) ω-theta measurements showing the rocking curves of Au nanoparticles for different VO ₂ thicknesses. d) ω-theta measurements showing the rocking curves VO ₂ as a function of VO ₂ thickness.	146
Figure V-13: HR-XRD temperature theta-2theta measurement performed during heating up of 200 nm VO ₂ containing Au nanoparticle arrays (a) and Ir nanoparticle arrays (b). c) 2theta temperature evolution, heating up and cooling down, of 200 nm VO ₂ containing Au nanoparticle arrays. d) 2theta temperature evolution, heating up and cooling down, of 200 nm VO ₂ containing Ir nanoparticle arrays. The metallic nanoparticles have a 50 nm thickness and are made using 3 μm polystyrene microspheres.	148
Figure V-14: HR-XRD temperature theta-2theta measurements used for peak intensity assessment and performed during heating up of 200 nm VO ₂ containing Au nanoparticle arrays (a) and Ir nanoparticle arrays (b). c) Peak intensity evolution of VO ₂ containing Au nanoparticle arrays, extracted using a Voigt fit of the experimental data. d) Peak intensity evolution of VO ₂ containing Au nanoparticle arrays, extracted using a Voigt fit of the experimental data.	149
Figure V-15: Raman spectra of a 200 nm VO ₂ thin film (the black line), Raman spectra of a 200 nm VO ₂ containing metallic nanoparticle arrays made with 3 μm polystyrene microspheres; the red and green lines are for VO ₂ with Ir nanoparticle inside, the orange and blue lines are for VO ₂ with Au nanoparticle inside. "Position I" represents the Raman measurement made directly on top of the nanoparticles, while "Position II" corresponds to Raman measurements made in the free space between the metallic nanoparticles.	150
Figure V-16: The evolution of Raman spectra as a function of temperature. a) Temperature dependence of Raman spectra of 200 nm VO ₂ thin films. b) Example of a fit used to extract the VO ₂ phases from Raman measurements. c) Temperature dependence of Raman spectra from Position "I" of 200 nm of VO ₂ containing Au nanoparticle arrays. d) Temperature dependence of Raman spectra from Position "II" of 200 nm of VO ₂ containing Au nanoparticle arrays. The Raman data are acquired during heating up.	151
Figure V-17: The evolution of Raman peak vibrations intensity of VO ₂ M ₁ , M ₂ , and T phases, extracted using a mix function (Gauss and Lorentz), as a function of temperature. a-b) The intensity of VO ₂ phases containing Au nanoparticle arrays (Position "I" and "II"). c-d) The intensity of VO ₂ phases containing Ir nanoparticle arrays (Position "I" and "II"). The data are collected during heating.	152
Figure V-18: Raman spectroscopy mapping of VO ₂ (M ₁ , M ₂ , T) phases as a function of temperature for a VO ₂ in which Au nanoparticle arrays are embedded. The thickness of the VO ₂ is 200 nm, and the Au nanoparticle arrays are made with 3 μm polystyrene microspheres.	154
Figure V-19: Raman spectroscopy mapping of VO ₂ (M ₁ , M ₂ , T) phases as a function of temperature for a VO ₂ in which Ir nanoparticle arrays are embedded. The thickness of the VO ₂ is 200 nm, and the Ir nanoparticle arrays are made with 3 μm polystyrene microspheres.	155

List of Tables

Table I-1: Maxwell's equations in differential and integral form [27].....	25
Table I-2: Comparison of numerical techniques used to simulate the scattering of electromagnetic radiation by metallic nanoparticles [43].....	39
Table I-3: Physical proprieties of Al ₂ O ₃ (Sapphire)-c substrates.	44
Table I-4: Physical properties of Iridium.....	45
Table I-5: Physical properties of Gold.	47
Table II-1: Pulsed Laser Deposition experimental conditions.....	83
Table III-1: Characteristic dimensions of the metallic nanoparticle arrays.	87
Table III-2. Experimental and theoretical LSPR peak position of the metallic nanoparticle arrays.....	91
Table IV-1: Comparison between experimental LSPR peak position shift induced by thermal treatment and the position deduced by FDTD simulation (gold arrays).	112
Table IV-2: Modulation of the plasmonic resonances metallic nanoparticle arrays by the VO ₂ active or passive matrix.	123
Table V-1: Influence of metallic nanoparticle array on the optical transmission contrast, the temperature of transition, and transition hysteresis width of VO ₂	139
Table V-2: Conclusion keywords.....	159

Introduction

Light interaction with surrounding objects has drawn the attention of humanity since the dawn of time. Human efforts to understand the nature of the light and also the vision endured at the forefront of intellectual endeavors for thousands of years. By attempting to explain how objects, near or far, with different shapes, sizes, and colors, are perceived by us, the Ancient Greeks have created a legacy lasting far longer than their civilization existed [1]. Thousands of years later, Sir Isaac Newton showed the dispersion of the light through a glass prism. This rainbow of colors, thereby providing that color is not a characteristic of the material, revealed the characteristics of light itself by light-object interaction [1]. Over time, the advancements in both understanding physical phenomena and the fabrication techniques have increased so much that the world of the studies of the interaction of light with very small objects is an open field.

Interestingly, when the "objects" are made of metals in a nanometric size, light-object interactions are so unexpected that they gave rise to a new emergent scientific topic at the interface of optics and condensed matter physics called plasmonics. These metallic nanometric objects (i.e., metallic nanoparticles) have tunable physicochemical characteristics such as light absorption, color change, properties that go beyond the limitations of the bulk material's inherent properties [2]. When the photons interact with the free electrons of metallic nanoparticles, the electron cloud is collectively excited as a plasmon [3]. The interaction of plasmons with photons permits to break the diffraction limit of light, in subwavelength dimensions [2]. Depending on the localization of this phenomenon, the excitation is known as surface plasmon polaritons (SPP), if the light interaction takes place as propagating waves at the metal-dielectric interface, or, as in our case, if it takes place inside a nanostructure, it is called localized surface plasmon resonance (LSPR) [4].

In general, having LSPR properties requires free-standing individual and random aggregates of nanoparticles or two and three-dimensional (2 and 3D) nanoparticle arrays placed on a solid substrate. For the free-standing nanoparticles and aggregates, the enhancement of the electromagnetic field can reach 10^{14} [5]. Their plasmonic properties depend on the metal used for making them, the size and the morphology, and the surrounding dielectric environment [6]. Surprisingly the plasmonic color-changing properties of metallic nanoparticles have been used since Roman times for making, as example, the famous Lycurgus cup. The Lycurgus cup exhibits a greenish hue when viewed in reflected light but appears red when a white light source is placed inside the cup due to the presence of gold (and silver) nanoparticles in the glass matrix that selectively absorb and scatter blue and green light [7]. The unusual optical effects observed by the Roman glassmakers (also seen by Faraday [8]) were explained in 1908 by Gustav Mie that provided a analytical solution for the absorption and the scattering of radiation by an arbitrarily sized sphere [7]. Nowadays, nanoparticles are used more often due to their large enhancement factors of the electromagnetic field in a variety of plasmonic-enhanced applications such as solar energy conversion [9], photocatalysis [10], or surface-enhanced Raman scattering (SERS) sensors [11].

Contrary to free-standing nanoparticles, the 2D or 3D nanoparticle arrays are ordered and periodic nanostructures deposited over a solid-state substrate. In general, the 2D arrays are fabricated on planar substrates,

whereas the 3D arrays are created by placing the array on top of another pattern, but with a spacing layer between them [12]. The coupling of properties of the 2D arrays is tuned by varying the distance between individual nanoparticles. Many 2D configurations have been used to generate tunable plasmonic systems, as nanohole arrays [13], nanorod [14], nano-pyramid [15], nanoring arrays [16], nanocube [17]. The electromagnetic field enhancement factor of the 2D nanoparticle arrays can reach 10^7 [18].

LSPR tuning in visible is obtained either by choosing the noble metallic material, e.g., Au or Ag, etc. in visible, manipulating the geometry of the nanoparticles, and/or playing on the surrounding dielectric environment. Nevertheless, new challenges are there, especially modulating the resonance response in the mid-infrared (MidIR, $\sim 4.5 \mu\text{m}$) and near-infrared (NIR, $\sim 1.5 \mu\text{m}$) part of the electromagnetic spectrum where applications linked to telecommunications are becoming more and more important.

The aim of this thesis is to address this context and it was proposed to study the properties of metallic particles organization into periodic arrays on a substrate for developing tunable LSPR platforms. The LSPR properties will be managed in particular in the IR range by acting upstream on the fabrication process by using flexible process and thermal treatments to manage the size and the shape of the metallic particles, and also by manipulating live the dielectric environment embedding the metallic nanoparticles arrays.

In order to achieve this flexibility, the development of the samples is made using the (polystyrene) microsphere lithography (by Langmuir-Blodgett) technique to define the sketch coupled with the Pulsed Laser Deposition (PLD) method to deposit the metal. The removal of the microspheres defines organized quasi-triangular platelets, from which different shapes can be obtained using, as proposed here, thermal post-treatment. The embedding of the nanoparticles periodic arrays is assured by the deposition by PLD of a covering layer leading to nanocomposite materials.

The studies are devoted to metallic gold and iridium nanoparticles arrays and to embed them in alumina and vanadium dioxide matrix. These different materials in both cases were chosen for their complementary properties such as, as examples, high difference of melting temperature for gold and iridium metal, passive and active material for alumina and vanadium dioxide under thermal stimulus.

The manuscript is presented in 5 chapters:

First, the Chapter I constitutes a short theoretical overview of the interaction of electromagnetic waves with sub-micrometric objects. It introduces fundamental concepts about the generation process of plasmons, surface plasmons resonances, localized surface plasmons resonances, and the coupling between localized plasmons, etc. Then, numerical methods (DDA, FDTD, etc.) used to simulate the scattering of electromagnetic radiation by metallic nanoparticles are briefly presented and compared. Chapter I continues with the description of the properties of the chosen materials. The characteristics of the metals Au and Ir used to fabricate the nanoparticles arrays are detailed, justifying their choice. Finally, the end of the chapter focuses on vanadium dioxide (VO_2). This material is later (Chapters III to V) developed as an active matrix in order to create a smart LSPR adaptive nanocomposite sensor, based on its first-order Semiconductor to Metal transition (SMT) at 341 K.

Chapter II is dedicated to the manufacturing methods used for making the metallic nanoparticle arrays and for depositing the matrix such as alumina or VO_2 . After a short presentation of the Pulsed Laser Deposition (PLD) used for the material deposition, the chapter concentrates on the nanosphere lithography, based on the Langmuir-Blodgett process. This technique is rigorously investigated in order to define the parameters to control the templates of nanoparticles arrays. Chapter II also presents all the steps and trials to make and optimize the samples from the nanoparticle's arrays to nanocomposites.

The study of the metallic nanoparticles arrays is developed in the Chapter III. The optical response, in terms of LSPR, is correlated with the nature of the metal, Au or Ir. The influence of the size and the thickness of the nanoparticles is investigated. Further, interestingly, the size and the shape of the metallic Au nanoparticles are managed by performing thermal treatments up to 1000 °C, inducing solid-state dewetting, that allows to tune the resonance peak position as expected, from MidIR to NIR ranges.

The approach developed in chapter III leads naturally to the Chapter IV which provides results on the role of the environment of the nanoparticles on their optical response. This chapter deals with the experimental investigation linked to a theoretical approach based on Finite-difference time-domain (FDTD) method to identify the nature of the optical response of the metallic nanoparticle arrays and its behavior when embedded in a matrix. So, the first nanocomposites are made by depositing a layer of alumina on nanoparticles arrays. In this case, because the initial shape of the nanoparticles is kept (deposition of alumina at room temperature), the optical response of the nanocomposite points out a LSPR behavior, only defined by the thickness of the matrix layer. The second nanocomposites developed will take benefit of the 'smart' properties of a vanadium dioxide matrix, which presents temperature-dependent properties due to its SMT (semi-conductor to metal transition at 68°C) in order to tune with temperature the nanocomposite properties.

Rigorous studies of the mutual effects, beyond plasmonics ones described in previous chapter, of metallic nanoparticles arrays on the vanadium dioxide matrix are presented in the Chapter V. Supported by investigations of the chemical and structural properties (Energy Dispersive X-Ray Spectroscopy (EDS), High-resolution X Ray Diffraction (HR-XRD), Raman spectroscopy and mapping), it aims to point out the influence of the metal nanoparticle array on the optical properties of the nanocomposite compared to pure VO_2 thin films in terms of VO_2 transition properties (optical contrast, hysteresis width, and transition temperature).

The manuscript ends by conclusion and perspectives and is completed by three appendices.

Chapter I

Interaction of Electromagnetic Waves with sub-micrometer objects (metallic nanoparticles)

Chapter I constitutes a theoretical approach to the interaction of electromagnetic waves with nanometric objects. We introduce and discuss concepts as electromagnetic waves, dielectric function of metals, plasmons, surface plasmons resonances, localized surface plasmons resonances, and the coupling between localized plasmons. "Objects" are made of metals and have a nanometric size, light-object interaction results are so unexpected that it gave rise to a new emergent field called plasmonics. These metallic nanometric objects (i.e., metallic nanoparticles) have tunable physicochemical characteristics such as light absorption, color change, and electrical and thermal properties that go beyond the limitations of the bulk material's inherent properties. Then the properties of the materials (Gold, Iridium, Vanadium dioxide, and Sapphire-c) that are used in this thesis are discussed. For these materials, the properties related to light-matter interactions (dielectric function, etc.) are presented.

I.1. Electromagnetic waves general framework

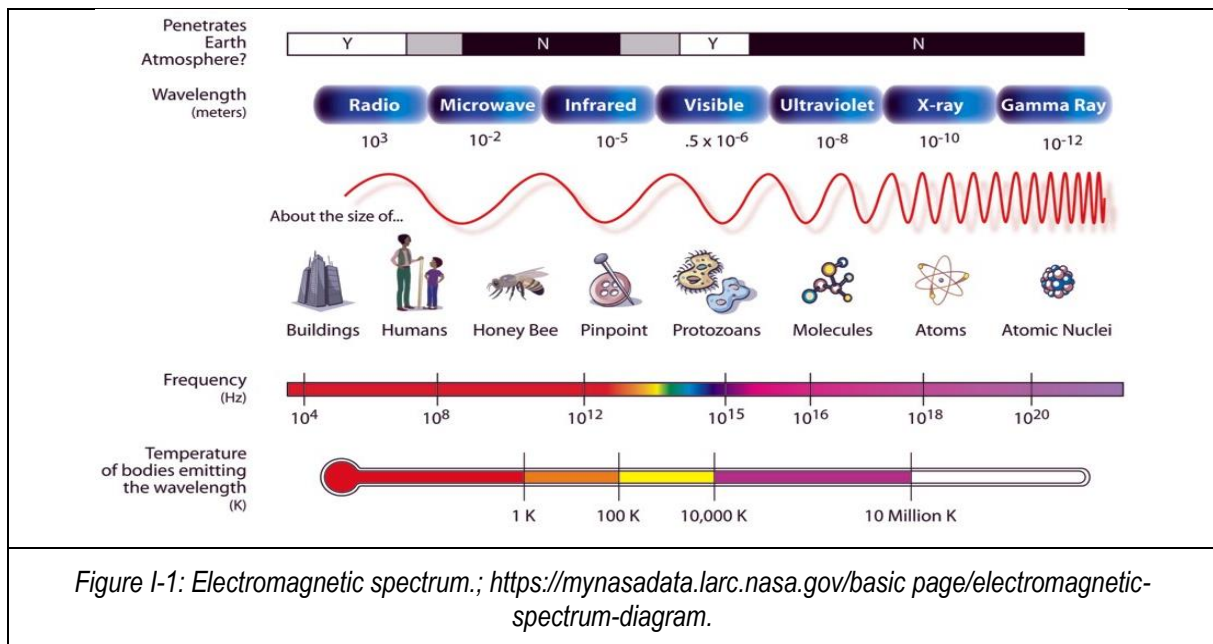
In nature, a wave is a disturbance/perturbation that travels across space of one or more "fields" in such a way that the field values oscillate repeatedly concerning a state of stable equilibrium. Therefore, waves can exist only in fields when there is a force that tries to restore the field to equilibrium. The wave is a standing wave if the relative amplitude of the oscillation at different points in the field remains constant and traveling wave if the relative amplitude changes. There are a variety of types of waves, such as gravitational waves, which are disturbances in a gravitational field that propagate according to general relativity [19], heat diffusion waves [20], plasma waves [21], etc. However, the most studied types of waves fall in one of the two categories: mechanical and/or electromagnetic waves. It is worth mentioning that mechanical and electromagnetic waves transfer just energy, momentum, and information, but they do not transfer the medium itself (e.g., particles). A mechanical wave induces a local deformation in a physical medium, a deformation that propagates from particle to particle by creating local stresses that cause strain also to the neighboring particles. Sound waves, seismic waves, shock waves, water waves are all examples of mechanical waves. An electromagnetic wave (light) consists of a combination of variable electric and magnetic fields that propagates through space without the need for a material medium, simultaneously behaving like waves and particles [22], and are intrinsically linked to the behavior of the space-time continuum [23]. Most simply, an electromagnetic wave is described in terms of its: frequency (f), wavelength (λ), and speed (c), entities that are related through Equation (1).

$$c = \lambda f \quad \text{Equation (1.1)}$$

The speed of an electromagnetic wave is determined by:

$$c = \frac{1}{\sqrt{\mu\epsilon}} \quad \text{Equation (1.2)}$$

where: ϵ and μ is the electrical permittivity and magnetic permeability of the space in which the wave exists [24]. Therefore, considering Equations (1.1) and (1.2), electromagnetic waves can be of any frequency. The range of possible frequencies is known as the electromagnetic spectrum, shown in *Figure I-1*



The electromagnetic spectrum extends from frequencies of $f = 3 \cdot 10^3$ Hz ($\lambda = 100$ km) to $f = 3 \cdot 10^{26}$ Hz ($\lambda = 10^{-18}$ m), which covers everything from ultra-long radio waves to high-energy gamma rays [24], [25].

The behavior of electromagnetic waves in free space is governed by Maxwell's equations, equations listed in Table I-1. In the Maxwell concept, an electromagnetic wave exists as a smooth wave motion in the magnetic and electric force fields. Concept based on the fact that in any region in which there is a temporal change in the electric field, there will appear automatically a magnetic field in that same region as a conjugal partner and vice versa [26].

Table I-1: Maxwell's equations in differential and integral form [27].

Description:	Differential form:	Integral form:	
Coulomb's law	$\vec{\nabla} \cdot \vec{D} = \rho_f$	$\oiint \vec{D} \cdot d\vec{S} = \iiint_V \rho_f dV$	Equation (1.3)
No magnetic monopoles	$\vec{\nabla} \cdot \vec{B} = 0$	$\oiint \vec{B} \cdot d\vec{S} = 0$	Equation (1.4)
Faraday's law	$\vec{\nabla} \times \vec{E} = -\frac{\partial \vec{B}}{\partial t}$	$\oint \vec{E} \cdot d\vec{l} = -\frac{d}{dt} \iint \vec{B} \cdot d\vec{S}$	Equation (1.5)
Ampere's law	$\vec{\nabla} \times \vec{B} = \mu_0 \vec{J}_f + \mu_0 \frac{\partial \vec{D}}{\partial t}$	$\oint \vec{H} \cdot d\vec{l} = \iint \vec{J}_f \cdot d\vec{S} + \frac{d}{dt} \iint \vec{D} \cdot d\vec{S}$	Equation (1.6)

Coulomb's law links the displacement field to the free charge density, ρ_f . In integral form, the displacement field can be imagined as space-filling lines that are tangent to the displacement vector field at each point, with the field lines starting on positive charges and ending on negative charges. The free charges (positive charges) are sources and sinks (negative charges) for the displacement field lines. In the differential form, $\vec{\nabla} \cdot$ is the divergence operator, when $\vec{\nabla} \cdot$ operates on the displacement vector field, the charge density is recovered. This can be visualized as an operation related to the fluid-like flow of the flux of D-field lines spreading through space. In other

words, Coulomb's law expresses the fact that D-field lines begin or end on free charges. This does not imply that a region of space that is free of charge is also a field-free region. The fields pass through space with the same number of lines passing into and out of the surface [27]. Equation (1.4) expresses the lack of magnetic monopoles, i.e., no sources or sinks. The lack of magnetic monopoles can be physically imagined as B-field lines closing on themselves. Equation (1.5) is Faraday's law of induction. Faraday's law expresses the relationship between a time-varying magnetic flux (where the magnetic flux is $\Phi_B = \iint \vec{B} \cdot d\vec{S}$) through a closed loop and an induced potential around the loop called the electromotive force ($\mathcal{E}_e = \oint \vec{E} \cdot d\vec{l}$). It is worth mentioning that the electromotive force is not a conserved quantity, a charged particle under the influence of this electric field may gain or lose energy by going around the closed path [27]. Ampere's law, Equation (1.6), shows the connection between the magnetomotive force ($\mathcal{E}_m = \oint \vec{H} \cdot d\vec{l}$) and the current flowing through a surface. In Ampere's law, the current has two contributions. The first one comes from the free charge current ($I = \iint \vec{J}_f \cdot d\vec{S}$) that flows through the material itself. In addition, the second contribution is given by the displacement current ($\frac{d}{dt} \iint \vec{D} \cdot d\vec{S}$) that may exist outside of the material (electrical conductors). Maxwell added the displacement current to the Ampere's law in order to ensure the conservation of charges.

1.1.1. . Electromagnetic waves (light) – metal interaction

The interaction of the electromagnetic field with metals can be understood easily using the theoretical framework of the free electron gas model [28], [29]. In this model, the metal is assumed to be a gas of free electrons with density n per unit volume moving in a fixed lattice of positive ions. In this case, the metals have filled valence bands and partially filled conduction bands. Special consideration has to be made for noble metals where also interband transitions have to be considered. This model is the same as the Drude-Lorentz-Sommerfeld approach, which considers an external force's influence on one valence electron. The macroscopic response can be deduced by multiplying the effect by the total number of conduction electrons in a given particle.

In the presence of an external electromagnetic field, the equation of motion for an electron is given by Equation (1.7).

$$m\vec{v}'' + m\gamma\vec{v}' = -e(\vec{E} + \vec{v} \times \vec{B}) \quad \text{Equation (1.7)}$$

where; m , e , and \vec{v} are the electron mass, charge, and velocity.

In this model, as in an ideal gas, electron-electron interactions and crystal lattice potential effects are neglected. However, the electron motion is damped by collisions with ions, whose frequency γ is on the order of 100 THz for noble metals. The first term on the right-hand side of Equation (1.7) is the Coulomb interaction between the electron charge and the electric field \vec{E} , while the second term is the Lorentz force due to the magnetic field \vec{B} [29]. The relation between the microscopic dynamics described by Equation (1.7) and the macroscopic response of the medium can be seen by introducing the polarization density \vec{P} . So, taking \vec{P} into account the Equation (1.7) can be rewritten as:

$$\vec{P}'' + \gamma\vec{P}' = \varepsilon_0\omega_p^2(\vec{E} + \vec{v} \times \vec{B}) \quad \text{Equation (1.7.1)}$$

where: $\omega_p = \left(\frac{ne^2}{\epsilon_0 m}\right)^{\frac{1}{2}}$ is the plasma frequency of the free electron gas. It is worth mentioning that the mass m in the free-electron model is an optical effective mass, which depends on the band structure of the medium and such, can significantly differ from the electron rest mass.

If we consider a time-harmonic excitation with time dependence $e^{-i\omega t}$ and neglect the magnetic force ($-e \vec{v} \times \vec{B}$), we obtain the frequency domain expression of the polarization density that has the following expression:

$$\mathbf{P}(\omega) = -\frac{\epsilon_0 \omega_p^2}{\omega^2 + i\gamma\omega} \mathbf{E}(\omega) \quad \text{Equation (1.8)}$$

The contribution of the magnetic force to the polarization density should be neglected only when a static magnetic field is not applied or when one is interested in the nonlinear response for frequency mixing problems, e.g., second-harmonic generation [29].

By analyzing the relation between the displacement field \mathbf{D} and the electric field, it is clear that the plasma dielectric function is negative below the frequency $(\omega_p^2 - \gamma^2)^{\frac{1}{2}}$ [9].

$$\mathbf{D}(\omega) = \epsilon_0 \mathbf{E}(\omega) + \mathbf{P}(\omega) = \epsilon_0 \epsilon_f(\omega) \mathbf{E}(\omega) = \epsilon_0 \left(1 - \frac{\omega_p^2}{\omega^2 + i\gamma\omega}\right) \mathbf{E}(\omega) \quad \text{Equation (1.9)}$$

where $\epsilon_f(\omega)$ is known as the Drude dispersion model for an ideal gas of free electrons.

From Equation (9), we can deduce the complex dielectric permittivity ϵ_f that has the following expression:

$$\epsilon_f = \epsilon_1' + i \epsilon_2'' = \left(1 - \frac{\omega_p^2}{\omega^2 + \gamma^2}\right) + i \left(1 - \frac{\omega_p^2 \gamma}{\omega(\omega^2 + \gamma^2)}\right) \quad \text{Equation (1.10)}$$

Considering that the induced current density is $\mathbf{J}_f(\omega) = -i \omega \mathbf{P}(\omega) = \boldsymbol{\sigma}(\omega) \mathbf{E}(\omega)$, the dynamic conductivity can be deduced and expressed as:

$$\boldsymbol{\sigma}(\omega) = \frac{\epsilon_0 \omega_p^2 \tau}{1 + \omega^2 \tau^2} \quad \text{Equation (1.11)}$$

1.1.1.1. Dielectric function of metals

In general $\epsilon(\omega) = \epsilon_1(\omega) + i \epsilon_2(\omega)$, and $\sigma(\omega) = \sigma_1(\omega) + i \sigma_2(\omega)$, are complex valued-functions of angular frequency ω linked by [28]:

$$\epsilon = 1 + \frac{i\sigma}{\omega \epsilon_0} \quad \text{Equation (1.12)}$$

where: $\epsilon_0 = \frac{1}{4\pi * 10^{-7} * c^2} \approx 8.85 * 10^{-12} \text{ F}\cdot\text{m}^{-1}$ is the permittivity of free space. The dielectric function $\epsilon(\omega)$ can be split in its real $\epsilon_1(\omega)$ and imaginary $\epsilon_2(\omega)$ component as in Equation (1.10).

For example, at optical frequencies, ϵ can be experimentally determined by reflectivity studies. The complex refractive index of the medium is $\tilde{n} = n(\omega) + ik(\omega)$ and is linked to the dielectric constant by $\tilde{n} = \sqrt{\epsilon}$. The link gives the following dependencies/relations:

$$n^2 = \frac{\epsilon_1}{2} + \frac{1}{2} \sqrt{\epsilon_1^2 + \epsilon_2^2} \quad \text{Equation (1.13)}$$

$$k = \frac{\epsilon_2}{2n} \quad \text{Equation (1.14)}$$

k is the extinction coefficient, and represents the optical absorption of electromagnetic waves propagating through a medium and is linked to the absorption α coefficient by:

$$\alpha(\omega) = \frac{2k(\omega)\omega}{c} \quad \text{Equation (1.15)}$$

where: α is the absorption derived from Beer's law, that describes the exponential attenuation of the intensity of a beam propagating through the medium ($I(x)=I_0e^{-\alpha x}$)

By examining Equation (1.14), it is visible that the absorption of an electromagnetic wave inside of a medium is determined by the imaginary part ε_2 of the dielectric function. If $|\varepsilon_1| \gg |\varepsilon_2|$, then the real part n of the refractive index is given mostly by the contribution of the real part ε_1 of the dielectric function. Therefore, considering this together with Equation (1.14) we can say that the real part of σ determines the amount of absorption, while the imaginary part contributes to ε_1 and therefore to the amount of polarization.

1.2. Plasmons-polaritons, definitions

Plasmons and polaritons are quantum mechanical quasi-particles used to describe the interactions in a solid [30]. In metals, the free electrons can be thought of as an electron plasma. Therefore, plasmons can be described as quasi-particles resulting from the quantization of the plasma oscillation of the free electron gas density concerning the fixed positive ions in a metal. Plasmons are Bosons with an energy that can be estimated as:

$$E_p = \hbar \sqrt{\frac{n * e^2}{m_e * \varepsilon_0}} = \hbar * \omega_p \quad \text{Equation (1.16)}$$

where: ω_p – characteristic plasma frequency, n is the conduction electron density, e is the elementary charge, m_e - electron mass, and \hbar is the reduced Planck constant.

Since plasmons are the quantization plasma oscillations, most of their properties can be deduced from Maxwell's equations. The excitation of a plasmon is known as plasmon resonance. Plasmons can be used to describe the optical properties of metals. When the light of frequency below the plasma frequency shines on the surface of a metal, the light is reflected because of the electrons in the metal that screens the electric field of the light. Light with a frequency above the plasma frequency is transmitted. This is because electrons cannot respond fast enough to screen it. Most metals and semiconductors have their corresponding plasma frequency in the ultraviolet; therefore, they will reflect the visible light. Metals such as Copper and Gold have electronic interband transitions in the visible range. The interband transitions will induce the absorption of light at a specific frequency giving metals their distinct colors. Polaritons are bosonic quasi-particles born from the strong coupling of electromagnetic waves with an electric or magnetic dipole-carrying excitation, i.e., a polariton is the result of the mixing of a photon with an excitation of the material.

In the case in which this excitation is a plasmon, an exciton, etc., the resulting quasi-particle is denoted as:

- phonon-polaritons: coupling of infrared photons with optic phonons,
- exciton-polaritons: coupling of photons of visible light with an exciton (an exciton is a bound state of an electron and an electron-hole which are attracted to each other by the electrostatic Coulomb force),
- plasmon-polariton: coupling of plasmon of light with a polariton,

- Surface plasmon-polaritons: coupling of surface plasmons with light.

There are three types of plasmons: bulk plasmon resonance, surface plasmon resonance (SPR), and localized surface plasmon resonance (LSPR). However, in this thesis, the concerning plasmon effect is LSPR. Therefore, we will start with a brief description of SPR then we will focus more on LSPR.

I.2.1. Surface Plasmon Resonance (SPR)

Surface plasmon resonances are coherent electron oscillations that are present at the interface between two materials where the real part of the dielectric function changes sign across the interface, i.e., SPR are electromagnetic excitations that propagate along the interface between a metal and a dielectric medium [30], [31].

These excitations can be deduced by solving the Maxwell equations, separately for the metal and the dielectric components. We start by considering a smooth and flat interface between a metal with relative permittivity ϵ_m and a dielectric medium with relative permittivity ϵ_d . The boundary between the two is on a plane $z = 0$, so that $\epsilon(z) = \epsilon_m$ for $z > 0$ and $\epsilon(z) = \epsilon_d$ for $z < 0$. The metal-dielectric interface extends infinitely in the $x - y$ plane at $z = 0$ (see Figure I-2).

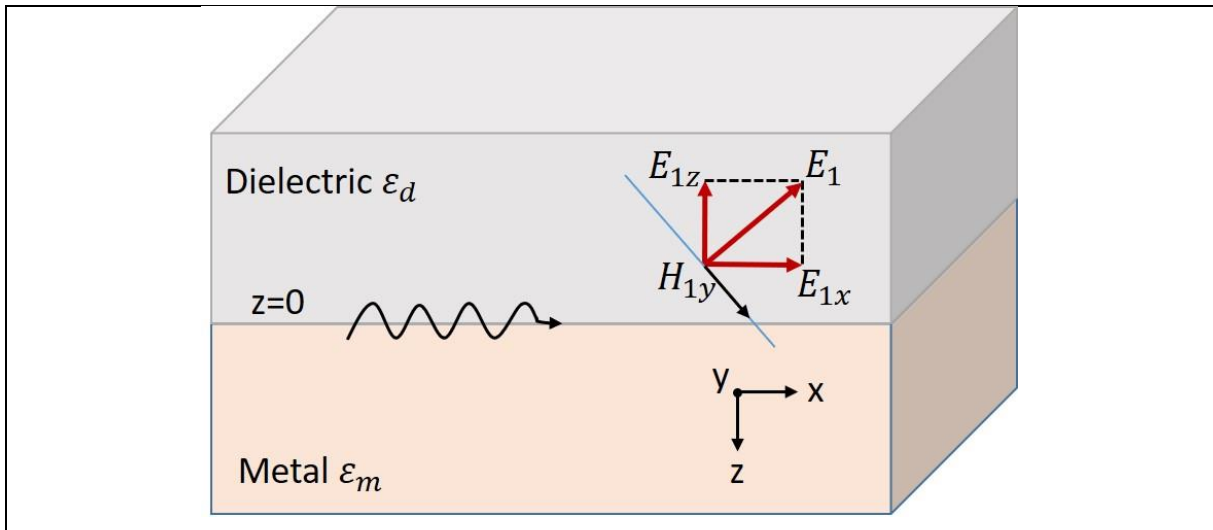


Figure I-2: Interface along the $x - y$ plane between a dielectric (top) and a metal (bottom) [31].

The conditions for the continuity of the normal and transversal field components on this interface are given by the following equations [31]:

$$D_{1,z} = D_{2,z}, \quad B_{1,z} = B_{2,z} \quad \text{Equation (1.17)}$$

$$E_{1,y} = E_{2,y}, \quad H_{1,x} = H_{2,x} \quad \text{Equation (1.18)}$$

where: the indices (1) and (2) indicate the dielectric and the metal components, respectively $\epsilon_d = \epsilon_1$ and $\epsilon_m = \epsilon_2$.

Under this condition, no transverse-electric (TE) modes can exist. Therefore, we analyze the transverse-magnetic (TM) mode for the field, which propagates along the x direction ($i = 1, 2$).

$$E_i = (E_{i,x}, 0, E_{i,y})e^{i(k_i \cdot r - i\omega t)} \quad \text{Equation (1.19)}$$

$$H_i = (0, H_{i,y}, 0)e^{i(k_x r - i\omega t)} \quad \text{Equation (1.20)}$$

$$D_i = \epsilon_0 \epsilon_i E_i, \quad B_i = \mu_0 H_i \quad \text{Equation (1.21)}$$

where $\mu_0 = 4 * \pi * \frac{10^{-7} \text{H(henry)}}{\text{m}}$ is the permeability of free space.

The wave vector is given by $k_i = (\beta, 0, k_{i,z})$ and $\beta = k_x$ (where β indicates the propagation constant along the x direction).

Coupling this approach with the above condition of continuity and Equation (1.3) and Equation (1.4) (see Table I-1. Maxwell equations), in the absence of charges and currents ($\rho = 0$ and $\vec{j} = 0$), there are the following relations of the $k_{i,z}$ components [31]:

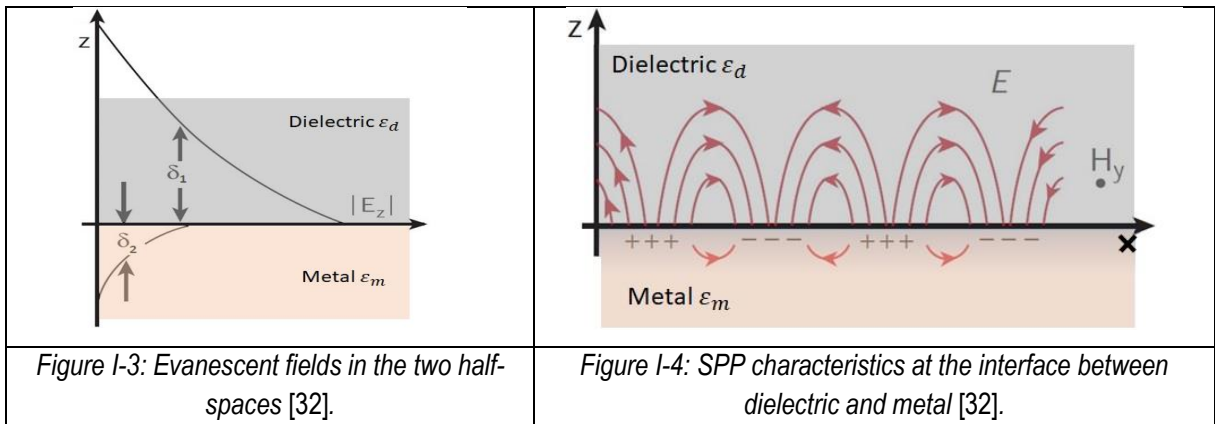
$$\frac{k_{1,z}}{\epsilon_d} = \frac{k_{2,z}}{\epsilon_m} \quad \text{Equation (1.22)}$$

Since we are interested only in solutions that describe modes bound to the interface, the $k_{i,z}$ components have to have an opposite sign and have to be imaginary [31].

$$k_{i,z} = +i k_2 \quad \text{Equation (1.23)}$$

In this manner, the fields decay exponentially into the respective half-spaces; i.e. $E_i \propto \exp(\pm i k_{i,z} z) = \exp(\pm k_{i,z} z)$. Considering Equation (1.22), it is obvious that this is true only if the dielectric constants of the two materials are of opposite sign ($\epsilon_d = -\epsilon_m$). Therefore, surface plasmons can exist at the interface between a metal ($\epsilon < 0$) and a dielectric medium ($\epsilon > 0$).

If photons couple to a surface plasmon, the resulting hybridized excitation is known as a Surface Plasmon Polariton (SPP). SPP can be seen/envisoned as a longitudinal wave in which the charge carriers provided by the conductor are moving parallel to the propagation direction. SPP decays exponentially from the interface, both in metal and dielectric mediums (see Figure I-3). The SPP has a plasma-like behavior inside the metal, behavior characterized by the accumulation of surface charge. Whereas, inside the dielectric, the SPP behavior resembles more to a free electromagnetic wave (see Figure I-4) [32]. The penetration depth or the decay length (δ_1) of the field into a dielectric material is usually of the order of half of the wavelength ($\frac{\lambda}{2}$) of the light involved; however, in metal, the skin depth is given by the decay length (δ_2) of the field.



If we derive the dispersion relations for surface plasmons from Equation (1.19) and we insert the result into Equation (1.22), it is possible to deduce the propagation constant β :

$$\beta = k_0 \sqrt{\frac{\epsilon_d \epsilon_m}{\epsilon_d + \epsilon_m}} = \frac{\omega}{c} \sqrt{\frac{\epsilon_d \epsilon_m}{\epsilon_d + \epsilon_m}} \quad \text{Equation (1.24)}$$

where $k_0 = \frac{\omega}{c}$ is the vacuum wave vector of light with frequency ω .

Considering the frequency dependence of $\epsilon_{d,m}(\omega)$, assuming that $\epsilon_d(\omega)$ in the dielectric is constant, while $\epsilon_m(\omega)$ in the metal above the plasmon frequency can be approximated by Equation (1.10) it is possible to express the dispersion relation $\omega(k_{SPP})$, as presented in *Figure I-5*.

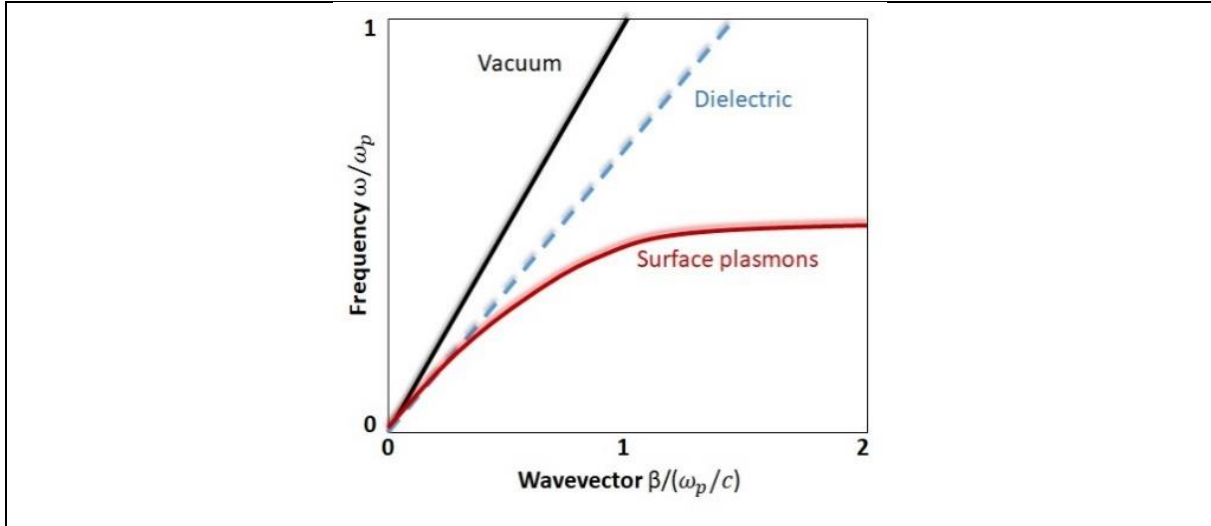


Figure I-5: The dispersion relation of the surface plasmons compared to light in vacuum and the dielectric medium [31], [33].

From *Figure I-5*, it is clear that the SPP dispersion relation resides below the light comes, with crossing occurring only in the limit $\omega = 0, \beta = 0$. Therefore, it is not possible to couple light directly to surface plasmons due to a wave vector mismatch, as energy and momentum conservation ($\omega_{light} = \omega_{SPP}$ and $k_{light} = k_{SPP}$) cannot be fulfilled at the same time. To excite SPPs, we have to rely on a system that can facilitate a momentum transfer, i.e., an additional wave vector component has to be added to that of light [31]. This can be done using prism coupling, grating coupling, excitation using highly focused optical beams, near-field excitation [34] for more information see Appendix 1.1.

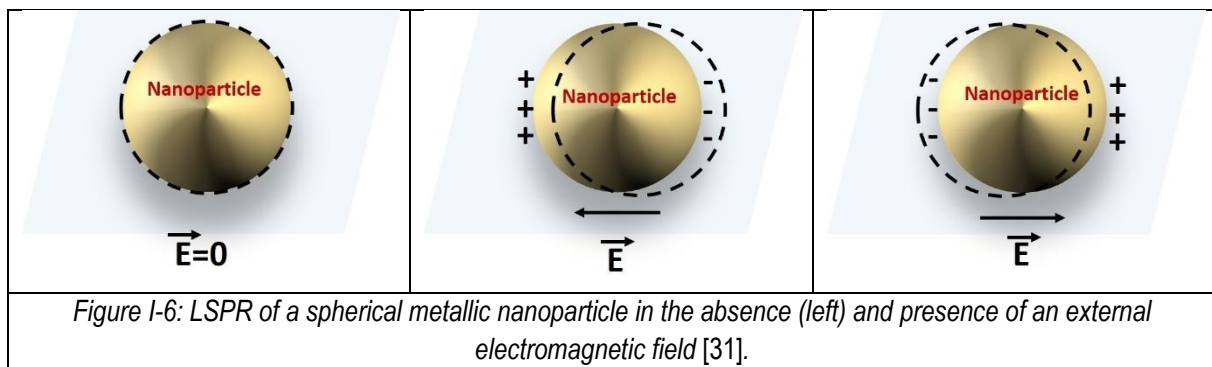
In this section linked to SPR, we did not consider the complex nature of the dielectric constant of metals. As seen in Equation (1.10), the dielectric function $\epsilon_m(\omega)$ can be split in its real $\epsilon_1(\omega)$ and imaginary $\epsilon_2(\omega)$ component. The imaginary component of the dielectric function produces Ohmic damping of the electron oscillations in the metal. This implies that when using Equation (1.24), the propagation constant β also becomes imaginary $\beta = \beta' + i\beta''$. Therefore, in the solutions for the SPPs, the exponential decaying damping term $\exp(-\beta''x)$ will lead to a characteristic propagation length of SPPs is given by: $\delta_{SP} = \frac{1}{2Im(\beta)}$. With a characteristic range of few micrometers at visible wavelengths and up to 100 micrometers in the infrared.

Moreover, the thickness of the metal layer and the presence of the dielectric layer on both sides of the metallic layer have to be considered. In the case of a thick metal layer encased between a dielectric substrate and another dielectric layer, the SPP has two independent modes related to the two adjacent metal-dielectric interfaces.

If the film is in a symmetrical environment, the two SPP modes will degenerate. If the metal is sufficiently thin such that the electromagnetic interaction between the two interfaces is significant, the SPP dispersion will change, and the coupling between SPP modes has to be considered. This interaction will split the surface plasmon frequently into two; one corresponding to the symmetric (low-frequency mode) and another corresponding to antisymmetric (high frequency mode) field distribution through the film. Simultaneously, the low thickness will lead to a very long propagation length (up to centimeters in infrared) of SPP, known as *long-range SPPs* [35].

1.2.2. Localized surface plasmon resonance (LSPR).

As in the case of SPR, the electromagnetic field of incident light can be used to collectively excite the electrons from the conduction band of a metallic nanoparticle (nanoparticle), resulting in coherent localized plasmon oscillations [30], [31], [36]–[38]. The external field can penetrate the nanoparticle volume and shift the conduction electrons concerning the ion lattice (see *Figure I-6*).



The resonant frequency of the oscillation depends strongly on the composition of the metallic nanoparticle, geometry, size, separation distance between nanoparticles, and the dielectric environment that surrounds the nanoparticles. In specific resonant conditions, the field is amplified in the near zone inside and outside the nanoparticle, resonance that is known as localized surface plasmon resonance (LSPR). The metallic nanoparticle supplies an effective restoring force to drive the electrons in an oscillating electromagnetic field.

Therefore, the LSPR can be directly excited by the incident light on the curved surface of nanoparticles. This is in contrast to the SPPs, where momentum matching coupling techniques such as prism coupling, grating coupling, etc., have to be employed. The radiative decay of LSPR induces strong enhancement of light scattering in the far-field while, non-radiative LSPR absorption leads to strong extinction at resonant frequencies. This strong enhancement of absorption and scattering of metallic nanoparticles leads to them being used in various applications such as surface-enhanced Raman scattering (SERS) and fluorescence enhancement, etc.

1.2.2.1. LSPR Quasi-static approximation

In the case of nanoparticles with dimensional sizes much smaller than the wavelengths of incident light ($a \ll \lambda$), the interactions between the nanoparticle and electromagnetic waves can be analyzed using a quasi-static approximation. We start to analyze the interaction between nanoparticle and light by taking a very convenient geometry; a homogeneous, isotropic metallic sphere of radius a and a dielectric function $\epsilon_m(\omega)$. The metallic nanoparticle is placed in a uniform and static electric field. Since in a quasi-static approximation, the oscillating field

phase is considered constant over the nanoparticle volume. Furthermore, the surrounding dielectric environment is considered isotropic and non-absorbing, having the dielectric constant $\varepsilon_d(\omega)$ (see Figure I-7).

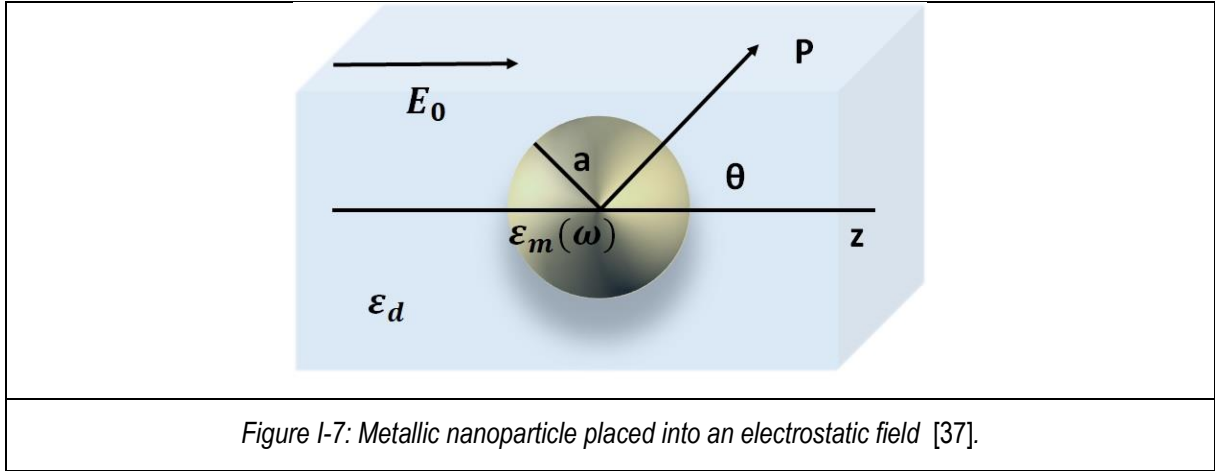


Figure I-7: Metallic nanoparticle placed into an electrostatic field [37].

Since we assume that the space inside and outside the metallic nanoparticle is free of charges, the electrostatic problem can be solved by using the Laplace equation for the potential $\nabla^2 \Phi = 0$ to deduce the electric field $\vec{E} = -\vec{\nabla}\Phi$, with the general solution given by Equation (1.25) (for a detailed description, see [39]).

$$\Phi(r, \theta) = \sum_{l=0}^{\infty} [A_l r^l + B_l r^{-(l+1)}] P_l \cos(\theta) \quad \text{Equation (1.25)}$$

where $P_l(\cos(\theta))$ are the Legendre Polynomials of order l and θ is the angle of the position vector r to the point P and the axis z .

However, the potential has to remain finite at the origin; consequently, the potentials Φ_{in} inside and outside Φ_{out} the nanoparticle can be expressed as:

$$\Phi_{in}(r, \theta) = \sum_{l=0}^{\infty} A_l r^l P_l \cos(\theta) \quad \text{Equation (1.26)}$$

$$\Phi_{out}(r, \theta) = \sum_{l=0}^{\infty} [B_l r^l + C_l r^{-(l+1)}] P_l \cos(\theta) \quad \text{Equation (1.27)}$$

where the coefficients A_l, B_l, C_l can be determined from the boundary conditions at $r \rightarrow \infty$ and the nanoparticle surface $r = a$.

Applying these boundary conditions will result in the following expressions for Φ_{in} and Φ_{out} (see [39]):

$$\Phi_{in} = -\frac{3\varepsilon_d}{\varepsilon_m + 2\varepsilon_d} E_0 \cos(\theta) \quad \text{Equation (1.28)}$$

$$\Phi_{out} = -E_0 r \cos(\theta) + \frac{\varepsilon_m - \varepsilon_d}{\varepsilon_m + 2\varepsilon_d} E_0 a^3 \frac{\cos(\theta)}{r^2} \quad \text{Equation (1.29)}$$

Equation (1.29) physically expresses that Φ_{out} describes the superposition of the applied field and that of a dipole at the nanoparticle center.

Considering the dipole moment \mathbf{p} the potential outside nanoparticle, Φ_{out} can be expressed as:

$$\Phi_{out} = -E_0 r \cos(\theta) + \frac{\mathbf{p} \cdot \mathbf{r}}{4\pi\varepsilon_0\varepsilon_d r^3} \quad \text{Equation (1.30)}$$

$$\mathbf{p} = 4\pi\varepsilon_0\varepsilon_d a^3 \frac{\varepsilon_m - \varepsilon_d}{\varepsilon_m + 2\varepsilon_d} E_0 \quad \text{Equation (1.31)}$$

As a result, we see that the applied field induces a dipole moment inside the nanoparticle, a field with a magnitude proportional to $|E_0|$.

The polarizability α , is defined using dipole moment \mathbf{p} as $\mathbf{p} = \varepsilon_0 \varepsilon_d \alpha E_0$, here the expression of the (complex) polarizability of a small spherical nanoparticle of sub-wavelength diameter in the electrostatic approximation is:

$$\alpha = 4\pi a^3 \frac{\varepsilon_m - \varepsilon_d}{\varepsilon_m + 2\varepsilon_d} \quad \text{Equation (1.32)}$$

When the denominator of Equation (1.32), $|\varepsilon_m + 2\varepsilon_d|$ reaches a minimum, the polarizability experiences a resonant enhancement that for the small or slowly varying $Im[\varepsilon_m]$ around the resonance becomes:

$$Re[\varepsilon_m(\omega)] = -2\varepsilon_d \quad \text{Equation (1.33)}$$

Equation (1.33) is known as the **Fröhlich condition** and the associated mode (in an oscillating field) the dipole surface plasmon of the metallic nanoparticle. For a spherical nanoparticle, placed in air and consisting of a Drude metal with a dielectric function expressed in Equation (1.10), the Fröhlich condition is met at a frequency $\omega_0 = \omega_p \sqrt{3}$. From Equation (1.33), it is evident that there is a strong connection between the resonant position and the dielectric constant of the medium that surrounds the metallic nanoparticle.

The value of the spectral shift of LSPR extinction, or the scattering wavelength maximum for small nanoparticles is given by the following expression [40]:

$$\Delta\lambda_{max} = m\Delta n \left[1 - \exp\left(\frac{-2d}{l_d}\right) \right] \quad \text{Equation (1.34)}$$

where m is the bulk refractive index of the response of nanoparticle (known as the sensitivity factor), Δn is the change in refractive index, d is the effective thickness of the adsorbed layer, and l_d is the characteristic electromagnetic field decay length.

1.2.2.2. Absorption and scattering cross-section of metallic nanoparticle

The metallic nanoparticle's optical properties can differ significantly from those of the metal from which particles are produced. One of the consequences of the resonantly enhanced polarization α is a simultaneous enhancement in the efficiency with which a metal nanoparticle scatters and absorbs light. The absorption C_{abs} and scattering C_{sca} cross-sections depend on the geometry, size, separation distance between nanoparticles, and the dielectric environment; therefore, LSPR frequency will also depend on. C_{abs} and C_{sca} for **spherical nanoparticle** can be calculated using the following expressions [36], [37]:

$$C_{sca} = \frac{k^4}{6\pi} |\alpha|^2 = \frac{8\pi}{3} k^4 a^6 \left| \frac{\varepsilon_m - \varepsilon_d}{\varepsilon_m + 2\varepsilon_d} \right|^2 \quad \text{Equation (1.35)}$$

$$C_{abs} = kIm[\alpha] = 4\pi k a^3 Im \left[\frac{\varepsilon_m - \varepsilon_d}{\varepsilon_m + 2\varepsilon_d} \right] \quad \text{Equation (1.36)}$$

Both expressions of C_{abs} and C_{sca} show that absorption and scattering are resonantly enhanced at the dipole particle plasmon resonance (when the Fröhlich condition is met).

The difference in radius a dependence of C_{abs} (a^3) and C_{sca} (a^6) shows that the scattering is the dominant process for big nanoparticles, while for the smaller nanoparticle, the absorption is the dominant process.

For a spherical nanoparticle with volume V and dielectric function $\varepsilon_m = \varepsilon_1 + i\varepsilon_2$ in the quasi-static approximation, the expression of the extinction cross-section $C_{ext} = C_{abs} + C_{sca}$ is defined as:

$$C_{ext} = 9 \frac{\omega}{c} \varepsilon_d^{\frac{3}{2}} V \frac{\varepsilon_2}{[\varepsilon_1 + 2\varepsilon_d]^2 + \varepsilon_2^2} \quad \text{Equation (1.37)}$$

In the case of small nanoparticles ($\frac{a}{\lambda} < 0.1$), only the dipole oscillations contribute to the C_{ext} . For this case, Gustav Mie presented a solution to the Maxwell equations to obtain the C_{ext} spectrum for well-separated nanoparticle [36].

$$C_{ext} = \frac{24\pi^2 R^3 \varepsilon_d^{\frac{3}{2}} N}{\lambda \ln(10)} \frac{\varepsilon_2}{(\varepsilon_1 + \chi \varepsilon_d)^2 + \varepsilon_2^2} \quad \text{Equation (1.38)}$$

where ε_d is the dielectric constant of the surrounding medium, $\varepsilon_m = \varepsilon_1 + i \varepsilon_2$ is the complex dielectric function of the bulk metal, R is the nanoparticle's radius, and N is the electron density. The factor χ accounts for the nanoparticle's shape and has a value of 2 for a sphere but can be as large as 20 for nanoparticles with high aspect ratio such as nanorods.

The LSPR will split into two distinct modes for ellipsoidal nanoparticles due to surface curvature and symmetry [38]. The C_{ext} of nanoparticle with various shapes can be theoretically modeled.

The C_{ext} of gold nanorods can be expressed as follows [38]:

$$C_{ext} = \frac{2\pi V}{3\lambda} \varepsilon_d^{\frac{3}{2}} \sum_j \frac{\left(\frac{1}{P_j}\right) \varepsilon_2}{(\varepsilon_1 + (1-P_j)/P_j) \varepsilon_d)^2 + \varepsilon_2^2} \quad \text{Equation (1.39)}$$

where: V is the volume of the nanoparticle and P_j is the depolarization factor.

The depolarization factor $P_{length,width}$ for elongated particles is written as [38]:

$$P_{length} = \frac{1-e^2}{e^2} \left[\frac{1}{2e} \ln \left(\frac{1+e}{1-e} \right) - 1 \right] \quad \text{Equation (1.40)}$$

$$P_{width} = \frac{1-P_{length}}{2} \quad \text{Equation (1.41)}$$

where e is the ellipticity is given by:

$$e^2 = 1 - \left(\frac{length}{width} \right)^{-2} \quad \text{Equation (1.42)}$$

Hence, ellipsoidal nanoparticles exhibit strong polarization-dependent spectra; thus, small changes in the aspect ratio will induce considerable changes in extinction bands [36].

For larger nanoparticles, LSPR modes of higher multipoles can occur (e.g., quadrupoles), where half of the electron cloud moves parallel and half anti-parallel to the electric field [39] and appear in the C_{ext} spectrum as multiples resonance peaks. Therefore, special attention must be paid to nanoparticles' size and shape when identifying the origin of the resonance maximum. Moreover, for larger nanoparticles, the resonance red-shifts result from retardation effects where conduction electrons do not move all in phase [41].

1.2.2.3. Absorption and scattering cross-section of metallic nanoparticle beyond the quasi-static approximation.

Having previously obtained the general expression of the polarizability of a metal sphere (see Equation 1.39) in the quasi-static approximation, we will now focus on seeing the changes in the spectral position and width

of the plasmon resonance for larger nanoparticles ($\frac{a}{\lambda} > 0.1$) [37]. The expansion of the first TM mode of Mie theory gives the polarizability of a sphere of volume V , with the following expression:

$$\alpha_{sphere} = \frac{1 - \left(\frac{1}{10}\right)(\varepsilon - \varepsilon_{env})x^2 + O(x^4)}{\left(\frac{1}{3} + \frac{\varepsilon_{env}}{\varepsilon - \varepsilon_{env}}\right) - \frac{1}{30}(\varepsilon - 10\varepsilon_{env})x^2 - i\frac{4\pi^2\varepsilon_2^2 V}{3\lambda_0^3} + O(x^4)} V \quad \text{Equation (1.43)}$$

where: $x = \frac{\pi a}{\lambda_0}$ is the *size parameter*, linking the radius of nanoparticle to the free-space wavelength λ_0 .

The term quadratic in x in the numerator includes the effect of retardation of the exciting field over the volume of the sphere, which induces a shift in the plasmon resonance. The denominator's quadratic term also induces a shift in the position of plasmon resonance due to the retardation of the *depolarization field* inside the nanoparticle. For noble and Drude metals, the shift is towards lower energies (higher wavelengths), the spectral position of the dipole resonance redshifts with increasing nanoparticle size. This can be seen as a consequence of the increase in the distance between the charges at opposite interfaces as nanoparticle size increases, leading to a smaller restoring force and a lower resonant frequency. This redshift indicates that the effect of the interband transition (characterized by an increase in $Im[\varepsilon_2]$) not considered by the Drude theory, decreases as the plasmon resonance moves away from the interband transition edge [37].

The quadratic term in the denominator increases the magnitude of the polarization and therefore diminishes the influence of absorption due to the imaginary part of ε . However, this magnitude increase is counteracted by the third, completely imaginary term in the denominator, which accounts for the *radiation damping*. The inclusion of higher-order terms in Equation (1.43) compared to Equation (1.32) will also account for the occurrence of higher-order resonances. A direct radiative decay route of the coherent electron oscillation into photons produces radiation damping. Radiation damping accounts for the weakening of the dipole plasmon resonance strength as the nanoparticle volume increases. With the nanoparticle volume increasing, the plasmon resonance significantly broadens, although an increase in nanoparticle volume decreases the strength of the non-radiative decay pathway (absorption).

Therefore, we can conclude that the plasmon resonance of particles beyond the quasi-static regime is damped by two competing processes: a radiative decay process into photons (dominant in larger nanoparticles) and a non-radiative process due to absorption. The non-radiative decay process is caused by the creation of electron-hole pairs via interband excitation within the conduction band or by the interband transition from the lower-lying d -bands to the sp -conduction bands (such is the case for noble metals) [37], [40], [42].

1.2.2.4. Coupling between localized plasmons

Until now, we have seen that the localized plasmon resonance of a single metallic nanoparticle can be shifted in frequency from the Fröhlich frequency by changing the nanoparticle shape, size, or surrounding dielectric environment (see Equation (1.34)). In nanoparticle arrays, the restoring force acting on each nanoparticle in the array is either increased or decreased by the charge distribution of the neighboring nanoparticles. This leads to a *blueshift* of the frequency of plasmon resonance for the excitation of transverse modes and *redshifts* for the excitation of longitudinal modes (see *Figure I-8*). Depending on the size of nanoparticles, the electromagnetic

interaction between nanoparticles can be pure of a dipolar nature (for small nanoparticles) but also can arise from the interaction between dipole and higher-order plasmonic modes (e.g., dipole-multipole, multipole-multipole interaction, etc.) [37].

If we take the case of nanoparticles with a size a arranged in a one or two-dimensional array, with an interparticle spacing d and we assume that $a \ll d$ then the nanoparticles can be treated as point dipoles.

Depending on the magnitude of the interparticle spacing, there are two possible regimes (see Figure I-9). If two nanoparticles are close to each other ($d \ll \lambda$), the near-field interaction with a distance dependence of d^{-3} is dominant and the array can be seen as an array of point dipoles interacting through their near-field. This leads to strong field localization in the nano-size gaps between the adjacent nanoparticles. Field localization, which is due to the suppression of scattering in the far-field by the excitation of plasmon modes in the nanoparticles along the chain axis, is mediated by the near-field coupling. This coupling leads to a *redshift* in the localized plasmon resonance position, shifting with a magnitude depending on the inter-particle distance.

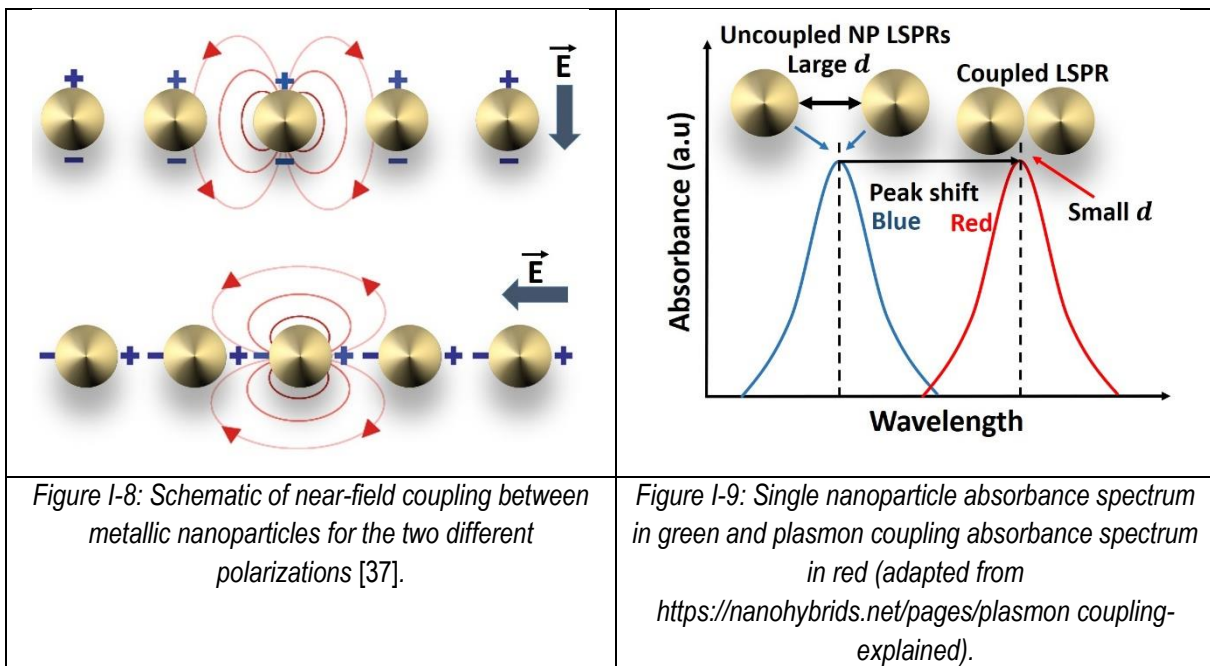


Figure I-8: Schematic of near-field coupling between metallic nanoparticles for the two different polarizations [37].

Figure I-9: Single nanoparticle absorbance spectrum in green and plasmon coupling absorbance spectrum in red (adapted from [https://nanohybrids.net/pages/plasmon coupling-explained](https://nanohybrids.net/pages/plasmon%20coupling-explained)).

If the nanoparticles are sufficiently apart, one to each other, so that the restoring force acting on each nanoparticle is not influenced by the neighboring nanoparticles, the resonant frequency will not be affected by near-field coupling effects. Therefore, far-field dipolar coupling with a distance dependence of d^{-1} dominates. In this case, the resonant frequency is linked to Fröhlich's condition and shape-size considerations.

I.2.3. Numerical approaches used to simulate the scattering of electromagnetic radiation by metallic nanoparticles.

An alternative way to calculate the LSPR spectra are based upon computational techniques. Simulation techniques such as Mie theory, the T-Matrix null-field method, the discrete dipole approximation (DDA), and the finite-difference time-domain method (FDTD) can be successfully implemented for determining the optical properties of metallic nanoparticles [38], [43]. These numerical approaches can, in principle, be applied to

nanoparticles of any arbitrary shapes and sizes, nanoparticles placed on a substrate, nanoparticles embedded in a dielectric medium, etc. A review of these techniques is beyond the scope of this thesis; therefore, we will briefly present FDTD, for more see also Appendix 1.3.

Finite-difference time-domain (**FDTD**) computational technique involves discretization of time and space; in the Maxwell curl equations (see Table I-1), all spatial and temporal derivatives are replaced by finite difference quotients [43]. Maxwell's equations that are linked to the temporal change of electric field E on the spatial change of magnetic field ($H = B/\mu$), and vice versa [44]. The FDTD method employs a second-order finite centered approximation to space and time derivatives in Maxwell's curl equations to obtain discrete electromagnetism [44]. In this method, usually, a Cartesian volume element of sides $\Delta x, \Delta y, \Delta z$ is used for the space discretization, while time discretization is made using a Δt step. Space discretization can be made using several methods, the most common employing an orthogonal cubic spatial grid called Yee unit cell [45].

The FDTD idea is to inject a plane wave at some initial time and compute new field components from differences calculated using the field components that applied during the previous time interval [43]. The electric field vector components in the volume element are solved at a given instant in time; after that, they have solved the magnetic field vector components in the same volume element but at the next instant in time. This procedure goes on iteratively until the transient solution for the fields has converged to a steady-state solution.

The near-field solution inside the computational domain is then Fourier transformed into the frequency domain and subsequently propagated into the far-field, by employing either a surface integration technique or in some cases a volume integration technique. Special consideration has to be made when simulating individual nanoparticles by this method to prevent the scattered fields from being reflected at the boundary of the computational domain. Another consideration is that the dispersion information must be specified over a much larger range of frequencies than that of interest because the FDTD method is solved in the time-domain. This implies that the permittivity of metallic nanoparticles has to be approximated using a frequency-dependent permittivity model [43]. The FDTD simulations technique use the Drude-Lorentz model.

In FDTD, the optical response in the frequency domain of metallic nanoparticles is found by taking a Fourier transform of the time-domain signal associated with the scattered electric and magnetic field distributions [43]. For a more in-depth description of the FDTD technique, see also [45]–[48].

Each of the simulation methods has its pros and cons. Many factors should be considered when selecting the most suitable method for determining the optical properties of a system that has LSPR. J. Parsons et al. [43] summarize each approach's significant advantages and disadvantages as a useful reference guide for future calculations. J. Parsons et al. [43] findings are presented in Table I-2. They [43] have simulated the scattering of electromagnetic radiation from metallic spherical nanoparticle of Au (size =80 nm) to compare the computation time, advantages and disadvantages of simulation techniques (Mie theory, the T-Matrix method, the DDA, and the FDTD method). They used a personal computer (Dell Vostro 200), with a dual-core processor (each with a clock speed of 2.19 GHz) and 2Gb of RAM). It is worth mentioning that, here, no validity tests are performed.

Table I-2: Comparison of numerical techniques used to simulate the scattering of electromagnetic radiation by metallic nanoparticles [43].

Method	Computation time for Au spherical nanoparticles ($radius \ll \lambda$)	Advantages	Disadvantages
Mie Theory	Rapid	Rapid computation time. It can also be used to compute the optical response of coated nanoparticles.	Applicable just to spherically symmetric nanoparticles. Not possible to include a substrate interaction, hence not possible to replicate many experiments.
	Few milliseconds for each frequency		
T-Matrix	Rapid	Supports a wide range of geometries. Has the possibility to include a substrate interaction.	Computations are numerically unstable for elongated or flattened objects (the matrices are truncated during computation; rounding errors become significant and accumulate rapidly)
	Few milliseconds for each frequency		
DDA	Moderate	Can be used to evaluate any arbitrary shaped nanoparticles by specifying a tabulated list of dipole location.	Convergence criterion: $n kd < 1$ n = complex refractive index, k = wavevector, d = inter-dipole separation (Not adapted for high aspect ratio/ elongated nanoparticles or those having a large refractive index)
	Depends on the number of dipoles and separation (usual 50s per individual frequency)		
FDTD	Lengthy	Can be used to evaluate scattering parameters from any arbitrarily shaped nanoparticles.	Computation time is lengthy. Permittivity values have to be specified over a much wider frequency range than just the range of interest. The Drude-Lorentz model may not be an accurate representation of experimental data.
	A broadband response is computed across a wide frequency range, usually taking around 3 hours to cover visible frequencies. A compromise is made between the computation time and element length.		

I.2.4. LSPR theoretical spectra of nanoparticles with different shapes, obtained by implementing the plasmonic simulation techniques (Mie Theory, DDA, and FDTD)

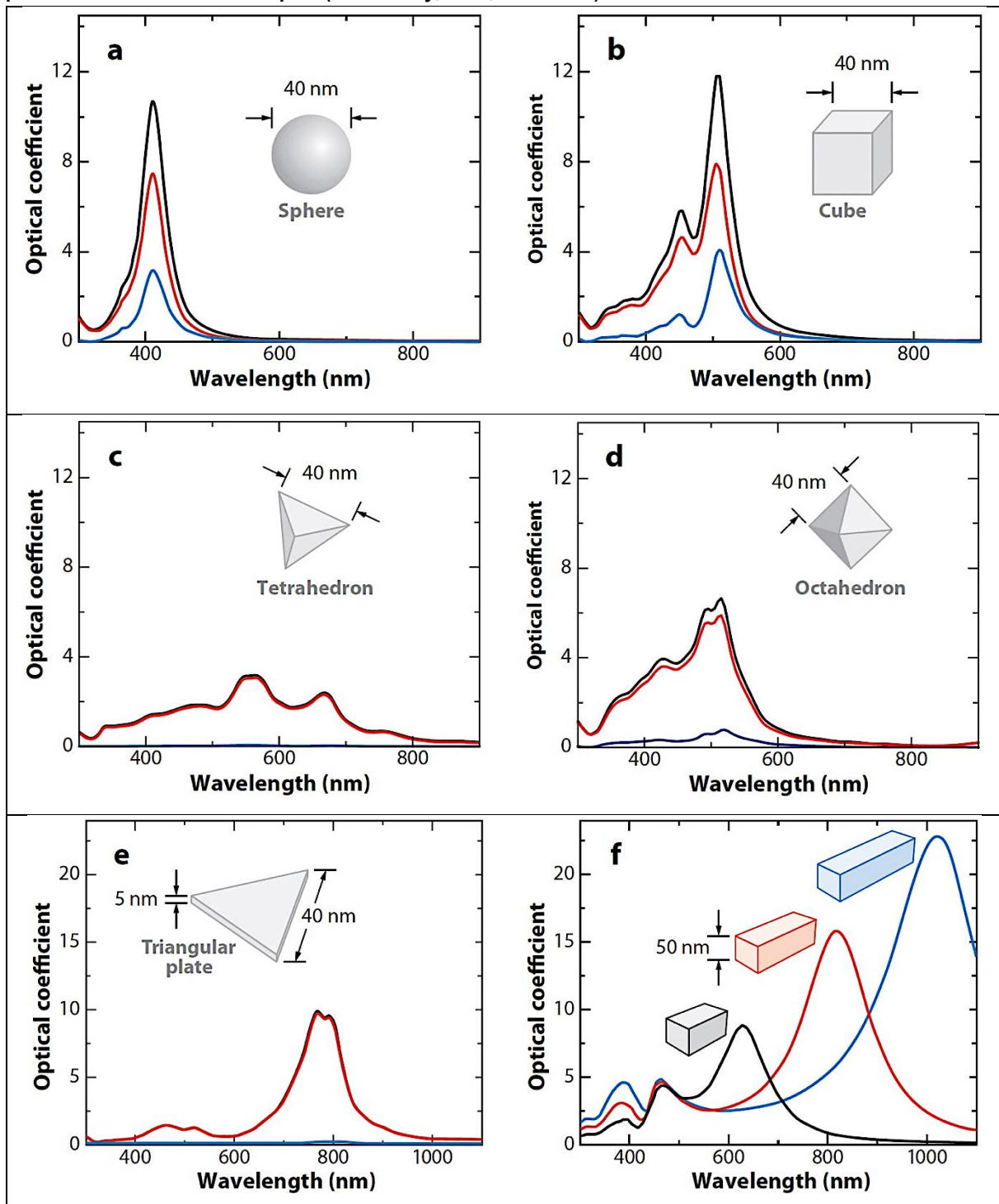


Figure I-10: LSPR resonance peaks of different nanoparticle shapes;(extinction- black curve, absorption – red curve and scattering- blue curve); for **a)** sphere, **b)** cube, **c)** tetrahedron, **d)** octahedron, **e)** triangular plate. **f)** Extinction spectra of rod-shaped nanoparticles with aspect ratios of 2 (the black curve), 3 (the red one), and 4 (the blue curve). These figures are taken from reference [49]; the panels **a)**-**e)** were modified by [49] from reference [50], while panel **f)** was also modified by reference [49] from reference [51].

Figure I-10 makes a comparison between the LSPR spectra theoretically calculated for silver (Ag) nanoparticles of different shapes, nanoparticles suspended in water. The LSPR spectra for a 40 nm Ag spherical nanoparticle, presented in *Figure I-10 a)*, were calculated using Mie Theory. In the spherical nanoparticle case, the LSPR has the main resonance peak at 410 nm, coming from the dipolar resonance and a small resonance shoulder, at 370 nm, that can be assigned to a quadrupole type of resonance. The **dipole** resonance is given by the charge separation at the surface of the nanoparticle (the side is positively charged while the other side is negatively charged), charge separation that gives to nanoparticle itself a dipole moment that reverses sign at the same frequency as the incident light [49]. The **quadrupole** resonance results from the energy losses that induce non-uniformity of the incident light across the nanoparticle, thus giving rise to the formation of two parallel dipoles of opposite sign [49].

In *Figure I-10 b)* is presented the extinction, absorption, and scattering spectra of a 40 nm Ag cube, determined by using the DDA method. In this case, the spectra show multiples peaks present because a cube has several distinct symmetries for dipole resonance [49]. Besides the presence of multiple peaks, the most intense peak is also redshifted compared to the one given by a spherical nanoparticle. A redshift comes from the accumulation of surface charges in the corners of the cube. This redshift is observed for any nanoparticle with sharp corners, compared to a spherical nanoparticle, and comes from the increased charge separation that reduces the strength of the restoring force for electron oscillation, resulting in a resonance shift to lower frequencies [52]. The LSPR shift evolves in the same way (redshifts) also for the tetrahedron and the octahedron (see *Figure I-10 c)* and *d)*). When the nanoparticle shape changes from spherical to a more two-dimensional nanoparticle, as is the case of the triangular nanoparticle (see *Figure I-10 e)*), the LSPR resonance redshifts even further based on increasing charge separation. Simultaneously, the intensity of the LSPR resonance changes; it decreases in intensity for the triangular nanoparticle compared to the spherical nanoparticle or the cubical nanoparticle because the triangular nanoparticle has a lower symmetry than the other nanoparticle shapes.

In *Figure I-10 f)* is presented the extinction spectra of a rod-shaped nanoparticle with varying aspect ratios (i.e., longer and longer compared to its width or thickness). The spectra show the same multiple peaks, as was the case of the cubical nanoparticle (see *Figure I-10 b)*), however as the aspect ratio changes, the main resonance red-shifts to higher and higher frequencies, changing the position of the resonance from visible to the near-infrared.

K. Schraml et al. [53] performed simulations based on the FDTD technique on Au nanoparticles with a cylindrical shape, triangle-shaped nanoparticles, and two coupled triangular nanoparticles (see *Figure I-11*). In this case, all the nanoparticles have a thickness of 35 nm and size defined as the length along the x axis of 140 nm. In the FDTD simulation, [53] has determined the LSPR peak position, the electric field enhancement in the vicinity of nanoparticles, using perfectly matched layers as boundary conditions, and a mesh size of 1 nm. The electric field enhancement is defined as the ratio of the steady-state electric field intensity $|E|^2$ compared to the electric field of the incoming plane wave $|E_0|^2$ [53].

Figure I-11 a) consists of a cylindrical nanoparticle of Au with a dipole type of resonance, with a single resonance peak as seen in *Figure I-11 d)*. From the map of electric field distribution (see *Figure I-11 a)*) it is visible the electric field has a higher intensity outside (in the near vicinity) the nanoparticle compared to the inside of it,

with a distribution proving the existence of charge separation. In the case of a triangular nanoparticle (see *Figure I-11 b*), we see a similar dipole type resonance, with a single peak (see *Figure I-11 e*), a peak that is shifted to lower photon energy (or higher frequencies) compared to the LSPR peak of a cylindrical nanoparticle.

More than this, the electric field is distributed outside the triangular nanoparticle in a way that proves the accumulation of charges on the corners of nanoparticles. These two facts, LSPR peak shift and charge accumulation on the corners, are in perfect agreement with the DDA simulation's conclusions (see *Figure I-10*).

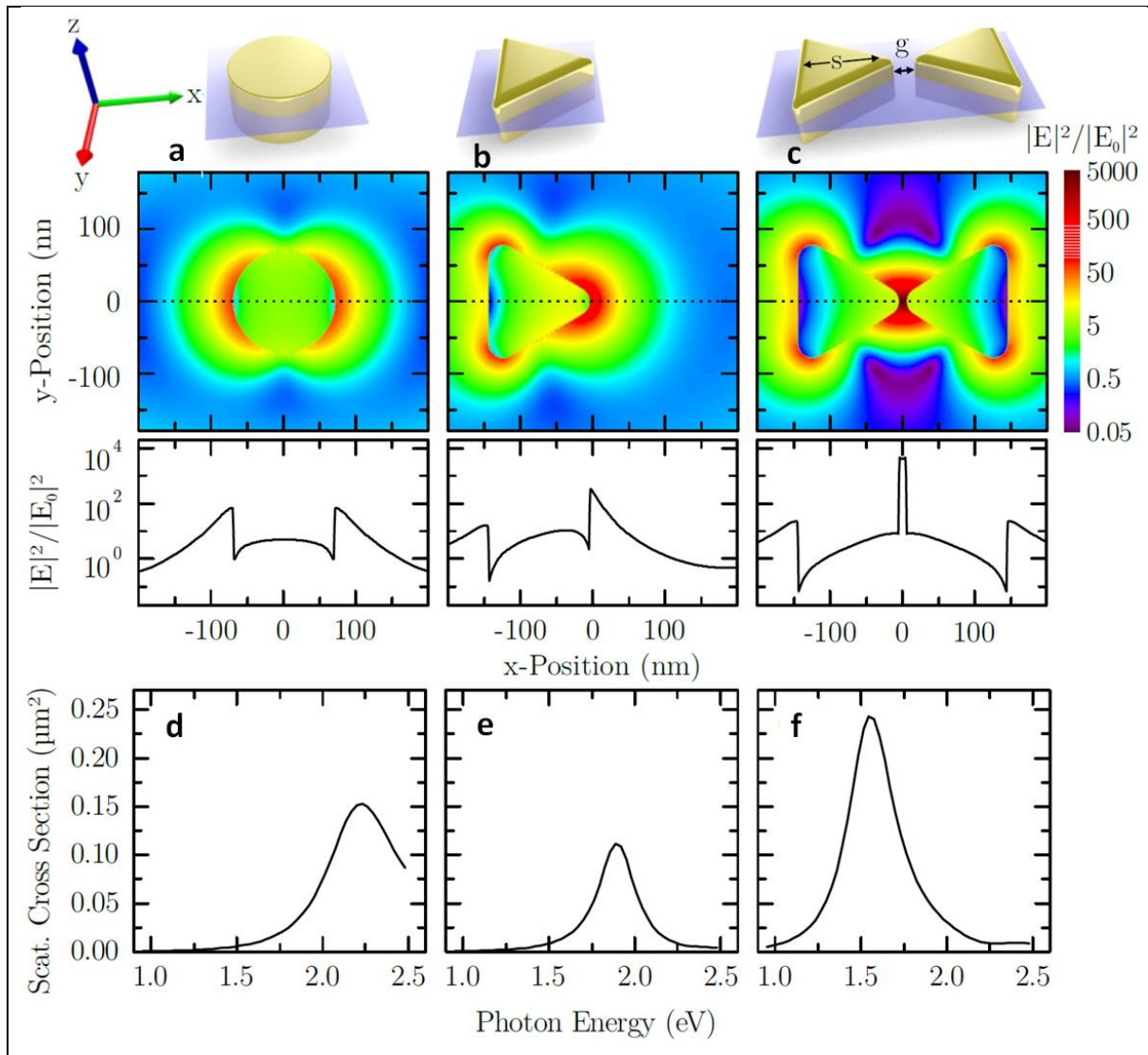


Figure I-11: Shape and electric field distribution of a) cylindrical nanoparticle, b) triangular nanoparticle, and c) two triangular nanoparticles. Scattering cross-section for d) cylindrical nanoparticle, e) triangular nanoparticle, and f) two triangular nanoparticles; Image is taken from [53].

When two nanoparticles are brought close one to another, as is the case of nanoparticles in *Figure I-11 c*), the position of the resonance peak (see *Figure I-11 c*)) red-shifts in rapport to the resonance peak of a single nanoparticle. The intensity of the resonance peak increases because of nanoparticle coupling. The electric field's intensity is greater in the gap between the two nanoparticles, proving that the charges of each nanoparticle have an impact on the charge distribution of the other one and vice versa. Considering all of this (*Figure I-10* and *Figure*

I-11), it is clear that DDA and FDTD can yield consistent results (i.e., even if the materials are different, the conclusion is the same). For more practical simplification see reference [43].

I.3. Applications of Localized Surface Plasmon Resonance: Surface-enhanced Raman scattering and Surface-Enhanced Infrared Absorption

One important application of surface plasmons is based on enhancing the scattering process of emitters (e.g., a molecule) near metal nanostructures. Surface-Enhanced Raman Scattering (**SERS**) is such an application [31], [54], [55]. Raman scattering is the inelastic scattering of photons that can occur when photons interact with matter. In the interaction, photons can lose energy to a molecule that gets excited from the ground state to its first excited vibrational state (known as Stokes Raman scattering) or, photons can gain energy from a molecule that undergoes the opposite process (anti-Stokes Raman scattering). By this way, inelastically scattered photons contain information on the vibrational modes of the materials through which they interact [54].

To a certain degree, it is possible to consider that Surface-Enhanced Infrared Absorption (SEIRA) and SERS phenomena have a similar mechanism behind their generation. The techniques are complementary, and both the electromagnetic and chemical effects play a crucial role. Nevertheless, there are significant differences.

The primary difference between SEIRA and SERS is that SERS happens when there is a change in the molecule's polarizability close to the substrate/surface, and SEIRA, there is a need for a change in the dipole moment perpendicular to the substrate surface [56].

In SEIRA, the incident photons are inelastically absorbed with a probability that is proportional to the product of incident light intensity and the enhancement at the plasmonic hot spot in which the absorbing material (molecule) is placed [57].

For more informations about SEIRA and SERS see Appendix 1.3.

I.4. Materials and their optical properties

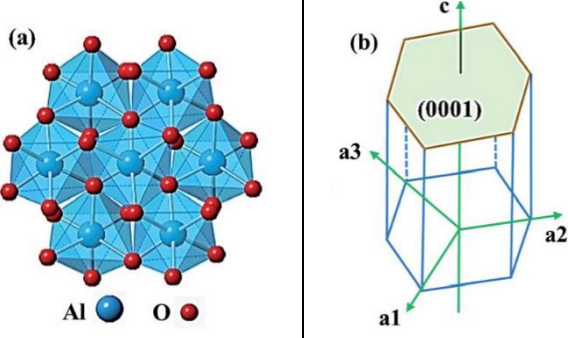
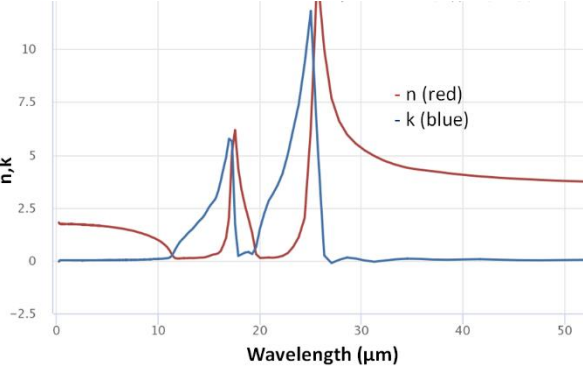
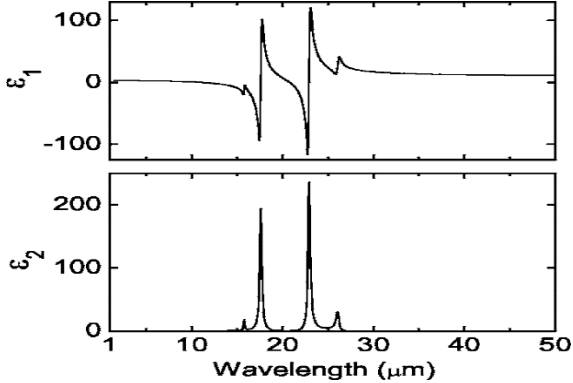
This section is dedicated to presenting the optical and physical properties of the materials used to manufacture the samples on which this thesis is based. The materials used are, Gold (Au), Iridium (Ir), Vanadium dioxide (VO_2), Alumina and Sapphire (Al_2O_3)

In our experiments, the Sapphire (Al_2O_3) is used as a substrate. It is a double polished single crystal with a hexagonal structure and (0001) c-plane orientation. It has a thickness of 500 μm and a size of approximately 1 cm^2 .

The data linked to the electrical, thermal, and mechanical characteristics of Al_2O_3 (0001) are taken from the data files provided by substrate suppliers (Neyco).

Figure I-13 shows that the real part of the dielectric function is almost constant, and the imaginary part is zero below a wavelength of 10 μm . And if we couple this with the refractive index and extinction coefficient measurements (see *Figure I-13*), it is clear that the sapphire substrate is transparent in this region. The thickness can also affect the transparent region, and in our experiments, the Al_2O_3 (0001) substrate is transparent between 0.2-0.3 μm up to 6 μm . The peaks of n , k , ϵ_1 , ϵ_2 seen in *Figure I-13* and *Figure I-14* are due to phonon absorptions [58].

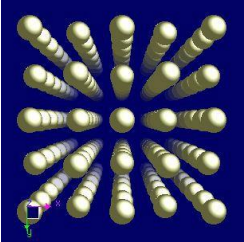
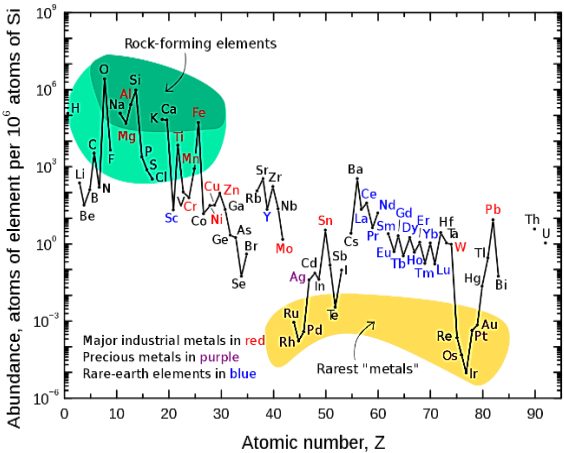
Table I-3: Physical properties of Al₂O₃ (Sapphire)-c substrates.

Crystal Structure		Mechanical Characteristics	
Hexagonal. a =4.758 Å c= 12.992 Å		Reference Density	3.97*10 ³ kg/m ³
	<p>Figure I-12: a) Crystal structure of Al₂O₃ (0001), b) A hexagonal (0001) plane [59].</p>	Flexural Strength	690 MPa
		Tensile Strength	2250 MPa
		Compressive Strength	2,940MPa
		Young's Modulus	470 GPa
		Electrical Characteristics	
		Dielectric Constant	11.5 (1MHz) IIC
			11.5 (1MHz) ⊥C
		Loss Factor	-(*10 ⁻⁴)
		Dielectric Loss Tangent	10 ⁻⁴ max
		Thermal Characteristics	
Melting Point	2,053°C		
Coefficient of Linear	7.7*10 ⁻⁶ /C IIC		
Thermal Expansion	7.0*10 ⁻⁶ /C ⊥C		
Thermal Conductivity	42W/(m*k)		
Specific Heat	0.75*10 ³ J/(kg*k)		
Optical Characteristics			
			
<p>Figure I-13: Refractive index (n) and Extinction coefficient (k) of Al₂O₃ (0001). Taken from https://refractiveindex.info/</p>		<p>Figure I-14: Dielectric function for the Al₂O₃ substrate is derived from the reflectance spectrum; ε₁, ε₂ real and imaginary part of the dielectric function, respectively [58]</p>	

I.4.1. Iridium (Ir)

The Iridium is used in our studies as a material for manufacturing the nanoparticles. The data related to the optical properties of Ir are extremely scarce. This is due, to on the one hand, to the very low abundance of Ir in the Earth crust (see *Figure I-15*) and, on the other hand, to its physical properties (see Table I-4) that make Ir rather hard to deposit as thin films and to work with, in general.

Table I-4: Physical properties of Iridium.

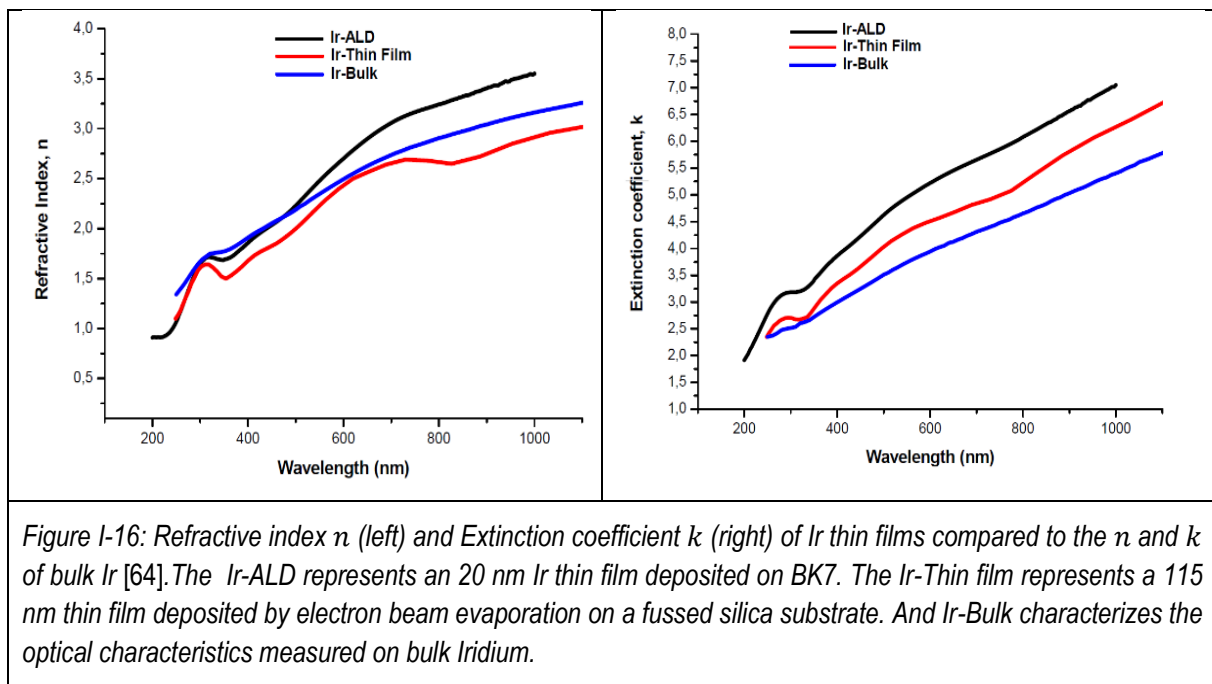
Crystal Structure		Physical properties	
	Cubic close-packed	Element category	Transition metal
	a: 383.9 pm	Electron configuration	[Xe] 4f ¹⁴ 5d ⁷ 6s ²
	b: 383.9 pm	Melting point	2719 K (2446 °C)
	c: 383.9 pm	Density	22.56 g/cm ³
	α: 90.000°	Heat of fusion	41.12 kJ/mol
	β: 90.000°	Heat of vaporization	564 kJ/mol
	γ: 90.000°	Molar heat capacity	25.10 J/(mol·K)
	Source: https://www.webelements.com	Thermal expansion	6.4 μm/(m·K)
	Thermal conductivity	147 W/(m·K)	
	Electrical resistivity	47.1 nΩ·m (20°C)	
	Young's modulus	528 GPa	
	Shear modulus	210 GPa	
	Bulk modulus	320 GPa	
	Poisson ratio	0.26	
	Mohs hardness	6.5	
	Discovery and the first isolation	Smithson Tennant (1803)	
	Source: https://www.webelements.com		
	<p><i>Figure I-15. Properties of Iridium and abundances of rare elements in Earth's crust relative to silicon [60].</i></p>		

Iridium is a Pt-group metal with a high melting point, low oxygen affinity, high chemical stability, and shows a lot of potential for various applications, such as protective coatings or as an electrode for future microelectronic devices [61].

Ir nanoparticles are synthesized by chemical means and show much potential in applications linked to the catalysis of many chemical reactions [62]. Ir was supposed to be an ideal catalyst candidate (between the Pt group metals) for oxygen evolution reaction, given its activity and stability [63].

A. Szeghalmi et al. [64] summarized the optical properties, in terms of refractive index and extinction coefficient in the UV to VIS range, of Ir thin films and compared them with their bulk counterparts. A. Szeghalmi et

al. [64] findings are presented in *Figure I-16*. In *Figure I-16*, the optical characteristics of Ir thin films are also taken from [65].



The Ir-ALD represents a 20 nm layer of Ir deposited on BK7 glass by atomic layer deposition (ALD), and the other data can be found in (<http://refractiveindex.info/>) database.

I.4.2. Gold (Au)

Gold (Au) has a special role in metal optics. In applications linked to optoelectronic, plasmonics or nano-optical devices, often, Au is used as a standard system for understanding the interaction of electromagnetic fields with metals. Although it is one of the most expensive metals (usually Platinum is more expensive), the relatively low quantities of Au used in plasmonics (in the form of nanoparticle the quantity of Au needed is usually low) makes it still a viable choice. Also, Au can be easily recycled (think of Au recycling from electronic devices such as cell phones, etc.).

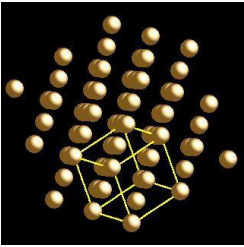

Gold is, and it was, essential for human society throughout history (see Table I-5) especially in jewelry and art in general, see *Figure I-17*. However, in today science Au is instrumental due to its particular properties such as relatively low melting point, high malleability, and ductility, it is a very good conductor of heat and electricity, low vapor pressure, and most important Au has a very low affinity towards oxygen (i.e., Au oxidized just in special conditions).

Gold was deposited as thin films by a variety of deposition techniques: sputter deposition [66], Pulsed laser deposition (PLD) [67] and electrochemical deposition [68].

Gold is made into nanoparticles by methods such as chemical methods [69], lithographic methods (using a template then removing the excess material, e.g., nanosphere lithography) [69] or directly by vapor deposition

methods (e.g., taking advantage of the Au wettability for the substrate and the growth mechanisms of Au layers (Volmer-Weber or "isolated islands")) [70].

Table I-5: Physical properties of Gold.

Crystal Structure		Physical proprieties	
	Cubic close-packed	Element category	Transition metal
	a: 407.82 pm	Electron configuration	[Xe] 4f ¹⁴ 5d ¹⁰ 6s ¹
	b: 407.82 pm	Melting point	1337.3K(1064°C)
	c: 407.82 pm	Density	19300 kg m ⁻³
	α: 90.000°	Heat of fusion	12.55 kJ/mol
	β: 90.000°	Heat of vaporization	334.4 kJ/mol
	γ: 90.000°	Molar heat capacity	25.6 J/(mol*K)
	Source: https://www.webelements.com		Thermal expansion
	Thermal conductivity	320 W m ⁻¹ K ⁻¹	
	Electrical resistivity	2.2 * 10 ⁻⁸ Ω m	
	Young's modulus	78 GPa	
	Shear modulus	26 GPa	
	Bulk modulus	220 GPa	
	Poisson ratio	0.44	
	Mohs hardness	2.5	
<p><i>Figure I-17: Oldest Gold treasure ever found. http://archaeologyinbulgaria.com Treasure from Europe's first human civilization, developed in the Neolithic in the Balkan Peninsula (Southeast Europe), 8,000 to 6,000 years ago. The treasure is 2000 years older than the Giza Pyramids (2504 BC). For more see info about: Varna Necropolis.</i></p>			

In plasmonics, the optical properties of Au thin films and nanoparticles are of great interest, and the literature is quite vast when it comes to this topic. However, there are significant discrepancies between the data of gold's optical properties. This is because surface quality considerably affects the optical response through crystal defects and morphology [71].

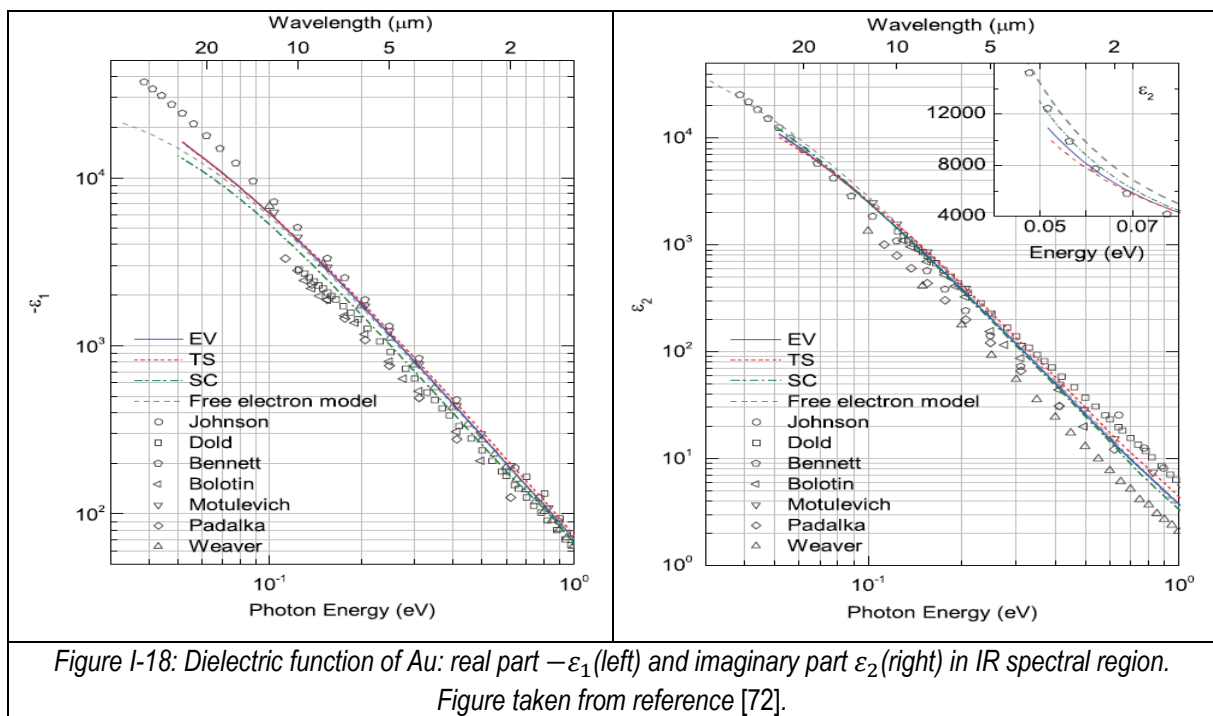
Optical data from the literature databases are often used to model any device function, such as plasmonic devices, but sometimes there is a significant difference between prediction (based on the modeling) and the result of the experimental measurements.

For a better understanding of the link among the characteristics of the samples (morphology, crystal defects, etc.) and the dielectric function, it is useful to split the optical range into two sections: low energy regime (i.e., IR part of the light spectrum) and the high energy part (associated with the visible and UV part of the light

spectrum). In IR, at low energies, the optical dielectric function of metals, like Au, is associated with electronic intraband transitions within the conduction band [72].

The optical feedback is governed by free-electron behavior in the IR range and offers information regarding the electron scattering rate and mean free path. In the VIS and UV range (high energy), the optical dielectric function is linked to the electronic interband transitions from the occupied d bands to the partially filled sp band [72].

Figure I-18 and Figure I-19 show the real and imaginary parts of Au thin films and bulk's complex dielectric function compared to the available data from the literature. The samples in Figure I-18 corresponds to SC single-crystal Au (111) with a thickness of 1 mm; EV to a 200 nm thick film deposited by evaporation onto a soda-lime glass substrate, and TS is a 200 nm thick template-stripped film deposited onto a silicon substrate in the same evaporation run while the others are data sets from the literature and from the included references [72].



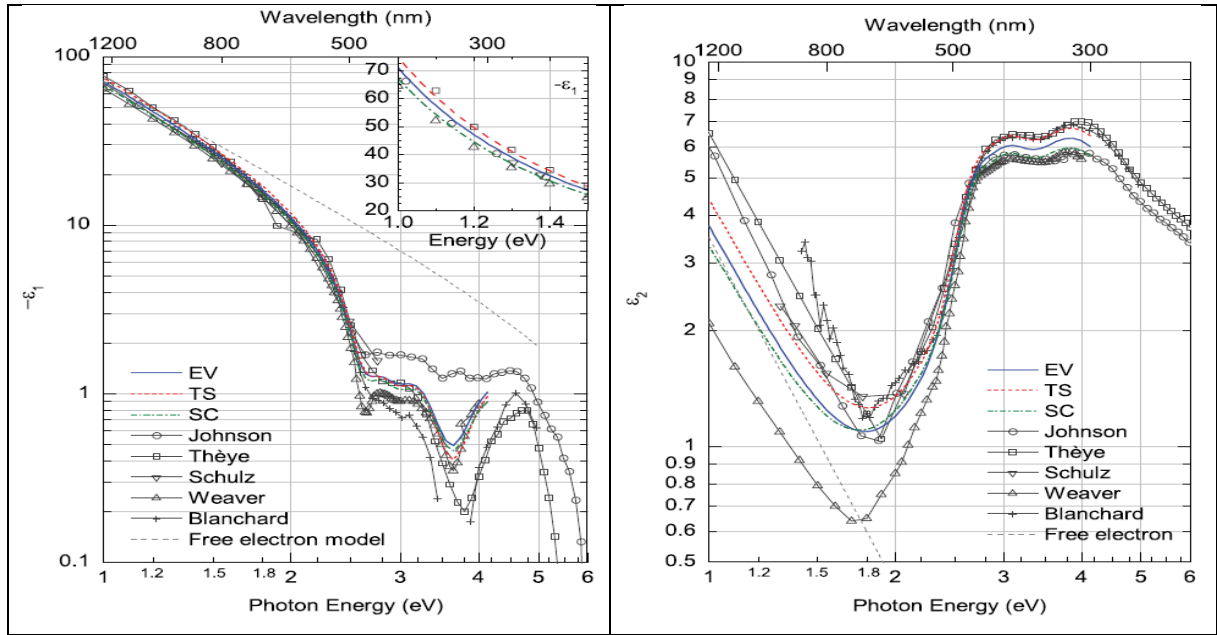


Figure I-19: Dielectric function of Au: real part $-\varepsilon_1$ (left) and imaginary part ε_2 (right) in UV, VIS and IR spectral regions. The figure is taken from reference [72].

Figure I-18 shows a variation between the optical properties of the samples in the IR regime. This variation can be due to voids' inclusion in a granular surface that causes depolarization of the local electric field on the metal surface and leads to a reduced plasma frequency and dielectric background [71]. Furthermore, electron scattering at the grain boundaries of crystallites dominates the scattering rate's behavior if the grains are smaller than the bulk electron mean free path, thus changing the optical response [71].

In the visible part of the spectral range, the real part of the optical dielectric function shown the greatest relative variation in the interband region, $E > 2.5 \text{ eV}$ (see Figure I-19). In the interband region, $E > 1.8 \text{ eV}$, the difference in imaginary part of the dielectric function can be attributed to differing effective volume densities of voids in the interaction region [72].

The fact that photons with low energy (IR) excite free charge carriers to intraband transition can be described using the Drude-Sommerfeld theory of the free electron; the theory which considers the motion of a gas of noninteracting electrons that are driven by an oscillating electric field and are scattered by different effects [71]. From which it is possible to deduce the Drude model for the dielectric function, with plasma frequency ω_p and the damping frequency ω_τ given by the following expressions [71]:

$$\omega_p [cm^{-1}] = \frac{1}{2\pi c} \left(\frac{Ne^2}{\varepsilon_0 m^*} \right)^{\frac{1}{2}} \text{ and } \omega_\tau [cm^{-1}] = \frac{1}{2\pi c\tau} \quad \text{Equation (1.44)}$$

where ε_∞ physically arises from the interband transition, N is the free electron density, e is the electron charge, m^* are the effective mass of the electron at the Fermi level and τ is the average scattering time.

From Equation (1.10), it is possible to calculate the dispersion relation of electromagnetic waves in Au (metals) at visible frequencies above the plasma edge as $\omega > \frac{\omega_p}{\sqrt{\varepsilon_\infty}}$, a relation that shows that electromagnetic waves can propagate in metals.

For Au, the plasma edge is difficult to determine precisely since it lies approximatively (~ 495 nm) in the same position where the interband resonances are located. This means that electromagnetic waves with energy smaller than $\frac{\omega_p}{\sqrt{\epsilon_\infty}}$ cannot propagate in Au. However, they can penetrate Au, with an intensity that decreases with distance [71].

The distance from which the electric field amplitude is attenuated by a factor of $\frac{1}{e}$ is called the *skin depth* δ_{skin} . For a plain wave the δ_{skin} is given by [71]:

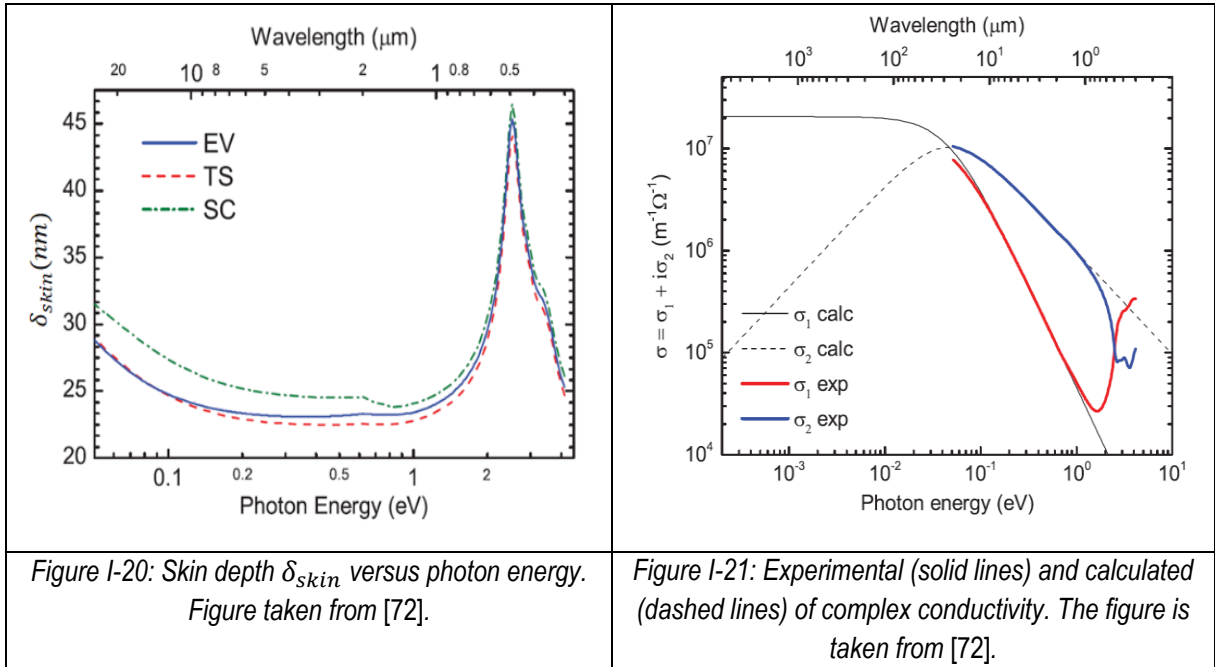
$$\delta_{skin} = \frac{c}{\omega k(\omega)} \quad \text{Equation (1.45)}$$

The Drude parameters are connected to the frequency-dependent conductivity $\sigma(\omega)$ by Equation (1.11).

$$\sigma(\omega) = \frac{\sigma_0}{1-i\omega\tau} \quad \text{Equation (1.46)}$$

where $\sigma_0 = \omega_p^2 \tau \epsilon_0$ is the Drude dc conductivity.

For Au thin films δ_{skin} and $\sigma(\omega)$ are presented in *Figure I-20* and *Figure I-21*, respectively.



In *Figure I-20*, the δ_{skin} is almost constant in the 1 to 10 μm range, close to 25 nm. The δ_{skin} small variation are a direct consequence of the variation of dielectric function between the samples. For all of the measured spectral range, the δ_{skin} value varies from 25 to 45 nm.

In *Figure I-21*, the experimental complex conductivity (solid lines) is a mean of the experimental values of the three samples (EV, SC, and TS), while the theoretical values (dashed lines) were deduced using the Drude-Sommerfeld model (with an electron relaxation time $\tau_D = 14$ fs and plasma energy $\hbar\omega_p = 8.45$ eV). The real part of the complex conductivity is noticeably reduced in the mid to near IR range, while the imaginary part is higher compared to lower frequencies due to a greater ohmic damping and a large phase offset between the excitation field and the charge motion [72].

I.4.3. Vanadium dioxide (VO₂)

With its discovery in 1959 [73], vanadium dioxide (VO₂), has rapidly become a material of great interest not just for scientific curiosity but also for research-driven towards the possibility to integrate it in different devices. VO₂ is a material with a temperature induced metal-insulator transition (MIT) accompanied by a structural phase transition (SPT).

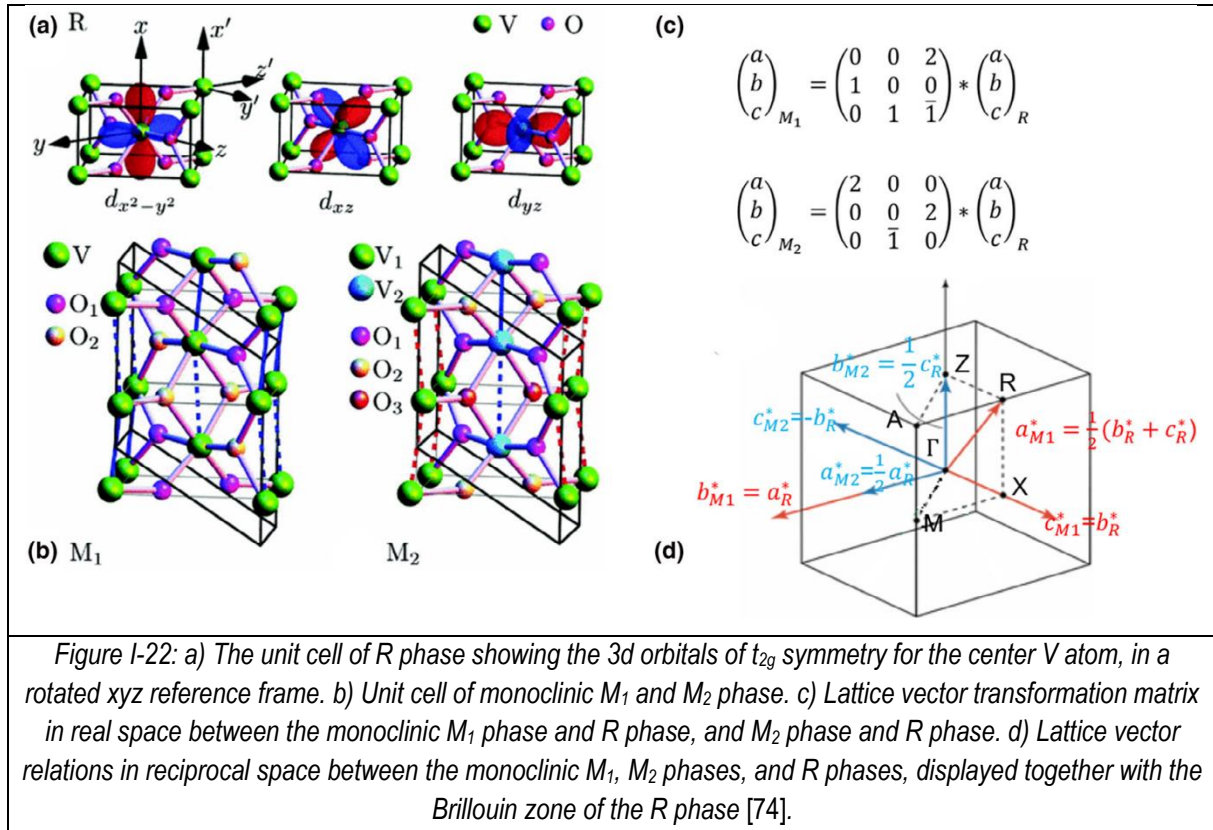
The MIT is characterized by a sharp change in VO₂ physical properties such as optical absorption, **dielectric function**, and electrical conductivity change. What is different from other materials is that in VO₂, the MIT and SPT are coupled and occur at relatively low and accessible temperature ($T_C \sim 340K$) [74]. MIT and SPT's coupling effect have sprouted a long-lasting debate in physics on trying to debate and eventually decide which comes first; MIT or SPT. Heating/cooling cycles, pressure, chemical doping, strain, intense optical fields, or intense electrostatic fields can drive the MIT in VO₂.

An impressive number of experimental and theoretical studies on the thermally driven MIT from the high-temperature metallic rutile (R) phase to the low temperature insulating monoclinic (M₁) phase, and still, the debate lives on. Some publications link the insulating M₁ phase to the vanadium-vanadium Peierls type pairing that leads to unit cell doubling, while others insist that the insulating M₁ phase is the result of Mott-Hubbard correlations [75].

In some cases, in VO₂ thin films exist at least two additional insulating phases: a monoclinic M₂ and a triclinic (T) phase. Determining this additional M₂ and T phases' exact properties could help bridge the knowledge gap in understanding the MIT in VO₂.

However, this has proven to be a challenge in itself since there is always a phase mixing in VO₂ during MIT (i.e., some VO₂ crystalline domains switch from M₁ to R, others go from M₁ to M₂ and then to R, in the same sample, and during the same heating cycle). The crystal structure of the most common phases of VO₂ is presented in *Figure I-22*.

When trying to understand the crystal structure of VO₂, the classical approach is to start from the high-temperature phase and then to go to the low temperature one. Above T_C (68°C) VO₂ adopts a tetragonal rutile (R) structure with space group $\frac{P4_2}{mmm}$ (#136) and lattice constants $a = b \approx 4.55 \text{ \AA}$ and $c \approx 2.85 \text{ \AA}$ (see *Figure I-22 a*) [74].

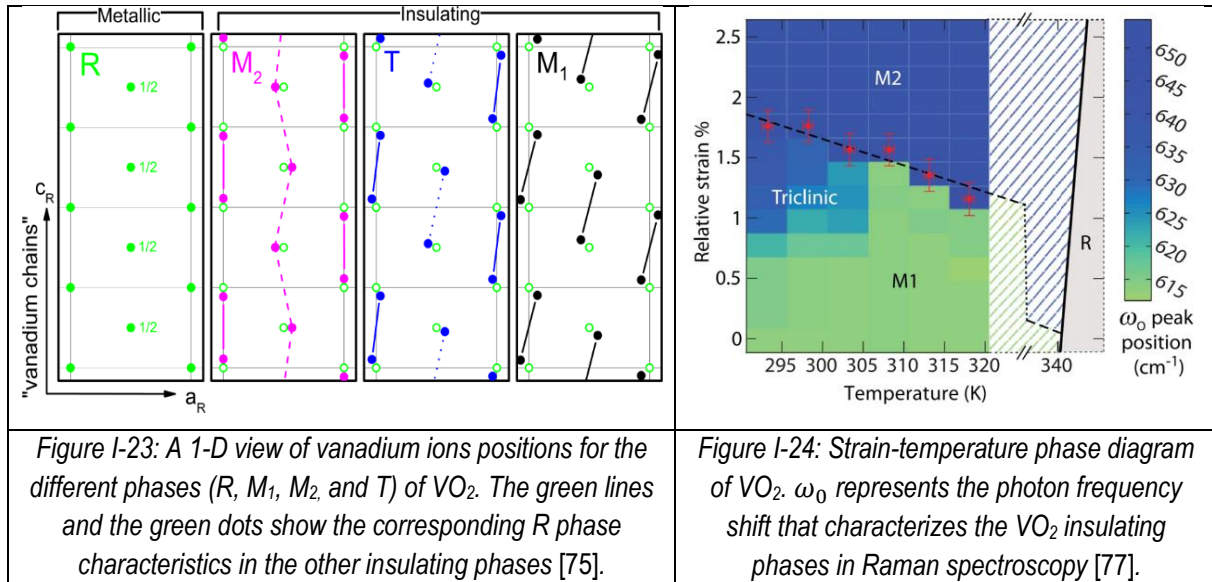


Below T_C the unstrained VO_2 has a monoclinic crystal structure M_1 , with a space group $\frac{P2_1}{c}$ (#14) and lattice constants $a \approx 5.75 \text{ \AA}$, $b \approx 4.53 \text{ \AA}$, $c \approx 5.38 \text{ \AA}$, and $\beta = 122.6^\circ$ [74]. Classically, M_1 is characterized by a doubling of the unit cell volume in comparison with the R phase (see Figure I-22) together with the dimerization pattern of vanadium chain along the c -direction of the parent R phase (see Figure I-22 b) [74]. This dimerization process results in a M_1 phase with two different $V - V$ bond lengths (see Figure I-23). A short 2.65 \AA intra dimer length of $V - V$ bond and a longer one of 3.12 \AA [74].

Besides R and M_1 phases, in VO_2 additional phases can be accessed by applying or because of strain (see Figure I-24). Such as monoclinic M_2 phase with space group $\frac{C2}{m}$ (#12) with $a \approx 9.066 \text{ \AA}$, $b \approx 5.797 \text{ \AA}$, $c \approx 4.526 \text{ \AA}$ and $\beta = 91.88^\circ$ [76]. And the T phase which is characterized by the space group $P\bar{1}$ (#2) with $a \approx 9.084 \text{ \AA}$, $b \approx 5.791 \text{ \AA}$, $c \approx 4.518 \text{ \AA}$, $\alpha = 90.03^\circ$, $\beta = 90.98^\circ$, and $\gamma = 90.1^\circ$ [76].

In the M_1 phase, the V ions all dimerize and tilt in equivalent chains along with the rutile c_R axes, while the M_2 phase has two different types of vanadium chains: in one case, the vanadium ions pair but do not tilt, and in the other case tilt but do not pair (see Figure I-22 b) and Figure I-23) [75]. In the latter chain, the vanadium ions are equidistant, and each of them carries a localized electron with a spin $-\frac{1}{2}$ magnetic moment and antiferromagnetic exchange coupling between the nearest neighbors [75]. In the M_2 phase, for vanadium chains that exhibit dimerization, the $V - V$ bonds have two sizes lengths: a shorter one of 2.538 \AA and a longer one of 3.259 \AA , while in the zig-zag chains all the $V - V$ bonds have a length of 2.933 \AA (see Figure I-23) [74].

The lattice vector transformation matrix in real space between the M_1 phase to R phase and M_2 to R phase is presented in *Figure I-22 c*), while the reciprocal lattice correspondence between the monoclinic phases and the rutile phases is presented in *Figure I-22 d*) [74].



The T phase can be considered an intermediate phase between the M_1 and the M_2 phases (see *Figure I-23*). In T's case, the phase has two types of inequivalent vanadium chains in which the vanadium ions are tilted and paired to different degrees [75].

By implying Raman spectroscopy, it is possible to distinguish between the different phases of VO_2 (see *Figure I-24* and, more explicitly *Figure I-25*). In Raman spectroscopy, the M_1 phase is associated with 18 Raman active vibrations ($9A_g+9B_g$). For the M_1 phase the A_g phonons are located at 137, 194, 224, 310, 340, 393, 499, 612 and 663 cm^{-1} and the B_g phonons have been found at 143, 224, 262, 393, 442, 484, 582, 820 cm^{-1} and the ninth B_g vibration is located probably at 450 cm^{-1} [76]. The vibration A_g mode at 194 cm^{-1} corresponds to vanadium atoms' motion along the c-axis of the VO_2 (i.e., stretching motion of $V - V$ dimers) [76]. The vibration s the mode at 339 cm^{-1} is linked to the perpendicular motion of metal ions, the tilting motion of $V - V$ dimers, whereas all the other bands are assigned to $V - O$ vibrations [76]. The R phase of VO_2 has a very different Raman signature then the other phases (see *Figure I-25*).

In general, the discussion of vibrational properties of the R phase of VO_2 is made in comparison with the rutile- TiO_2 , which has a similar structure. However, the VO_2 R phase has extremely weak and broad Raman bands. For the VO_2 R, weak bands have been found at 240, 390, 510, and 625 cm^{-1} and are associated with the motion of oxygen atoms [76].

The M_2 and T phases have similar spectral features as the M_1 phase (see *Figure I-25*). There are 18 allowed Raman active modes $10A_g+8B_g$ for M_2 and 18 A_g for T phases, like in the case of M_1 . In comparison with the M_1 , for the M_2 phase, the band position assigned to $V - O$ vibrations at 612 cm^{-1} shifts to 640 cm^{-1} , whereas the band associated with the stretching motion of $V - V$ dimers at 194 cm^{-1} shifts to 202 cm^{-1} for the M_2 phase

[76]. For the T phase of VO₂ the phonon wave number shifts to 126, 376, and 630 cm⁻¹, in rapport to M₁. This shift band position leads to a visual splitting of some T phase spectrum lines, especially the one at 575 cm⁻¹ (see *Figure I-25*) [76]. Note that the values of the phonon frequencies assigned above to the different vibration of V – V or V – O bonds may vary slightly from study to study due to strain (see *Figure I-24*) or different manufacturing techniques of the VO₂.

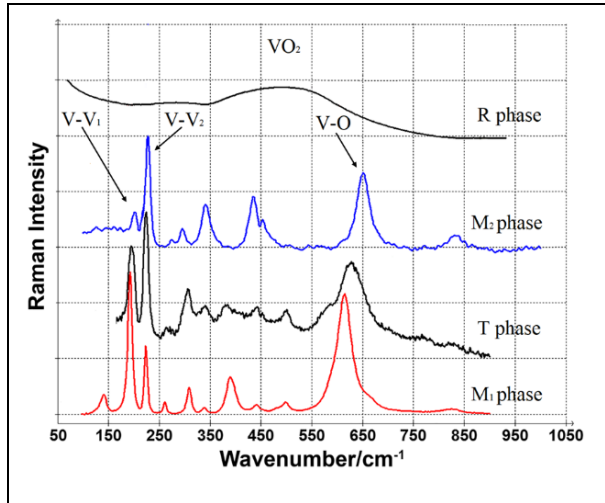


Figure I-25: Raman scattering in different phases of VO₂ (M₁, M₂, T, and R). Adapted from [76], [78]. Depending on the value of strain, the scattering of the VO₂ T can differ greatly from the spectrum presented here.

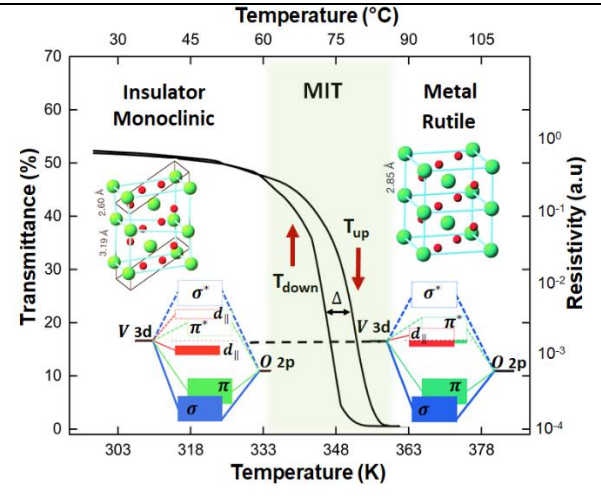
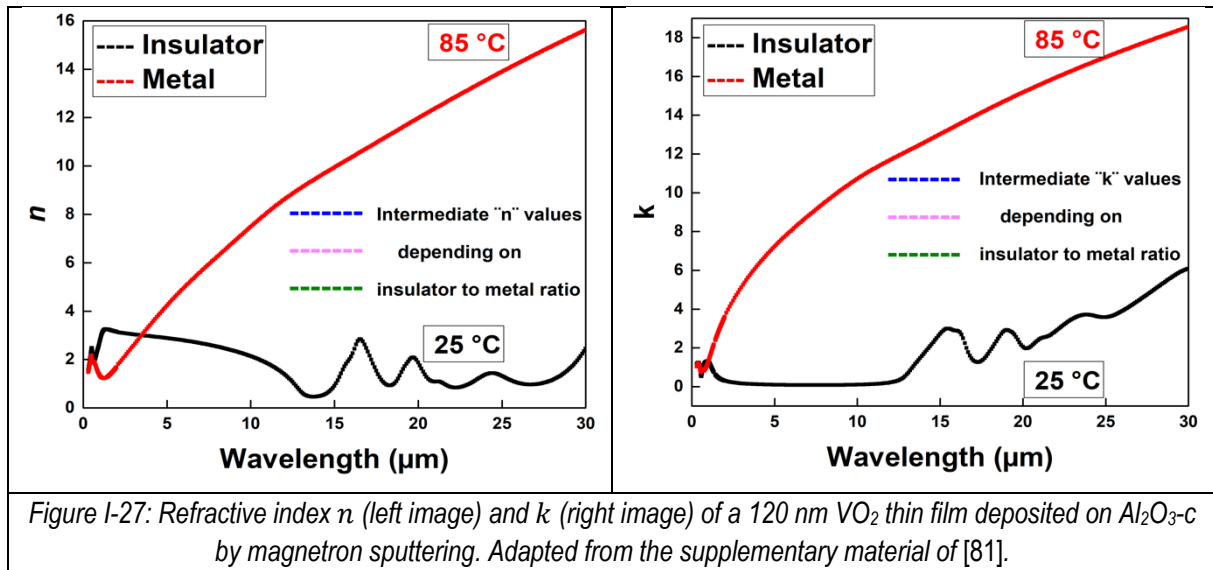


Figure I-26: Change of physical properties (resistivity, transmittance) of VO₂ as a temperature and phase function. Figure adapted from reference [79].

Goodenough [75] has proposed a model based on band theory for independent electrons to explain the overall band structure of the R phase of VO₂. In his model, the vanadium 3d orbital manifold splits into e_g and t_{2g} symmetry states because of the octahedral coordination with oxygen atoms [74]. Due to the orthorhombic component of the local crystal field, the t_{2g} split into two d_π orbitals and one d_\parallel [74]. The d_π orbitals point at the faces of the coordination octahedron and the d_\parallel orbital points along the c_R axes. The vanadium 3d orbitals are presented in *Figure I-22 a*). The zig-zag distortion (see *Figure I-23*) induces an upward shift of the π^* band above the Fermi energy E_F that leads to the formation of the d_\parallel bonding and antibonding states, and the dimerization of vanadium chains along the c_R axe increasing the band gap [74]. In Goodenough model, the combination of these band rearrangements leads to the opening of a bandgap in the insulating M₁ phase, presented in the insert of *Figure I-26* (for more information see Appendix 1.4)

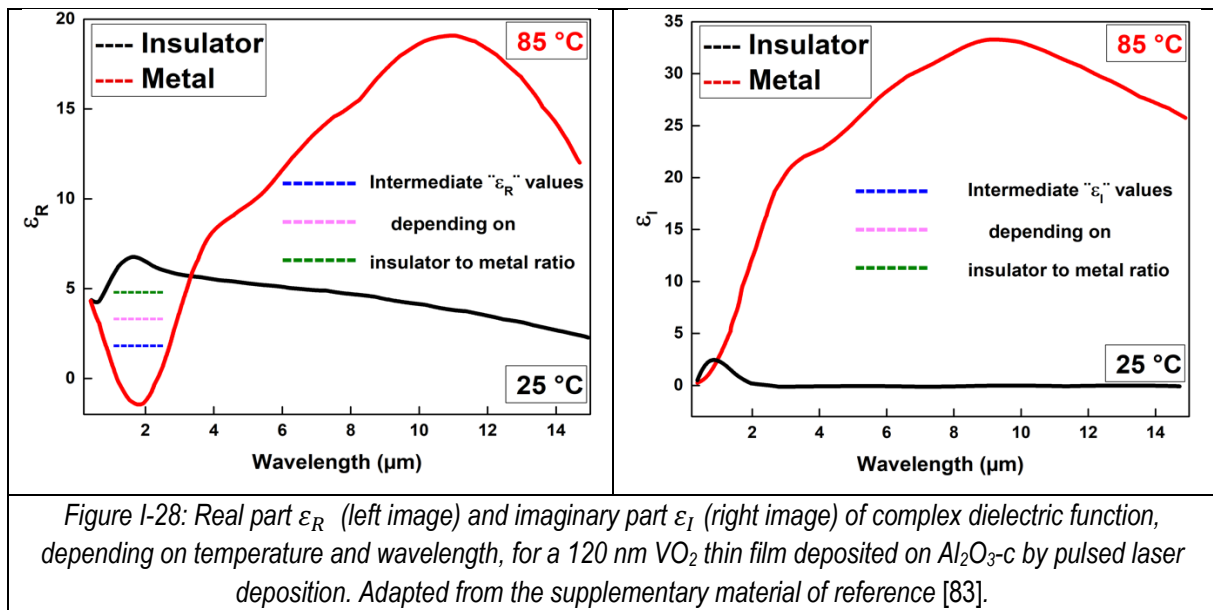
As presented in *Figure I-27*, the value of refractive index n and extinction coefficient k differ greatly from one phase to another.



Usually, the changes in physical properties given by MIT in VO_2 thin films are not as sharp as in the case of a VO_2 single crystal. Upon transition from an insulating phase to a metallic one and back to the starting insulating phase, the changes in VO_2 thin films properties have a hysteresis (i.e., there is an offset between the rate of properties change when going from M_1 to R compared to going from R to M_1 phase) (see Figure I-26). VO_2 thin films have two temperatures of transition, one for the insulator to metal transition and another one for metal to insulator transition. The value of the hysteresis would depend on many factors such as the crystalline quality of the VO_2 thin film, the substrate and if the thin film was doped or not (by using Ti, W, Nb, etc.). It also depends on the manufacturing technique used for making the thin film, etc. In a VO_2 thin film, there is a certain amount of delay between the transitions of each crystalline domains from the starting insulator phase to the final metallic one and back [82]. This may come from the fact that not all the crystallites follow the same transition path (some go from M_1 directly to R while others go from M_1 to M_2 and then to R). Besides, strain, defects, etc., can play a role in the temperature of transition and give rise to the coexistence of multiple phases of VO_2 at the same temperature.

The ratio between the coexisting phases changes with temperature (i.e., initially 100 % M_1 , then x % M_1 + y % M_2 , after x' % M_1 + y' % M_2 + z' % R and in the end 100 % R as we go up in temperature).

This implies that often in VO_2 , the global physical properties change gradually from the properties of the insulating phase to the properties of the metallic phase, and the most significant changes do not occur at the same temperature for heating up and cooling down. Therefore, it is possible to select as many values for n and k as possible for the temperature. However, for clarity of Figure I-27, we have chosen the values for n and k , measured during heating up and as a function of wavelength for the insulator and metallic phase, respectively. The same thing is real also for the complex dielectric function of VO_2 thin films. As presented in Figure I-28, both the real and imaginary parts of the complex dielectric function of VO_2 thin films depend a lot on the temperature and wavelength. Temperature changes the VO_2 phase, and with the increase of temperature, so does the ϵ_R and ϵ_I especially in the IR part of the optical spectrum.



I.5. Conclusions

In the *Chapter I* is given a brief theoretical approach of the interaction of electromagnetic waves with sub-millimeter objects. In metals, the free electrons can be thought of as an electron plasma. Plasmons can be described as quasi-particles resulting from the quantization of the plasma oscillation of the free electron gas density concerning the fixed positive ions in a metal. Surface plasmon resonances are coherent electron oscillations that are present at the interface between two materials where the real part of the dielectric function changes sign across the interface (i.e., SPR are electromagnetic excitations that propagate along the interface between a metal and a dielectric medium). As in the case of SPR, the electromagnetic field of incident light can be used to collectively excite the electrons from the conduction band of a metallic nanoparticle, resulting in coherent localized plasmon oscillations. The external field can penetrate the nanoparticle volume and shift the conduction electrons concerning the ion lattice. A way to calculate the LSPR spectra are based upon computational techniques. Simulation techniques such as Mie theory, the T-Matrix null-field method, the discrete dipole approximation (DDA), and the finite-difference time-domain method (FDTD) can be successfully implemented for determining the optical properties of metallic nanoparticles.

The metallic nanoparticle's optical properties can differ significantly from those of the metal from which they are produced. Metallic nanoparticles have tunable physicochemical characteristics such as light absorption, color change, and electrical and thermal properties that go beyond the limitations of the bulk material's inherent properties. The plasmonic characteristics of nanoparticles depend on geometrical characteristics (shape, size, etc.), on the material properties and on the dielectric environment.

Then the properties of the materials (Gold, Iridium, Vanadium dioxide, and Sapphire-c) that are used in this thesis are discussed. For these materials, the properties related to light-matter interactions (dielectric function, etc.) are presented. Thereby, taking all of this into account is possible to tune the LSPR position to the desired

wavelength. If we consider *Equation (1.33)* it is visible that the temperature tunability of the dielectric properties (VO_2 MIT) of the environment will induce a temperature tunability of LSPR.

Chapter II

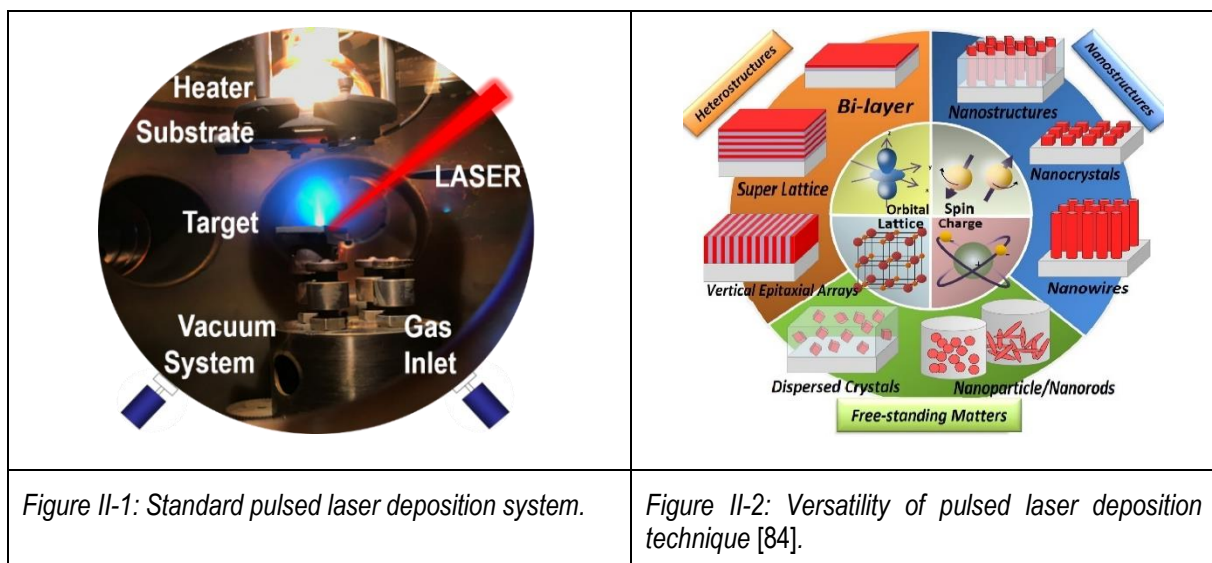
Experimental techniques and procedures for sample preparation - Optimization of the manufacturing steps

Chapter II. Experimental techniques and procedures for sample preparation - Optimization of the manufacturing steps

This chapter is devoted to presenting different aspects of the experimental techniques used in samples' manufacturing process. The manufacturing process of metallic nanoparticles arrays consists of three practical steps. The first step is based on the Langmuir-Blodgett technique for the manufacturing of colloidal masks by depositing polystyrene microspheres on Al_2O_3 -c substrates. The second step is the deposition of materials (Au, Ir, VO_2) using Pulsed Laser Deposition. The third step consists of removing the excess polystyrene microspheres using a solvent. All these approaches are described in this chapter with a focus on the extensive study on the optimization of the deposition of polystyrene microspheres.

II.1. Pulsed Laser Deposition (PLD)

Modern technology relies greatly on thin-film based deposition techniques. If we stop for a second and think about the devices that surround us every day and make our life easier (cell phones, laptops, etc.), we will discover that their manufacturing process involves at least one step in which thin film deposition techniques are used. On the other hand, thin film growth techniques also help us drive forward and enrich our fundamental understanding of the physical process that lay behind the universe's inner workings by making possible devices such as James Webb Space Telescope, etc. James Webb Space Telescope is due to be launched on 30 March 2021 from Guiana Space Centre, using the Ariane 5 ECA rocket; and will have a light-collecting primary mirror with 6.5 meters in diameter, made from depositing by vacuum vapor deposition 100 nm of Au on beryllium support. Therefore, techniques such as RF sputtering, chemical solution methods, chemical vapor deposition, molecular beam epitaxy, pulsed laser deposition (PLD), etc., of thin films are essential. The experimental setup of a PLD system is presented in *Figure II-1*.



Pulsed laser deposition is a physical vapor deposition method often performed in a vacuum or a controlled environment (i.e., a gas). PLD process shares some common characteristics with molecular beam epitaxy or sputter

deposition and holds advantages such as fast growth rate, the high crystalline quality of the thin films, and a precise stoichiometric transfer of material from a target to a substrate. *Figure II-1* presents our PLD system, in which a pulsed laser is focused on a moving (rotating and translating) solid target (metal or ceramic), a target made from the material intended to be deposited. If the laser is focused on a target with a sufficient energy density to exceed the ablation threshold, the laser pulse will vaporize a small amount of material from the target, forming a plasma plume that preserves the original target stoichiometry. The vaporized material will be ejected with a high directionality (i.e., perpendicular to the surface of the target) and serve as a flux of material for a substrate (on which the thin film grows) placed in front of the plasma plume. It is worth mentioning that the transfer of material from the target to the substrate is not always 100% stoichiometric. If the target is a complex compound involving a mixture of heavy and volatile light elements [85] or if the laser power density (fluence) is too low or too high [86], there can be small issues with the stoichiometry. These issues can be partially solved using the proper laser fluence and enriching the target in the lightest component (element). Today, PLD can compete with other thin film deposition techniques, atomic layer deposition (ALD), etc., in terms of stoichiometry and deposition rate (see *Figure II-3*).

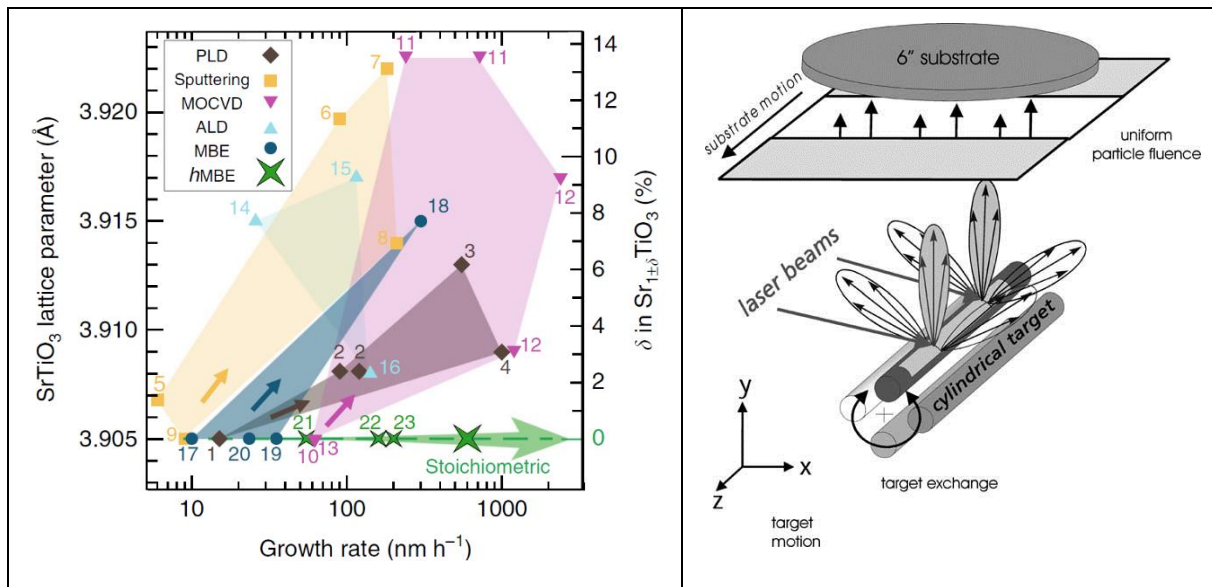


Figure II-3: Control of thin film stoichiometry and growth rate by different deposition techniques. The number close to data points shown refer to references, for more details see [87].

Figure II-4: Large area pulsed laser deposition system for thin films [88].

Stoichiometry problems can also be solved by introducing a gas inside the deposition chamber (i.e., the loss of oxygen from the target can be supplemented during the PLD process from the chamber's ambient gas). Depending on the application and the material that will be deposited, the environment inside the PLD chamber can be an inert gas such as argon or a reactive one such as oxygen (especially in the deposition of oxides). Usually, before each deposition, the PLD chamber is vacuumed/evacuated to a pressure between 10^{-5} to 10^{-10} mbar. The vacuum is made using a combination of at least two pumps. The preliminary pump (can be oil-based or dry pump) can maintain a vacuum in the chamber of approximately 10^{-2} mbar. After evacuating the PLD chamber, even more, it is used as a turbo-molecular vacuum pump that can lower the pressure down to 10^{-10} mbar. Most of the time, the depositions are made in a gas flow, and at constant pressure, the pressure is maintained by evacuating the gas

(with the vacuum system) at the same rate that the gas flows into the PLD chamber. PLD has become an exciting and popular deposition technique with D. Dijkkamp et al. [89] paper on high-temperature superconducting thin films (Y-Ba-Cu oxide), published in 1987. This paper proved that PLD could be successfully used in growing epitaxial films with a complex stoichiometry. To date, PLD is used in the deposition of a broad range of materials: semiconductors, metals, insulators, and even polymers (using a complementary technique called Matrix-Assisted Pulsed Laser Evaporation (MAPLE)) and has become a versatile process (see Figure II-2). One of the biggest challenges of the PLD system was the possibility of adapting the system for large area deposition. Although the initial acquisition of the system is quite expensive, today, this is possible (see Figure II-4), and PLD can be used for deposition of thin films (with complex stoichiometry) on a large area (up to 200 mm in diameter of the substrate). The high acquisition cost of the large area PLD system is compensated in time by the low day-to-day operating costs. The deposition of a thin film by PLD involves the following physical process: generation of photons in the laser process, laser-matter interaction (i.e., ablation of the target material), plasma plume formation and dynamics, and thin film growth process. Therefore, in the following sections, we will describe them individually, with special consideration to our system's particularity. Also, we will present the exact deposition parameters used in our experiments.

II.1.1. LASER system and matter interaction (target ablation)

In our team, we used a **KrF laser (TUI ThinFilmStar100)** working at a wavelength of 248 nm, with a pulse duration of 25 ns. The choice of laser type and laser characteristics is always up to the user. In the PLD process, the energy source can be an excimer laser, a solid-state laser, with a wavelength ranging from IR ($\lambda=1064$ nm Nd: YAG lasers) up to UV ($\lambda=193$ nm ArF excimer laser). The pulse duration can range from a few femtoseconds up to nanoseconds (as is the case of our laser). For more information about the characteristics of the laser used in this study see Appendix 2.2.

The targets are made from Vanadium, Gold, and Iridium in the metallic form with a purity of 99.9999 %, commercially available (from Neyco). The laser was focused on the targets at the same spot size of 2 mm². The laser fluence was about 3 J/cm². Especially for Ir, the laser fluence decreases significantly during the ablation process. This decrease comes from the deposition of Ir on in the laser access window into the PLD chamber. In general, in PLD, the laser ablation of materials starts with considering the target's optical properties in relation to the wavelength of the laser that can be used. Metals are known for their high reflectivity, but they also absorb light. When an electromagnetic wave strikes a medium's plane surface (the metal target), the electromagnetic wave is partially reflected, partially absorbed, and partially transmitted. At short wavelengths, in the UV, the light-matter interaction is mediated by the electrons' collisions with the lattice. Because of the lattice collisions, the electrons cannot follow the incoming light leading to a high absorption (*Figure II-5*) at the surface that prevents the light to penetrate deep into the metal.

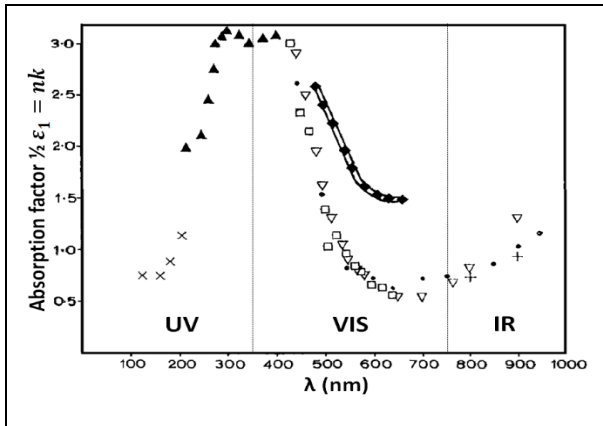


Figure II-5: Absorption factor of Au as a function of wavelength, compiled from multiple studies by [90].

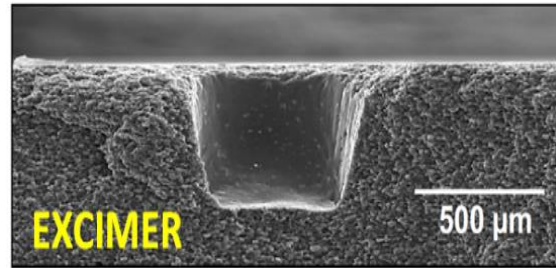


Figure II-6: Target ablation profile of the excimer laser [91].

This strong absorption close to the surface leads also to a high reflection. The penetration depth of light at a wavelength of 248 nm is less than 50 nm, in Au's case (see Figure I-20, Chapter I). Besides the target's intrinsic optical properties, surface morphology can change the optical absorption, and laser pulse characteristics can significantly impact the ablation process (see Figure II-6). An excimer laser promotes layer-by-layer ablation (not changing the surface), while solid-state lasers, due to their beam profile, change the target surface, during the ablation process.

A more significant impact than the laser beam profile or surface characteristics on the ablation is played by laser pulse duration. Laser pulse duration also impacts the ablation threshold and penetration depth; when the pulses are in the nanosecond regime the ablation threshold increases, and the adequate energy penetration depth decreases compared to a femtosecond laser pulse [95], see Appendix 2.3. In the nanosecond regime, the target surface first heats up, which leads to melting and vaporization. When the electron and ions have the same temperature ($T_e = T_i = T$), i.e., the laser pulse duration is longer than the electron-phonon energy transfer time ($\tau_L \gg \tau_i$) the heat equation can be expressed as [92]:

$$C_i \frac{\partial T}{\partial t} = k_0 \left(\frac{\partial^2 T}{\partial z^2} \right) + I_\alpha \alpha e^{-\alpha z} \quad \text{Equation (2.1)}$$

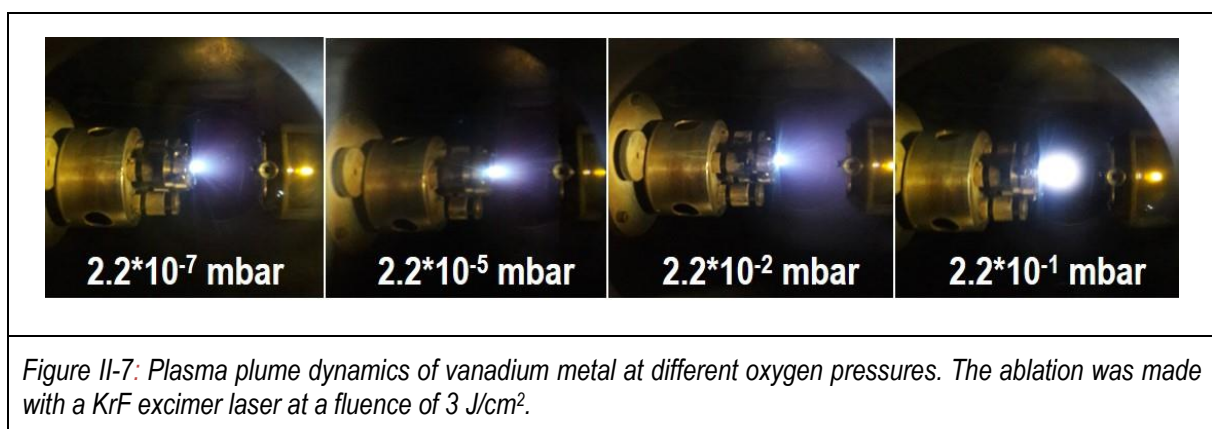
where: C_i is the lattice heat capacity per unit volume, α is the absorption coefficient of the target material, k_0 is linked to thermal conductivity, z is linked to the heat flux's direction, I is linked to the laser intensity.

In the interaction of a nanosecond laser beam with a material, the laser beam will heat and melt the target material's surface; then, the temperature will reach the vaporization temperature. In the process of nanosecond laser-matter interaction, energy is lost as heat conduction into the target. The heat penetration depth l is given by $l \sim (D_t)^{1/2}$, where D is the heat diffusion coefficient given by $D = \frac{k_0}{C_i}$ and t is the characteristic time, here τ_{laser} . The thermal penetration depth is larger than the optical penetration depth [92]. In nanosecond laser ablation, there is sufficient time for thermal waves to propagate into the target material and to create a relatively large layer of the melted material target [92]. Nanosecond laser pulses can ablate the target materials even at low laser intensities

in both the vapor and liquid phases, so a recoil pressure that expels the liquid will be created due to the vaporization process [92].

II.1.2. Laser ablation, Plasma plume dynamics.

Besides the intrinsic target material properties (thermal conductivity, skin depth, etc.) and the laser characteristics (wavelength, beam profile, etc.), the PLD process is also influenced by the environment in which the ablation occurs, the pressure at which the deposition is carried out [93]. The deposition of Au, Ir, and Al_2O_3 is performed in an argon gas flow at a pressure of 3.5×10^{-5} mbar. The deposition of VO_2 , is realized from a metallic vanadium target, and to obtain the desired stoichiometry and material phase, the ablation/deposition was carried out in a flow of oxygen at a pressure of 2.2×10^{-2} mbar. *Figure II-7* shows the plasma plume characteristics for the ablation at different pressures and a fixed laser fluence of 3 J/cm^2 .

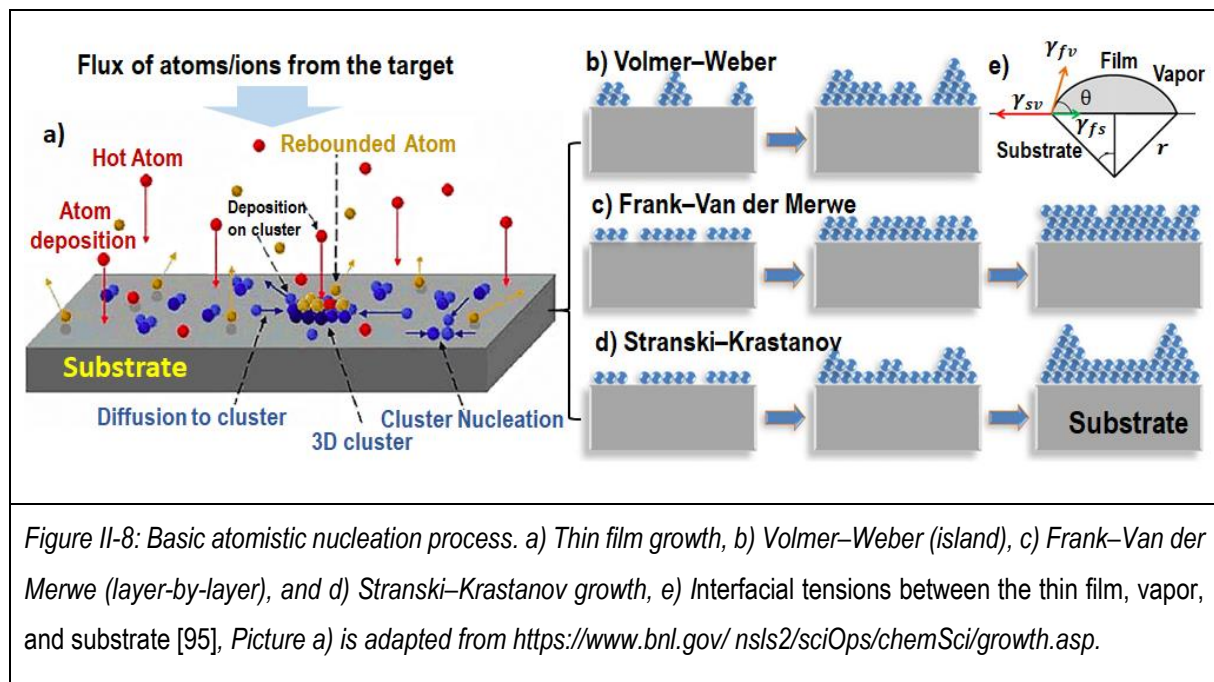


The plasma plume is directional in the PLD process; it expands normal, perpendicularly to the target and as the pressure increases, the plasma is confined more and more and directed towards the substrate (see *Figure II-7*). As the plasma plume reaches the substrate, some species can also rebound back from the substrate and will be re-deposited on the target. Alejandro Ojeda-G-P et al. [94] showed that in the case of a $\text{La}_{0.4}\text{Ca}_{0.6}\text{MnO}_3$ target with a KrF excimer laser at a fluence of 3 J/cm^2 . A significant quantity of material is re-deposited on the target and will account, likely, for 20% to 30 % of the ablated material by the next laser pulse. This could lead to surface enrichment of the target, especially in the target composition's heaviest atoms. In our case, this rebounding phenomenon, although present, does not influence the depositions process. The plasma will contain every time electrons, ions, and neutral species coming from the same element.

II.1.3. Deposition, thin film growth mechanisms and substrate influence on the deposition process.

In our experiments, the used substrate was both-sides polished Al_2O_3 -c cut, but different optimization experiments have been carried out on Si, BK7 (borosilicate glass) substrates. Al_2O_3 -c cut was chosen due to its board range transparency (200 nm up to $6 \mu\text{m}$) to electromagnetic waves and to its compatibility with growing high-quality VO_2 thin films. The deposition of metals (Au and Ir) was made at room temperature. As for the deposition of VO_2 , the Al_2O_3 -c cut substrate was heated up to $500 \text{ }^\circ\text{C}$ in order to achieve stoichiometry and phase (M_1) of vanadium dioxide.

When the different species contained in the plasma plume reach the substrate, they start to bond to the surface and a thin film or islands start to grow (see *Figure II-8*).



In thin film growth, there can be distinguished three significant modes: Volmer-Weber or island growth, Frank-Van der Merwe or layer-by-layer growth, and Stranski-Krastanov growth (see *Figure II-8*). Volmer-Weber growth model is characterized by the appearance of small and stable clusters on the substrate, clusters that grow into three-dimensional islands. This model is often found when the thin film and the substrate are of dissimilar materials, a case in which the deposited atoms are bonded stronger to each other than to the substrate [95]. The Stranski-Krastanov model starts with a layer-by-layer type of growth then evolves very rapidly towards an island type of growth (similar to the Volmer-Weber model).

The third growth model is the Frank-Van der Merwe or layer-by-layer growth, which is the opposite of the Volmer-Weber model. In layer-by-layer growth, the deposited atoms are stronger bonded to the substrate than to each other. This leads to a rapid 2D expansion, and the material is deposited on the substrate as planar sheets [95]. As the thickness increases, the newly deposited atoms start to “feel” less and less the substrate's presence; eventually, atoms reaching the bulk bonding strength.

The distinction between the three distinctive growth models can be easily made based on a thermodynamic model adapted for thin films' nucleation and growth [95]. The thermodynamic model starts with assessing the surface energy of materials in a simple nucleation process as the one presented in *Figure II-8 e*). The mechanical equilibrium among the horizontal components of the interfacial tensions between the thin film, vapor, and substrate gives the Young equation [95]:

$$\gamma_{sv} = \gamma_{fs} + \gamma_{fv} \cos \theta \quad \text{Equation (2.2)}$$

where γ_{sv} is the interfacial energy between the substrate and the vapor phase, γ_{fs} is interfacial energy (film and substrate), γ_{fv} is interfacial energy (film and vapor), and θ is the contact angle.

In Volmer–Weber model $\theta > 0$, and $\gamma_{sv} < \gamma_{fs} + \gamma_{fv}$, if we neglect γ_{fv} then the island growth is dominant when $\gamma_{sv} < \gamma_{fs}$ (i.e., when the film's surface energy is greater than the substrate's surface energy). In layer-by-layer growth (Frank–Van der Merwe) $\theta \sim 0$ and $\gamma_{sv} \geq \gamma_{fs} + \gamma_{fv}$ (the film wets the substrate), and if $\gamma_{fs} = 0$ the interface between the film and substrate vanishes leading to so-called homoepitaxy. In Stranski–Krastanov, the condition of $\gamma_{sv} \geq \gamma_{fs} + \gamma_{fv}$ is initially fulfilled, leading to a layer-by-layer growth, but the accumulation of strain energy from the lattice mismatch between the film and substrate eventually transitions to island growth [95]. Epitaxial growth refers to extended single-crystal thin film formation on top of a crystalline substrate (see *Figure II-9*) [95].

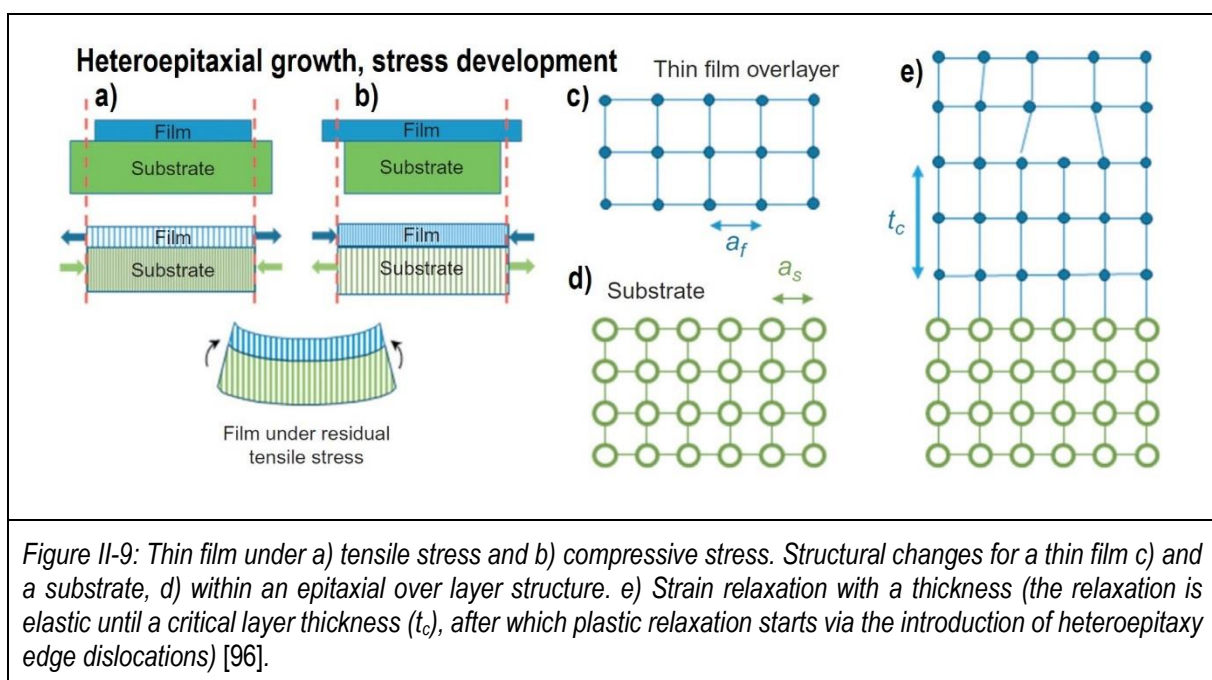


Figure II-9: Thin film under a) tensile stress and b) compressive stress. Structural changes for a thin film c) and a substrate, d) within an epitaxial over layer structure. e) Strain relaxation with a thickness (the relaxation is elastic until a critical layer thickness (t_c), after which plastic relaxation starts via the introduction of heteroepitaxy edge dislocations) [96].

Epitaxy can be divided into two major categories: homoepitaxy and heteroepitaxy.

In homoepitaxy, the deposited material coincides with the substrate composition, whereas heteroepitaxy refers to the case in which the thin film and substrate are made from different materials, but the substrate has a structure that can guide the growth of the film [95].

In general, if thin film and substrate materials are different from their native (in the bulk form), lattice parameters are mismatched, leading to the formation of one of two types of interfaces. The interface can be strained (compressive or tensile), or if the lattice-mismatched is very big, the critical thickness (t_c) is small and the thin film grows to have dislocations directly at the interface (see *Figure II-9*). As the thin film thickness increases, growing stress causes nucleation of dislocations which partially relaxes the strain due to lattice mismatch. This thickness at which the partial relaxation of stress occurs is defined as a critical thickness. The probability that one of these different heteroepitaxial interfaces will form can be assessed by measuring the lattice mismatch Δa [95]:

$$f = \frac{2(a_f - a_s)}{a_f + a_s} \approx \frac{a_f - a_s}{a_s} \approx \frac{a_s - a_f}{a_f} \quad \text{Equation (2.3)}$$

where: a_f , a_s are the lattice parameters of the thin film and substrate, respectively. In general, $f < 0.1$ for epitaxy to be possible.

However, f is also a function of temperature, if the thin film and substrate's thermal expansion coefficients are different. The growth of VO_2 on Al_2O_3 -c fits well with the Stranski–Krastanov model (see *Figure II-10*). Moreover, in our depositions the VO_2 grows epitaxially and highly strained (-0.75 % for 200 nm of VO_2) on the Al_2O_3 -c substrate. The strain and epitaxial relationships between the VO_2 and the Al_2O_3 -c substrate are discussed in detail in *Chapter V*.

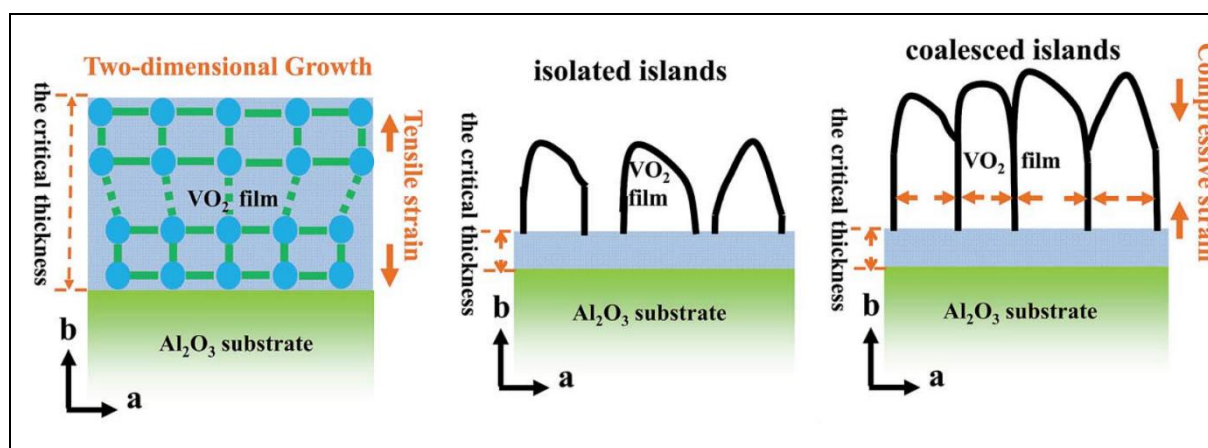


Figure II-10: VO_2 growth modes: initially 2D, then island growth followed islands coalescence as the thickness increases [97].

It is worth mentioning that the experimental deposition conditions can greatly influence the growth mode of VO_2 on Al_2O_3 -c. The temperature during deposition, oxygen pressure, laser fluence, etc. can have an impact on the thickness of the critical layer and the size of the island that nucleates and grows after the critical thickness. If the deposition is stopped before t_c we may consider that VO_2 grows strained but layer-by-layer.

For Gold, Thorwald G. Andersson [98] presented that the initial growth model of vapor-deposited thin films can be the Volmer–Weber mode if the substrate is alkali halides and Stranski–Krastanov for a silicon oxide substrate. Since our depositions of Au and Ir are made at room temperature and the metal atoms do not have sufficient energy to move long distances on the substrate, and the film's surface energy is also greater than the surface energy of the substrate, the growth process matches the Volmer–Weber model.

II.2. Colloidal lithography- Langmuir-Blodgett

Langmuir-Blodgett films have been praised for their possible applications since the 1930s, many interesting devices have been made, and even more, have been proposed [99], [100]. Historically speaking, Langmuir-Blodgett technology has been widely used to fabricate ultra-thin highly ordered organic films by assembling amphiphilic molecules to form two or three-dimensional structures [101]. Langmuir-Blodgett films play a significant role in a plethora of applications, ranging from the fabrication of antireflection structures [102] to the photonic crystals [103],

surface-enhanced Raman scattering [104], or even biological sensing [105]. In simpler terms, the Langmuir-Blodgett method consists of the transfer onto a substrate of a one-molecule thick layer (Langmuir monolayer) spread at the air/water interface, a process that can be repeated several times with the same substrate to form a multilayer film (see *Figure II-11 a*). For the molecule to form a layer on the water's surface, it must be composed of a submerged hydrophilic part and a non-submerged hydrophobic part (i.e., the molecule is then called amphiphilic).

Based on the Langmuir-Blodgett classical process, the technique has been adapted for nano/microsphere lithography, where the amphiphilic molecules' role is played by microspheres of polystyrene, silica, etc. [106]. Thus, enabling the Langmuir-Blodgett technique to become one of the best techniques for self-assembly of closely packed colloidal spheres into two-dimensional (2D) ordered arrays.

The Langmuir-Blodgett process is controlled by compression isotherm as presented in *Figure II-11 b*.

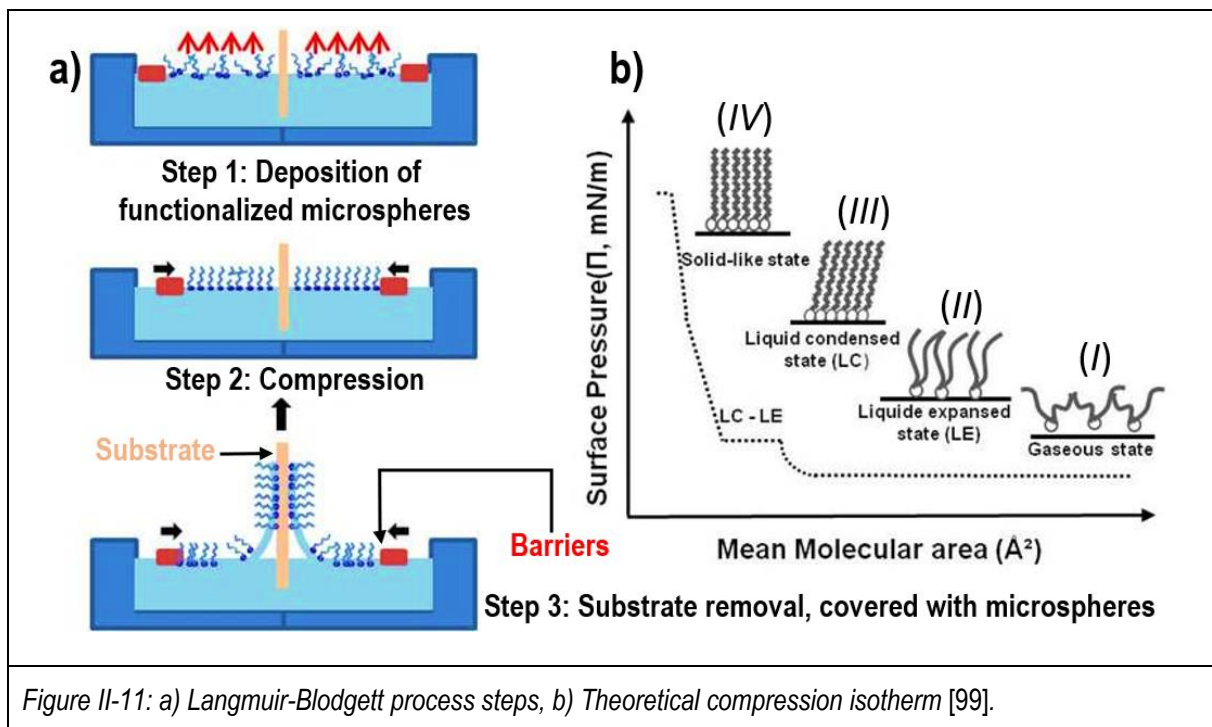
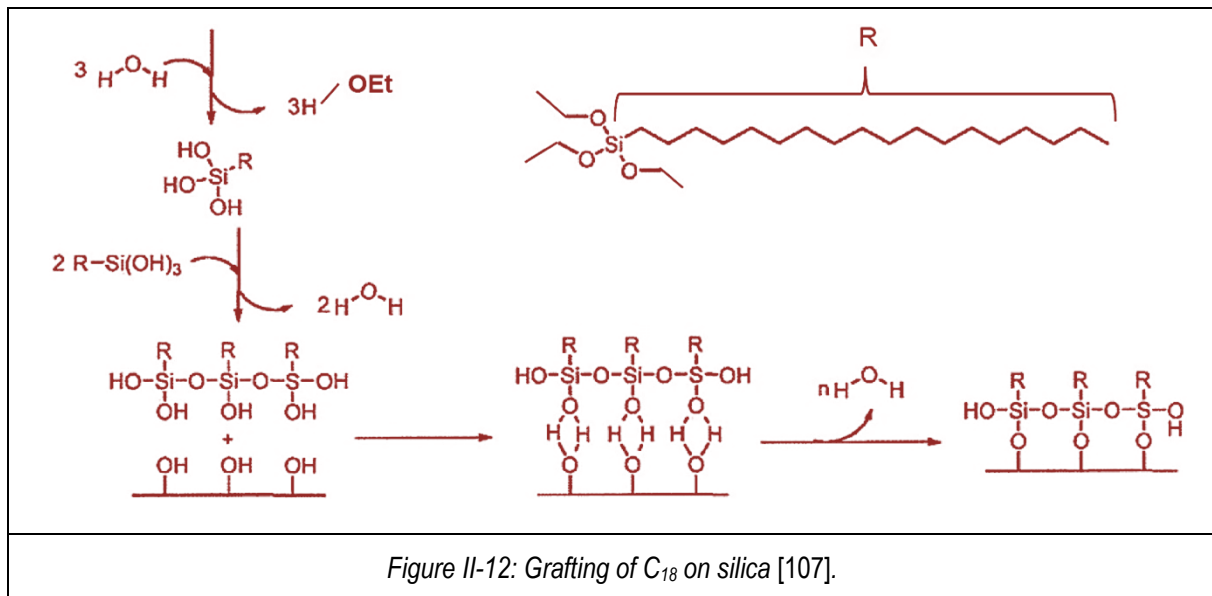


Figure II-11: a) Langmuir-Blodgett process steps, b) Theoretical compression isotherm [99].

These so-called compression isotherms indicate the pressure between the steps of the Langmuir-Blodgett process (steps I-IV, *Figure II-11 b*) which are essential for a smooth transfer of microspheres on a substrate. The isotherms can be split into several characteristic phases (see *Figure II-11 b*), with each phase being characterized by a change in the isotherm's slope. The first phase (step I) occurs when there is a large surface area of sub-phase (water) available per microsphere, so they do not interact with each other, and therefore their behavior is analogous to that of a gas. The second phase (step II) occurs when the barriers approach each other; the repulsion forces between microspheres appear and increase in the same way as the surface pressure, with the monolayer behaving like a liquid. In the last phase (compact phase, step III), the microspheres are very close to each other, and the forces of repulsion are used to self-structure the monolayer in the same way as a two-dimensional crystal.

The surface pressure in the colloid (step IV) is controlled by measuring the surface tension, and they are linked through $\pi = \gamma - \gamma_0$; where γ_0 is the surface tension of sub-phase (without the microsphere monolayer) and γ is the surface tension of the system with the microspheres monolayer. The surface tension is measured with a Wilhelmy plate that is connected to a microbalance. The Wilhelmy plate that is made from paper.

The polystyrene microspheres are hydrophilic. However, the microspheres are functionalized with stearic acid groups to give them a behavior similar to that of an amphiphilic molecule and better control the surface tension. So, microspheres are functionalized with a hydrophobic molecule that can be a fatty acid derivative such as stearic acid $C_{18}H_{36}O_2$ (commonly known as C_{18} or octadecyl) [106].



The functionalization with C_{18} takes place in two stages: first hydrolysis and then condensation, as shown in *Figure II-12* with C_{18} . Hydrolysis leads to the formation of alcohol and silanol. The condensation of silanol groups occurs on the hydroxyl sites on the microspheres' surface (in our case, polystyrene) and eventually forms covalent bonds.

II.2.1. Langmuir-Blodgett deposition system and experimental procedure

All the colloidal lithography experiments have been performed with a Langmuir Blodgett deposition system manufactured by KSV Nima << Langmuir-Blodgett Deposition Through Medium, KN 2002 >> and presented in *Figure II-13*. A software program developed by KSV Nima controls the deposition parameters such as surface pressure, barrier position, and sample position. One of the specific features of this system is the addition of a thermostatic bath developed in-house. This thermostatic bath works in conjunction with the thermocouple already integrated into the software program and allows the control of the water sub-phase temperature. The sub-phase temperature is controlled from room temperature up to $50^{\circ}C$.

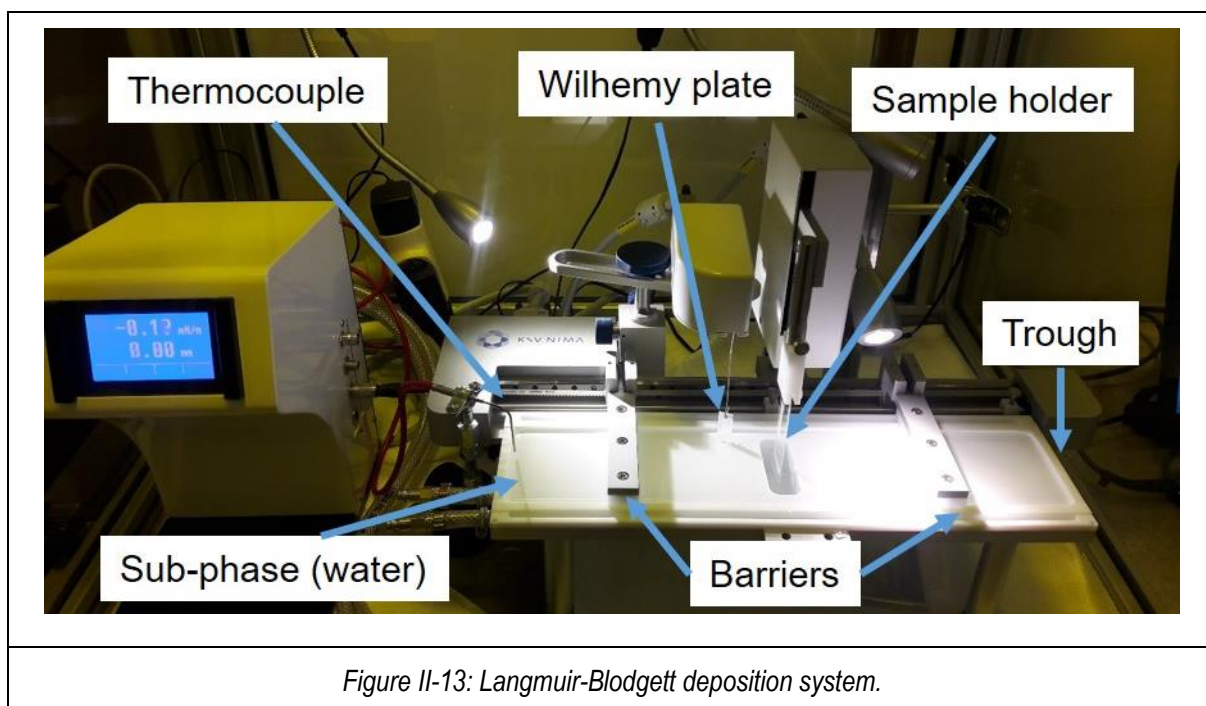


Figure II-13: Langmuir-Blodgett deposition system.

As substrates, we have used in our experiments: BK7, Si, Al₂O₃, and MgO. The experiments have been carried out using Polystyrene microspheres (PS) with sizes ranging from 2 μm, 3 μm and 5 μm commercially available at microparticles GmbH and Micro Partikeltechnologie GmbH. The polystyrene microspheres are, beforehand, functionalized with octadecyl carbon chain C18 and sold as a water suspension of 10ml, 50mg/ml (see Figure II-14).

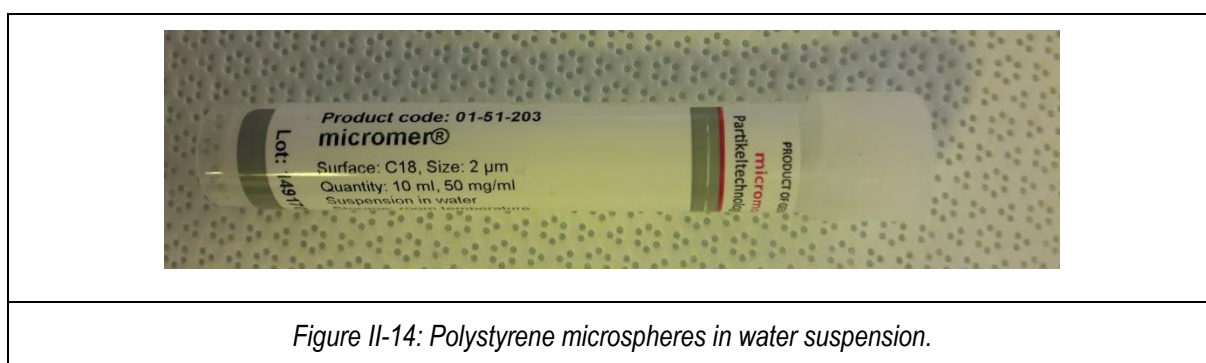


Figure II-14: Polystyrene microspheres in water suspension.

The deposition procedure starts by putting the polystyrene microspheres suspension, presented in Figure II-14, in the ultrasonic bath for 1 hour at a frequency of 37 kHz and a power of 100% in the sweep mode, while the water from the ultrasonic bath is continuously changed to keep the microspheres suspension at room temperature. The ultrasonication process ensures the homogeneity of the microsphere suspension. During this time, all the surfaces (trough, barriers, sample holders, etc.) that will be in contact with the microspheres are thoroughly cleaned with ethanol and distilled water. After the ultrasonication process is finished, 2500 μl of microsphere suspension is transferred to another beaker together with 7500 μl of ethanol. These values ensure the total coverage of the sub-phase with microspheres.

The resulting suspension is placed in an ultrasonic bath for a second homogenization process (in the same condition as the first). Then, 230 ml of distilled H₂O (acts as a sub-phase) are added in the Langmuir-Blodgett

Deposition Trough, the substrates are lowered into the sub-phase, and the system's temperature is set at the desired value. After the temperature is stable at the desired value, the spreading of the microspheres on top of the sub-phase can start. Using a micropipette, the microspheres are placed gently on top of the sub-phase by forming a small droplet and then touching the sub-phase's surface with the droplet. This process usually takes between 20 and 30 minutes. After the spreading process is over and the sub-phase coverage by the microspheres is as good as possible, the surfactant is left to evaporate for around 2 hours. At the end of this time, the distance between the barriers is decreased, and therefore, the microspheres monolayer that has formed on top of the sub-phase is compressed. During the compression process, the surface pressure is continuously measured, and a surface pressure isotherm is recorded (see *Figure II-15*).

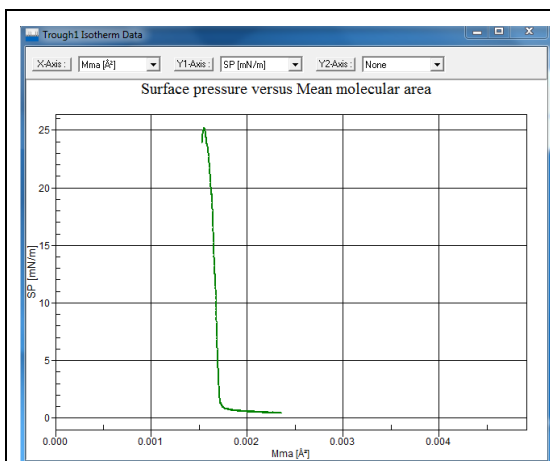


Figure II-15: Surface pressure isotherm.

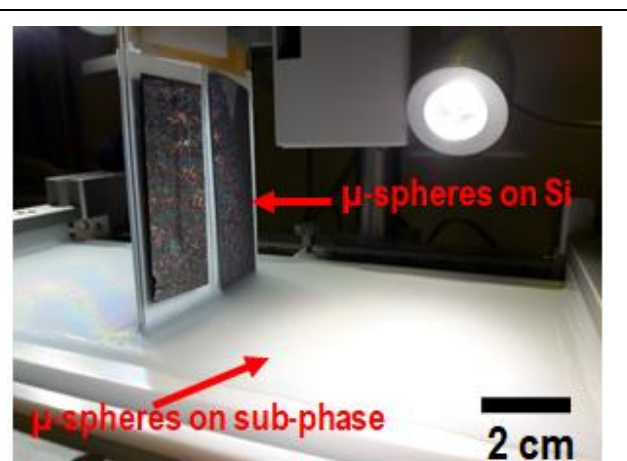


Figure II-16: Langmuir-Blodgett deposition process.

As seen in *Figure II-15*, when the surface pressure has reached the maximum value and starts to decrease, the monolayer's compression has reached the maximum value, and the compression process has to be stopped (similar to molecular isotherms). After this point, further compression will result in a collapse of the monolayer and the formation of highly irregular layers. At the end of the compression process, the samples are drawn out through the monolayer (see *Figure II-16*), with a speed usually of $1 \text{ mm} \cdot \text{s}^{-1}$, while keeping the surface pressure at the value that was at the end of the compression process. As an example, the *Figure II-16* shows microspheres ($3 \mu\text{m}$) on a Si substrate.

II.2.2. Langmuir-Blodgett microspheres arrangement

In the Langmuir-Blodgett system, the most common microsphere (particles) arrangements resemble a 2D crystal with a hexagonally close-packed or/and a cubic close-packed structure [108]. These structures' formation can be described by looking at the thermodynamic minima or entropic differences between the two crystal lattices. In terms of minimum Gibbs energy, the cubic close-packed (ccp) structure has been determined to be more stable than the hexagonally close-packed (hcp) structure [109] in 3D. Although both share a similar two-dimensional close-packed structure, the difference between the two being the stacking within the third dimension [110], for 2D arrangements, hexagonal close-packed structures are more stable. Packing density τ is used to express the total

amount of space occupied by microspheres versus available space; for 2D hexagonal close-packed structures, the packing density is around 90.7% (see *Figure II-17*), while for a square packed lattice, it is 79% [111].

$$\tau = \frac{S_{\text{microsphere}}}{S_{\text{total}}} \quad \text{Equation (2.4)}$$

$$\tau_{\text{max}} = \frac{\text{Area}_{\text{disk}}}{\text{Area}_{\text{hexagon}}} \quad \text{Equation (2.5)}$$

$$\tau_{\text{max}} = \frac{3 \frac{\pi D^2}{4}}{\frac{3\sqrt{3}}{2} D^2} = \frac{\pi}{2\sqrt{3}} \approx 0.91 \quad \text{Equation (2.6)}$$

where $S_{\text{microsphere}}$ is the surface occupied by the microspheres on the substrate, S_{total} is the total surface available on the substrate, D is the diameter of the microspheres; A_{disk} is the surface occupied by the microspheres in the hexagonal region and A_{hexagon} is the surface of the hexagon (elementary unity).

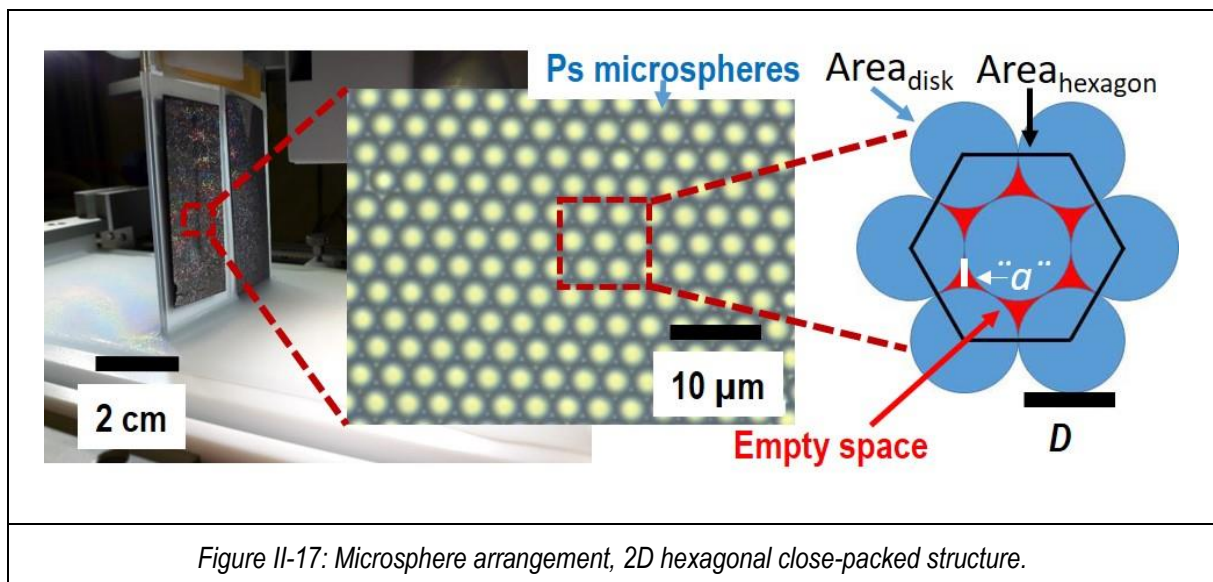


Figure II-17: Microsphere arrangement, 2D hexagonal close-packed structure.

As we can see in Equation (2.6), τ_{max} is independent of the microsphere diameter, which implies that changing the size of the microsphere will not change the total area occupied by the microspheres (see also *Figure II-17*). After the removal of the polystyrene microspheres, the resulting nanoparticles have specific size " a " (*i.e.*, the perpendicular bisector of the resulting nanoparticles) and interparticle distance d that is linked to the diameter D of the polystyrene microspheres used for manufacturing of nanoparticles arrays by the Equation (2.7).

$$a = \frac{3}{2} \left(\sqrt{3} - 1 - \frac{1}{\sqrt{3}} \right) D \quad \text{Equation (2.7)}$$

II.2.3. Defects in the microsphere arrangement of the Langmuir-Blodgett system

Langmuir-Blodgett method has some advantages: easiness of forming a monolayer and high packing density compared with the other coating techniques. However, the monolayer still contains a small number of crystal imperfections, mainly consisting of grain boundaries, vacancy defects, and line defects, with the gap of the grain boundary and line defects being around one period (= diameter of a particle) or less and vacancy mostly one

period [112]. The majority of these crystalline defects are formed when the microspheres are released at the water–air interface and form a self-assembly membrane. The particles' nucleation mode is sporadic, and the subsequent crystal growth results in a 2D polycrystalline entity, which will inevitably have grain boundaries leading to the formation of defects [112].

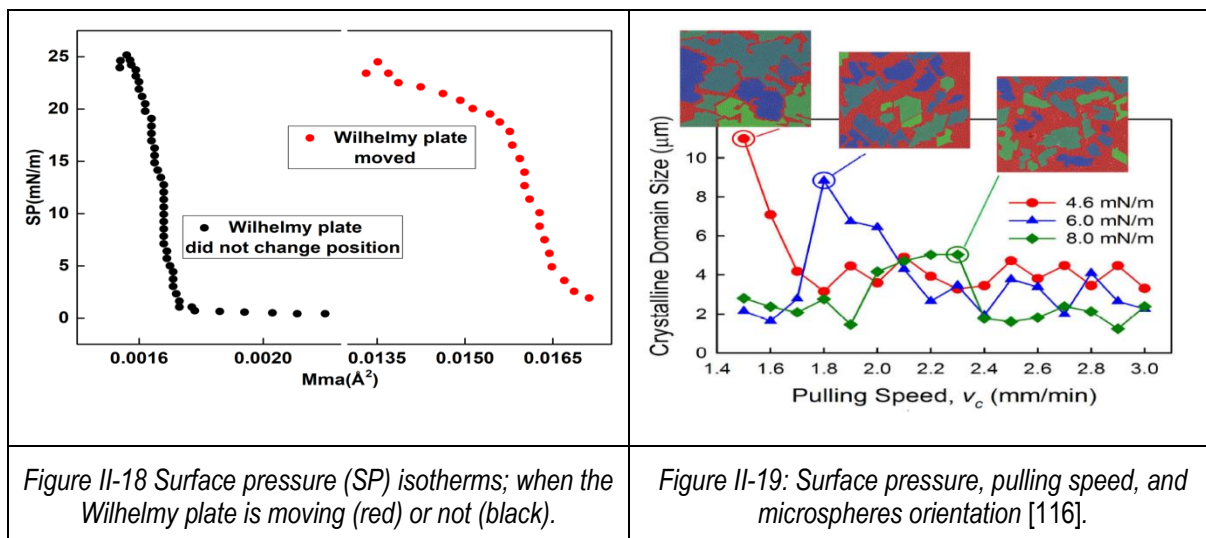
II.2.4. Langmuir-Blodgett monolayer formation and interaction between microspheres

The monolayer formation can be achieved by self-assembly of the microsphere, driven by the balance of the different forces, forces that can be either attractive or repulsive, with some of the forces counteracting the effect of the others and playing a significant role in the colloidal stability. Forces such as Van der Waals interaction (vdW), electrostatic interaction, steric effect, and capillary forces govern microspheres' interaction. In the next section, we will make a short theoretical overview of each of them, emphasizing their contribution to monolayer formation and stability. Van der Waals's interactions originate from the interaction present between the microspheres' individual constituent [113]. The van der Waals force between two identical bodies in any medium is always attractive, and such interactions are expected to play a role for microspheres at an interface. For spheres with sizes in the nm- μm range, the corresponding energies typically in the range $0.1\text{--}1\text{ k}_B\text{T}$ [114]. The electrostatic interactions are given by the microparticle's surface charges and can be either attractive or repulsive (like Van der Waals forces). Colloidal microspheres (functionalized with C_{18}) in highly concentrated media are subject to steric effects, where the presence of other microspheres in the liquid physically blocks further ordering or material deformation [115]. When two microspheres approach each other, as soon as the inter-particle distance is below twice the unperturbed layer thickness δ , the polymer functionalization layers (C_{18} molecules) will touch each other leading to interpenetration and or compression. The attractive capillary forces appear as a consequence of the formation of liquid bridges, typically observed in meniscus effects, forming between microspheres (microparticles) due to surface tension [109]. Capillary interactions for sub-micrometer and micrometer-sized floating microspheres can become non-negligible if there is an irregular contact line between microspheres, microspheres, and sub-phase. For more discussions about microspheres interactions see Appendix 2.3.

II.3. Langmuir-Blodgett- Results

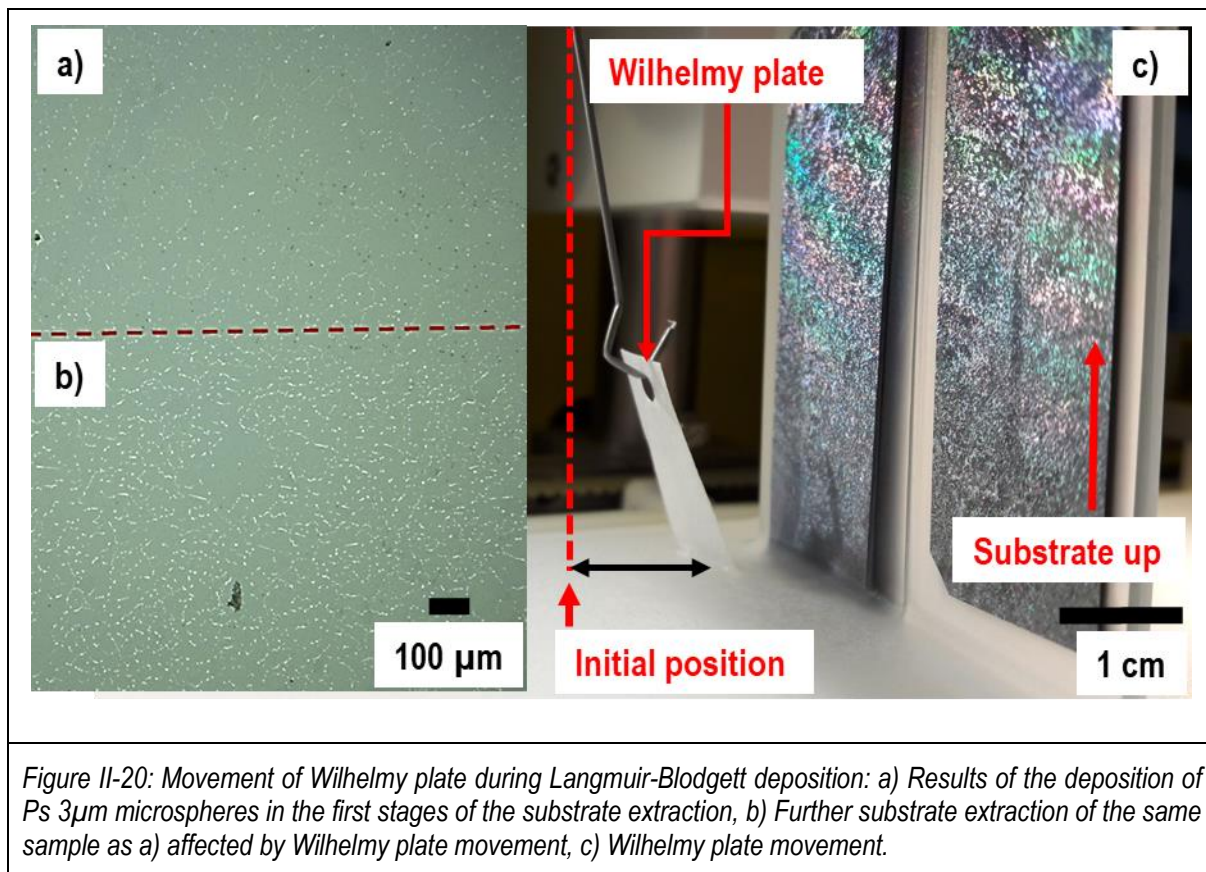
II.3.1. Surface pressure (SP) measurements

Surface pressure (SP) is probably the most used parameter in the fabrication of samples using Langmuir-Blodgett systems.



In a paper published by Atiganyanun et al.[116] in 2017, the authors concluded that there is a direct link between the value of the surface pressure, pulling speed, and the randomness of the microspheres' orientation (see Figure II-19) [116]. The results from Atiganyanun et al. [116] are difficult to reproduce since the surface pressure is measured using a Wilhelmy plate most of the time. Microspheres can move the Wilhelmy plate during the compression step (see Figure II-18) or/and the microsphere monolayer can move the plate when the substrate (covered with the microspheres) is extracted from the Langmuir-Blodgett Through (see Figure II-20 c)).

In the deposition of molecules, the Wilhelmy plate is "transparent," and the molecules' movement does not change the plate's position. However, in our case, the monolayer's movement during the pulling process induces the Wilhelmy plate's movement (as seen in Figure II-20 c)). This, in turn, gives rise to a change of the plate's value based on its movement, not on the change in surface.



Here, the initial shape of the SP isotherm cannot be predicted since the plate movement can change the shape of the isotherm (see Figure II-18). But the consequences of the plate movement (see Figure II-20 a) and b)) can be mitigated. In the deposition's initial steps (extraction of the substrate covered with microspheres), we can rely on the SP isotherm. Then, when the plate's movement is visible, we compress further the microsphere monolayer at an SP value almost double (43 mN/m) than the one suggests by the initial SP isotherm (25 mN/m). This can be a double-edged sword, but it is a way that can increase the yield of the Langmuir-Blodgett deposition process (i.e., deposition on multiple Al₂O₃ substrates (1.5*1.5 cm) at the same time). This later compression can be used to cover bigger substrates with the same quality as the microsphere monolayer (i.e., it is possible to cover four (two on each side) BK7 microscope plates). Thereby, for microspheres, the SP isotherm is recorded in a multi-step process.

II.3.2. Langmuir-Blodgett– Fast Fourier transform (FFT)

The generation of a Fast Fourier transform (FFT) of the surface images can be used to reveal regularity and periodicity (i.e., quality of deposited microspheres monolayer) of the deposition result of Langmuir-Blodgett.

The details of the directional nature and periodicity can be extracted by observing peaks in the FFT spectrum. Peaks in the Fourier spectrum will correspond to directions along which strong periodicity exists [117]. We will apply the FFT by using the freely available ImageJ software.

This arrangement and different combinations of it will give an FFT spectrum as the ones presented in Figure II-21.

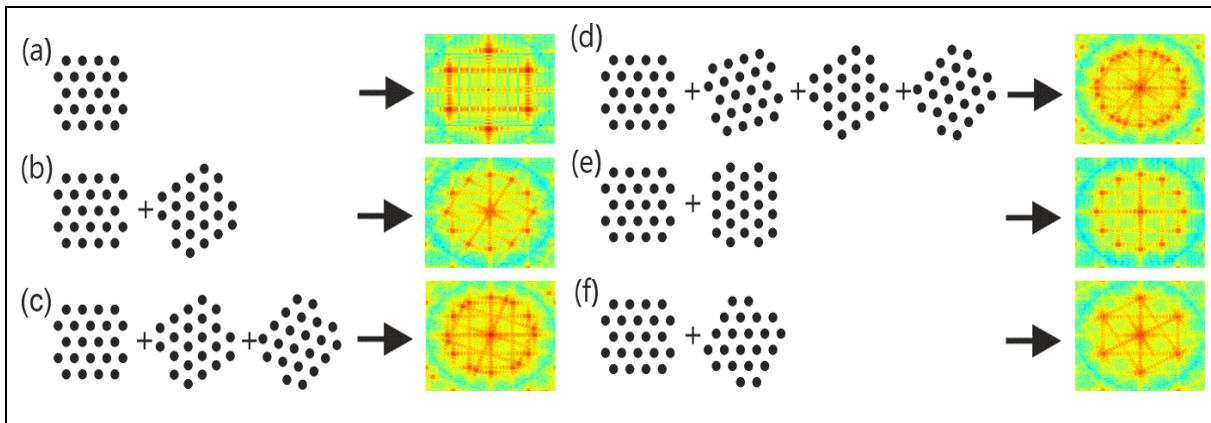
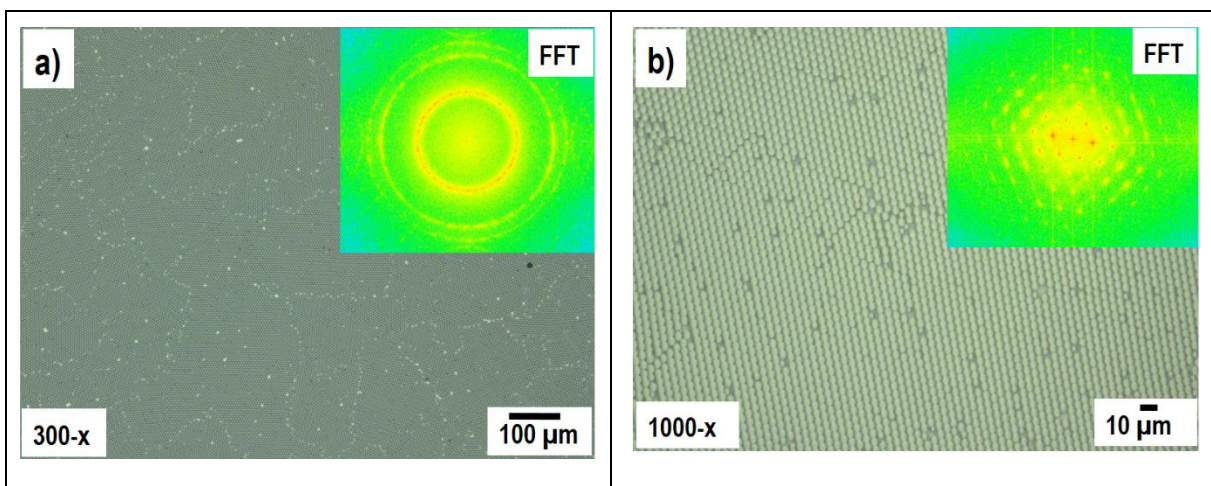


Figure II-21: Fourier transforms of combinations of the 2D hexagonal close packed structure for different orientations: a) 0 degrees, b) 0 and 30 degrees, c) 0, 30 and 45 degrees, d) 0, 15, 30 and 45 degrees, e) 0 and 90 degrees, f) 0 and 60 degrees [117].

When applying the FFT procedure, there is a trade-off between magnification and resolution that we have to make. A low magnification will include many crystalline microsphere single domains but will decrease the FFT image's clarity. Simultaneously, high magnification will be challenging to say that it represents our samples' real quality.

The presence of defects and different crystalline domains' orientations will inevitably lead to an FFT resembling the one presented in Figure II-21 d). If the magnification is sufficiently high (5000-x), the FFT will be close to the one in Figure II-21 a). This is seen better in Figure II-22, where we take a series of optical pictures (taken on our microsphere deposited samples) at different magnifications and then apply the FFT procedure.

The FFT of an optical image taken at magnification of 300-x is presented in the insert of Figure II-22 a) and corresponds to the optical image. At 300-x, the FFT in Figure II-22 a) resembles the one in Figure II-21 d). If we increase the magnification, the FFT will evolve towards an FFT specific of single or double domain orientation (see Figure II-21 and Figure II-22 a-d). At high magnification (5000-x, Figure II-22 d)) the FFT spectrum is different, although the polystyrene microspheres' arrangement is almost perfect. This difference is due to the low contrast of optical images.



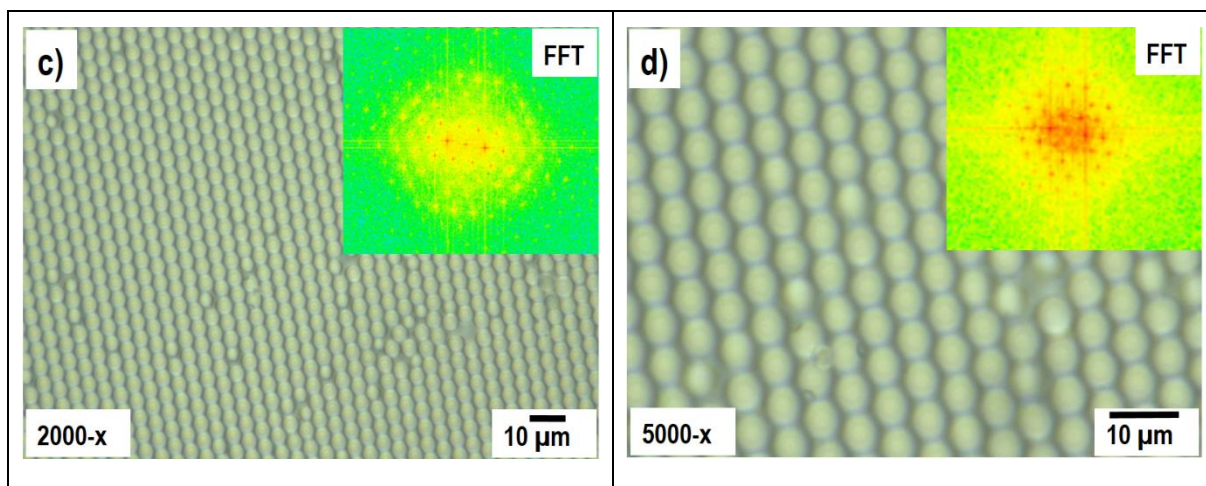


Figure II-22: Fourier transform of 5 μm polystyrene microspheres on Si, at low (a) 300-x and high magnification (b) 1000-x, c) 2000-x and d) 5000-x). The FFT procedure makes the insert of each optical microscopy image.

Figure II-22 shows a direct relation between magnification and the FFT image. Thereby, in the next sections we will present the result the Langmuir-Blodgett depositions by selecting the magnifications (for each figure) that better shows the influence of specific parameters (temperature, etc.)

II.3.3. Temperature dependence of microsphere monolayer quality

The temperature of the system can play a massive role in the deposition of microspheres by Langmuir-Blodgett, first, by changing the surface tension of the sub-phase air interface (H_2O) and second by changing the surfactant's effectiveness. The surface tension of water-air interface at 20 $^\circ\text{C}$ is 72.75 mN/m and changes to 69.6 mN/m at 40 $^\circ\text{C}$ while the surface tension of ethanol-air interface is 22.39 mN/m at 20 $^\circ\text{C}$ and 21.55 mN/m at 30 $^\circ\text{C}$. Adding ethanol to the sub-phase lowers, even more, the surface tension of the sub-phase-air interface, and coupling this with the temperature dependence of surface tension creates a complex system, with multiple parameters, all changing the dynamics of microspheres monolayer, which in turn changes the size of the crystalline domains.

To get a better understanding of the influence of temperature on the size of the crystalline domains, we performed experiments at different temperatures: 16 $^\circ\text{C}$, 20 $^\circ\text{C}$, 25 $^\circ\text{C}$, 30 $^\circ\text{C}$, and 40 $^\circ\text{C}$, using a thermally controlled bath. Figure II-23 presents a general picture of the temperature dependence of the Langmuir-Blodgett deposition process. The FFT on an optical picture of each temperature's microsphere monolayer and at two magnification is presented in the figure's inserts. The 4 $^\circ\text{C}$ difference between Figure II-23 a) and b) is enough to give rise to the formation of isolated microspheres islands on top of a microspheres monolayer for the sample made at 16 $^\circ\text{C}$.

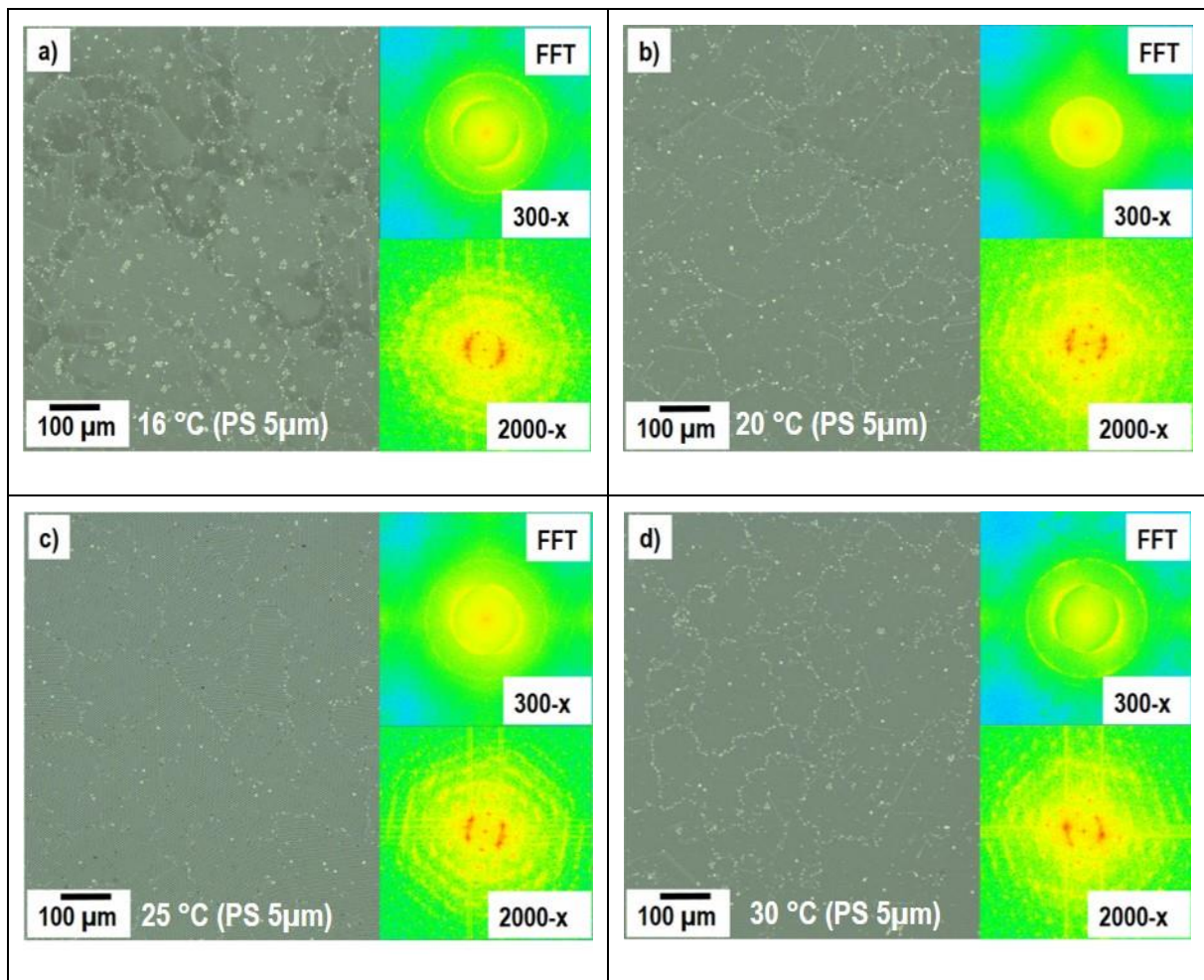


Figure II-23: Optical images at a 300-x magnification of polystyrene microspheres (PS) 5 μm deposited on Al_2O_3 -c at a) 16 $^\circ\text{C}$, b) 20 $^\circ\text{C}$, c) 25 $^\circ\text{C}$, c) 30 $^\circ\text{C}$. The inserts represent the FFT (for 300-x and 2000-x respectively).

If we further increase the temperature at which the microspheres are deposited, the islands disappear, and we have a perfect monolayer, with the size of the crystalline domains increases with the increase of temperature. At 25 $^\circ\text{C}$, the deposition of microspheres yields the best results. Further increasing the temperature to 40 $^\circ\text{C}$ has yielded bad results. At 40 $^\circ\text{C}$, (not shown here) the sub-phase evaporation rate becomes a problem, so depositing the microsphere at this temperature is impossible without the addition of water after the time when the microsphere has been spread on the sub-phase. Adding small droplets of water to the sub-phase induces the raising and collapse of the microsphere layer, giving rise to the formation of microsphere islands or even entire lines of microsphere on top of the deposited monolayer if much water is added at once.

In Figure II-23, the white part of the images corresponds either to grain boundaries or to other microspheres on top of the main microsphere monolayer. The 300-x magnification in FFT images is chosen to show the influence of temperature on a large area and the 2000-x to show the arrangement of individual microspheres.

At 16 $^\circ\text{C}$, Figure II-23 a), the FFT's maximum (the red part) has a circular distribution or symmetry that results from a combination of multiple 2D hexagonal close-packed structures with different orientations. Therefore, Figure II-23 a) can be associated with FFT's theoretical results in Figure II-21 c) and d). Increasing the temperature

to 20 °C changes the circular symmetry towards a more hexagonal one (see *Figure II-21 b*). The FFT result at 25 °C and 30 °C are quite similar except for two additional central peaks in *Figure II-21 c*). At 30°C, an additional microsphere is on top of the main microsphere monolayer that can induce this difference.

A similar temperature dependence is also observed for polystyrene microspheres with a diameter of 3 μm (see *Figure II-24*).

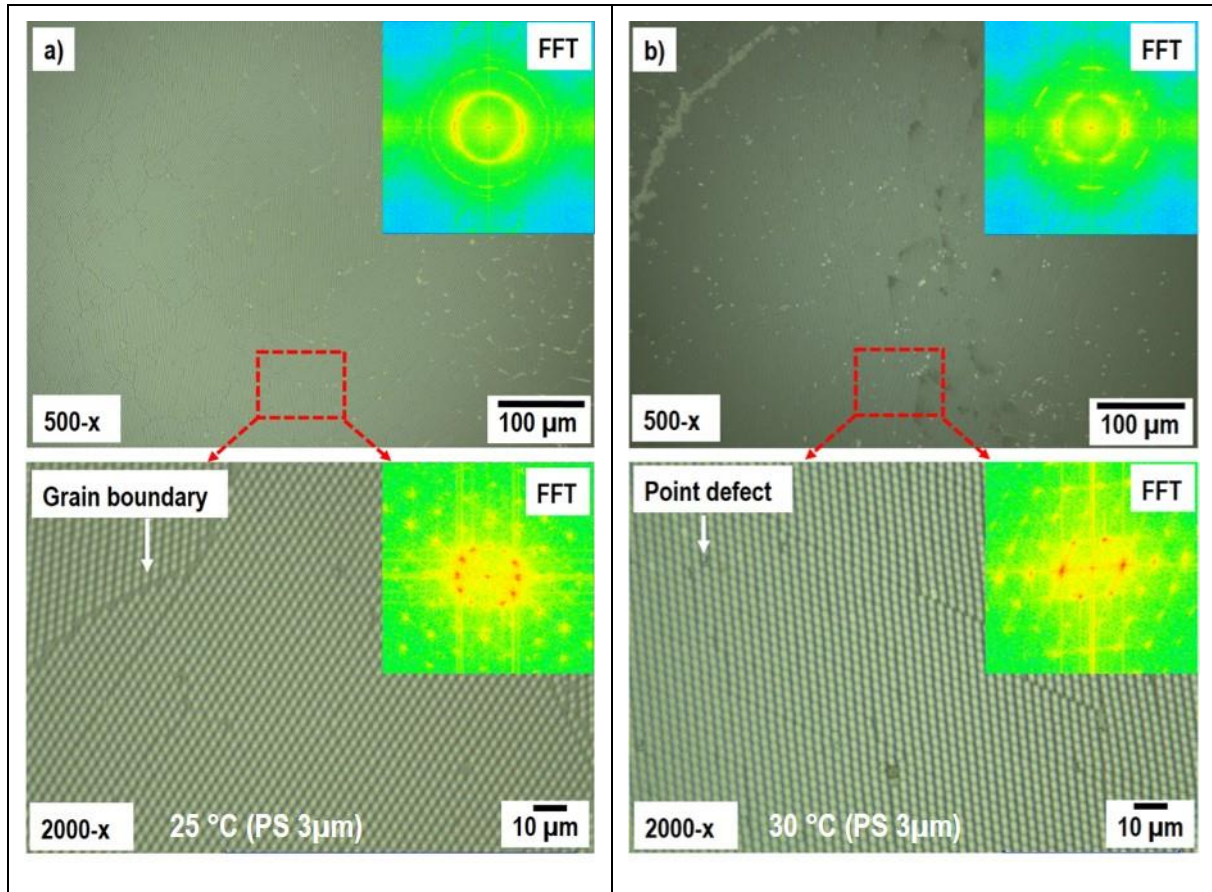


Figure II-24 Optical images at 500-x and 2000-x magnification of polystyrene microspheres 3 μm deposited on Al_2O_3-c at a) 25 °C, b) 30 °C. The inserts represent the FFT (for 500-x and 2000-x respectively).

In *Figure II-24* the magnification was increased to 500-x compared to 300-x for *Figure II-23* to maintain the same general view of an FFT spectrum's image, despite the smaller size of the polystyrene microspheres. The deposition of 3 μm polystyrene microspheres is comparable to that of the 5 μm microspheres, and the temperature has a significant impact on the size of crystalline domains in both cases. At 30 °C, the crystalline domains' size reaches the maximum size as proven by the FFT images, but at this temperature, we also have additional microspheres on top of the main microsphere monolayer (see *Figure II-24 b*). This can be due to the increased mobility of the microspheres and the decrease of surface tension as temperature increases, leading to the monolayer's partial collapse. At 25 °C, this phenomenon rarely happens, but the grain boundaries are a little bit larger (see *Figure II-24 a*).

Going further and using 2 μm polystyrene microspheres, we obtained a similar temperature dependence of the Langmuir-Blodgett results (see *Figure II-25*).

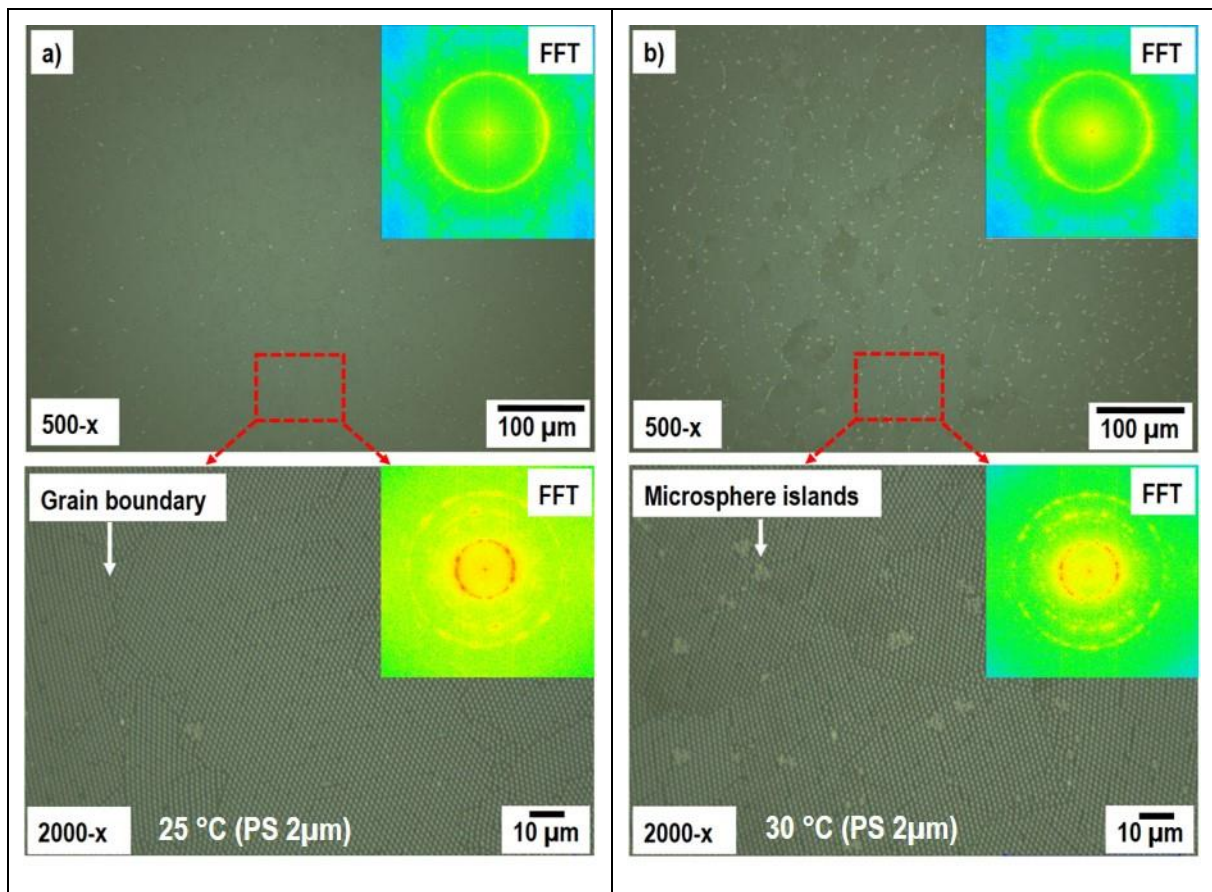


Figure II-25: Optical images at 500-x and 2000-x magnification of polystyrene microspheres 2 μm deposited on Al₂O₃-c at a) 25 °C, b) 30 °C. The inserts represent the FFT (for 500 -x and 2000-x respectively).

Figure II-25 shows the result of a deposition process of 2 μm polystyrene microspheres on the Al₂O₃-c substrate, at 25 °C vs 30 °C. As in the case of 3 and 5 μm polystyrene microspheres, the monolayer forms best at 25 °C. At 30 °C, additional microspheres are present on top of the main microsphere monolayer.

Having these considerations in mind, we can conclude that the best temperature for Langmuir-Blodgett deposition, in our particular experimental conditions, is 25 °C. Since the crystalline domains' quality is higher at this temperature, with most defects concentrated around grain boundaries. This can be further expanded in to an independent study by precisely measuring the surface tension as a function of temperature and ethanol concentration into the sub-phase.

II.3.4. Substrate dependence and barrier-sway effects

All our substrates (Al₂O₃-c, Si, and BK7) are hydrophilic and have not been submitted to any chemical or physical process (except cleaning with acetone, ethanol, distilled water), which can modify their chemical properties and morphological characteristics. The substrates' roughness is in the order of nanometers, and they are chemically inert to all substances used in the deposition process.

Figure II-26 a-c shows the deposition results of 3 μm polystyrene microspheres in the same conditions but on different substrates (Al₂O₃-c, Si, and BK7).

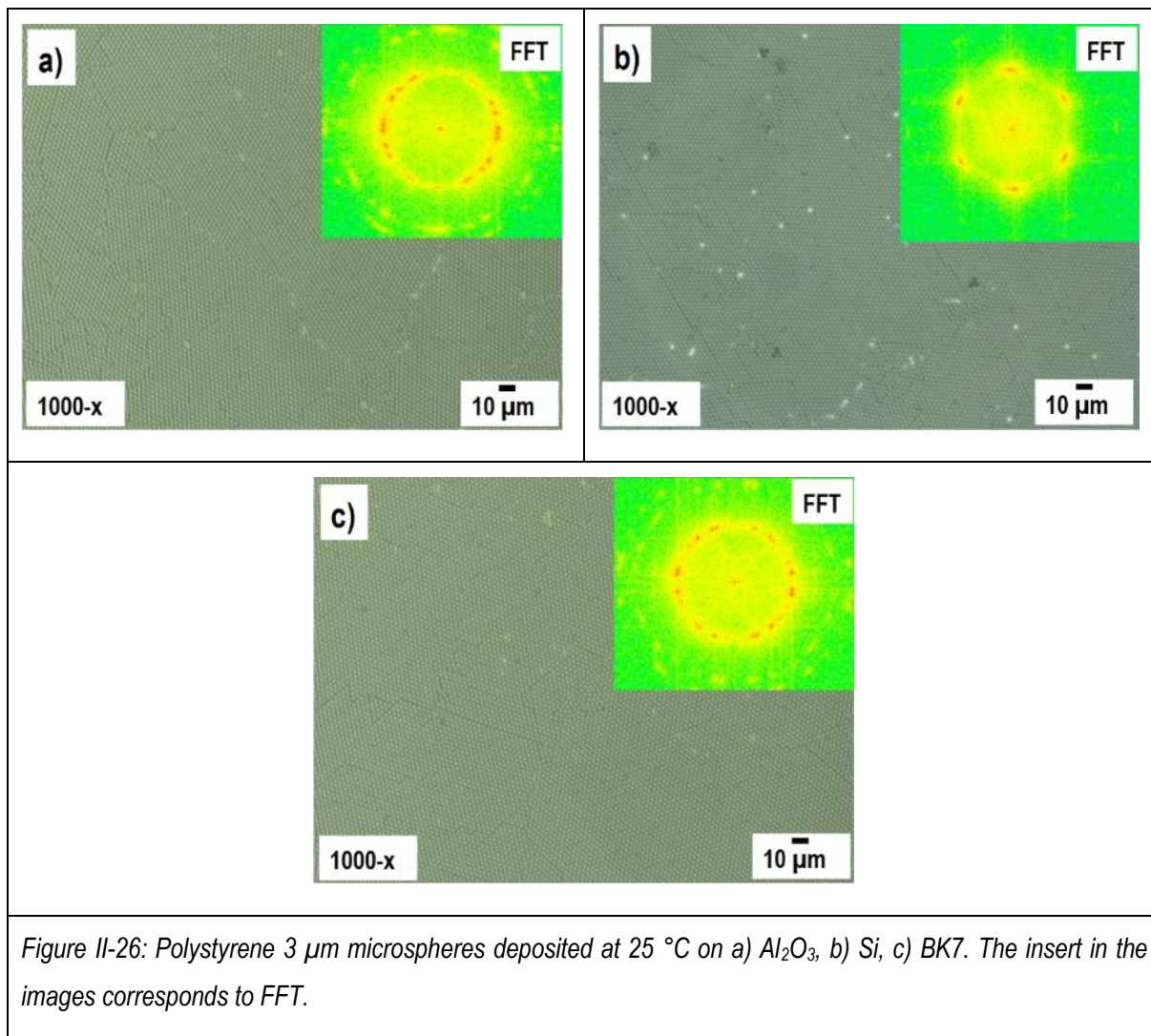


Figure II-26: Polystyrene 3 μm microspheres deposited at 25 $^{\circ}\text{C}$ on a) Al_2O_3 , b) Si, c) BK7. The insert in the images corresponds to FFT.

On Al_2O_3 , the deposition of microspheres is similar to the deposition on BK7 as revealed by optical images and the FFT results (Figure II-26 a) and c)). On Si, the deposition has a higher quality, and the crystalline domains are bigger (see Figure II-26 b)). The size of crystalline domains is in the range of 1 mm^2 for Si substrate, while for the Al_2O_3 , the size of crystalline domains is in the range of 0,1 mm^2 .

When microspheres are released at the water–air interface, the nucleation mode of the microspheres is sporadic, and the subsequent crystal growth results in a 2D polycrystalline entity. Shinotsuka et al. [112] proposed that the size of crystalline domains could be increased by introducing a kinetic perturbation into the system via a barrier-sway process. The barrier-sway process consists in a continuous back and forward (oscillating) motion of both barriers around a predefined position. Here, we have taken a similar approach with a barrier-sway process as [112] and the results are presented in Figure II-27.

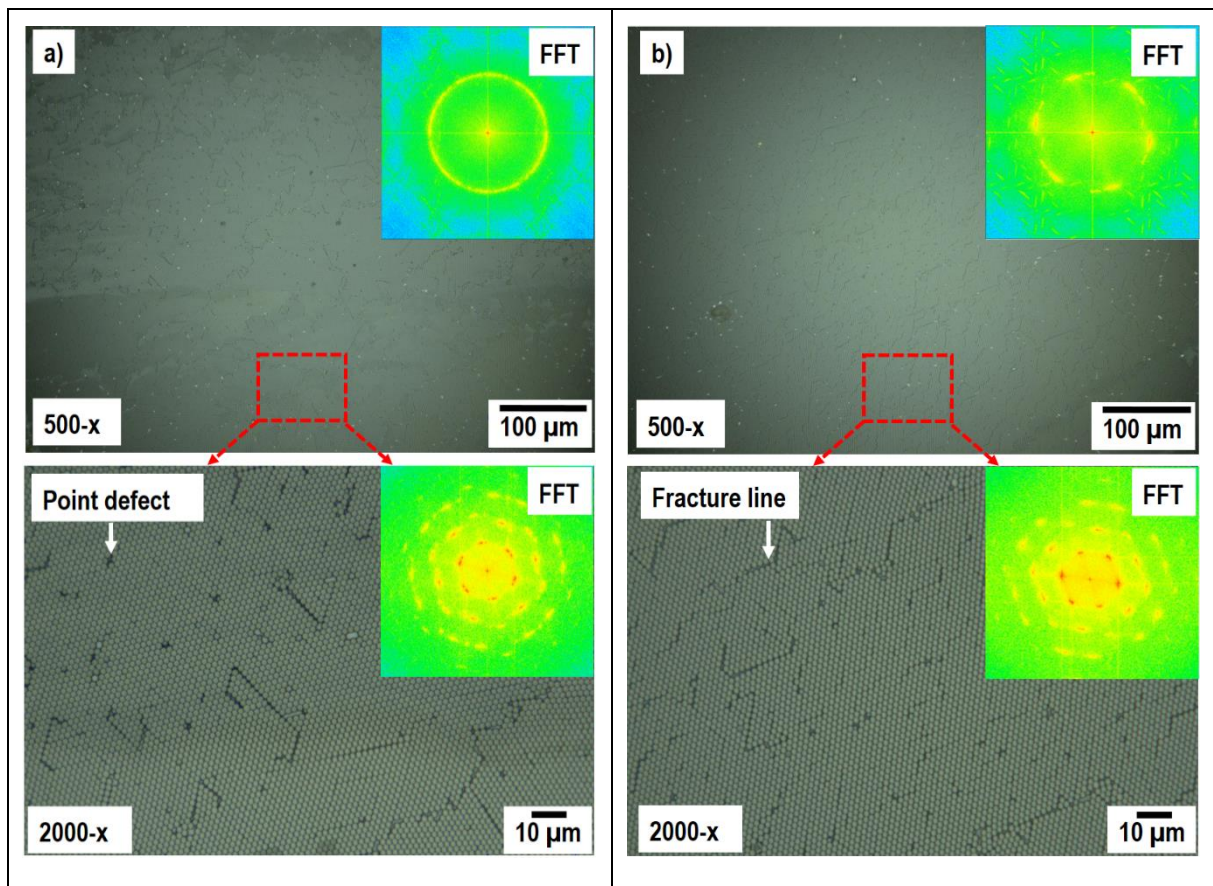


Figure II-27: Polystyrene 2 μm microspheres deposited at 25 $^{\circ}\text{C}$ on Si: a) Conventional deposition of microspheres, b) Deposition of microspheres with an additional barrier sway process at 200 mHz for 30 min. The insert in the images corresponds to FT.

Figure II-27 a) shows the result of a deposition process of polystyrene 2 μm microspheres on the Si substrate, deposition performed as at 25 $^{\circ}\text{C}$. On the sample shown in Figure II-27 b), we performed a barrier-sway process at 200 mHz and an area change of 1% for 30 minutes after the surface tension has reached a constant value. This process is followed by the compression of the microspheres layer and by the deposition of them on a substrate.

The addition of a barrier-sway process increased the crystalline domains' size but decreased the quality of the domains. The Fourier transforms inserted in Figure II-27 b) show that even at low magnification (500-x), the microspheres are arranged in a 2D hexagonal close-packed structure with almost a single orientation.

II.4. Description of the experimental techniques used in sample investigation

This section will briefly present the experimental techniques we are using to characterize the samples. We will not present them with many technical details or in a particular order since this is not the purpose of this thesis. In general, we have used the settings recommended by the manufacturer for each particular system.

The size of the polystyrene spheres that we are using in Langmuir-Blodgett deposition is in the micrometer range, therefore visible under an optical microscope in visible light. Hence, the first assessment of the microsphere deposition results is made using a Keyence optical microscope (VHX-700F).

Information about the sample's surface morphology is extracted using Atomic force microscopy (AFM) from Bruker (IconXR) (for more on AFM, see [118]). Scanning electron microscopy (FEI, model "Quanta FEG 450") together with Focussed Ion Beam Scanning Electron Microscopy (SEM-FIB) was used to assess information on the surface morphology of the samples (for more about SEM see [119], for SEM-FIB systems see [120]). The chemical, EDS, investigations were made using the integrated system of the SEM setup. Temperature-dependent *in-situ* SEM observation was performed with the same system by using an integrated electric furnace. The *in-situ* SEM thermal treatment results were recreated by using a conventional electric furnace in an argon / controlled atmosphere (Nabertherm, model "VHT 08/22 GR").

The optical absorbance spectra were deduced from the transmittance measurements carried out with a UV-VIS system (spectrophotometer, UV-Visible-NIR, model "Varian-Cary 5000") for the 0.2 to 3.3 μm and with an FTIR system (ThermoFisher, model "Nicolet 6700") for the 1.5 to 5.5 μm range, respectively [121], [122].

For the optical measurements in temperature, an external Peltier plate is used for controlling the temperature. It is worth mentioning that the same temperature control system is used both in UV-VIS and FTIR.

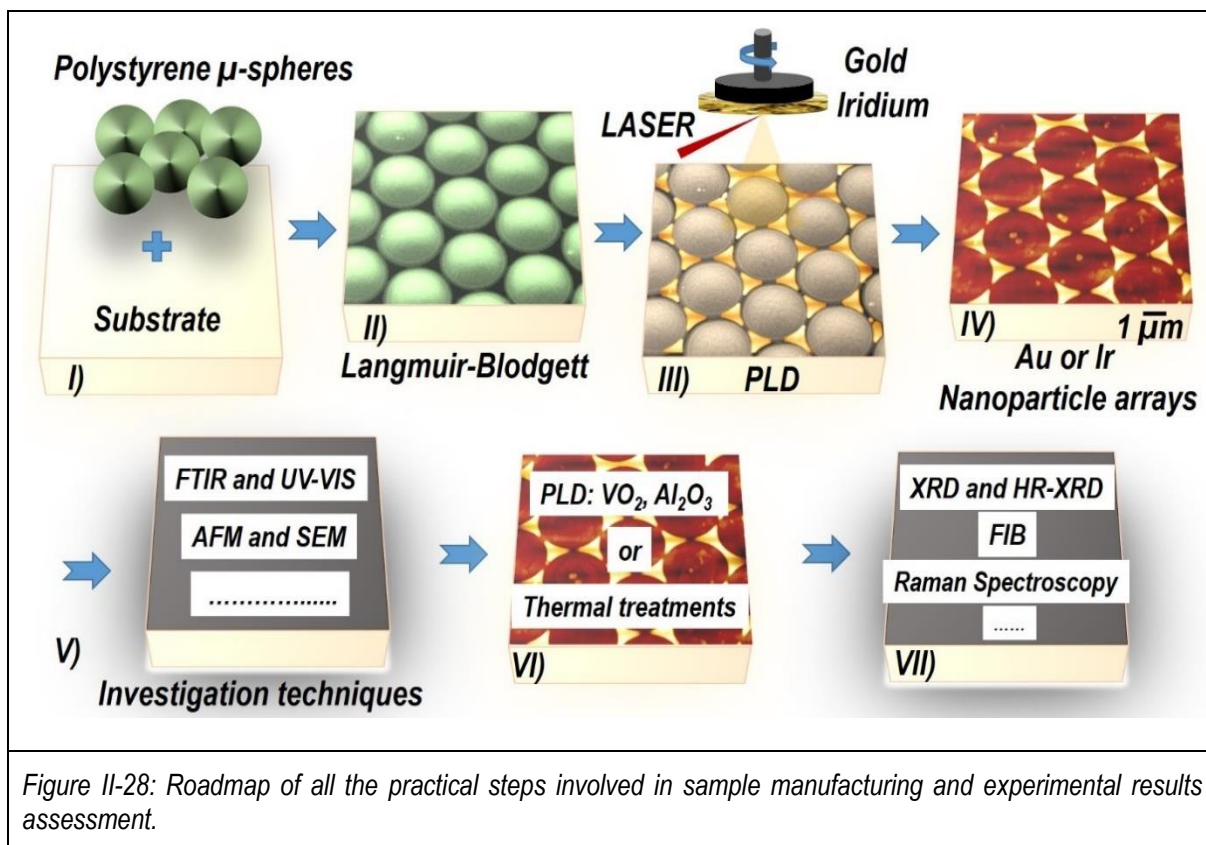
The structural properties of the samples were studied by X-ray diffraction (XRD) in theta/2theta geometry (Bruker, model D8 "Advance," $\text{Cu}_{\text{K}\alpha}$ X-ray source, $\lambda = 0.154 \text{ nm}$, equipped with a focusing $\text{K}\alpha_1$ mono filter, and detector LynxEye, model "A17-B60") (for more info about XRD see [123]). In general, the XRD measurements are made in the 10° - 90° theta/2theta interval, with a step size of 0.009° , an acquisition time of 2 seconds per step, and a rotation of the sample at 30 rpm. Further high-resolution (HR-XRD) investigations have been achieved in various angular configurations (Bruker, model D8 "Discover," $\text{Cu}_{\text{K}\alpha}$ X-ray source, $\lambda = 0.154 \text{ nm}$, similar design) [124].

Raman spectroscopic measurements were performed by using a low energy system (0.1mW at the sample level) to avoid any laser-induced VO_2 transitions (Horiba JobinYvon, model "T64000" spectrometer, associated to an Ar^+/Kr^+ laser, 514.5 nm wavelength) [125]. Temperature-dependent Raman measurements were performed using a heating stage (Linkam Scientific, model "THMS 600"), ensuring precise temperature control in the range 300-370 K.

The numerical data extracted from XRD, HR-XRD, EDS, UV-VIS, FTIR, and Raman measurements are processed using: Origin 2015 (from OriginLab), Microsoft Excel, and Fityk1.3.1 [126]. For XRD data processing, we have also used DIFFRAC.EVA and for Raman data: WiRE™ Software from Renishaw. For image processing, we have used ImageJ and GIMP.

II.5. Sample manufacturing roadmap

Figure II-28 shows a short roadmap of all the practical steps involved in manufacturing our samples and our results' assessments.



The PLD process's energy source was a KrF laser with a wavelength of 248 nm and a fluence of 2-3 J/cm². The distance between the target and the substrate is fixed at 4 cm. After the deposition of metals by PLD, the polystyrene microspheres are removed in an ultrasonic bath using acetone. After the polystyrene is removed and the metal nanoparticle arrays are revealed, the resulting samples are investigated. Then, VO₂ or a layer of amorphous Alumina is further deposited on top of the metallic arrays in the conditions summarized in Table II-1.

Table II-1: Pulsed Laser Deposition experimental conditions.

Target material	Substrate	Laser frequency (Hz)	Time of deposition (min)	Pressure during deposition	Temperature of substrate (°C)	Measured thickness (nm)
Gold Au	Ps: 2, 3, 5... on Al ₂ O ₃ -c	20	5	2 x 10 ⁻⁷ (vacuum)	25 (298 K)	50
Iridium Ir	Ps: 2, 3, 5... on Al ₂ O ₃ -c	20	30	2 x 10 ⁻⁷ (vacuum)	25 (298 K)	50
Alumina Al ₂ O ₃	Au or Ir nanoparticles on Al ₂ O ₃ -c	20	1'50" (110 s)	2 x 10 ⁻⁷ (vacuum)	25 (298 K)	50
Vanadium V	Au or Ir nanoparticles on Al ₂ O ₃ -c	10	3'30" (210 s)	2.2 x 10 ⁻² mbar of O ₂	500 (773 K)	50

II.6. Conclusions

This chapter has presented different aspects of the experimental techniques used in our samples' manufacturing process. The samples are made in three steps. The first step is the manufacturing of colloidal masks of polystyrene microspheres using the Langmuir-Blodgett technique. Then Au or Ir is deposited on top the colloidal masks by using Pulsed Laser Deposition. Finally, the polystyrene microspheres are removed using a solvent using a solvent, revealing an array of metallic nanoparticles on an Al_2O_3 -c substrate (presented in *Chapter III*). The nanoparticles arrays are further embedded in Alumina or Vanadium dioxide (see *Chapter IV*).

The manufacturing colloidal masks using the Langmuir-Blodgett technique has proven to be successful and with reproducible results. The best results for the deposition of polystyrene microspheres using for Langmuir-Blodgett system were obtained at 25°C and without a barrier-sway-assisted process. We found no major influence of the substrate material or of the size of polystyrene microspheres (2,3 and $5\ \mu\text{m}$) on the characteristics of the manufactured colloidal masks. The most important parameters in the Langmuir-Blodgett are temperature and surface pressure.

As for material (Au, Ir, Alumina, VO_2) deposition, PLD is a reliable technique, with highly reproducible samples. For PLD sample manufacturing conditions see Table II-1.

Chapter III

Gold and Iridium nanoparticle arrays - Study of nanoparticles dewetting process by thermal treatments

Chapter III. Gold and Iridium nanoparticle arrays - Study of nanoparticles dewetting process by thermal treatments

Chapter III presents the experimental result in the manufacturing of metallic nanoparticles arrays. The link between the size of polystyrene microspheres and the resulting metallic nanoparticles array is presented here. The correlation between the nanoparticle arrays optical properties (particularly LSPR) and the nanoparticles geometrical characteristics (size and shape), and metal composition is presented. The LSPR peak is modulated by changing the size of the polystyrene microspheres (i.e., changing the size of metallic nanoparticles), changing the thickness of the nanoparticles, or changing the nature of the metal from which the nanoparticles are made (Au vs. Ir). Furthermore, we propose a method based on solid-state dewetting that changes the size and shape of metallic nanoparticles and allows the precise tuning the LSPR. The solid-state dewetting process is studied by in-situ SEM and HR-XRD investigations. The in-situ SEM and HR-XRD investigations revealed a connection between the geometrical characteristics and the crystallographic structure of the nanoparticles.

III.1. Influence of nanoparticle size and metal composition on the LSPR maximum position

The array of metallic nanoparticles made using the procedure presented in Chapter II are shown in Figure III-1 and is representative for all the nanoparticles arrays obtained.

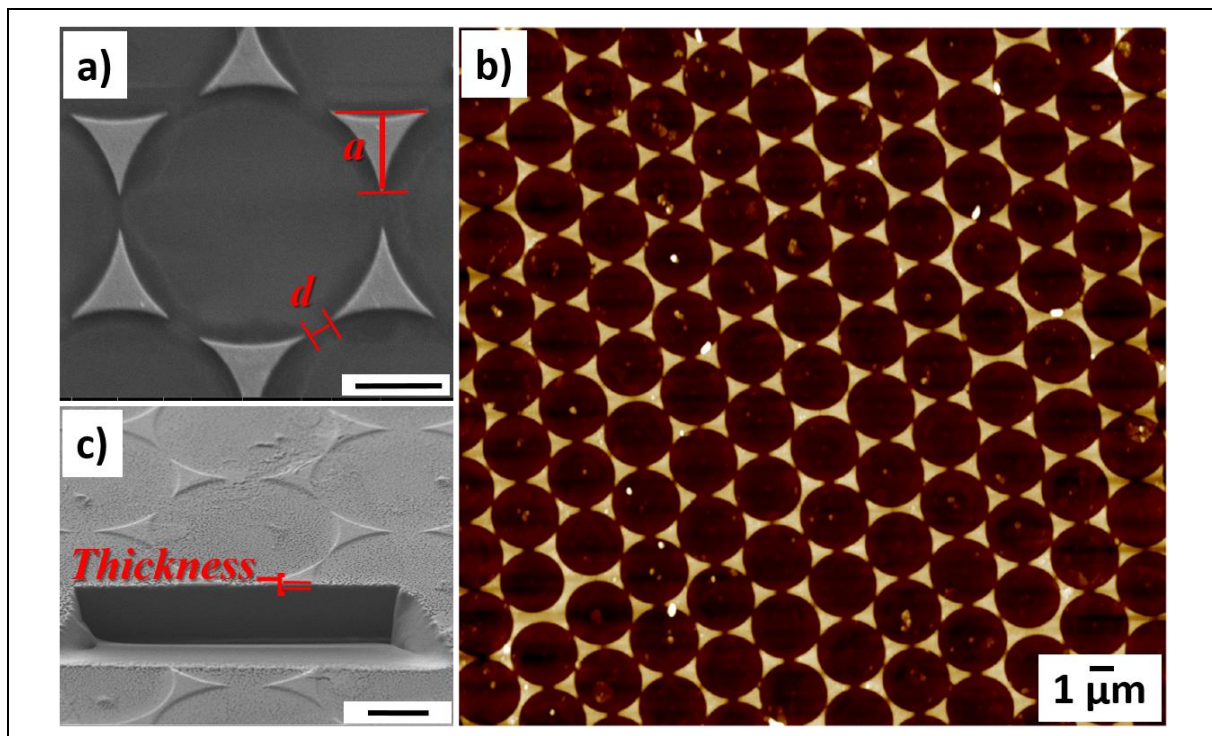


Figure III-1: a) Scanning electron microscopy picture of Au nanoparticle showing the nanoparticles characteristic size **a** and the distance tip to tip **d** between two adjacent nanoparticles. b) AFM image of the global nanoparticle arrays. c) Focused ion beam scanning electron microscopy image used for nanoparticle's precise thickness quantification.

The focused ion beam scanning electron microscopy (FIB) image is used for quantifying and optimizing the thickness of the Au nanoparticles.

The polystyrene microspheres are arranged in 2D hexagonal close-packed structures and lead to the possibility of downsizing or upsizing the nanoparticle arrays while maintaining the same nanoparticle shape and general aspect of the array (i.e., it is an effect similar to the fractal effect). Using in the Langmuir-Blodgett process, polystyrene microspheres with a diameter of 2, 3, or 5 μm will yield similar results in the nanoparticle's general aspect arrays. In this condition, the shift in LPSR peak position can be only linked to the changes in nanoparticle specific size " a " (the perpendicular bisector of the resulting nanoparticles) and the distance between individual nanoparticles. As expressed by Equation (2.7), there is a direct correlation between the diameter D of the polystyrene microspheres and the specific size " a " of the resulting metallic nanoparticles. By applying Equation 2.7 the characteristics dimensions of the metallic nanoparticles are extracted and presented in Table III-1.

Table III-1: Characteristic dimensions of the metallic nanoparticle arrays.

Polystyrene microsphere diameter " D " (μm)	Nanoparticle specific distance tip-to-tip d (μm) (experimental/measured)	Nanoparticle specific size " a " (μm)	
		Calculated (Equation 2.7)	Experimental (measured)
2	0.31	0.46	0.48
3	0.42	0.70	0.90
5	0.70	1.16	1.44

The values may vary slightly between experimental conditions and the calculated ones due to the compactness of the polystyrene microspheres during the deposition process.

The characteristics dimensions of the metallic nanoparticles presented in Table III-1 have an effect in the optical properties of the obtained metallic arrays (see Figure III-2). The thickness of the Au and Ir nanoparticles for Figure III-2 is 50 nm. This thickness is selected following Au's growth model on an $\text{Al}_2\text{O}_3\text{-c}$ substrate (see Section II.1.4 and Equation 2.2) to ensure that the metallic nanoparticles are continuous. Further than that, a 50 nm thickness of metal will prevent electromagnetic waves (IR and the ones from the visible range) from passing through the nanoparticles (see Figure I-20: *Skin depth δ_{skin} versus photon energy*). The absorbance (A) spectrum of metallic nanoparticle arrays presented in Figure III-2 is deduced from transmittance (T) measurement by using $A = -\log(\%T)$. The optical transmission is measured by FTIR spectroscopy and using air as background. The optical transmission of the $\text{Al}_2\text{O}_3\text{-c}$ substrate in the 0.20 up to 6 μm reaches almost 100 %, with no absorption peak presented in this range. Close and after 6 μm , the optical absorption increases significantly due to phonon absorption modes (see Figure I-14). The absorption spectra seen in Figure III-2 are given by the localized surface resonance of the metallic nanoparticle arrays visible in Figure III-1. For Au nanoparticle arrays made with 3 μm polystyrene microspheres, the resonance peak maximum is located at $\lambda \approx 4.45 \mu\text{m}$; while using 2 μm polystyrene microspheres has produced samples with a resonance peak maximum at $\lambda \approx 2.85 \mu\text{m}$. Changing the metal will slightly shift the position of the resonances; for Ir nanoparticles made with 2 and 3 μm polystyrene microspheres $\lambda \approx 4.39 \mu\text{m}$ and $\lambda \approx 2.95 \mu\text{m}$, respectively. A more noticeable difference is the lower intensity of Ir LSPR

compared to Au LSPR. This could be a consequence of the lower electron mobility of Ir compared to Au electron mobility (see Table I-4 and Table I-5). Here the measurement is made with unpolarized light. The light polarization can shift the position of resonances if the individual nanoparticles are all orientated in a particular direction (see Chapter I). In our case the nanoparticles do not have a particular orientation, hence the polarization of light does not influence the position of the resonances.

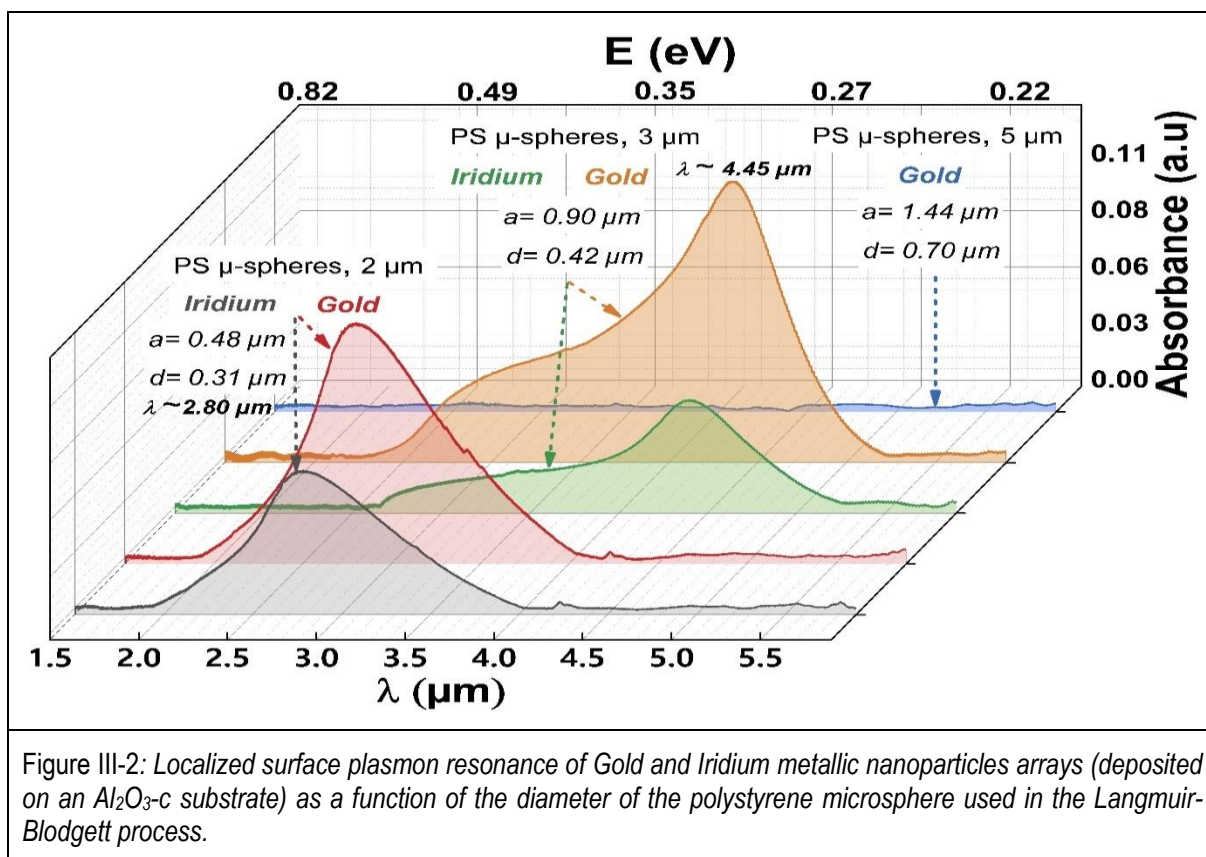
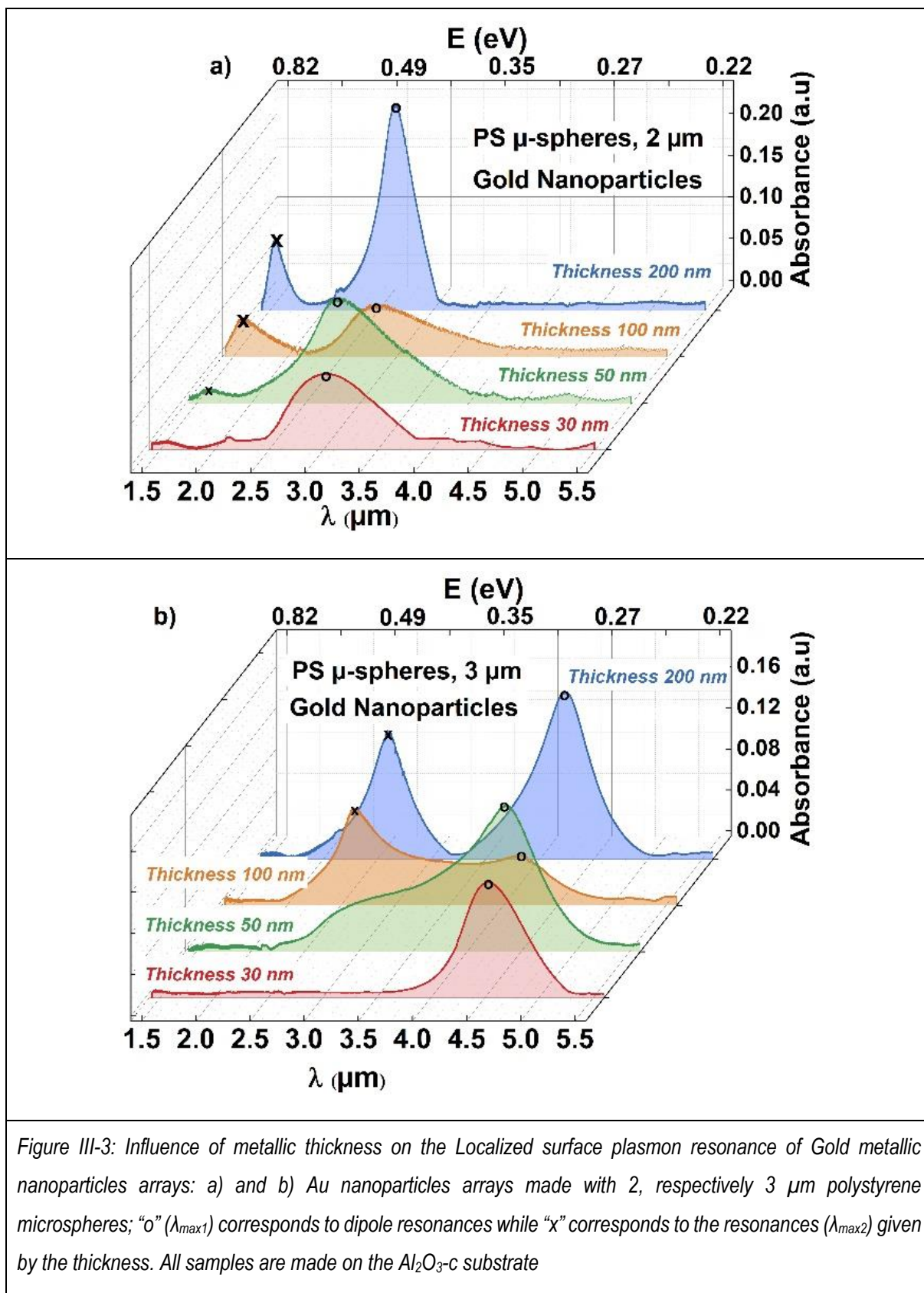


Figure III-2: Localized surface plasmon resonance of Gold and Iridium metallic nanoparticles arrays (deposited on an Al_2O_3 -c substrate) as a function of the diameter of the polystyrene microsphere used in the Langmuir-Blodgett process.

For both Au and Ir nanoparticles arrays, the LSPR maximum can be assigned to the dipolar resonances of the metal nanoparticles, and the shift in the position of the peaks can be justified through the change in the size of nanoparticles (see also Figure I-10). Therefore, optical spectra's can be used, also, as a tool to characterize the metallic nanoparticles.

A detailed study on the influence of thickness on LSPR properties is presented in Figure III-3. As seen in Figure III-3, changing the metallic nanoparticles' thickness drastically changes the shape of the absorbance spectra. For nanoparticles (Au or Ir) with a thickness of 30 nm or 50 nm, the absorbance spectra show one LSPR peak that can be assigned to dipolar resonances of the metallic nanoparticles. The shoulder in the absorbance spectra that is close to the main resonance peak, in the case of Au and Ir nanoparticles with a thickness of 50 nm (see Figure III-3 b and d) may be assigned to the plasmonic coupling between the nanoparticles (see Section I.2.2.4 and also Figure I-11 c). When the thickness of nanoparticles increases to 100 nm, the primary resonance peak shifts to higher wavelengths and splits into two components; a dipolar one, the peak at higher wavelengths, and a dipole one that is linked to the thickness of the peak at lower wavelengths.



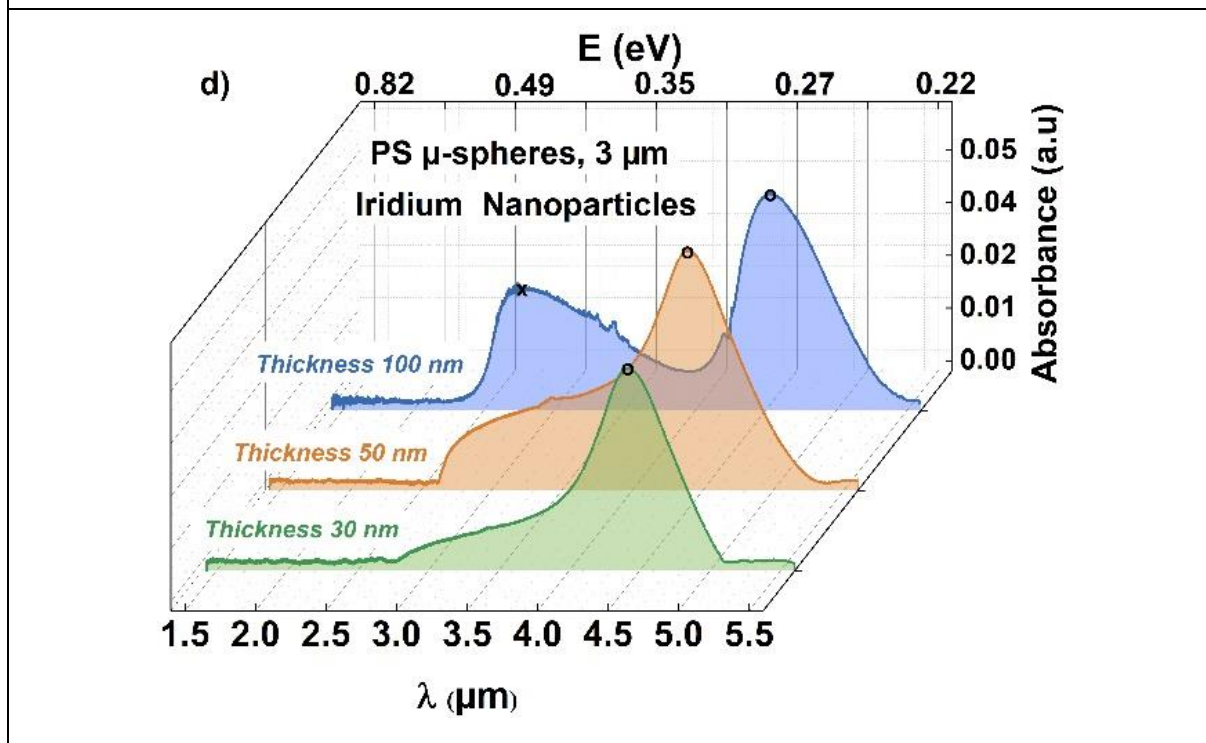
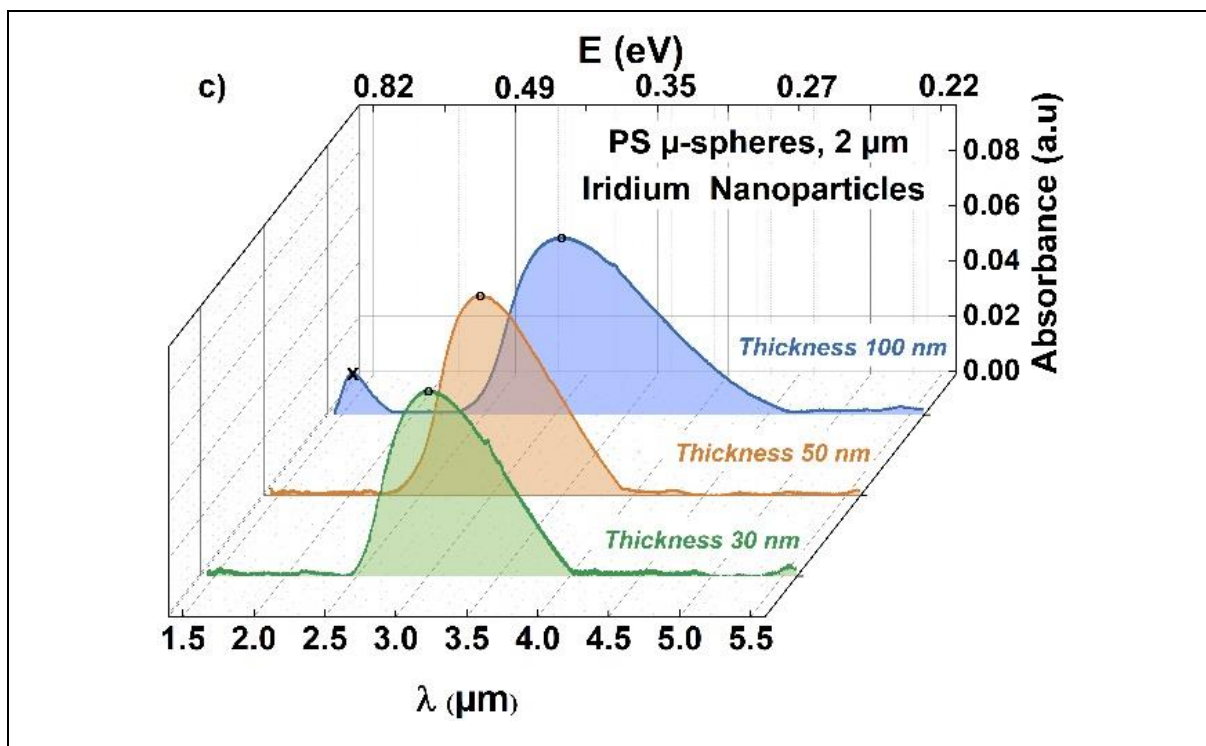


Figure III-3: Influence of metallic thickness on the Localized surface plasmon resonance Gold and Iridium metallic nanoparticles arrays; a) and b) Au nanoparticles arrays made with 2, respectively 3 μm polystyrene microsphere c) and d) Iridium nanoparticles arrays made with 2, respectively 3 μm polystyrene microspheres; "o" ($\lambda_{\text{max}1}$) corresponds to dipole resonances while "x" corresponds to the resonances ($\lambda_{\text{max}2}$) given by the thickness. All samples are made on the $\text{Al}_2\text{O}_3\text{-c}$ substrate

A analytical link between the position of the LSPR maximum of absorption of the metallic nanoparticles (with a shape like ours) and the diameter of the polystyrene microsphere, is given by Piotr Patoka et al. [127]. He assumed that the resonances seen in Figure III-3 are from a highly dispersive, plasmon polariton mode, since similar resonances have also been seen in metallic clusters. In this model, each side of the quasi-triangular particle equals approximately 1/6 of the polystyrene microsphere circumference/perimeter πD , the perimeter of the metallic nanoparticle is equal to:

$$Particle\ perimeter = \frac{3\pi D}{6} = \frac{\pi D}{2} \quad \text{Equation (3.1)}$$

The circumferential quantization condition requires that this circumference is equal to an integer multiple of the wavelengths of the resonating surface/edge plasmon wave [127]. In this condition, he envisioned the resonances “as circumferentially quantized surface plasmon waves”. The link between peak position and resonance positions is expressed as:

$$l * \lambda_{LSPR} \approx \pi * \frac{D}{2} \quad \text{Equation (3.2)}$$

where $l=1,2,3...$ is the order of resonance [127]. The results of his model in our experimental condition are presented in Table III-2.

Table III-2. Experimental and theoretical LSPR peak position of the metallic nanoparticle arrays.

(A) Experimental geometrical characteristics				(B) LSPR _{experimental}		(C) LSPR _{theoretic} calculated using the size of polystyrene microspheres		(D) LSPR _{theoretic} calculated using measured metal nanoparticles	
Polystyrene Microsphere size (μm)	Metal	a (μm)	Thickness (nm)	λ _{max 1} (μm)	λ _{max 2} (μm)	λ _{max 1} (μm)	λ _{max 2} (μm)	λ _{max 1} (μm)	λ _{max 2} (μm)
2	Au	0.48	30	3.2	-	3.14	1.57	3.25	1.62
2	Au	0.48	50	2.85	1.60	3.14	1.57	3.25	1.62
2	Au	0.48	100	2.80	1.58	3.14	1.57	3.25	1.62
2	Au	0.48	200	2.66	1.56	3.14	1.57	3.25	1.62
2	Ir	0.48	30	3.01	-	3.14	1.57	3.25	1.62
2	Ir	0.48	50	2.95	-	3.14	1.57	3.25	1.62
2	Ir	0.48	100	2.90	1.58	3.14	1.57	3.25	1.62
3	Au	0.90	30	4.54	-	4.71	2.35	6.09	3.05
3	Au	0.90	50	4.45	-	4.71	2.35	6.09	3.05

3	Au	0.90	100	4.20	2.63	4.71	2.35	6.09	3.05
3	Au	0.90	200	4.20	2.60	4.71	2.35	6.09	3.05
3	Ir	0.90	30	4.45	-	4.71	2.35	6.09	3.05
3	Ir	0.90	50	4.39	-	4.71	2.35	6.09	3.05
3	Ir	0.90	100	4.48	2.71	4.71	2.35	6.09	3.05
5	Au	1.44	50	-	-	7.85	3.92	9.74	4.87

The column **(A)** in Table III-2 represents the experimentally measured (by AFM) characteristic dimensions of the metallic nanoparticles. The column **(B)** reports the resonant peak position of the metallic nanoparticle arrays extracted using a fit (with Voigt function) of the measured absorbance spectra (Figure III-3). The column **(C)** represents the calculated resonant peak position using the model from reference [127] in which the nanoparticles characteristic dimensions are deduced using the size of the polystyrene microspheres. While, column **(D)** is associated with the resonance peaks calculated (from [127]) using the characteristic dimensions of the metallic nanoparticles measured by AFM (column **A**).

The model from reference [127] offers a good way to find the approximative position of the resonance peaks (see Table III-2). The model does not consider the nature of the metal, or the dielectric environment surrounding the nanoparticles and tends to overestimate the resonance positions (see Table III-2). This empirical model gives similar results when using the polystyrene microsphere size or the measured geometrical characteristics of the metallic nanoparticles. According to the model, the LSPR peak position of metal nanoparticles made with polystyrene microspheres of 5 μm is close to 8 μm , far from the 6 μm optical transmission cut-off of the $\text{Al}_2\text{O}_3\text{-c}$ substrate. This can explain the lack of a resonance peak in Figure III-2 for the Au nanoparticles made with 5 μm polystyrene microspheres.

The second-order resonance ($\lambda_{\text{max}2}$) may be a quadrupole resonance peak or a resonance due to the in-plane and out-of-plane splitting of a dipolar resonance on the bases of nanoparticles' geometrical characteristics [127]. Richard P. van Duyne et al. [125] proposed an empirical model for determining the LSPR peak position sensibility to the nanoparticles' geometrical characteristics. In his model, the LSPR peak position is affected by the in-plane width sensitivity is $\Delta\lambda_{\text{max}}/\Delta a \cong 4$ and the out-of-plane thickness sensitivity $\Delta\lambda_{\text{max}}/\Delta \text{thickness} \cong 7$ (see Figure III-1). These relations support the possibility to decouple the in-plane and out-of-plane components of the LSPR from one to another. Therefore, both peaks may be dipolar but came from the two nanoparticle geometrical characteristics (**a** and thickness). He [125] suggested that it is easier to decouple the in-plane and out-of-plane plasmonic response of nanoparticles with a greater thickness than nanoparticles with a smaller thickness. Following this idea, it is clear that, the intensity of the second resonance peak increases with increasing thickness. Taking this intensity increase together with reference [125] findings and with the DDA simulation result on the plasmonic nanoparticles (see also Figure I-10 e), we conclude that the second resonance peak is a result of in-plane and out-

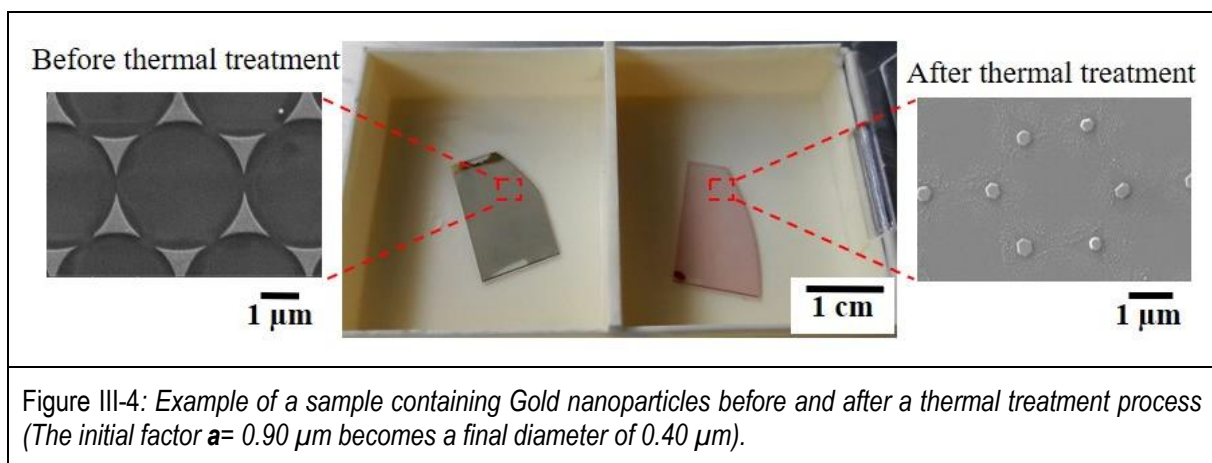
of-plane decoupling of the dipolar resonance based on geometrical characteristics and not to quadrupole resonance.

III.2. Tunable absorption: Influence of the nanoparticle shape on the LSPR response - Role of dewetting process

III.2.1. Thermal treatment effects on Au nanoparticle arrays

In the previous section, the shifting of the LSPR maximum was made based on changing the size of the polystyrene microspheres used in the Langmuir-Blodgett process. This is an attractive and useful way of shifting the position of LSPR maximum to different wavelengths. However, in practice, the metal nanoparticles cannot be made to resonate at a particular wavelength since there is always a link between the polystyrene microsphere's size and the LSPR peak position. A method of tuning the LSPR peak position is to act directly on characteristic size (**a**) and shape of the metallic nanoparticles.

Changing the **a** factor of the metallic nanoparticles can shift the LSPR maximum to the desired resonance position actively. The change of **a** factor and shape can be made through thermal treatment. Thermal treatment is performed in a conventional furnace and in a furnace placed inside a SEM system. Figure III-4 shows the thermal treatment results of Au nanoparticles arrays with an initial $a=0.90\ \mu\text{m}$. This treatment induces changes at the nonmetric level, directly affecting the macroscopic appearance (i.e., the sample is reddish after the treatment).



The changes in terms of shape and size of the Au nanoparticles subjected to a thermal treatment has been studied extensively for two main reasons. Au is a noble metal with a very low affinity for oxygen, and the vapor pressure of Au remains relatively low up to its melting point [128]. This makes Au the ideal candidate for assessing the geometrical changes of nanoparticles as a function of temperature. The low vapor pressure prevents the loss of material by evaporation and the low oxygen affinity prevents any oxide interface formation, making Au suitable for shifting the LSPR peak position by thermal treatment [129].

The temperature at which the geometry (i.e., the surface to volume ratio) of nanoparticles changes depends on various factors, such as shape, size, and supporting substrate, etc. All these factors are of significant influence and lead to the shifting of nanoparticles' melting point compared to the bulk material. For spherical Au

nanoparticles with a radius of less than 10 nm, the melting temperature is lower than the melting temperature of the corresponding bulk material [130]. For example, the melting point of 2.5 nm gold nanoparticles is close to 930 K, much lower than its bulk value of 1337 K [131].

G.L. Allen et al. [132] predicted that if the vibration of atoms' amplitude becomes 10 % of the distance to the nearest neighbor, the crystal will undergo a melting transition [133]. The atoms at the surface have a greater amplitude of vibration than the bulk atoms, meaning that the melting will start at the surface. The ratio between surface atoms and bulk atoms changes with the shape and size of nanoparticles. This implies that small nanoparticles, with a shape as different as possible from a spherical shape, will melt faster than their bulk counterparts will [128], [132]–[136].

If the nanoparticles have a radius bigger than 10 nm, then melting will be close to the melting temperature of the bulk materials [128], [132]. However, this does not mean the nanoparticles will not change their shape and size upon heating. At this scale, the mechanism of solid-state dewetting becomes predominant and drive the evolution of a nanoparticle's shape towards one more energetically favorable [137]. The solid-state dewetting is driven by a competition between the thermodynamics and kinetics of the system [138].

Thermodynamic effects always drive the system toward the most energetically favorable state. However, atoms often encounter energy barriers for which they do not have sufficient kinetic energy to overcome, confining the system to a metastable state [138]. When more energy is brought into the system, such as by a thermal treatment, the atoms have more kinetic energy, and the system moves towards a more energetically favorable morphology.

The equilibrium morphology depends on the relative ratio between the three interfacial energies: nanoparticle-vapor (γ_{nv}), substrate-vapor or substrate surface energy (γ_{sv}), and nanoparticle-substrate interfacial energy (γ_{ns}) (see also Section II.1.4). The result of a thermal treatment process performed in a conventional furnace in an atmosphere of 1 bar of Argon at a heating rate of 10 K/min are presented in Figure III-5.

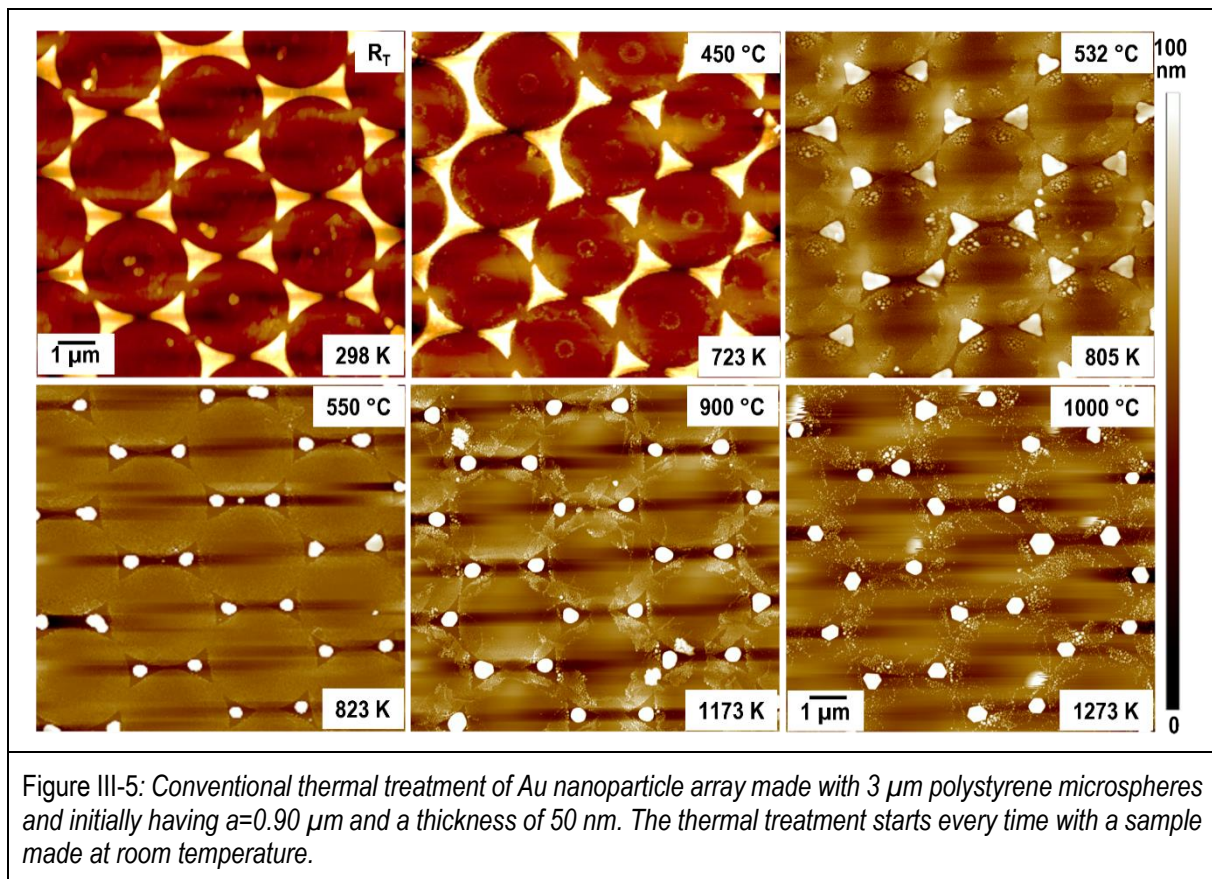


Figure III-5: Conventional thermal treatment of Au nanoparticle array made with 3 μm polystyrene microspheres and initially having $a=0.90 \mu\text{m}$ and a thickness of 50 nm. The thermal treatment starts every time with a sample made at room temperature.

The surface energy of $\text{Al}_2\text{O}_3\text{-c}$ is between 1.5 to 1.7 J/m^2 , and of Au is 1.5 J/m^2 [139]–[142] while, the surface energy of gold/sapphire interface is close to 2.5 J/m^2 [130], [143]. It is worth mentioning that for Au, the surface energy varies with the crystallographic orientation and the nanoparticles' size [142], [144]. The expression of the thermodynamic equilibrium, derived by Young, between the three phases written as $\gamma_{sv} = \gamma_{ps} + \gamma_{pv} \cos \theta$ (Equation 2.2); where θ is the equilibrium contact angle at the three phases boundary. For the above Young expression to hold, the contact angle θ must be estimated between 122 to 132 degrees, close to 180 degrees total dewetting process. Consequently, the system will minimize the total energy by driving each Au nanoparticles towards a quasi-spherical Au nanoparticle.

In addition to this, $\text{Al}_2\text{O}_3\text{-c}$ represents a well-suited substrate for studying solid-state dewetting of Au nanoparticles due to its high chemical and thermal stability, crystallographic perfection, and high resistance to diffusion of Au atoms into it. This mechanism of isolated island formation is also present in Figure III-5. Here, the Au nanoparticles are made using 3 μm polystyrene microspheres, which serve as a mask. The Au material has to be deposited in the form of nanoparticles, but after the thermal treatment process, the nanoparticles do not coalesce together, and they remain isolated islands. Initially, the Au nanoparticles have a triangular shape, but as the temperature goes up, the shape changes and evolves towards nanoparticles with a more rounded shape (see Figure III-5). The *in-situ* SEM evolution of Au nanoparticles as a function of temperature during a thermal treatment process from 25 °C (298 K) up to 1000 °C (1273 K) is given in Figure III-6 a-f.

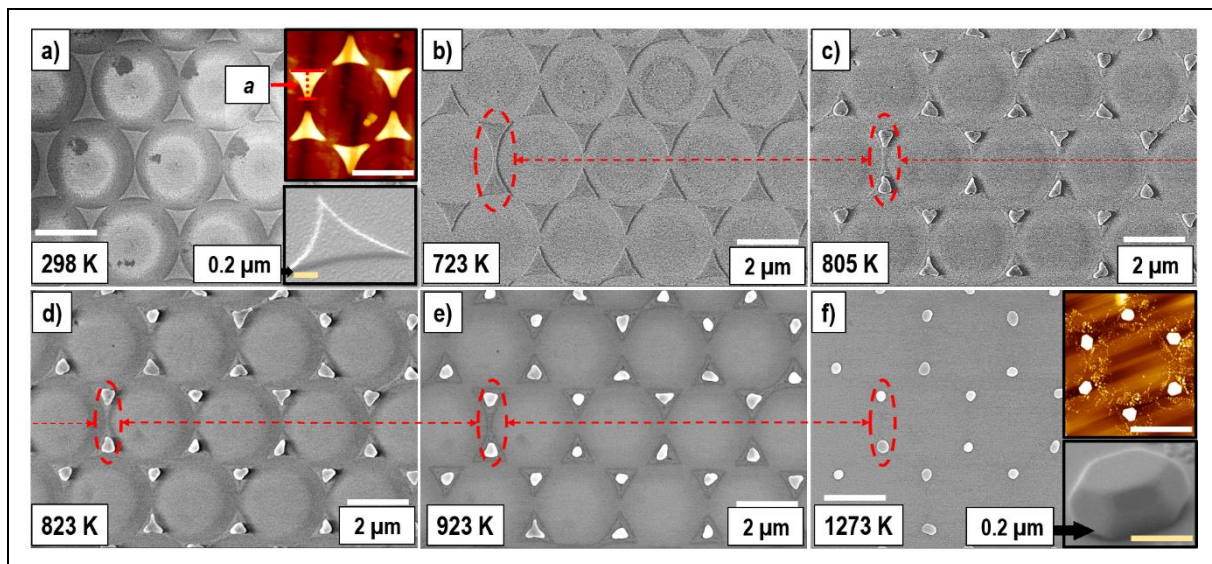


Figure III-6: Dewetting of Au nanoparticle, with a thickness of 50 nm and initial $a=0.90 \mu\text{m}$ on an $\text{Al}_2\text{O}_3\text{-c}$ substrate. The thermal treatment is made in furnace inside a SEM system. The starting temperature is R_T and the process stops at 1273 K or 1000 °C. The white scale bar is 2 μm and the yellow one is 0.2 μm . The inserts are AFM and SEM-FIB analyses of samples submitted to conventional thermal treatment (see also SEM movie).

From the experimental standpoint, assessing the geometrical changes of nanoparticles from a temperature to a different, higher temperature can be problematic. There will always be minimal fluctuations in nanoparticles' size; fluctuations linked to the manufacturing process. Observing the precise evolution over a relevant temperature range may involve probing as many temperatures as possible and probing as many sites on the sample as possible. This approach can be accomplished; however, the most suitable and fastest/elegant way to quantify the geometrical changes is to observe the in-situ solid-state dewetting phenomenon, more specifically, to focus on a selected area of the sample and follow the same nanoparticles' evolution from 298 K up to the desired temperature. This was achieved by performing the thermal treatment in a furnace placed inside the SEM system, at a heating rate of 10 K/min, and a pressure of 4-5 mbar of Argon. In the beginning (Figure III-6 a), because the Au PLD deposition was performed at R_T , the atoms lack the kinetic energy needed to move a great distance across the surface of the substrate. This will freeze the nanoparticles in a metastable state with a prismatic shape, with a greater surface area than that for which the surface energy reaches a minimum. By thermal treatment, energy is brought into the system (Figure III-6 b-f), and surface energy minimization mechanisms start to occur, leading to solid-state dewetting. Other mechanisms of surface energy minimization that may lead to growing a bigger few of the nanoparticles at the expense of all the other nanoparticles, such as Ostwald ripening [145] via evaporation or surface diffusion, are challenging to assess. However, based on Au's low vapor pressure and relatively short thermal treatment time (10 °C /min and 30 min at the desired temperature), nanoparticles cannot lose or collect atoms. Hence, any subsequent change in nanoparticles' optical properties can come only from the direct geometrical changes of nanoparticles and changes in the contact area between nanoparticles and substrate. Ideally, when the temperature rises, the Au nanoparticles will evolve towards a shape resembling a truncated octahedron, i.e., Wulff construction [134]. However, the sapphire/Au interface is non-deformable. Therefore, a portion of the nanoparticle interface is constrained to replace the image of the removed interface. Thus the

Winterbottom construction will give an equilibrium to the Au nanoparticle's shape [146], [147]. As the temperature goes up, the nanoparticles start to solid-state dewet, with Au atoms migrating from edges towards each nanoparticle's center. The shape of nanoparticles changes, and the whole system evolves similarly as in the case of thermal treatment performed in the conventional argon furnace, except for 1000 °C (1273 K) (Figure III-6 f). Indeed, at this temperature Au nanoparticles have rounded shape. This is a direct consequence of the in-situ observation procedure, where the additional energy of the electron gun leads to local supercritical heating of nanoparticles. In time, the local temperature gets higher than the melting temperature of bulk Au (1337 K), and the formation of Winterbottom construction is no longer possible. When the thermal treatment is performed in a conventional furnace, at 1000 °C (1273 K), as presented in the insert of Figure III-6 f and Figure III-7, the top of the Au nanoparticles becomes flat or truncated due to the formation of lower surface energy planes [145].

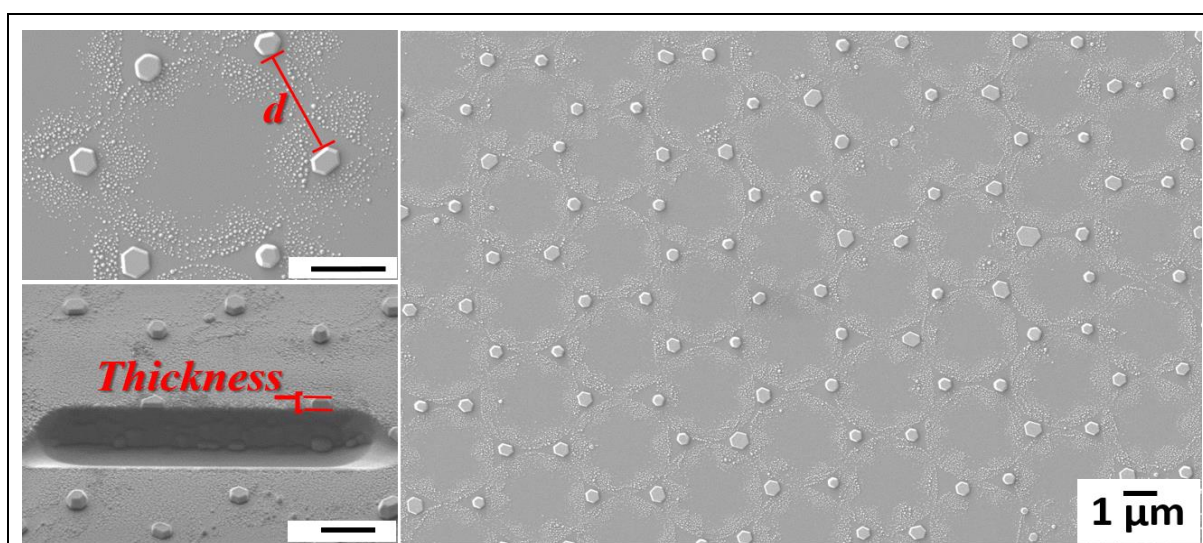


Figure III-7: SEM-FIB image of Au nanoparticle arrays after thermal treatment in a conventional furnace at 1000 °C (1273 K).

This is a highly reproducible and global effect (Figure III-7) and the facets-forming phenomenon was correlated by Mullins et al. [148], [149] also to the density of defects in the particles not just to the thermally activated kinetics of the process. A lack of step propagating defects can inhibit shape equilibrium just by the kinetics of thermal activation. Hence, towards a Winterbottom construction, the shape equilibrium is also promoted by the presence of defects and nanoparticle-substrate interaction. The formation of the specific nanoparticle shapes in the dewetting process is also influenced by the hexagonal crystallographic structure of the underlying *c-plane sapphire* substrate [145]. For the ideal packing density of 90.7%, the area occupied by each resulting Au nanoparticle is approximately $0.35 \mu\text{m}^2$. If Au nanoparticles, with 50 nm in thickness, are considered to have straight sides so that the nanoparticle area that is in contact with the substrate mirror the area of the opposite side of the top of the nanoparticle, then the volume of a single Au nanoparticle will be equal to $17.5 \times 10^{-3} \mu\text{m}^3$. In reality, the specific size "a" of Au nanoparticles is $\sim 0.9 \mu\text{m}$, and the area occupied on the substrate by an Au nanoparticle is $\sim 0.45 \mu\text{m}^2$, for a maximum thickness of 50 nm. The distance between the tips of two adjacent nanoparticles is $\sim 0.5 \mu\text{m}$. The difference between theoretical and experimental values may come from three factors: defects in the packing of the

polystyrene microsphere, polydispersity of polystyrene microspheres or shadowing, and Au atoms migration under the polystyrene microspheres during the Au deposition process. In experimental conditions, these three factors induce a slope on the sides of the resulting Au nanoparticles. The resulting volume of such a prismatic nanoparticle is $\sim 8 \pm 1 \times 10^{-3} \mu\text{m}^3$, equal to a spherical nanoparticle with a diameter of $250 \pm 20 \text{ nm}$ ($\sim 0.25 \pm 0.02 \mu\text{m}$). When the Au nanoparticles are thermally treated at $1000 \text{ }^\circ\text{C}$ (1273 K) like in Figure III-7, the thickness increases to 100 nm while the volume remains the same. A summary of the *in-situ SEM* observation of the temperature effects on Au nanoparticles' geometrical characteristics is presented in Figure III-8 a-d. The experimental data points presented in Figure III-8 are extracted using the ImageJ software from SEM images as the ones presented in Figure III-6. In Figure III-8, each data point represents an average value of the nanoparticle geometrical characteristics, at a particular temperature, for approximately 25 Au nanoparticles. Figure III-8 shows the temperature range from $25 \text{ }^\circ\text{C}$ (298 K) to $1000 \text{ }^\circ\text{C}$ (1273 K) can be divided into three sub-sections. First, in the $25 \text{ }^\circ\text{C}$ (298 K) to $450 \text{ }^\circ\text{C}$ (723 K) temperature interval, the nanoparticles area (projected on the substrate) and shape change slowly, almost unnoticeable, and the inter-particle distance increases as the temperature goes up. In the second temperature range, from $450 \text{ }^\circ\text{C}$ (723 K) to $550 \text{ }^\circ\text{C}$ (823 K), the temperature significantly impacts the nanoparticle and inter-particle distances. Between $450 \text{ }^\circ\text{C}$ (723 K) and $550 \text{ }^\circ\text{C}$ (823 K), almost all of the geometrical changes in solid-state dewetting occur. After $550 \text{ }^\circ\text{C}$ (823 K), even though the temperature goes up, geometrical characteristics (area, inter-particle distance, shape factor) become smaller and smaller (see Figure III-8 a). The evolution of interparticle distance between two adjacent nanoparticles' tips in rapport to the average interparticle distance is presented in Figure III-8 b). In the beginning, at $450 \text{ }^\circ\text{C}$ (723 K), the two nanoparticles are connected by a thin strip of Au. As the temperature goes up, the two connected nanoparticles split into two individual nanoparticles. In the $450 \text{ }^\circ\text{C}$ (723 K) and $550 \text{ }^\circ\text{C}$ (823 K) temperature range, the speed of separation of the two connected nanoparticles is so high that the nanoparticles can catch up with the rest of the nanoparticles and have almost the same interparticle distance between them as the average interparticle distance. This phenomenon constitutes a evidence of a solid-state dewetting effect which prevail in competition with the coalescence processes. Coalescence that otherwise will result in the formation of a single nanoparticle. The nanoparticle separation process may also be seen as a path to improve the nanoparticle array's quality since the total size and shape polydispersity of nanoparticles will decrease. At $25 \text{ }^\circ\text{C}$ (298 K), nanoparticles have a prismatic shape with a "triangular" base and sharp corners (tips).

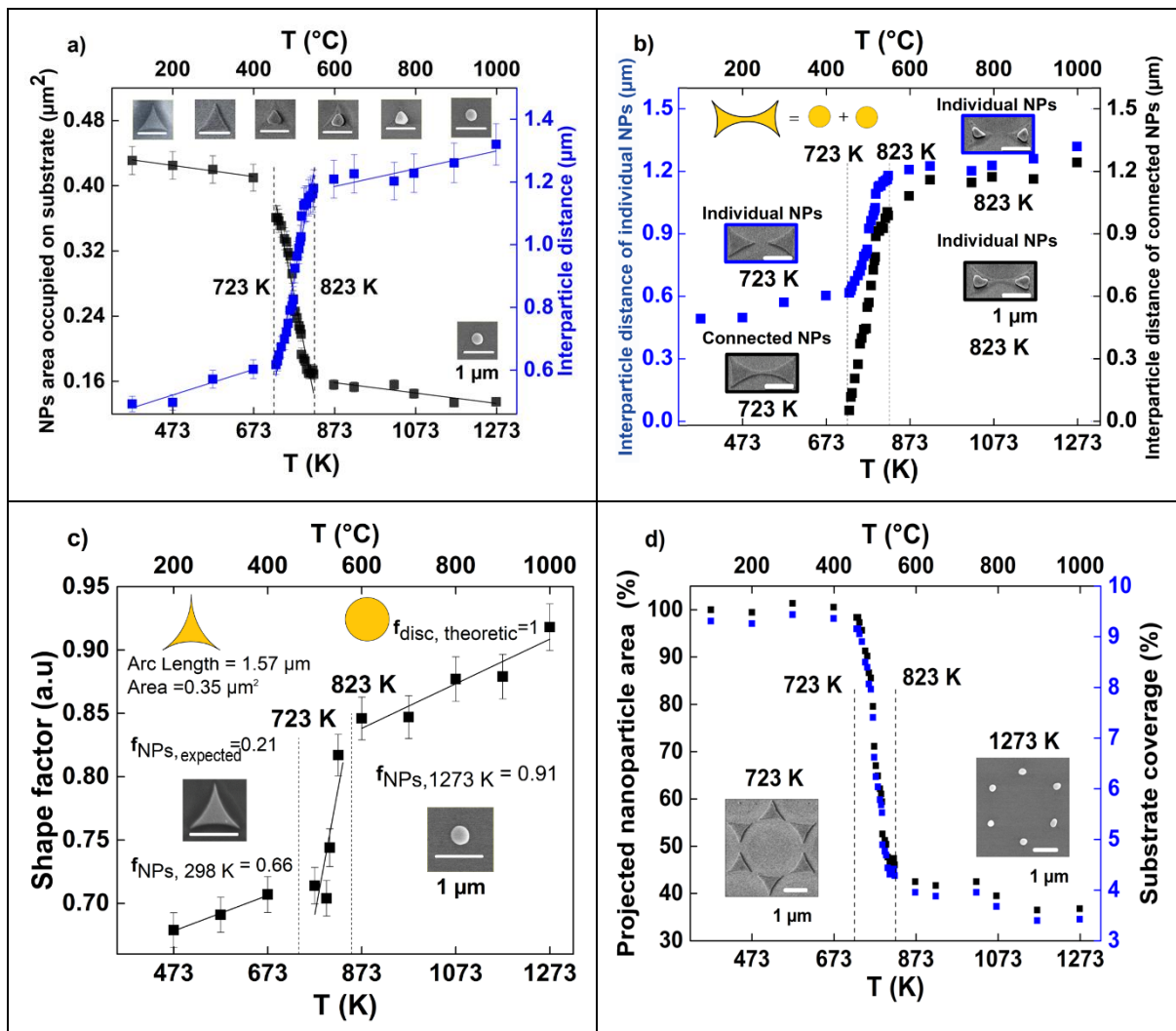


Figure III-8: a) Effects of thermal treatment on the Au nanoparticles projected area and inter-nanoparticles distance (tip-to-tip) d_{it} . (b) Evolution of inter-nanoparticles average distance between the tips of non-connected adjacent nanoparticles compared to the distance between the tips of two nanoparticles connected before the thermal treatment. (c) Shape factor of nanoparticles as a function of the thermal treatment temperature. (d) Percentage of nanoparticles projected area change and percentage of the substrate coverage as a function of temperature. The data from (a)-(d) are extracted from the step by step in-situ SEM observation using the ImageJ software. The nanoparticles projected area refers to the 2D area of the nanoparticles projected on the substrate, as seen in from the SEM images and should not be confused with the total 2D area (surface) of the nanoparticles.

The nanoparticles that undergo solid-state dewetting change their shape from “triangular” to “rounder” or “rounded.” The shape factor f (circularity) observed in Figure III-8 c) is determined by assessing the ratio: $f = 4\pi * \frac{A}{P^2}$, where: A is the projected area of nanoparticles and P is the perimeter. For the “triangular” nanoparticles, this formula holds since the nanoparticles are never perfect triangles; at 25°C (298 K), the nanoparticles have a shape factor of 0.66 that changes to 0.91 at 1000°C (1243 K). For perfect circular nanoparticles, the shape factor is equal to 1, and for our initial geometry, the expected shape factor is 0.21. Simultaneously, the solid-state dewetting process also changes the total area occupied by nanoparticles on the surface of the $\text{Al}_2\text{O}_3\text{-c}$ substrate (see Figure III-8 d). Initially, 9.3 % of the substrate was covered by Au nanoparticles, and at the end of the solid-state dewetting process, the coverage ratio drops to 3.5 % (from calculation based on Figure III-6). Solid-state dewetting controls

the shape of nanoparticles, and the shape strongly influence the electromagnetic behavior of nanoparticles. During the thermal treatment process, the shape factor, interparticle distance, and nanoparticle area evolution show three temperature-regimes. Despite the sharp corners and the low aspect ratio (50 nm thickness / $a = 900$ nm) of the Au nanoparticles (see Figure III-1 a) and Figure III-6 a), in this temperature range, the rapid evolution cannot be attributed to the partial melting due to Gibbs-Thomson effect (37).

III.2.2. Investigation of solid-state dewetting of Au nanoparticle arrays by HR-XRD

Solid-state dewetting is also controlled by crystallographic symmetries of nanoparticles and the substrate. Therefore, a direct influence of the acceleration of morphological changes by crystallographic changes may be present. For assessing this possibility, the crystallographic changes of nanoparticles as a function of temperature, the evolution of the rocking curve (RC) is monitored by in-situ HR-XRD from 25 °C (298 K) up to 1000 °C (1273 K) and back to 298 K (R_T), yielding the results presented in Figure III-9.

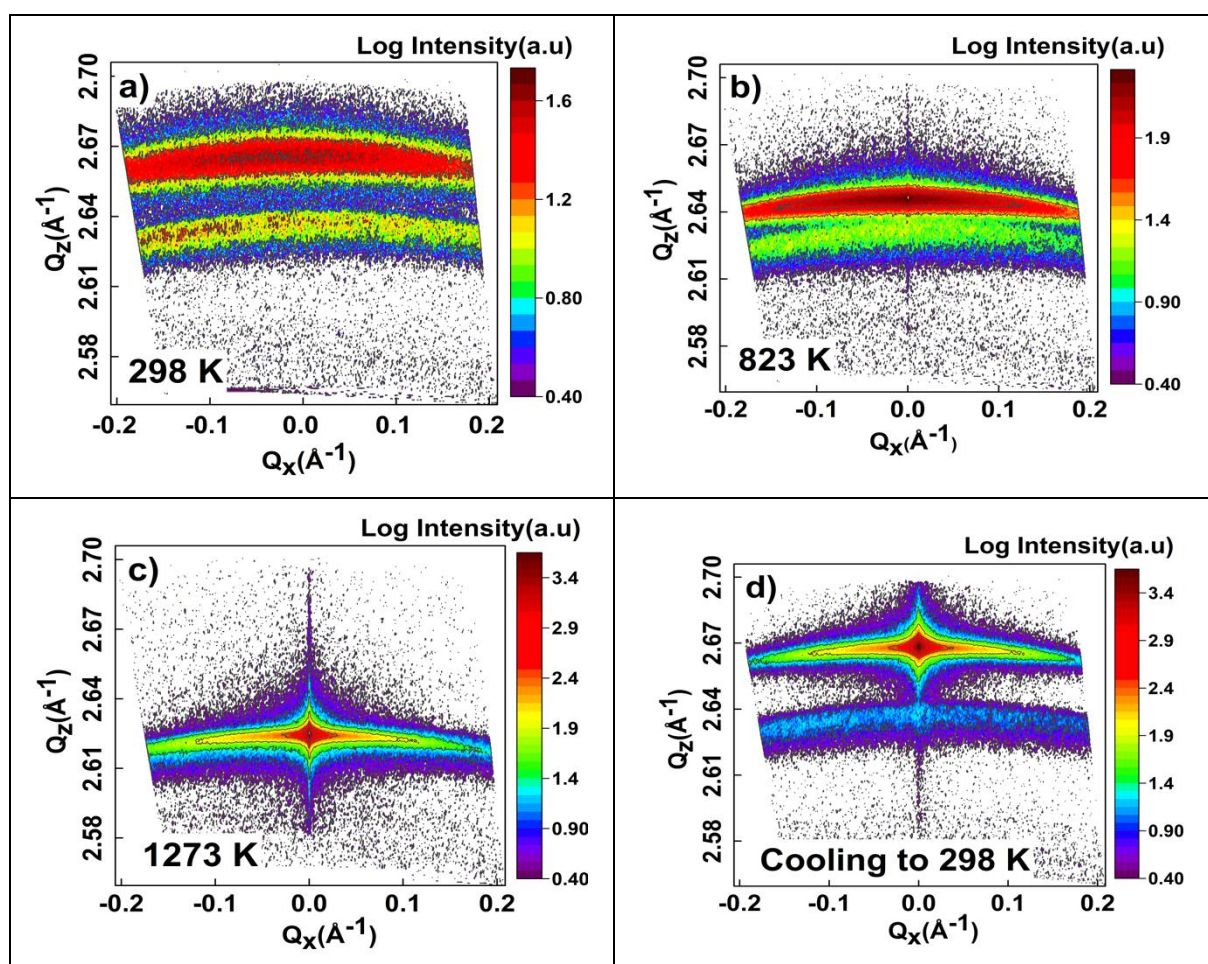
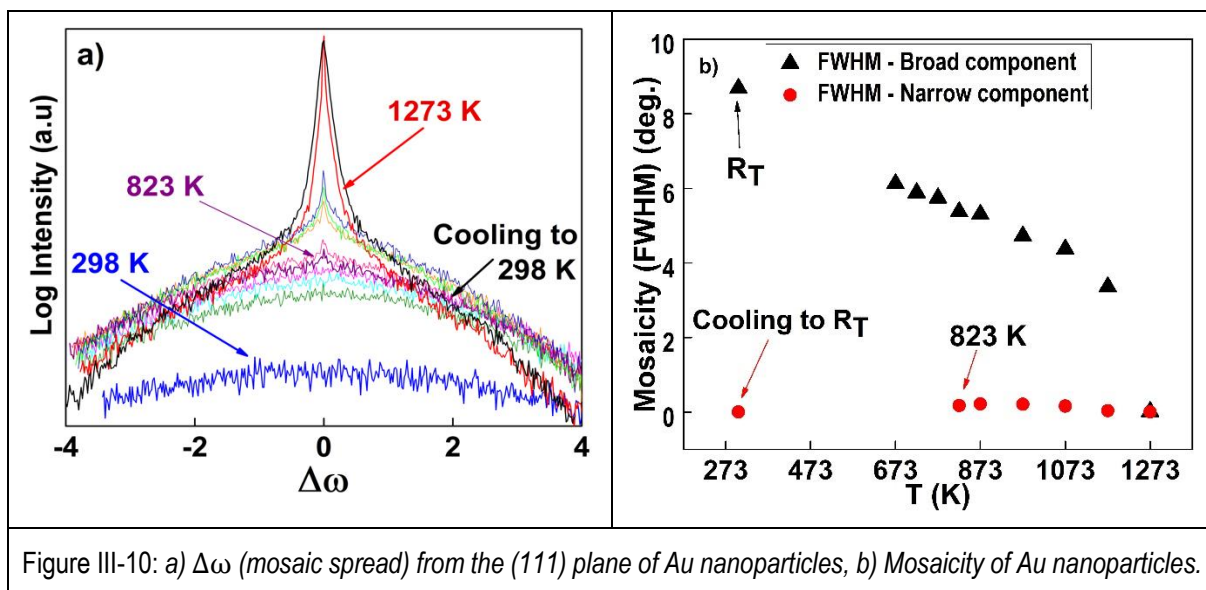


Figure III-9: a-d: In-situ HR-XRD scan; Reciprocal space mapping of the (111) Au QTPs reflection as a function of the terminal treatment temperature, from (a) room temperature up to (c) 1000 °C (1273 K) and back to room temperature (d). The maps are plotted as a function of the diffraction space coordinates Q_z and Q_x .

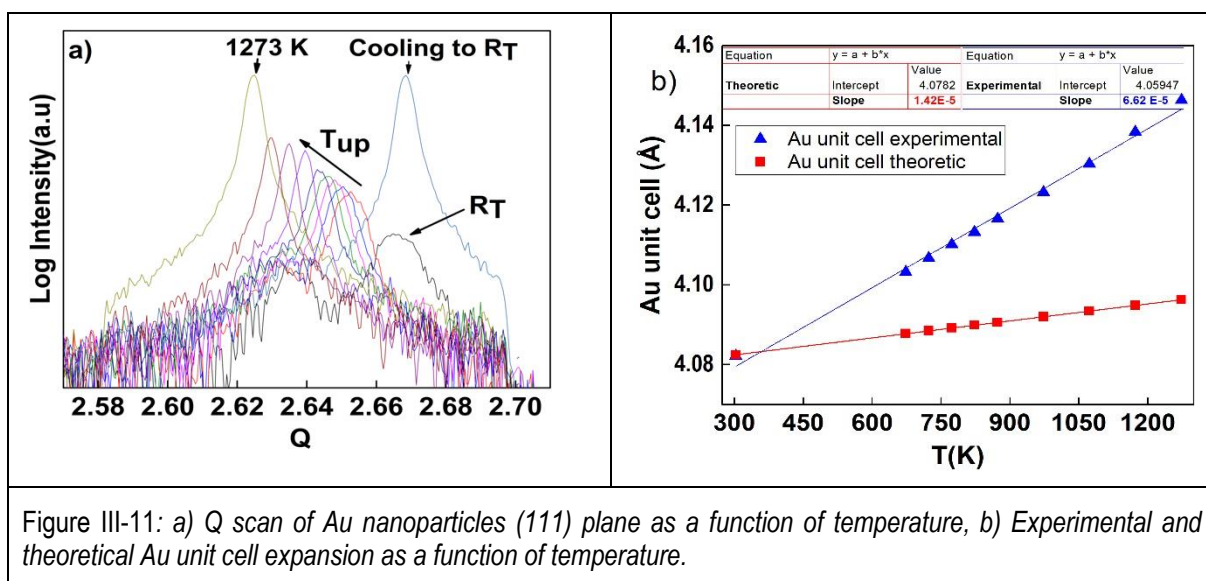
Figure III-9 a-d, presents the 2D section of the position in the reciprocal space of the vector that is normal to the (111) plane of Au. Figure III-9 a) corresponds to a Q_z value of 2.66, while the maximum centered around 2.63 comes from the tantalum holder used to secure/fix the sample during the experiment/measurement. At 25 °C

(298 K), in the reciprocal space map of (111), the vector has a high dispersion compared to that of a perfect crystal (underlying substrate). This suggests that the (111) planes of Au nanoparticles are not parallel to the substrate's surface. The planes are distorted or rotated (with respect to the substrate's surface) and have a very weak orientation; thus, the normal to the vector is almost entirely randomly distributed in space. A small, preferred orientation or preferred growth gives rise to an excess of intensity in the middle of the 2D section (ring). In an ideal grain-to-grain epitaxy situation with the substrate, the vector normal to the (111) plane should be perfectly orientated. This is not our case; hence, no structural relation between the Au nanoparticles and substrate can exist for Au's deposition at 25 °C (298 K). Thus, the small (111) texture seen in Figure III-9 a) must originate from the growth mechanism of the Au itself, not from the influence of the substrate. During heating, the position of the vector parallel to the (111) plane starts to move from a higher Q_z (2.66) value to a lower one Q_z (2.62). After the cooling process, the vector returns to almost the original position (see Figure III-9 d). This movement originates from the dilatation of the unit cell of Au. As the temperature goes up, the grains with the lowest interfacial energy will start to grow and consume the ones with higher interfacial energy. This grain growth process is reflected in the reciprocal space maps in two ways. First, the "ring" associated with the vector normal to the (111) plane starts to contract (decrease in spatial distribution) as the temperature increases. Secondly, by developing a high intensity peak (Figure III-9 b), highlighted by the presence of a narrow streak/line. This is a crucial point since it shows the development of facets, planes that are developing parallel to the surface starts at 550 °C (823 K). As the temperature reaches 1000 °C (1273 K), the streak/line intensity increases, and so does the number of facets (Figure III-9 c). This high intensity of the central line is also maintained after the cooling to 25 °C (298 K) process.

This evolution of high intensity central line is also observed in the variation of $\Delta\omega$ (mosaic spread) as a function of temperature, Figure III-10 a. At low temperatures the rocking curve (RC) is broad, with an FWHM of 8.68 degrees at 298 K (Figure III-10 b). At 823 K, a narrow peak appears at the $\Delta\omega = 0$ position (i.e. the corresponding plane being parallel to the substrate), with an FWHM of 0.17 degrees, while the FWHM of the broad peak decreases to 8.68 degrees. The FWHM is extracted from Figure III-10 a data using a Pearson VII function of the Fityk program (for both the narrow and broad peaks). The width of broad component decreases with temperature, and the width of the narrow component remains constant (Figure III-10 b), even after cooling down to R_T whereas its intensity relative to the broad component increases significantly. This indicates that the volume fraction of oriented Au nanoparticles increases at the expenses of the misoriented ones.



Vertical sections performed through the center of the maps (Figure III-9) allow to assess the lattice parameter of the lattice plane parallel to the surface. Because of thermal expansion, the position is shifted towards lower angles (Figure III-11 a) with magnitude proportional to the Au thermal expansion coefficient. Gold has a cubic close-packed structure (Table I-5) and $d_{hkl} = a/\sqrt{(h^2 + k^2 + l^2)}$, therefore the Bragg's Law ($\lambda = 2d\sin\theta$) can be expressed as $\lambda = 2(a/\sqrt{(h^2 + k^2 + l^2)})\sin\theta$. Since Au nanoparticles are 111 textured, the unit cell (a) can be further expressed as $a = \lambda\sqrt{3}/(2\sin\theta)$. Using the definition of Q, $Q = 4\pi\sin\theta/\lambda$, the lattice parameter is obtained from the peak position in (Figure III-11 a) using $a = 2\pi\sqrt{3}/Q$. The evolution of the lattice parameter is displayed in (Figure III-11 b), together with the theoretical evolution.



The measured (experimental) values of the Au nanoparticles crystalline lattice parameters are different than the theoretical lattice parameters of the bulk Au (Figure III-11 b). This is a consequence of the different thermal expansion coefficient of Au nanoparticles compare to that of bulk Au ($6.64 \times 10^{-5} \text{ K}^{-1}$ for Au nanoparticles vs $1.42 \times 10^{-5} \text{ K}^{-1}$ for bulk Au) [150]. Besides the lattice parameter, two additional observations can be made. Firstly, the width of the peak decreases, indicating grain growth in the direction normal to the surface. Secondly, as previously observed, the intensity of the peak increases as a result of the growth of the oriented Au nanoparticles. The Au 111 peak position's shift occurs with no drop in the peak intensity, a drop that can indicate that the Au nanoparticles are melting. This implies that Au nanoparticles evolve through solid-state dewetting mechanisms, not by the melting and recrystallization process. There is a difference between the slopes of unit cell thermal expansion of Au nanoparticles on a substrate and the bulk material. This difference in slopes comes from strain/stress development at the Au-sapphire interface. Since the Au nanoparticle shape evolves towards Winterbottom shape, a portion of the nanoparticle interface is constrained to replace the image of the changed interface.

III.2.3. Optical detection of LSPR in the visible part of the electromagnetic spectrum and the correlation to the thermal treatment of Gold nanoparticles arrays.

The Au nanoparticles and Ir, made using different sizes (diameters) of the polystyrene microsphere (with a 2, 3, 5 μm) diameter have no plasmonic resonances in the visible part of the electromagnetic spectrum (350 - 780 nm). By thermal treatment, the situation changes, and an LSPR peak appears in the visible part of the electromagnetic spectrum (see Figure III-12 a). After a critical thermal treatment temperature at 532 $^{\circ}\text{C}$ (805 K) a LSPR appears in the visible range.

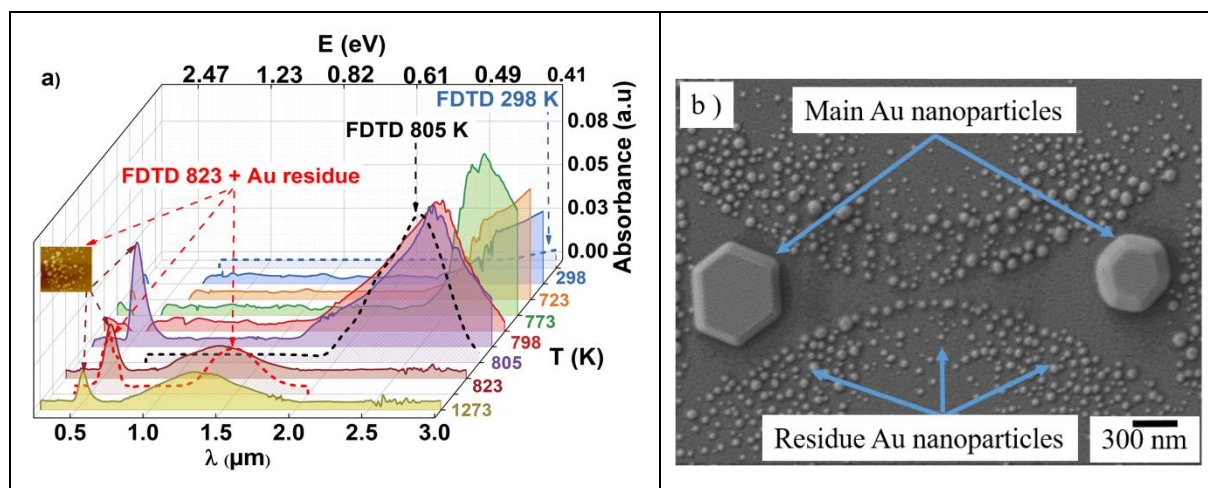


Figure III-12: LSPR resonances in the visible part of the electromagnetic spectrum. a) Absorbance spectra of thermally treated Au nanoparticle arrays (before thermal treatment “a” = 0.9 μm) measured by UV-VIS spectroscopy and corroborated with the FDTD based simulation (the dotted lines). b) SEM image of Au nanoparticle array thermally treated at 1273 K and used to identify the LSPR visible resonances' origin. Note that the Au residue nanoparticles (in figure b) have an enlarged diameter due to the deposition of an additional 20 nm platinum layer that prevents electron charging effects during SEM observation.

The origin of the LSPR visible resonance is linked to the Au residue left after the polystyrene microsphere removal. In fact, thermal treatment, the Au residue coalesce together, resulting in spherical Au small nanoparticles

with an average diameter close to 15 nm. Introducing in the FDTD simulations (also by Mie theory (discussed more in Chapter IV) the Au nanoparticles with a diameter of 15 nm), showed an additional resonance peak at $\lambda \approx 0.56 \mu\text{m}$, Figure III-12 a. Since these Au residue nanoparticles are spherical and have a diameter close to 15 nm, their plasmonic resonance peak can also be explained in the theoretical framework presented in *Chapter I*. All the samples treated at a temperature lower than 805 K do not show any LSPR peak in the visible. As is presented in Figure III-12 b, there is a clear physical separation between the Au residue nanoparticles and the main Au nanoparticles. This is a consequence of the size dependence effect of thermal treatment on Au nanoparticles. The Au residue nanoparticle probably melts at a lower temperature, while the main Au nanoparticle follows solid-state dewetting mechanisms with increasing temperature. The formation of Au residue nanoparticles does not influence the investigation of the Au nanoparticle array's evolution with increasing the thermal treatment temperature. In the *in-situ HR-XRD*, the FWHM is inverse proportional to the size of nanoparticles. The smaller the nanoparticle is, the larger is the FWHM. This implies that the Au residue nanoparticles do not have any noticeable contribution to the result of the *in-situ HR-XRD* measurements. Besides the LSPR peak in the visible range, the Au residual nanoparticles may be used as sensors to probe the existence of the Ostwald ripening phenomenon. If present, Ostwald ripening should induce a transfer of Au atoms to form the residue nanoparticles to the main Au nanoparticles [145]. As long as the residue nanoparticles are present on the thermally treated samples is reasonable to assume that Au nanoparticles change their shape with volume conservation. This is additional proof of the LSPR wavelength modulation, made based on nanoparticle shape evolution without a volume evolution. If desired, a method for the total removal of the residual Au nanoparticles is by increasing the time of the thermal treatment [134].

III.2.4. Influence of polystyrene microsphere diameter and nature of the metal on LSPR properties

The thermal treatment procedure applied in Au nanoparticle arrays made with 3 μm polystyrene microspheres was implemented for Au nanoparticle arrays made with 2 μm polystyrene microspheres (Figure III-13). Since in both cases the polystyrene microspheres are arranged in 2D hexagonal closed packed structures, the resulting Au nanoparticles exhibit a so-called "fractal effect"; i.e., the structure can be downsized/upsized while maintaining the same geometry of the nanoparticles (see *Chapter II*). As presented in Figure III-2, the "a" parameter of the Au nanoparticles made with 2 μm polystyrene microsphere is equal to 0.48 μm , which is not so far from the characteristic size "a" of Au nanoparticles made with 3 μm polystyrene microspheres.

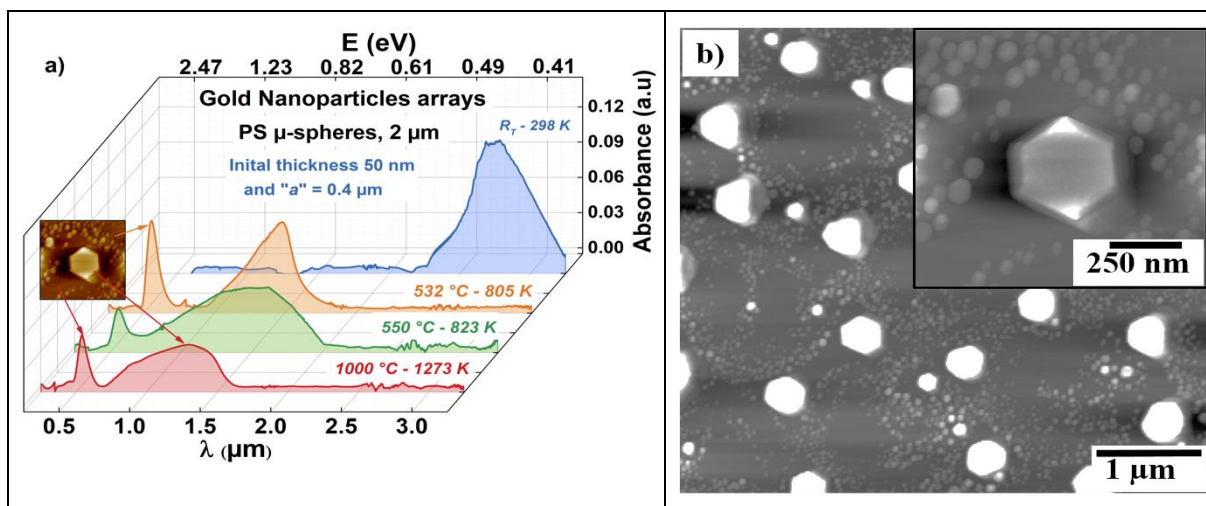


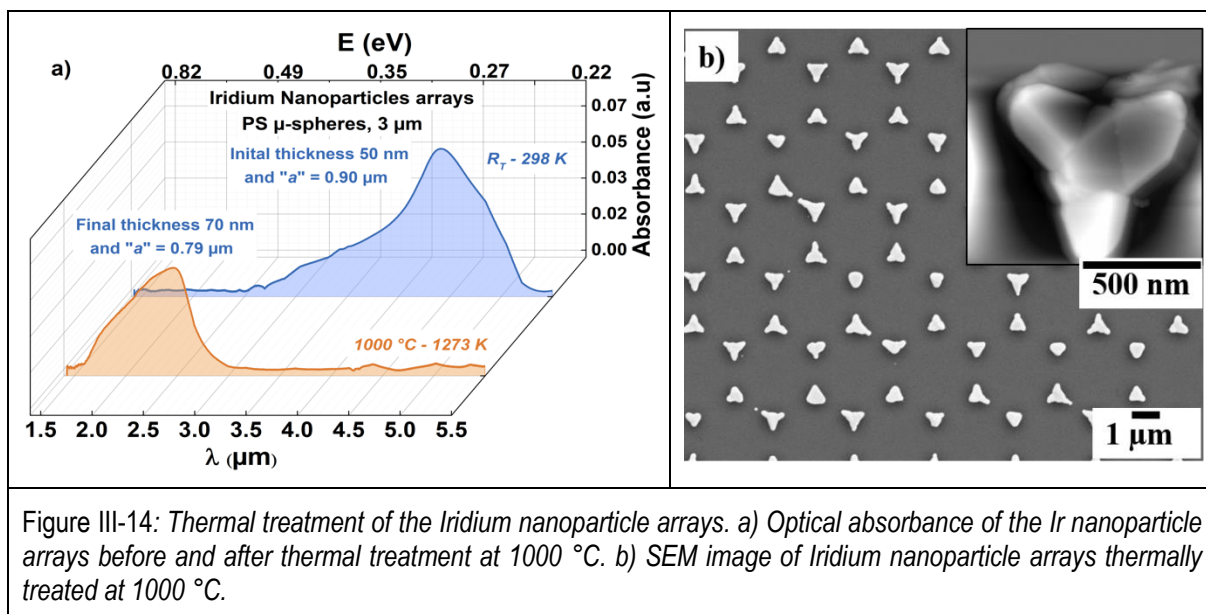
Figure III-13: Effect of the thermal treatment on Au nanoparticle arrays deposited on an $\text{Al}_2\text{O}_3\text{-c}$ substrate and made with 2 μm polystyrene microspheres. a) Absorbance spectrum pointing out the wavelength blue shift. b) Au nanoparticle array made with 2 μm polystyrene microspheres and thermally treated at 1000 °C (1273 K).

Before the treatment, the Au nanoparticle arrays have an LSPR maximum at a wavelength $\lambda \approx 2.85 \mu\text{m}$. When the Au nanoparticles made with 2 μm polystyrene microsphere are subjected to a thermal treatment, the LSPR peak position blueshifts to a lower wavelength. For the Au nanoparticles array thermally treated at 1000 °C, the LSPR peak position is blueshifted to $\lambda \approx 1.30 \mu\text{m}$.

After a thermal treatment at 1000 °C (1273 K), the resulting Au nanoparticles made with 2 μm polystyrene microsphere, Figure III-13 b, have a hexagonal shape. Au nanoparticles' diameter in Figure III-13 b) is close to 0.33 μm , while the average distance between neighboring nanoparticles is 0.56 μm . At 532 °C (805 K) the Au nanoparticle array shows the same resonance in the visible range ($\lambda \approx 0.56 \mu\text{m}$). As previously discussed, the origin of the LSPR peak in the visible range is represented by the formation of Au residue nanoparticles around the main Au nanoparticles (see Figure III-13 b).

The same thermal treatment process has also been implemented for Ir nanoparticles made with 3 μm polystyrene microspheres. Iridium is a noble metal with a high melting point; 2466 °C (2739 K) (see Section I.4.2 and Table I-4).

Iridium has a cubic close-packed crystal structure similar to Au, and the Ir nanoparticles are deposited on the same $\text{Al}_2\text{O}_3\text{-c}$ substrate. Hence, we expect a similar influence of thermal treatment temperature on the Ir nanoparticle's geometrical characteristics. However, due to the high melting point, when Ir nanoparticles are thermally treated at 1000 °C, they retain their initial shape (see Figure III-14 b). The "a" parameter decreases from 0.90 μm to 0.79 μm , and the average distance between two adjacent nanoparticles increases from 0.42 μm to 0.69 μm after the thermal treatment.



As shown in Figure III-14 a, these geometrical modifications of the Ir nanoparticles directly impact the LSPR peak position. Before the thermal treatment, the Ir nanoparticle arrays have an LSPR maximum at $\lambda \approx 4.39 \mu\text{m}$ and after the thermal treatment at 1000 °C, the LSPR peak is blue shifted at $\lambda \approx 2.38 \mu\text{m}$. It is reasonable to think that if the temperature of the thermal treatment is increased by more than 1000 °C, eventually, the Ir nanoparticles will take the shape of the Winterbottom construction. However, assessing this possibility is beyond the scope of the current work. Further than that, making a thermal treatment at a higher temperature than 1000 °C will have to include assessing the substrate's surface morphological stability.

As a proof of concept, Figure III-14 shows that it is possible to shift the LSPR peak position of the Ir nanoparticle arrays, and even at 1000°C, the shape of Ir nanoparticles does not change much. Also, for the Ir nanoparticles arrays, the thermal treatment did not produce any residual Ir small nanoparticles. The absence of Ir residual nanoparticles may be due to the low temperature of the thermal treatment compared to the melting point of bulk Ir. After the thermal treatment the Ir nanoparticle array don't have LSPR in the visible part of the electromagnetic spectrum.

III.2.5. Conclusions

In *Chapter III*, we have probed the modulation of LSPR peak position by a variety of means. The influence of nanoparticle size (obtained from 3 or 2 μm LB - polystyrene microspheres), thickness (range 50-200 nm), and metal composition (Au and Ir) on the LSPR peak position is investigated. Thermal treatments promoting a metallic solid-state dewetting process demonstrated the continuous modulation of the LSPR peak position of Au nanoparticle arrays, from MidIR ($\sim 4.5 \mu\text{m}$) to NIR ($\sim 1.5 \mu\text{m}$), particularly in the critical temperature range (727K to 832 K), which favors the highest geometric variation of Au nanoparticles. After this critical temperature range, the Au nanoparticles arrays' LSPR peak position cannot be further modulated.

Interestingly, during thermal treatments, when the LSPR peak position reaches $\sim 1.5 \mu\text{m}$ stabilization temperature the Au nanoparticles undergo a massive crystallographic reorganization. The Au nanoparticles evolve from systems with a weak crystallographic orientation to perfect crystals through thermal treatment.

Furthermore, in addition to the LSPR in IR range, the optical response in the visible range of the gold nanoparticles arrays (submitted to higher thermal treatment ($> 800 \text{ K}$) was attributed to smaller nanoparticles (about 10 nm).

Chapter IV

Nanocomposites:

Matrix influence on the LSPR properties

Chapter IV. Nanocomposites: Matrix influence on the LSPR properties.

This Chapter first investigates a theoretical approach based on Finite-difference time-domain (FDTD) method to identify the nature of the optical absorption peaks of the metallic nanoparticle arrays. The theoretical calculations on arrays of Au nanoparticles subjected to the solid-state dewetting process show that the plasmonic properties of the nanoparticles evolve throughout the dewetting process. This first approach aims to investigate further the influence of the dielectric environment on the plasmonic properties of the metallic (Au and Ir) nanoparticles. So, the first nanocomposites are made by depositing a layer of Alumina on Au nanoparticle arrays. Because the deposition of Alumina is carried out at room temperature by PLD, the initial shape of the Au nanoparticles is kept and the optical response of the nanocomposite points out a red shift in the nanoparticles LSPR, which can be defined using different thicknesses of the Alumina layer.

Further, the second step is to modulate live the LSPR by using a 'smart' matrix such as vanadium dioxide, which possesses temperature-dependent properties due to its SMT (semi-conductor to metal transition at 68°C). The active modulation of the dielectric environment in nanocomposites corresponding to embedded metallic (Au and Ir) nanoparticles arrays into VO₂ matrix can be seen as a transfer of properties from VO₂ to the nanoparticles. The plasmonic properties are investigated experimentally and theoretically to understand the behavior of the nanocomposite versus the temperature of the system (VO₂). The metallic nanoparticles arrays-VO₂ system acts as a temperature adaptive array. During the SMT of the VO₂, the LSPR wavelength redshifts. This property is particularly studied by a rigorous FDTD simulation of the optical response of the nanocomposite leading to propose the formation of a core-shell structure. The core-shell structure is made from a core (metallic nanoparticles (Au or Ir)) surrounded by a shell of metallic VO₂ and embedded in dielectric VO₂.

IV.1.1. Optical response of Gold nanoparticles arrays – Experimental and FDTD studies of the LSPR linked to the solid-state dewetting process.

The optical properties of Au nanoparticles arrays were investigated and compared with the simulated results based on the finite difference time domain (FDTD) approach, the method described in *Chapter I*. The FDTD calculation are made using Lumerical software. The nanoparticle arrays are modeled on an Al₂O₃-c substrate by using the real AFM images obtained from the structures. The surrounding medium considered in the modeling is air and has a permittivity equal to 1. The simulated region presents periodic conditions in the x and y directions, and the array of nanoparticles is considered infinite. The boundary conditions imposed along the Z direction are perfectly matched layer (PML) that will absorb all the waves moving towards the exterior of the simulation zone without reintroducing reflection. Here, the light source is a plane wave that is circularly polarized. After the convergence test, the space mesh size depends on the nanoparticles' size and has a maximum size of 1 nm at the Au-Al₂O₃ interface. The convergence criterion is reached when the energy in the simulation zone's volume drops down to 10⁻⁵ multiplied by the injected energy. Absorbance is specifically calculated and compared directly with the experimental measurements (see Figure IV-1 a-b). The values of optical indices for Au were fitted on a spectral range extending from 600 nm up to 5.5 μm, extracted from reference [151]. Simultaneously, the FDTD theoretical

calculations are performed on an area $\sim 25 \mu\text{m}^2$, an area that includes 6 individual nanoparticles (see Figure IV-2 a-c). The simulated FDTD absorbance spectra correspond to the dotted lines in Figure IV-1 a-b and are made for the Au nanoparticle arrays before thermal treatment (FDTD 25 °C (298 K)), on the arrays treated at 532 °C (805 K) (FDTD 805 K) and 550 °C (823 K) (FDTD 823 K).

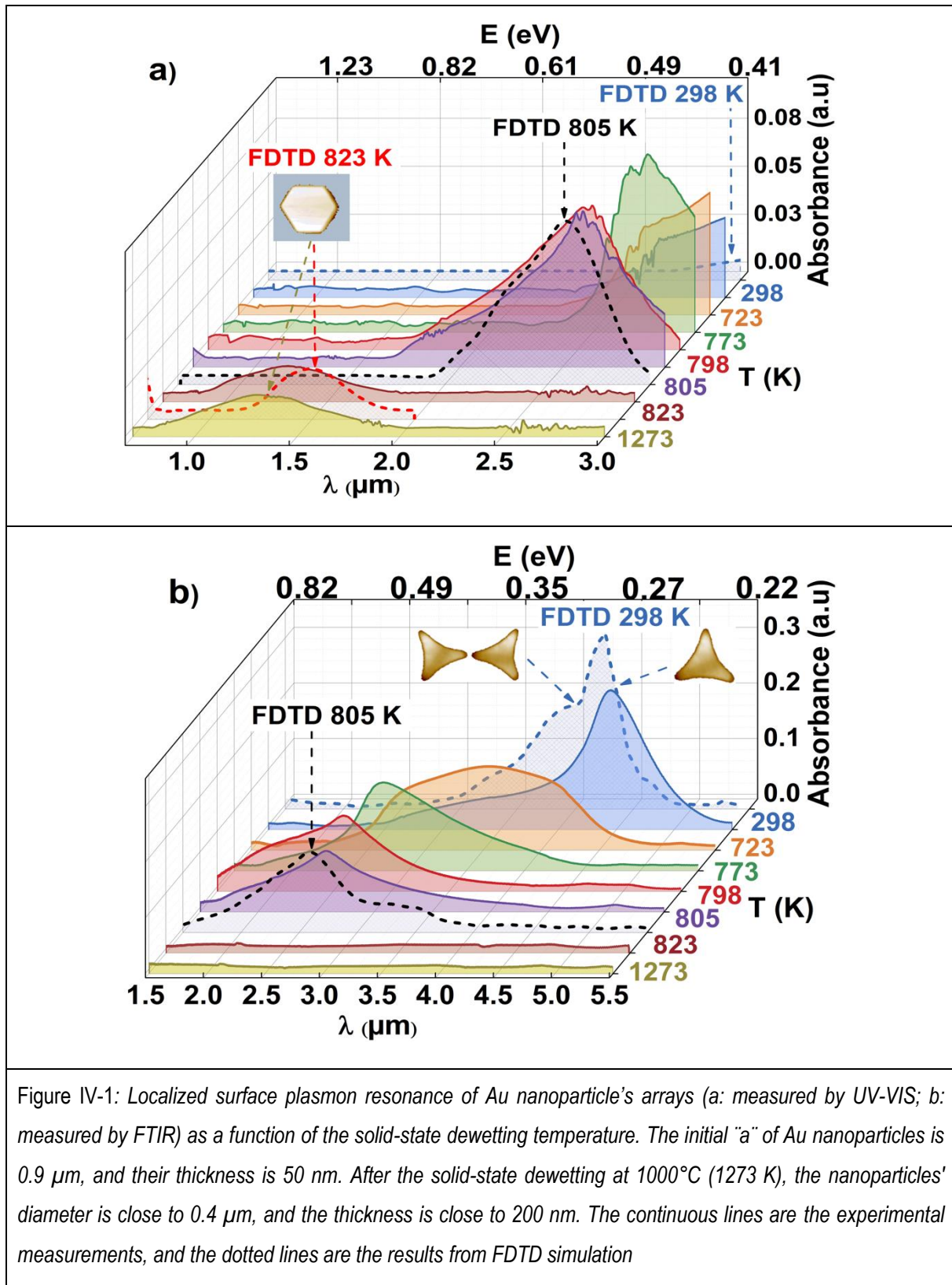


Figure IV-1: Localized surface plasmon resonance of Au nanoparticle's arrays (a: measured by UV-VIS; b: measured by FTIR) as a function of the solid-state dewetting temperature. The initial "a" of Au nanoparticles is $0.9 \mu\text{m}$, and their thickness is 50 nm . After the solid-state dewetting at 1000°C (1273 K), the nanoparticles' diameter is close to $0.4 \mu\text{m}$, and the thickness is close to 200 nm . The continuous lines are the experimental measurements, and the dotted lines are the results from FDTD simulation

Before any thermal treatment (at 298 K), the Au nanoparticle arrays show resonance in the absorbance spectrum with a maximum located at $\lambda \approx 4.45 \mu\text{m}$ (see Figure IV-1 b). The map of the polarized electric field enhancements in the logarithmic scale (Figure IV-2 a) shows that the enhancements are located on nanoparticle corners and correspond to the dipolar localized surface plasmon resonances (LSPR) of the Au nanoparticle arrays. At 25° C (298 K), the FDTD simulation reveals that the smaller gap between nanoparticles leads to plasmonic coupling effects highlighted by the intensity of the electric field distribution between the adjacent nanoparticles accompanying the dipolar resonance (Figure IV-2 a). Coupling effects appear in the calculated optical absorbance spectrum of the sample at 25° C (298 K) as a shoulder located close to the main resonance maximum (Figure IV-1 b); the blue dotted line's shoulder is named FDTD 298K).

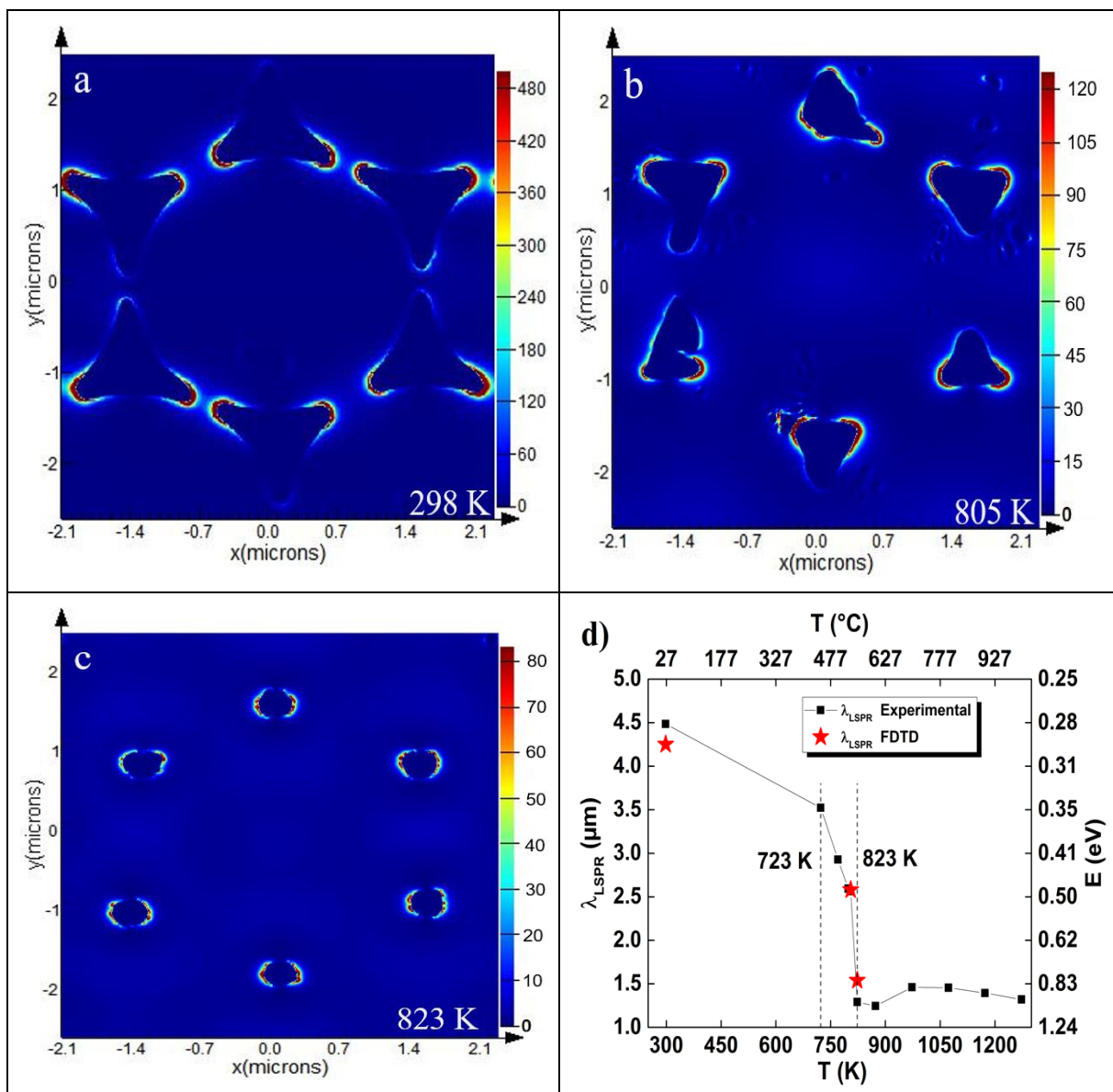


Figure IV-2: a-c: Electric field cartography, obtained by FDTD, of LSPR of Au nanoparticles arrays as a function of thermal treatment temperature a) at $\lambda = 4.45 \mu\text{m}$ for RT sample b) $\lambda = 2.58 \mu\text{m}$ for sample treated at 805 K and c) $\lambda = 1.54 \mu\text{m}$ for sample treated at 823 K d) Evolution of the LSPR position - Comparison between experimental and theoretical (FDTD) values. The FDTD calculation at 1273 K ($\lambda_{\text{LSPR}} = 1.59$) are written in the Table IV 1.

As the solid-state dewetting temperature increases, the resonance starts to blue-shift (Figure IV-1 a-b), and the resonance's dipolar characteristics are preserved up to 550 °C (823 K) (Figure IV-2 a-c).

After 550° C (823 K), the Au nanoparticle arrays show resonance in the absorbance spectrum with a peak maximum located at $\lambda \approx 1.29 \mu\text{m}$, a peak position that remains unchanged by further thermal treatments up to 1000 °C (1273 K) (Figure IV-1 a).

The solid-state dewetting process also changes the shape of the resonance peak (Figure IV-1 a-b). At the beginning of the thermal treatment, the shape of the resonance peak is influenced by the size and shape polydispersity of the nanoparticles and coupling effects between nanoparticles. Then, as the distance between nanoparticles grows, the coupling effect stop (Figure IV-2 b), and only the small size and shape polydispersity influence the shape of the peak.

The modeled absorbance spectra are in good agreement with the experimental measurements (Figure IV-2 d). The LSPR peaks' values as a function of the thermal treatment temperature and the correlation with the values obtained by FDTD are presented in Table IV-1.

Table IV-1: Comparison between experimental LSPR peak position shift induced by thermal treatment and the position deduced by FDTD simulation (gold arrays).

Temperature of thermal treatment (K)	Average nanoparticles projected area (μm^2)	Average distance between two nanoparticle (μm)	λ_{LSPR} (μm) Experimental	λ_{LSPR} (μm) FDTD
298	0.45	0.50	4.45	Main peak: 4.25
				Shoulder: 3.70
723	0.39	0.61	3.52	-
773	0.24	0.82	2.92	2.80
798	0.22	1.11	2.59	-
805	0.21	1.12	2.56	2.58
823	0.14	1.18	1.29	1.54
1273	0.13	1.24	1.31	1.59 (see Figure IV-2)

The resonance peak positions presented in Table IV-1 are extracted from the absorbance spectra presented in Figure IV-1, using a single Voigt function for fitting each experimental absorbance spectra. The Voigt function is one of the built-in functions of the Fityk 1.3.1 software program.

As seen in Table IV-1 and Figure IV-2 d, there is good agreement between the (FDTD) calculations and the experimental data (UV-VIS and FTIR). The experimental absorbance spectra are collected on an area of ~ 7.06

mm² (for both UV-VIS and FTIR), and it represents a global contribution coming from all the nanoparticles and is influenced by nanoparticle size (**a**) polydispersity.

IV.2. Nanocomposites - Influence of dielectric environment on the optical response of the metallic nanoparticle arrays

IV.2.1. Gold nanoparticles arrays in an Alumina matrix

As discussed in *Chapter I*, the position of LSPR maximum is directly linked to the dielectric environment that surrounds the metallic nanoparticle arrays. Initially, a part of the metallic nanoparticles is in contact with the Al₂O₃-c, and all of their other sides are surrounded by ambient air.

In the case of a dielectric material environment on the nanoparticle arrays, Equation (1.33) predicts a redshift of the plasmonic resonance peak position. Moreover Equation (1.34) states that the value of the resonance position shift is also proportional to the thickness of the dielectric layer. To test this, we studied the role of Alumina's layer on top of the Au nanoparticles arrays (made with 2 and 3 μm polystyrene microspheres). The permittivity of ambient air is considered to be equal to 1, while Alumina (Al₂O₃) is regarded as a material with a high dielectric constant/function [152], [153].

Alumina's deposition was made by PLD in the conditions presented in Table II-1. The alumina deposition, which is made at room temperature, can be considered as inducing any modification of the plasmonic structure geometry. So, the resonance peak position is only related to the change of dielectric environment and not, of course, to the Au nanoparticle geometrical modifications.

The evolution of the optical LSPR response of gold nanoparticles arrays covered with different thicknesses of Alumina is reported in Figure IV-3.

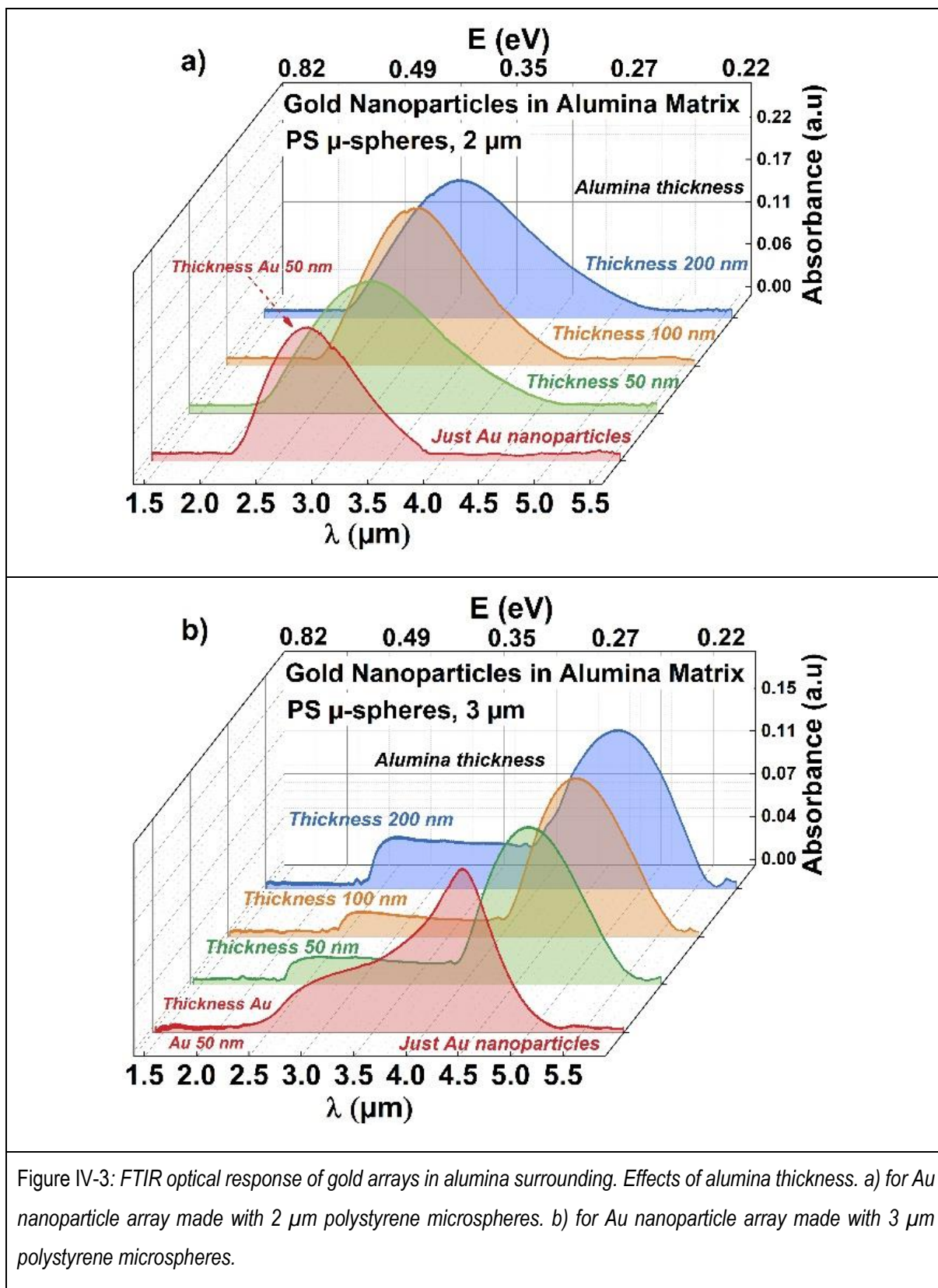


Figure IV-3: FTIR optical response of gold arrays in alumina surrounding. Effects of alumina thickness. a) for Au nanoparticle array made with 2 μm polystyrene microspheres. b) for Au nanoparticle array made with 3 μm polystyrene microspheres.

The addition of 50 nm of Alumina redshifts the wavelength peak position of the Au nanoparticle arrays (2 μm polystyrene microspheres) from $\lambda \approx 2.8 \mu\text{m}$ to $\lambda \approx 2.98 \mu\text{m}$. While for the Au nanoparticles made with 3

μm polystyrene microsphere, the LSPR shift is from $\lambda \approx 4.45 \mu\text{m}$ to $\lambda \approx 4.88 \mu\text{m}$ for the same 50 nm of the Alumina matrix. A further increase in Alumina matrix's thickness will shift the Au nanoparticle arrays' LSPR peak position to higher wavelengths (see Figure IV-3). The LSPR redshift to higher wavelengths does not increase linearly with the increase of Alumina thickness. A reason for this may be the dependence of the Alumina dielectric properties on the wavelength of the incident the light [152].

IV.2.2. Influence of a Vanadium dioxide matrix on the LSPR peak position of metallic nanoparticles arrays

Compared to Alumina, VO_2 can be used as a matrix with multi states. In one state, at room temperature, VO_2 acts as a static matrix that shifts the LSPR nanoparticle array peak to higher wavelengths, a shift based on the permittivity change of the nanoparticle surrounding environment (like in the case of the Alumina matrix). As presented in *Chapter I*, the dielectric properties of VO_2 are dependent on temperature. Heating the VO_2 from room temperature to 68°C (341 K) will activate a semiconductor to metal transition (of VO_2) that changes its dielectric properties. The VO_2 can be considered as an active matrix that produces a tunability of the metallic nanoparticle arrays' LSPR peak position.

In this part, we propose to investigate both gold and iridium nanoparticles arrays - based nanocomposites (Figure IV-4).

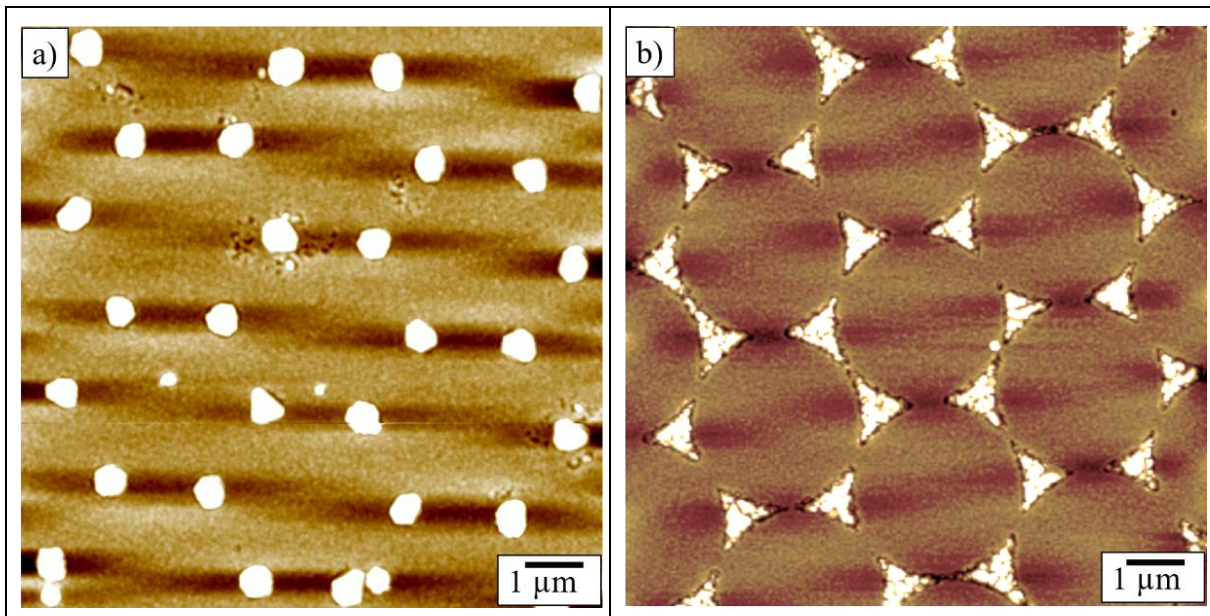
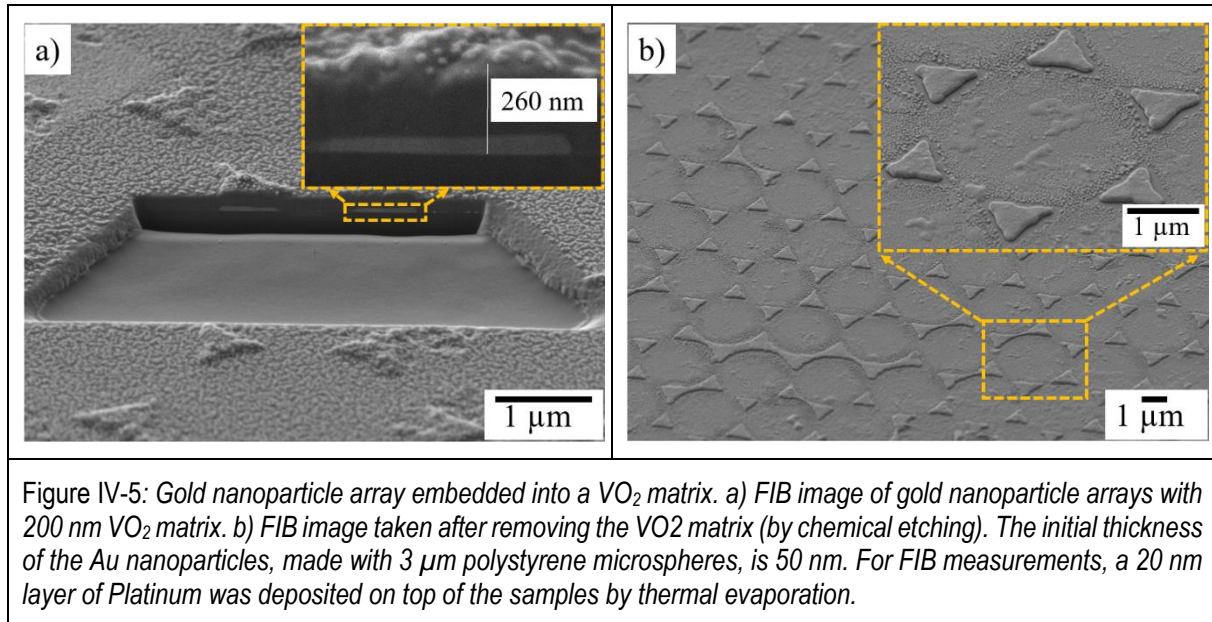


Figure IV-4: AFM image of metallic nanoparticle array embedded into a 200nm- VO_2 matrix. a) gold nanoparticle arrays. b) Iridium nanoparticle arrays. The initial thickness of the Au and Ir made with $3 \mu\text{m}$ polystyrene microspheres nanoparticles is 50 nm.

The VO_2 matrix is deposited by PLD on top of the metallic nanoparticle arrays in the deposition conditions detailed in Table II-1 (Section II.5). With the PLD system, to obtain VO_2 with good properties, the deposition has to be performed at a temperature close to 500°C (773 K). This elevated deposition temperature will inevitably induce a dewetting of the Au nanoparticle arrays. The dewetting of Au nanoparticle arrays during VO_2 is visible in Figure IV-4 a, where the Au nanoparticles have a more “rounded” shape compared to their shape before VO_2 (Figure III-1).

For the Ir nanoparticle arrays, the dewetting during VO₂ deposition, Figure IV-4 b, may be present but to a less extent than in the case of Au nanoparticle.

To ensure that VO₂ fully surrounds the metallic nanoparticles a part of the VO₂ layer is removed by FIB. The FIB investigations (Figure IV-5 a) reveal that, indeed, the VO₂ entirely surrounds the metallic nanoparticles and the features seen in Figure IV-4 are the projection of the nanoparticles underneath the VO₂ layer.



The VO₂ layer has a thickness close to 200 nm on top of the Au nanoparticle arrays, while the thickness of the Au nanoparticles slightly increases to 60 nm. This thickness increase is to be expected since the Au shape is slightly modified with a constant volume. Beyond FIB measurements, we have removed the VO₂ layer by using a liquid chemical etching process. The etching process is performed by submerging the samples in Chromium etchant for 20 seconds. Then the samples are rinsed in distilled water. After the etching process of VO₂, the shape of the Au nanoparticles is revealed.

When embedded into VO₂, the Au nanoparticles have a triangular shape but with rounded edges (Figure IV-5 b). During VO₂ deposition, the “a” parameter of the Au nanoparticles changes from 0.90 μm (before the VO₂ deposition) to “a” = 0.50 μm, and the inter nanoparticle distance increases from 0.42 μm to 0.56 μm. The evolution of the Au nanoparticles shape during VO₂ deposition is in perfect agreement with the results of thermal treatments performed on the Au nanoparticles alone. The optical absorbance measurements of the samples presented in Figure IV-6, Figure IV-7 and Figure IV-8, are made by FTIR. VO₂ alone has no absorbance peaks in the measured wavelength range (1.5 to 5.5 μm), but its absorbance depends on thickness Figure IV-8 b. So, the absorbance thickness dependence of VO₂ was subtracted from all of the experimental data presented in this figure using Figure IV-8 b as a reference. The baseline was subtracted using OriginPro 2015 software (build-in function *Subtract Baseline*). This function allowed us to extract the absorbance spectra of different metallic nanoparticle arrays and compare them on the same scale of absorbance.

FTIR measurements have revealed for all the samples that after VO₂ removal, the Au nanoparticle arrays have a plasmonic resonance peak located at $\lambda \approx 2.8 \mu\text{m}$ (see Figure IV-6). This new position of the LSPR peak is wavelength blue shifted compared to the initial resonance peak position ($\lambda \approx 4.45 \mu\text{m}$) for the Au nanoparticle arrays. This blue shift of the plasmonic resonance of $1.65 \mu\text{m}$ fits perfectly with the value of the resonance peak shift measured on the thermally treated Au nanoparticles at the same temperature as the one of VO₂ deposition at 500 °C (773 K).

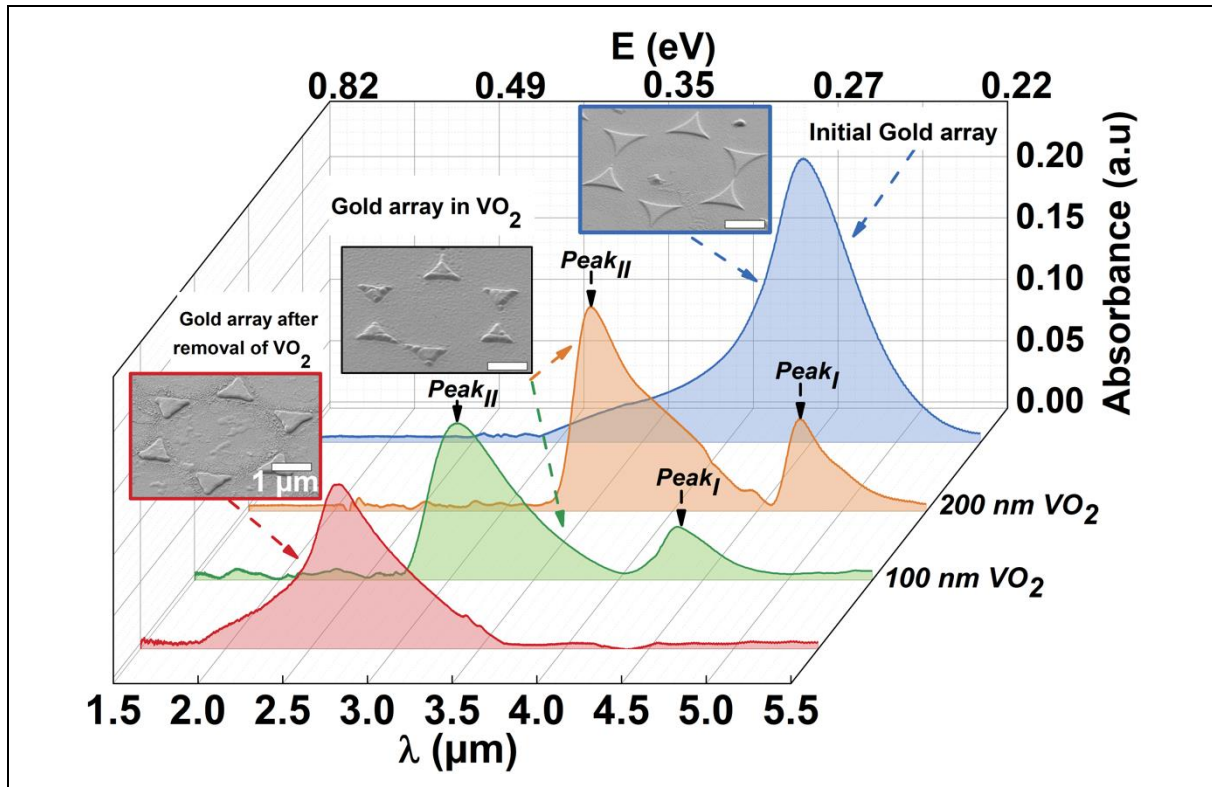


Figure IV-6: Optical absorbance spectra of Au nanoparticle arrays, before VO₂ deposition (in blue), in different thicknesses of the VO₂ matrix (200 and 100 nm, in orange and green resp.) and optical absorbance of the Au nanoparticle arrays after total removal of the VO₂ matrix (in red). The optical measurements are performed by FTIR spectroscopy on Au nanoparticle arrays made with 3 μm polystyrene microspheres,

The resonance position redshifts to a higher wavelength for Au in VO₂ nanocomposite than for Au nanoparticle arrays' after VO₂ removing (Figure IV-6). As shown for alumina matrix (see Figure IV-3), the resonance peak redshift value depends on the thickness of the VO₂ matrix. Nevertheless, compared to alumina layer, the thermally induced blue shift of the Au nanoparticle arrays must be considered for VO₂ matrix. The optical absorbance measurements of Au nanoparticles in a VO₂ matrix show two resonance peaks (Figure IV-6), respectively named as Peak_I, for the resonance peak at a higher wavelength, and Peak_{II}, for the resonance at a lower wavelength (compared to Peak_I) (see Figure IV-6). Two resonance peaks are also seen for the Iridium nanoarrays in VO₂ (Figure IV-7) for the same thickness range, i.e., exceeding 100 nm.

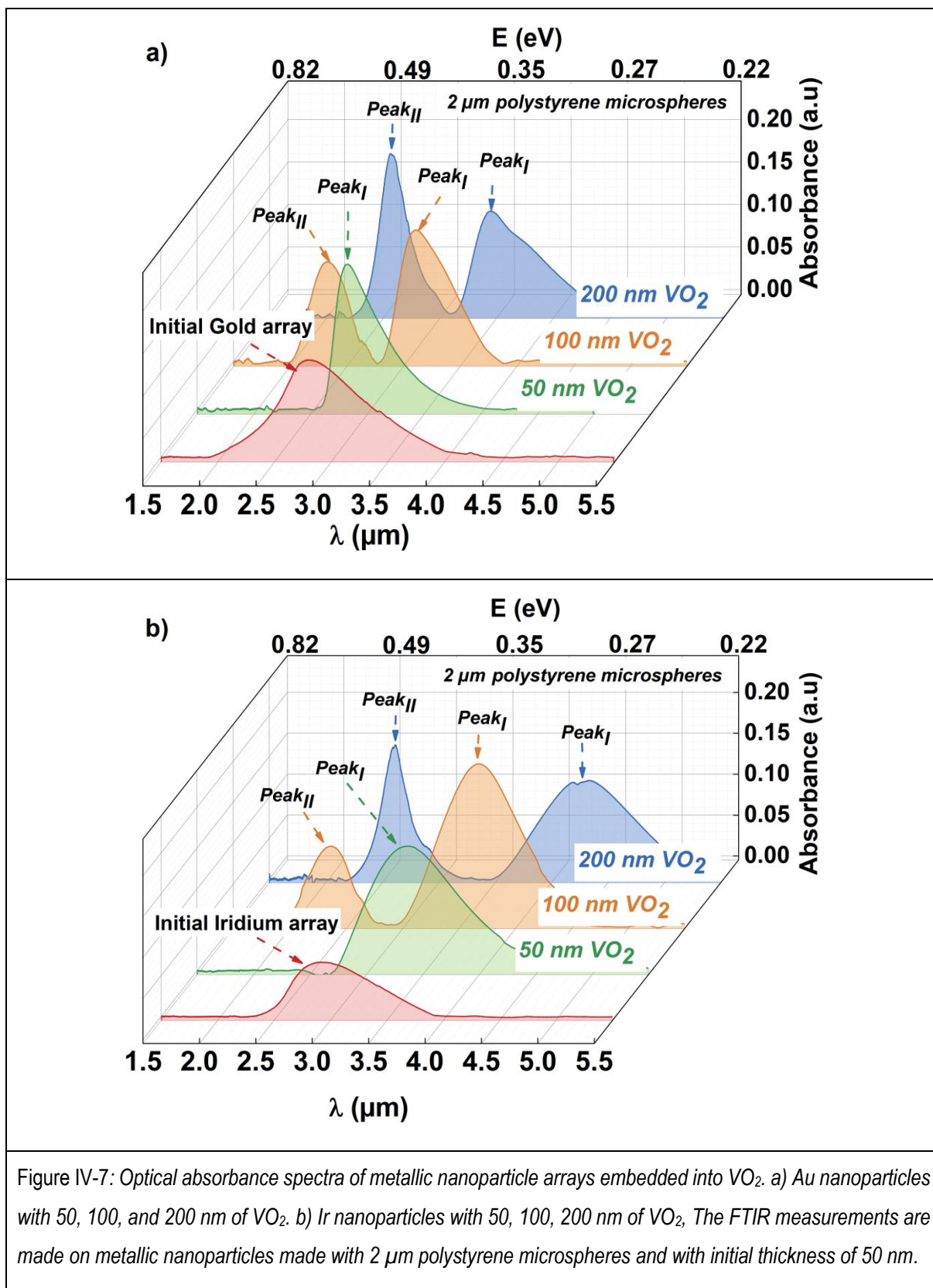


Figure IV-7: Optical absorbance spectra of metallic nanoparticle arrays embedded into VO₂. a) Au nanoparticles with 50, 100, and 200 nm of VO₂. b) Ir nanoparticles with 50, 100, 200 nm of VO₂. The FTIR measurements are made on metallic nanoparticles made with 2 μm polystyrene microspheres and with initial thickness of 50 nm.

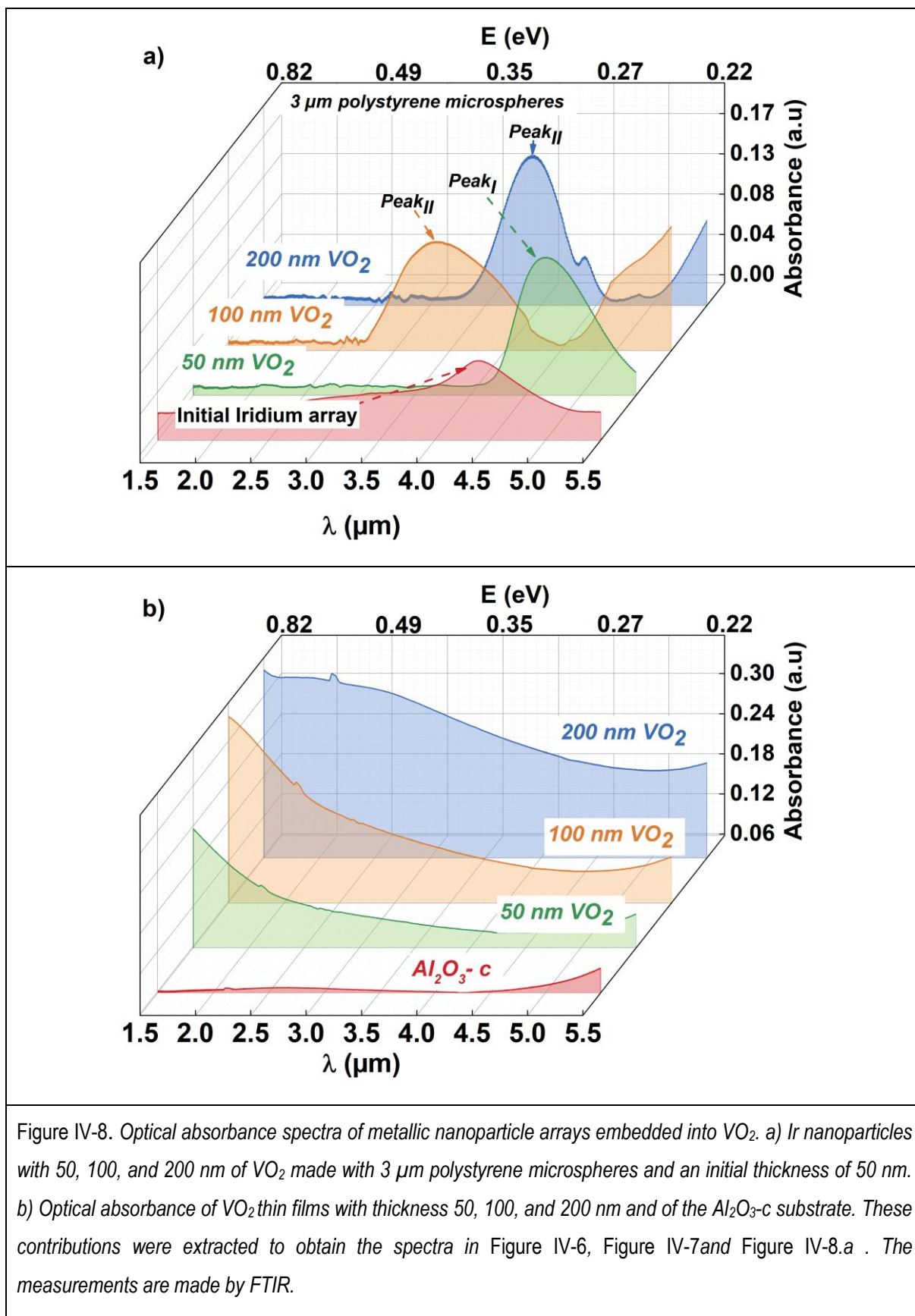


Figure IV-8. Optical absorbance spectra of metallic nanoparticle arrays embedded into VO_2 . a) Ir nanoparticles with 50, 100, and 200 nm of VO_2 made with 3 μm polystyrene microspheres and an initial thickness of 50 nm. b) Optical absorbance of VO_2 thin films with thickness 50, 100, and 200 nm and of the $\text{Al}_2\text{O}_3\text{-c}$ substrate. These contributions were extracted to obtain the spectra in Figure IV-6, Figure IV-7 and Figure IV-8.a. The measurements are made by FTIR.

All the VO₂ deposition has been carried out in the same experimental conditions, except the deposition time. The deposition time was adjusted to obtain the desired thickness of the VO₂ (for detailed experimental condition, see Table II-1).

For the case of Ir nanoparticles made with 3 μm polystyrene microspheres, if the thickness of the VO₂ is greater than 50 nm, then the first resonance peak (Peak_I) is located at a wavelength greater than 5.5 μm. Therefore, it was impossible to determine this peak's position since the Al₂O₃ is no longer transparent after 5.5 μm, but the optical absorbance spectra's shape suggests that they are present Figure IV-8 a).

As presented in Section I.4, the optical properties (i.e., the dielectric function, transmittance, etc.) of VO₂ are dependent on the temperature at which those optical measurements are made. Changing the VO₂ matrix's temperature will change the environment surrounding the metallic nanoparticle arrays and, consequently, the resonance peaks' positions (Peak_I and Peak_{II}). Therefore, we will also present the influence of the temperature on the metallic nanoparticle arrays' resonance peaks embedded into the VO₂ matrix. Then we will summarize all the results (regarding resonance peak positions and influence of temperature on resonance peak positions) in Table IV-2. The influence of temperature on an Au nanoparticle array's optical absorbance spectrum (made with 3 μm polystyrene microspheres) embedded into a 200 nm VO₂ matrix is presented in Figure IV-9.

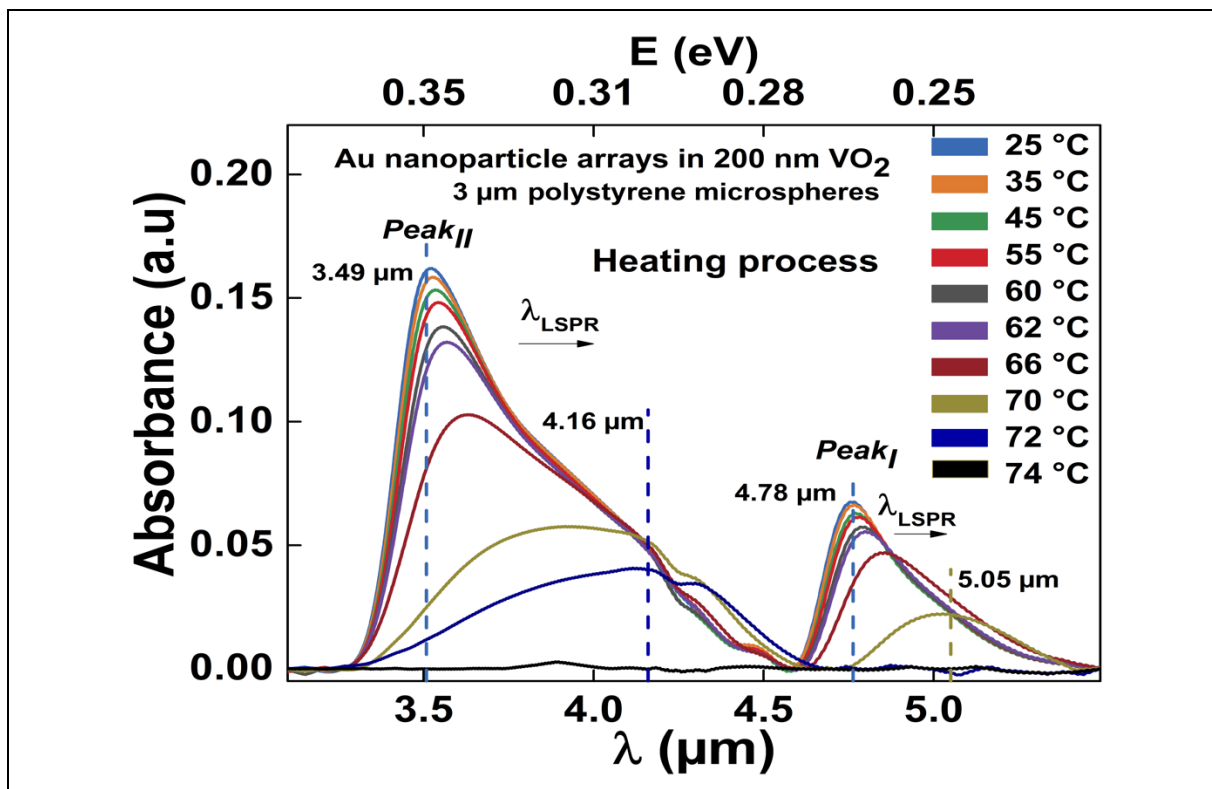


Figure IV-9: Optical absorbance spectra of Au nanoparticle arrays embedded into a 200 nm VO₂, as a function of the temperature matrix. The Au nanoparticles are made using 3 μm polystyrene microspheres and have an initial thickness of 50 nm. The data are measured by FTIR spectroscopy, and the baseline was subtracted using OriginPro 2015 software.

At room temperature, the Au nanoparticles arrays embedded in 200 nm of VO₂ have two resonance peaks. As the temperature is raised, the two peaks start to gradually redshift in the position of the resonance wavelength

(Figure IV-9). The value of the resonance redshift depends on temperature. In our optical measurements, the temperature is controlled using an external *Peltier plate* attached to the sample. The *Peltier plate* has a circular hole in the middle, with a diameter of 3.5 mm to allow optical transmittance measurements. The optical measurements are performed on a sample area equal to 9.6 mm². As a function of temperature, VO₂ properties vary from dielectric to metallic-like. This variation is fully reversible. With the *Peltier plate*, we can actively control the heating up from room temperature to 68 °C and cooling back down to the room temperature process of the VO₂; we can modulate the system's optical response. The 68 °C is the temperature of transition (from monoclinic to rutile) of a single crystal of VO₂, but for thin films of VO₂, the transition temperature can vary slightly (see Section I.4.4). To consider the variation of the transition temperature of VO₂, we measured the optical characteristics of the metallic nanoparticle arrays embedded into VO₂ from 25 °C to 50 °C using a step of temperature equal to 5 °C and from 50 °C to 90 °C using a step of 2 °C. The same steps were also used for optical measurements during cooling down from 90 °C to 25 °C. All the collected data are processed with Fityk software and the resonance peak position is extracted as presented in Figure IV-10.

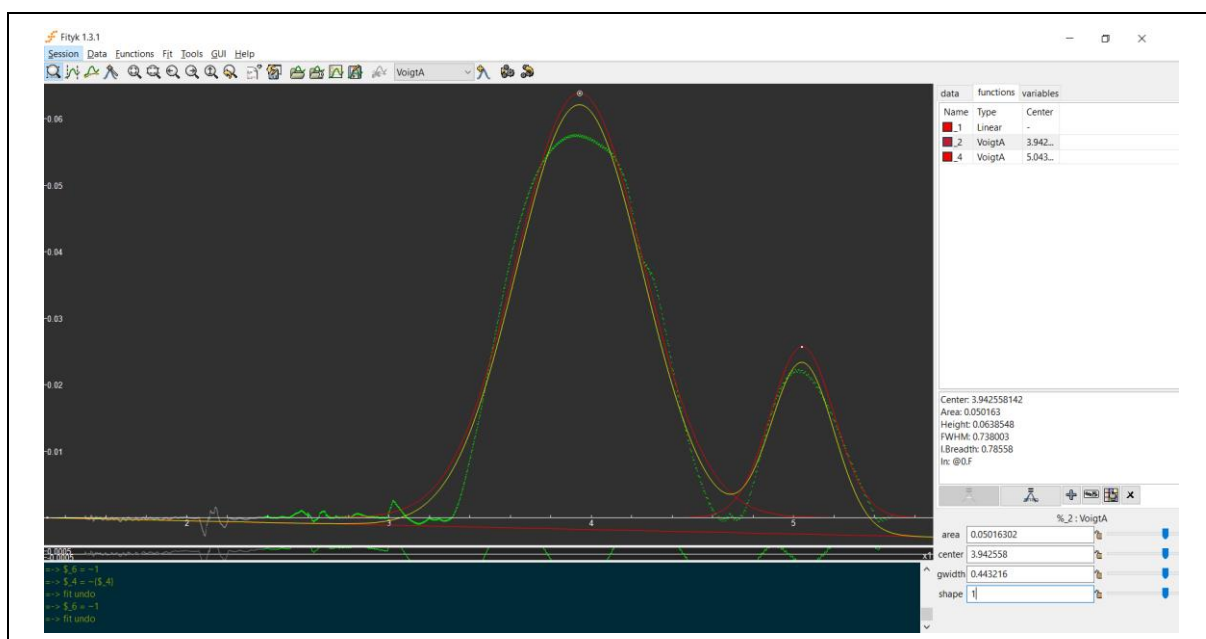


Figure IV-10: Example of resonance peak position determination of the Au nanoparticle arrays, made with 3 μm polystyrene microspheres, and embedded into 200 nm of VO₂. In this example, the experimental data (green curve) are collected at 70 °C. The baseline is subtracted from the experimental data, and a Voigt function is used for resonance peak determination.

The peak position of the resonances has been extracted using the build-in Voigt function of the Fityk software. The Voigt was used since it offered the best fit for the experimental data. For the shape of the resonance peaks (see Figure IV-9) a simple function like the Gaussian function or Lorentzian function is not sufficiently well adapted for extracting the resonance peak positions. The Voigt function is a convolution of Gaussian and Lorentzian functions (for more, see [154]. The evolution of position and intensity of the resonance peaks of the Au nanoparticle arrays embedded in 200 nm (a,c), 100 (b,d) nm of VO₂ matrix as a function of temperature is presented in Figure IV-11.

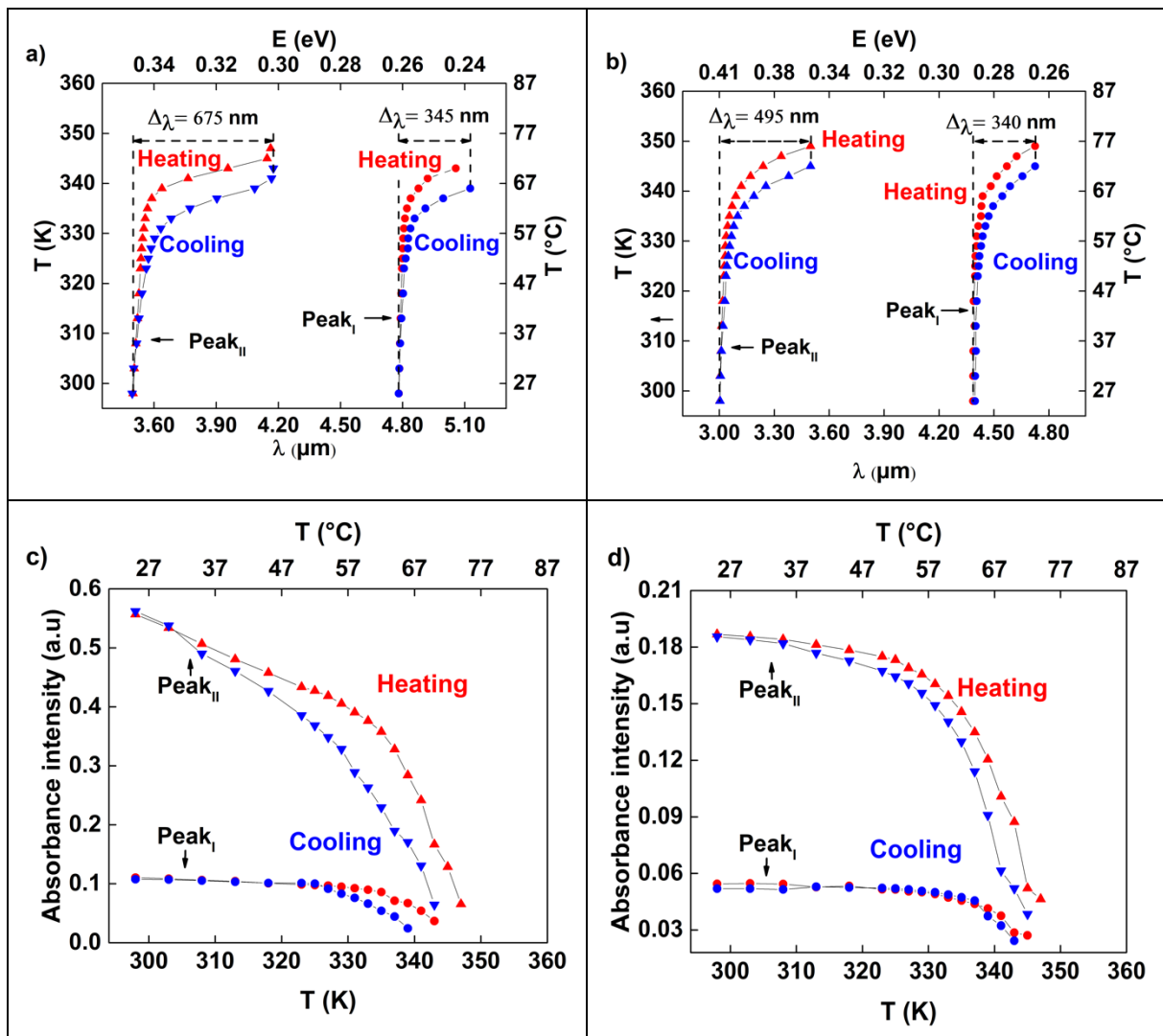


Figure IV-11: Temperature evolution of a) resonance peaks wavelength of Au nanoparticle arrays in 200 nm VO₂ matrix. b) resonance peaks wavelength of Au nanoparticle in 100 nm VO₂ matrix. c) resonance peaks intensity of Au nanoparticle arrays in 200 nm VO₂ matrix. d) resonance peaks intensity of Au nanoparticle arrays in 100 nm VO₂ matrix. Au nanoparticles are made with 3 μm polystyrene microspheres and thickness of 50 nm in both cases.

For each resonance peak, we have assigned a single Voigt function. In the Voigt fit, the peak position, intensity, shape, and area are let free. However, we imposed limits so that the calculation is performed on a wavelength interval that contains a single resonance peak. By applying this procedure, we extracted all the data corresponding also to Au nanoparticles made using 2 μm polystyrene microspheres and Ir nanoparticles embedded in VO₂ (see Appendix 3).

When the VO₂ matrix's temperature is increased from 25 $^{\circ}\text{C}$ towards 90 $^{\circ}\text{C}$, the resonance peaks' position starts to redshift, moving from a lower wavelength value to a higher one as VO₂ transits from an insulator to a metallic state. If the VO₂ is cooled down, the metallic nanoparticle resonance position will blueshift back to its initial position. In general, for both resonance peak position and peak intensity, there is a visible difference between the value at the same temperature if the measurement is made when heating up compared to when the measurement is made during cooling down. The data on the influence of the nanoparticle nature, nanoparticle size, thickness,

and the temperature of the VO₂ matrix on the plasmonic resonance of the metallic nanoparticle arrays are summarized in Table IV-2.

Table IV-2: Modulation of the plasmonic resonances metallic nanoparticle arrays by the VO₂ active or passive matrix.

	Metal nanoparticle arrays	VO ₂ thickness (nm)	Resonance peak position (μm)		Resonance peak redshift (nm)	
			Peak _I	Peak _{II}	Peak _I	Peak _{II}
3 μm polystyrene microspheres	Au	100	4.39	3.00	340	495
	Au	200	4.78	3.49	345	675
	Ir	50	4.71	-	123	-
	Ir	100	-	3.43	-	120
	Ir	200	-	3.91	-	134
2 μm polystyrene microspheres	Au	50	2.83	-	447	-
	Au	100	3.11	2.33	468	298
	Au	200	3.49	2.58	343	279
	Ir	50	3.34	-	210	-
	Ir	100	3.68	2.35	396	150
	Ir	200	4.26	2.60	196	80

In literature, the resonance position blueshifts during the VO₂ transition from insulator to the metallic state [155]–[158]. In general, the modulation of plasmonic resonances using VO₂ is made for nanoparticles that have resonance in the visible part of the electromagnetic spectra. However, Richard F. Haglund et al. [158] worked with Au nano-disks arrays that have a plasmonic resonance in the IR and still obtained a blue shift plasmonic resonance peak during VO₂ heating. Further, on the basis of the thermal treatment of Au nanoparticle arrays (Chapter III) we have deposited a matrix of VO₂ on Au nanoparticle array that has a plasmonic resonance peak in the visible part of the electromagnetic spectrum (see Figure IV-12).

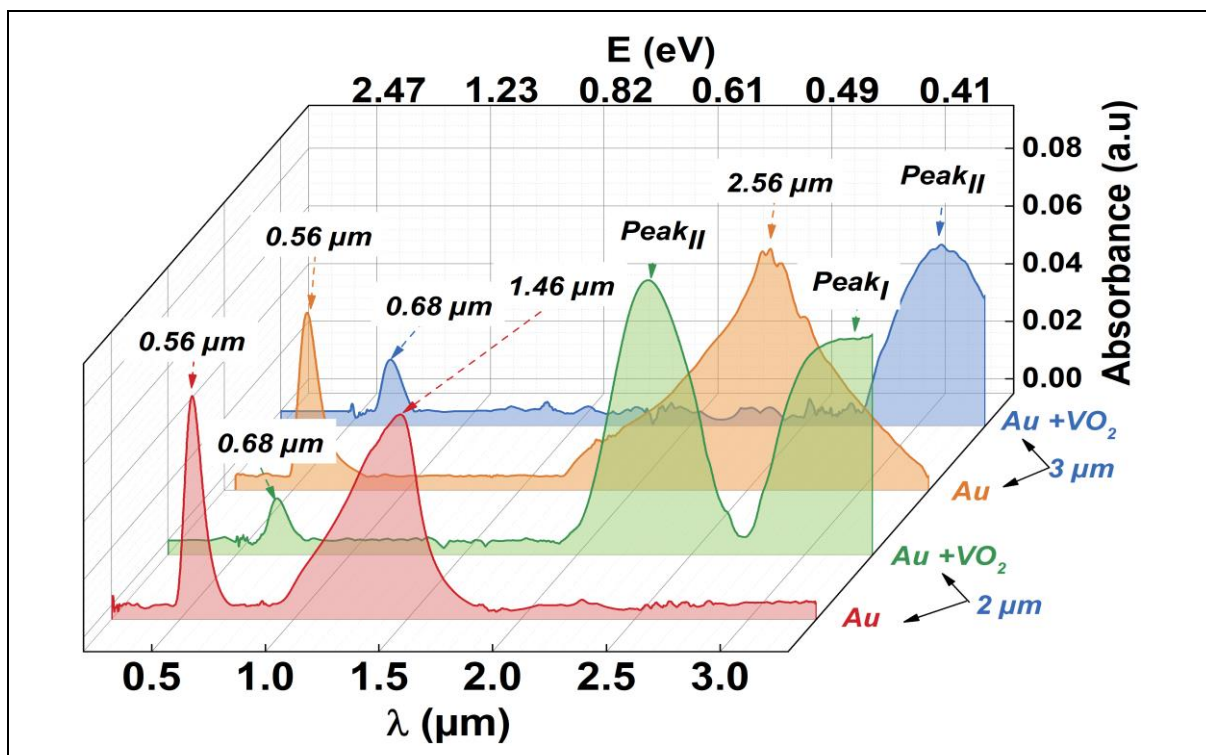


Figure IV-12: Optical absorbance spectra of Au nanoparticle arrays thermally treated at 532 °C and embedded in VO₂. The red curve represents Au nanoparticle arrays made with 2 μm microspheres and thermally treated at 532 °C. The green curve represents Au nanoparticle arrays made with 2 μm microspheres, thermally treated at 532 °C, then embedded in 100 nm of VO₂. The orange curve represents the Au nanoparticle arrays made with 3 μm polystyrene and thermally treated at 532 °C. The blue curve represents the Au nanoparticle arrays made with 3 μm polystyrene, thermally treated at 532 °C, then embedded in 100 nm of VO₂. The data are collected by UV-VIS spectroscopy.

The initial thickness of the Au nanoparticle is 50 nm. The Au nanoparticle arrays made with 2 and 3 μm polystyrene microspheres were preliminarily thermally treated at 532 °C (805 K) to obtain samples presenting two plasmonic resonances peaks, one peak in IR and another in the visible. Then on these arrays was deposited by PLD a layer of 100 nm of VO₂. As expected, the Au nanoparticle arrays treated at 532 °C exhibit a plasmonic resonance in the visible at $\lambda = 0.56 \mu\text{m}$ and maintain a resonance peak in the IR located at $\lambda = 1.46 \mu\text{m}$ for arrays made from 2 μm polystyrene microspheres and at $\lambda = 2.56 \mu\text{m}$ for arrays made from 3 μm polystyrene microspheres (see Figure IV-12).

After the deposition of 100 nm of VO₂ on top of the previously thermally treated Au nanoparticle arrays, the visible plasmonic resonance redshifts from $\lambda = 0.56 \mu\text{m}$ to $\lambda = 0.68 \mu\text{m}$. This redshift is due to the change in the dielectric environment surrounding the residue nanoparticles (environment change from ambient air to VO₂). The redshift (120 nm) is equal for both samples. This plasmonic resonance in the visible is only linked to the residue Au nanoparticles and not to the main Au nanoparticle arrays.

The temperature dependence of the residue Au nanoparticles' plasmonic resonance peak during VO₂ matrix heating is given in Figure IV-13.

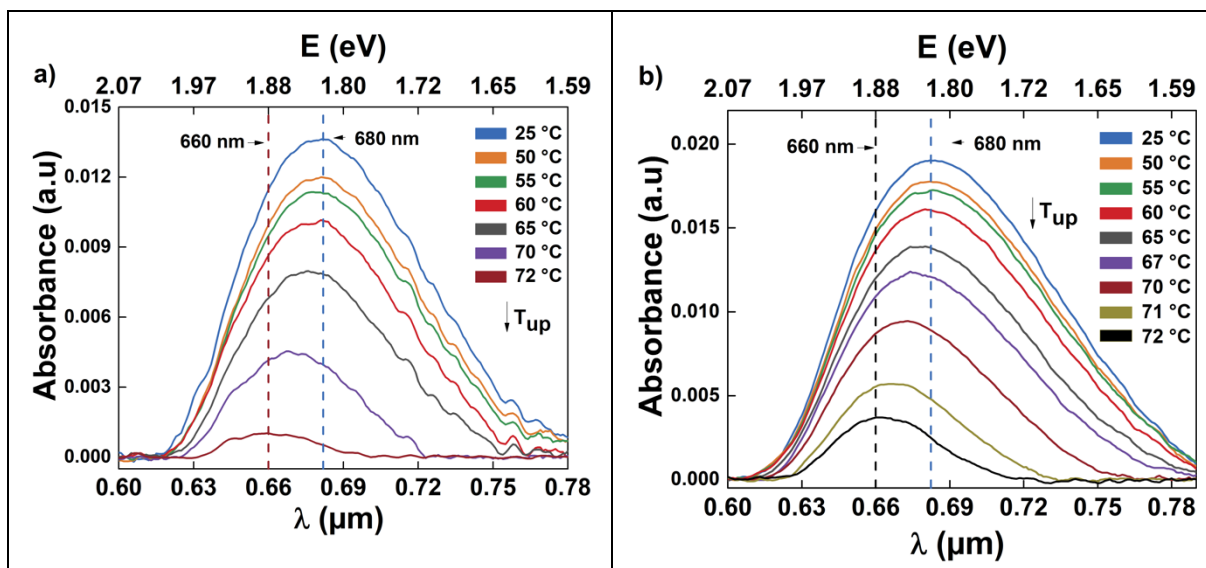


Figure IV-13: Temperature evolution of the plasmonic resonance peak located in the visible part of the electromagnetic spectrum of residue Au nanoparticles embedded into 100 nm of VO₂. a) Au residue nanoparticles made by thermally treating at 532 °C; the Au nanoparticle array was made with 2 μm polystyrene microspheres. b) Au residue nanoparticles made by thermally treating at 532 °C the Au nanoparticle array was made with 3 μm polystyrene microspheres.

As the temperature is raised, from room temperature to the semiconductor to metal transition temperature of the VO₂, the position of the plasmonic resonance peak at $\lambda = 0.68 \mu m$ blue shifts gradually to $\lambda = 0.66 \mu m$ for both samples (see Figure IV-13). If the samples are cooled to room temperature, the plasmonic resonance position returns to the original position. The blueshift of the resonance peak during VO₂ heating up is in perfect agreement with literature data and is based on the dielectric evolution of VO₂ during insulator to metal transition [155].

Further, both samples have two new plasmonic resonance peaks in IR (see Figure IV-14). The appearance of two new resonance peaks on both Au nanoparticle arrays (made with 2 and 3 μm polystyrene microspheres) and treated at 532 °C is in agreement with our previous results. For the Au nanoparticle arrays made with 3 μm polystyrene microspheres, Peak_I is located at $\lambda = 4.60 \mu m$ while Peak_{II} is at $\lambda = 3.02 \mu m$. For the Au nanoparticle arrays made with 2 μm polystyrene microspheres, Peak_I is located at $\lambda = 3.03 \mu m$ while Peak_{II} is at $\lambda = 2.31 \mu m$.

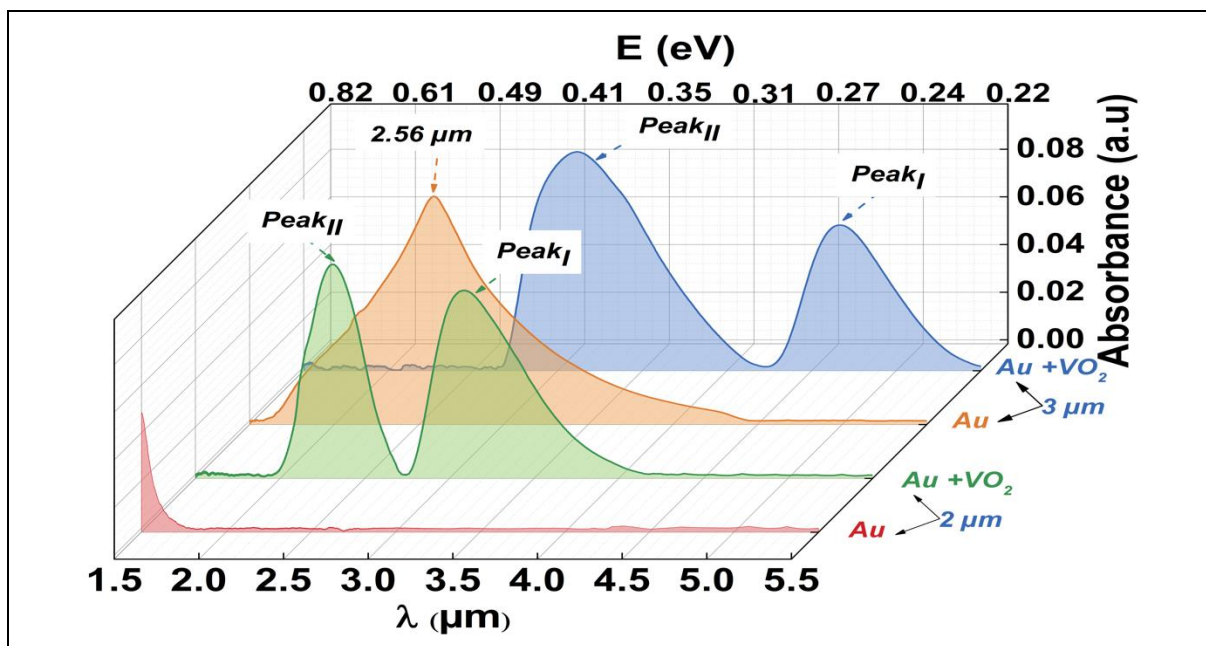


Figure IV-14: Optical absorbance spectra of Au nanoparticle arrays thermally treated at 532 °C and embedded in VO₂. The red curve represents Au nanoparticle arrays made with 2 μm microspheres and thermally treated at 532 °C. The green curve represents Au nanoparticle arrays made with 2 μm microspheres, thermally treated at 532 °C, then embedded in 100 nm of VO₂. The orange curve represents the Au nanoparticle arrays made with 3 μm polystyrene and thermally treated at 532 °C. The blue curve represents the Au nanoparticle arrays made with 3 μm polystyrene, thermally treated at 532 °C, then embedded in 100 nm of VO₂. The data are collected by FTIR spectroscopy.

During heating up of VO₂, the position of Peak_I and Peak_{II} for both Au nanoparticle arrays start to redshift, with a redshift value that is dependent on the temperature (see Figure IV-15). This is the same phenomenon that we saw on the samples with resonances in the electromagnetic spectrum's infrared part.

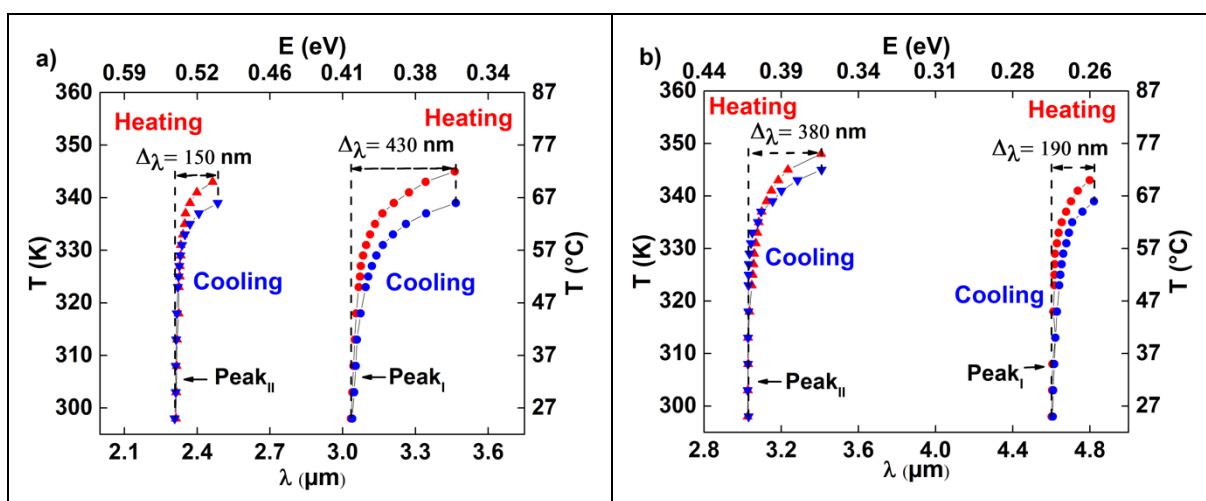


Figure IV-15: a) Temperature evolution of resonance peak of Au nanoparticle arrays made with 2 μm polystyrene microspheres thermally treated at 532 °C and then covered by 100 nm of VO₂. b) Temperature evolution of resonance peaks of Au nanoparticle arrays made with 3 μm polystyrene microspheres thermally treated at 532 °C then covered by 100 nm of VO₂.

During the cooling down process, the resonance peaks return to their respective original positions.

IV.2.3. Origin of the double plasmonic resonance peaks of the metallic nanoparticle arrays embedded into VO₂ and origin of the resonance peak redshift during VO₂ insulator to metal transition.

For understanding the origin of the double plasmonic resonance peak of the metallic nanoparticle arrays when they are embedded in VO₂, we will focus on this section on a sample consisting of Au nanoparticle arrays made with 3 μm polystyrene microspheres and 200 nm of VO₂. Moreover, for clarity, we will combine multiple results in Figure IV-16 in order to create a general image of the double resonance peak origin.

The VO₂ deposition changes the Au nanoparticles shape and produces a resonance peak shift from $\lambda_{LSPR} \approx 4,45 \mu m$ to $\lambda_{LSPR} \approx 2,8 \mu m$ after VO₂ removal (Figure IV-16). This new peak position of the Au nanoparticles was determined after removing the VO₂ layer through chemical etching (see Figure IV-5). The resonance wavelength blueshift ($\approx 1.65 \mu m$) of the Au nanoparticles arrays during VO₂ deposition at 500 °C is in perfect agreement with just Au nanoparticles' thermal treatment results on a substrate.

In Figure IV-16, the presence of a single LSPR peak (after VO₂ removal) shows that there is no interaction between the localized plasmons of the neighboring Au nanoparticles. Hence, the influence of the Au nanoparticles array on the coupling effect described next is consequently negligible. When the Au nanoparticles arrays are embedded into a 200 nm VO₂ matrix, two clearly defined peaks appear in the absorption spectrum (Figure IV-16). At R_T , Peak_I of the Au-VO₂ is located at $\lambda = 4.78 \mu m$, while Peak_{II} is located at $\lambda = 3.52 \mu m$. For the R_T measurements, a FDTD model (*FDTD-N_i*) of the absorbance spectra constructed for Au nanoparticles embedded in a 50 nm semiconductor VO₂ matrix points out both peaks, Peak_I located at $\lambda = 4.15 \mu m$ and Peak_{II} at $\lambda = 3.55 \mu m$ (Figure IV-16 a bottom panel). The difference between the experimental and calculated data are induced by the thickness of the VO₂ which has to be limited to 50 nm in the model and also by the incomplete reproducibility of the geometry of the nanoparticles (rounded edges and corners) from the image to the *FDTD-N_i* model. Nevertheless, the E-field distributions extracted for both peaks Peak_I and Peak_{II} suggest that the two resonance peaks have a plasmonic nature with dipolar characteristics (Figure IV-16 c-d). The double plasmonic peaks may be linked to a selective E-field enhancement at different interfaces [159]. Considering the discussed nanocomposite, the presence of VO₂ obviously increases the number of interfaces (Au nanoparticles -substrate, Au nanoparticles -VO₂, substrate-VO₂) and may also explain the small difference in intensity between the two peaks.

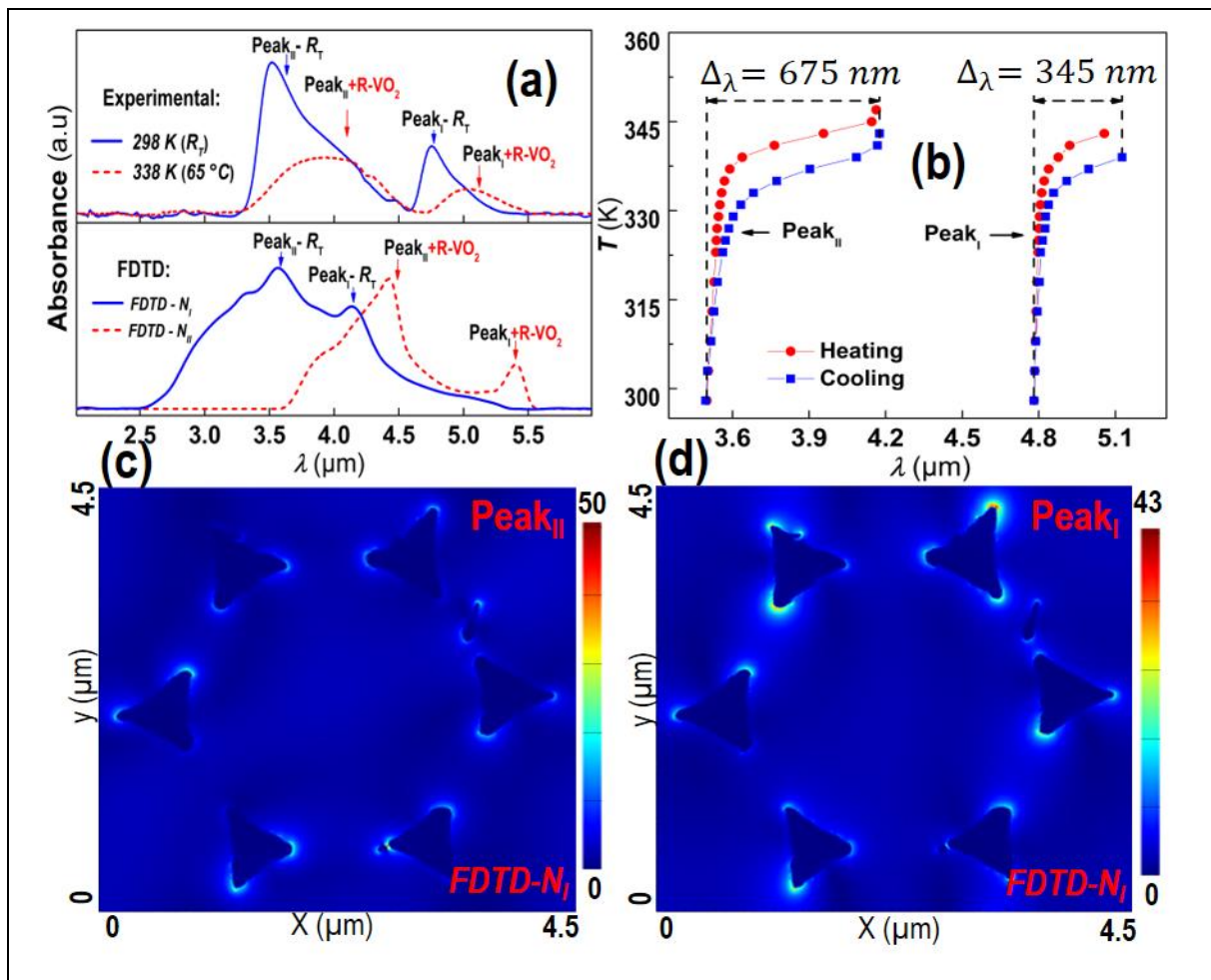


Figure IV-16: Localized surface plasmon resonance of Au nanoparticles-VO₂ system: a) Absorbance spectra of Au nanoparticles embedded in 200 nm of VO₂ (top panel) at different temperatures (R_T and 338 K), vs theoretical absorbance spectra (bottom panel) obtained from FDTD calculations. b) Temperature dependence of the LSPR position measured during a heating/cooling cycle (from R_T to SMT temperature and back to R_T). The LSPR positions are extracted from a Voigt function fit of experimental data. c-d) FDTD deduced Electric field cartography for the two resonant peaks at: $\lambda = 4.15\mu\text{m}$ (Peak_I) and $\lambda = 3.55\mu\text{m}$ (Peak_{II}) (model FDTD-N_I). The Au nanoparticles are made using 3 μm polystyrene microspheres.

When the absorbance spectra of the n Au-VO₂ nanocomposite is recorded at a higher temperature (338 K) (Figure IV-16 a, top panel), both peaks are red shifted compared to their R_T counterparts. Figure IV-16 b) shows the step by step evolution during heating (SMT) and cooling (MIT) of the position of the LSPR peaks extracted using a Voigt function data fit of the experimental absorbance spectra. During the heating-cooling cycle, the LSPR peaks red shift gradually as the temperature rises and return to the original position as the temperature becomes again R_T and also reveal the optical hysteresis of the VO₂. In the heating-cooling cycle, between R_T and SMT temperature, the total LSPR peak modulation is equal to 635 nm for Peak_{II} and 345 nm for Peak_I (Figure IV-16 b). The active LSPR modulation can be induced by a change in the dielectric characteristics of VO₂ during SMT or by Au nanoparticles -VO₂ coupling phenomenon [160]. There are two possible types of nanoparticles coupling that affect the LSPR peaks position through the near-field and far-field interactions [161]. Firstly, the far-field interaction at the long-range produces a red shift of the LSPR peaks as the distance between nanoparticles increases, and secondly, the near-field interaction at short-range results in a blue shift of the LSPR peaks as the distance between

nanoparticles increases. The red shift of the LSPR peaks to higher wavelengths, related to long-range plasmon coupling based on the far-field, can also result from an increase of the nanoparticles size [162]. The size of the Au nanoparticles and their inter-distance remain constant during VO₂ SMT. Therefore, the red shift of LSPR peaks must more probably originate from the VO₂ component of the Au nanoparticles-VO₂ system. A possible origin of the active wavelength red shift in LSPR peaks during SMT can be induced by the VO₂ transition at specific zones inside the nanocomposite. During heating, a thin shell of metallic VO₂ may be formed around the Au nanoparticles while the rest of the VO₂ remains in the semiconductor-like state. The VO₂ metallic shell can “artificially” increase the size of the “metallic nanoparticle zone”, leading to a red shift of the LSPR peaks (due to long-range plasmon coupling) based on the far-field interaction [162]. This is possible since, in the metallic VO₂, the Fermi level is located in the t2g(π^* orbital) level, which is partially overlapped with the t2g(d//orbital) level. In this configuration, the optical excitations of metallic VO₂ are governed by three interband transitions E₁, E₂, and E₃ that were detected around ~ 1.22 , ~ 3.37 , and ~ 5.90 eV, respectively [163]. Strain alters the orbital occupancy near the Fermi energy level, and since the E₁ transition corresponds to the optical excitation from the filled t2g(d//) to empty t2g(π^*) bands, this transition broadly exists in the range 0.5–2 eV [164]. Hence, metallic VO₂ can also support plasmon resonances based on free carriers intraband excitations in the conduction band. This strengthens the hypothesis of a shell of metallic VO₂ increasing the size of the nanoparticles which can be the origin of the LSPR red shift through far-field interactions during SMT. A second FDTD model (*FDTD-N_{II}*) is developed to test the hypothesis of resonance peaks red shift. *FDTD-N_{II}* consists of Au nanoparticles (core) enveloped by metallic VO₂ (shell) and embedded in 50 nm of a semiconductor VO₂ matrix.

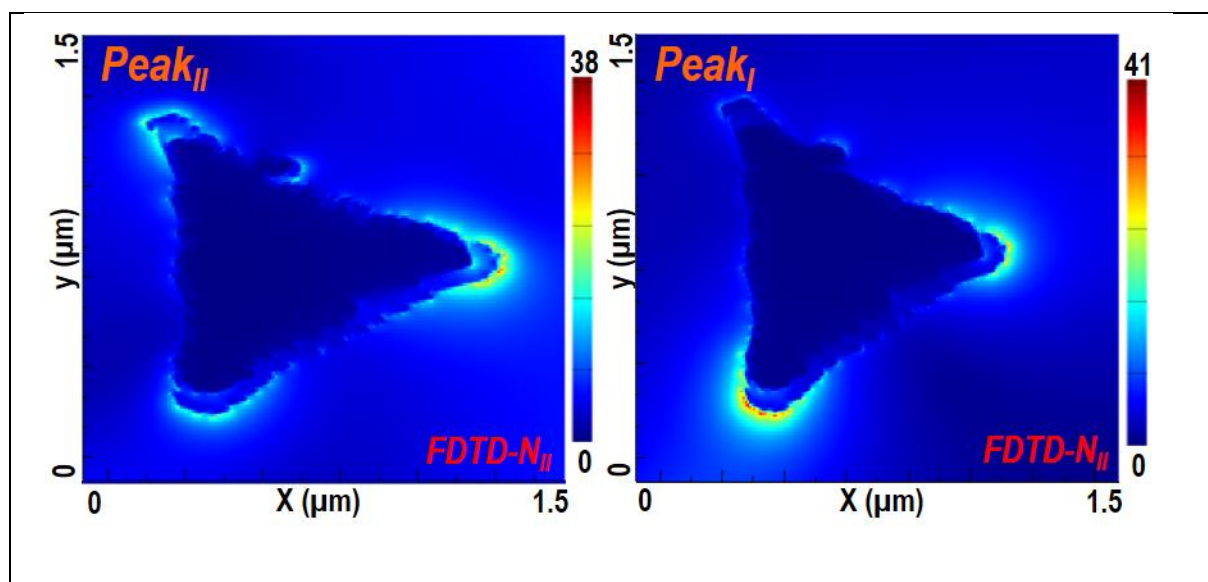


Figure IV-17: Simulated electric field cartography of an array of Au nanoparticles covered with a shell of metallic VO₂ and embedded in a VO₂ dielectric matrix. The electric field is plotted at $\lambda = 3.7 \mu\text{m}$ for Peak_{II} and $\lambda = 4.7 \mu\text{m}$ for Peak_I. The thickness of the dielectric matrix is 50 nm. The simulation is performed on the actual image of the Au nanoparticle array obtained by AFM measurements made on the Au nanoparticle arrays after the chemical removal of VO₂, and the scale bar is 1 μm .

The size of the metallic VO₂ shell is taken ~10 % larger (on the x-y directions) than the size of the Au nanoparticles. The *FDTD-N_i* model for the absorbance spectra of the nanocomposite points out the presence of two resonance peaks (Figure IV-16 a bottom panel). The Peak_i is located at $\lambda = 5.42 \mu\text{m}$ and the Peak_{ii} at $\lambda = 4.40 \mu\text{m}$, both peaks being red shifted from their *FDTD-N_i* equivalents. The *E*-field distributions extracted from *FDTD-N_{ii}* model show that the plasmonic dipolar characteristics of both peaks are maintained after the introduction of the metallic VO₂ shell (Figure IV-17). The FDTD approaches (*FDTD-N_i* and *FDTD-N_{ii}*) show qualitatively that Au nanoparticles-VO₂ resonances have a plasmonic origin and the red shift during SMT is induced by the formation of adaptive core-shell structure. The FDTD calculations are made on a limited area ($4.5 \times 4.5 \mu\text{m}^2$ for *FDTD-N_i* and $1.5 \times 1.5 \mu\text{m}^2$ *FDTD-N_{ii}*) far smaller than the one used in experimental measurements ($\approx 20 \text{ mm}^2$), explaining differences between the calculated and the experimental results. Moreover, some experimental details of the nanoparticles that cannot be exactly captured by the FDTD models, could not be considered. The experimental absorbance spectra have to be thought as the envelop function of the response of multiple regions on which FDTD calculations are made.

IV.2.4. Conclusions

The *Chapter IV* probed the optical properties of nanoparticles arrays and nanocomposites constituted of nanoparticles arrays covered by PLD thin layer, and particularly the modulation of LSPR by the dielectric environment that surrounds the metallic nanoparticle arrays. The deposition of Alumina induces a thickness-dependent redshift on the LSPR of nanoparticles array. When the chosen matrix is 'smart' VO₂, a material with a temperature dependent dielectric function, it is possible to modulate the metallic nanoparticle arrays' plasmonic response actively. Changing the temperature of the VO₂ can induce a red or blueshift in the LSPR position. As FDTD demonstrates, the LSPR modulation originates as the formation of an adaptive temperature-dependent VO₂ metal shell that surrounds the metallic nanoparticles (i.e., a core-shell structure). When temperature rises, a VO₂ (R) shell starts to grow on and close to the Au (or Ir) nanoparticles surface, while the rest of VO₂ follows normal transition pathways. This R shell "increases the volume" of the metallic nanoparticles, and red shifts the wavelength position of the LSPR peaks. The formation of the VO₂ metal shell causes the system to behave like an adaptive periodic metal architecture. This new approach to considering the metallic nanoparticles –VO₂ system as an adaptive metallic periodic architecture may be further adapted in other Mott-type insulating oxide systems towards implementing Mott-type practical applications' insulating materials electronic devices and optics. The metallic nanoparticles – VO₂ based system appears as an ideal candidate that can be readily tuned to specification to enhance the IR modes of specific chemical compounds for more straightforward sensing and detection.

Chapter V

Beyond plasmonic resonances; Chemical composition, optical and structural properties of metallic nanoparticle- VO₂ system

Chapter V. Beyond plasmonic resonances; Chemical composition, optical and structural properties of metallic nanoparticle- VO₂ system.

Chapter V will be dedicated to presenting the interaction between metal nanoparticle arrays and the VO₂ matrix, focusing on the structural interaction between the two of them. We will start *Chapter IV* by assessing our samples' chemical composition by Energy Dispersive X-Ray Spectroscopy (EDS). We will then show the differences in optical transition contrast, optical hysteresis width, and transition temperature of VO₂ between samples of pure VO₂ and samples of VO₂ that contain metallic (Au and Ir) nanoparticle array inside. After that, we will discuss the crystalline structure of our samples, and we will also show the temperature evolution of VO₂ and metallic nanoparticles (by HR-XRD). *Chapter IV* ends by assessing the temperature dependence of different VO₂ crystalline phases (M₁, M₂, T, and R) and their relation to the metallic nanoparticles by Raman spectroscopy and Raman spectroscopy mapping, respectively. *Chapter V* experimentally proves the existence of a temperature dependent core-shell structure of metallic (Au or Ir) core, surrounded by a metallic VO₂ shell and embedded in a dielectric VO₂ matrix.

V.1. Metallic nanoparticle arrays and VO₂ chemical composition.

The chemical composition of our samples was assessed by Energy Dispersive X-Ray Spectroscopy (EDS). The EDS investigation is performed together with SEM investigations. For more information about EDS, please see reference [165]. EDS can rapidly generate information about the chemical composition of a sample, showing the chemical elements and their distribution and concentration of chemical elements on the sample on an area of 6x6 μm².

The EDS investigation performed on Au nanoparticle arrays (PS 3 μm) and embedded into 200 nm of VO₂ are presented in Figure V-1.

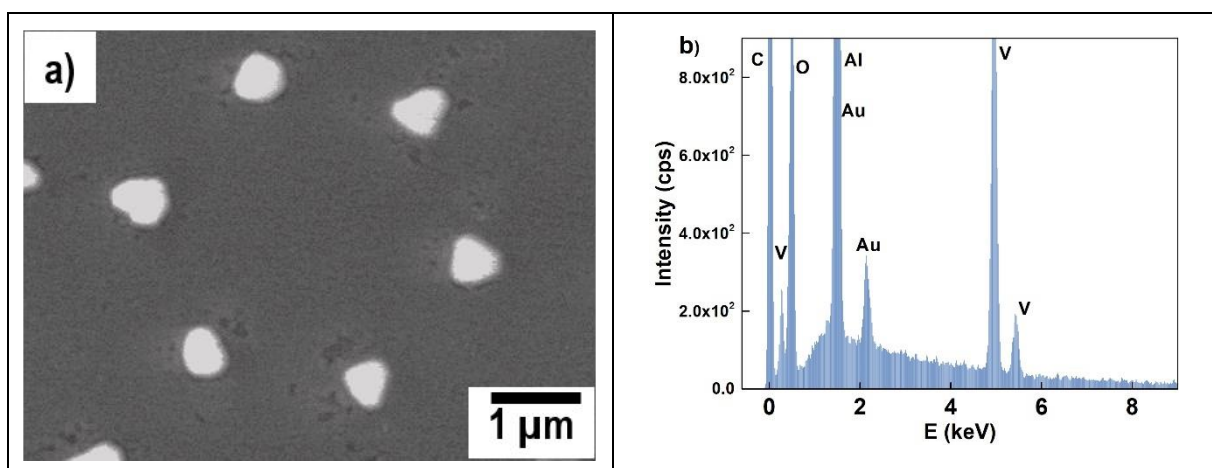


Figure V-1: Energy Dispersive X-Ray Spectroscopy results. a) SEM image of Au nanoparticle arrays made with 3 μm polystyrene microsphere and embedded into 200 nm of VO₂. b) Corresponding EDS elemental analyses.

From Figure V-1 b) it is evident that our sample contains just the elements that we have anticipated to be present: Au, V, O, and Al. The Al present in Figure V-1 b) can be traced back to the sapphire substrate. In Figure

V-1 b), there is also a peak of carbon (at 0.277 KeV), and this carbon peak is linked to the preparation procedure of our samples for EDS investigation. Before making EDS, the samples are covered with a conductive carbon layer.

The elemental mapping of the chemical elements identified in samples are presented Figure V-2. The elemental maps can be obtained for each element (Au, Al, O, and V) and use varying color intensities to show the particular element concentrations across the investigated area visually. The SEM image of the investigated area by the elemental mapping is presented in Figure V-1 a).

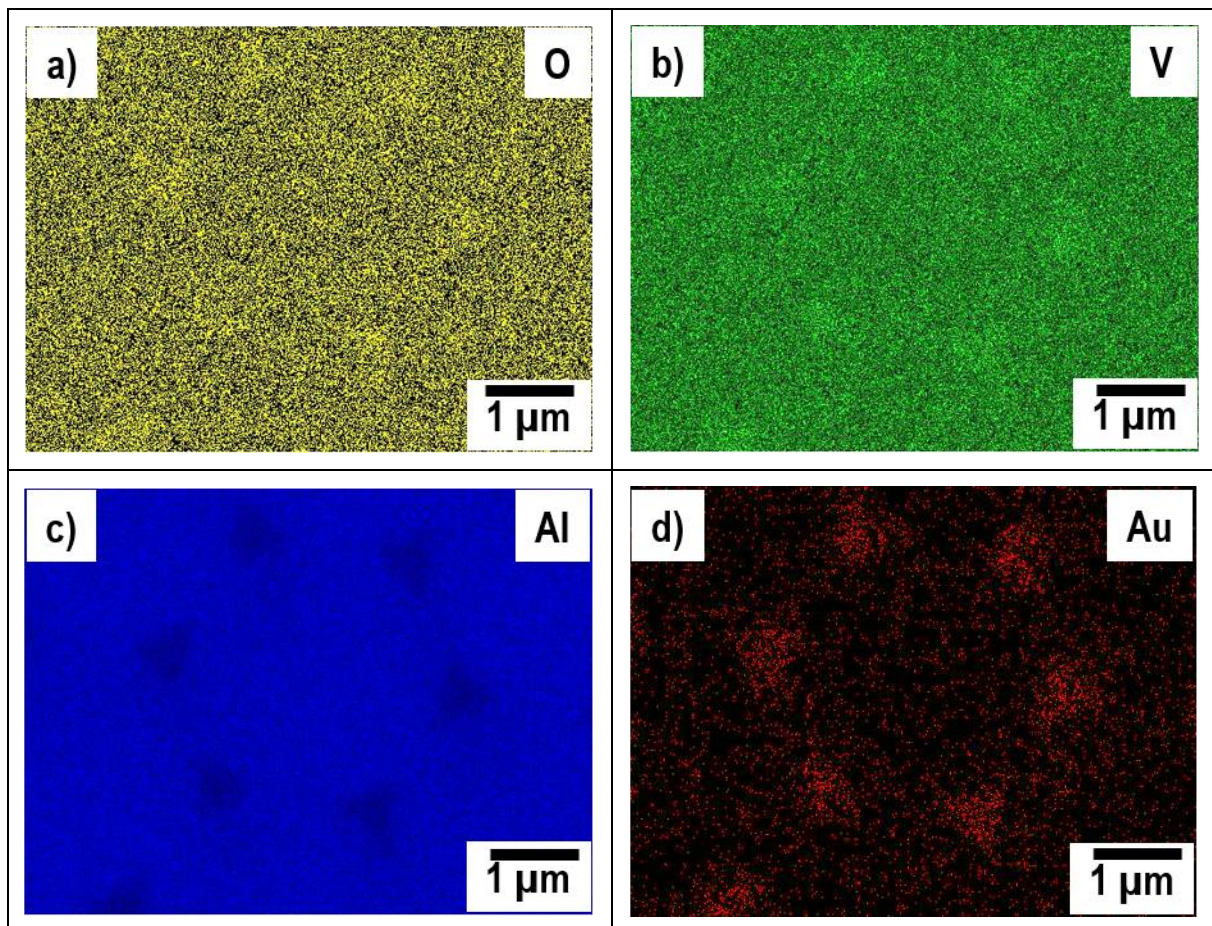


Figure V-2: Elemental mapping of a sample consisting of Au nanoparticle arrays made with 3 μm polystyrene microsphere and embedded into 200 nm of VO₂. a) Elemental map of Oxygen. b) Elemental map of Vanadium. c) Elemental map of Aluminum. d) Elemental map of Iridium.

The elemental mapping in Figure V-2 confirms that oxygen and vanadium are distributed uniformly in our sample (Figure V-2 a-b). The elemental mapping of Al shows that Al is distributed uniformly with a slight drop in intensity in the position where we expect the Au nanoparticles to be present (see Figure V-2 c)). This intensity drop may be due to the shielding of Al by Au. As for the Au nanoparticle arrays, we see an excess of intensity in Figure V-2 d) of elemental Au. This excess of intensity in the Au signal can be correlated with the Au nanoparticles that are underneath the VO₂ layer; furthermore, if we couple Figure V-2 c) with Figure V-2 d), it is reasonable to conclude that Au metal is concentrated into selected areas forming our Au nanoparticle arrays. The EDS investigation results performed on Ir nanoparticle arrays and embedded into 200 nm of VO₂ are shown in Figure V-3.

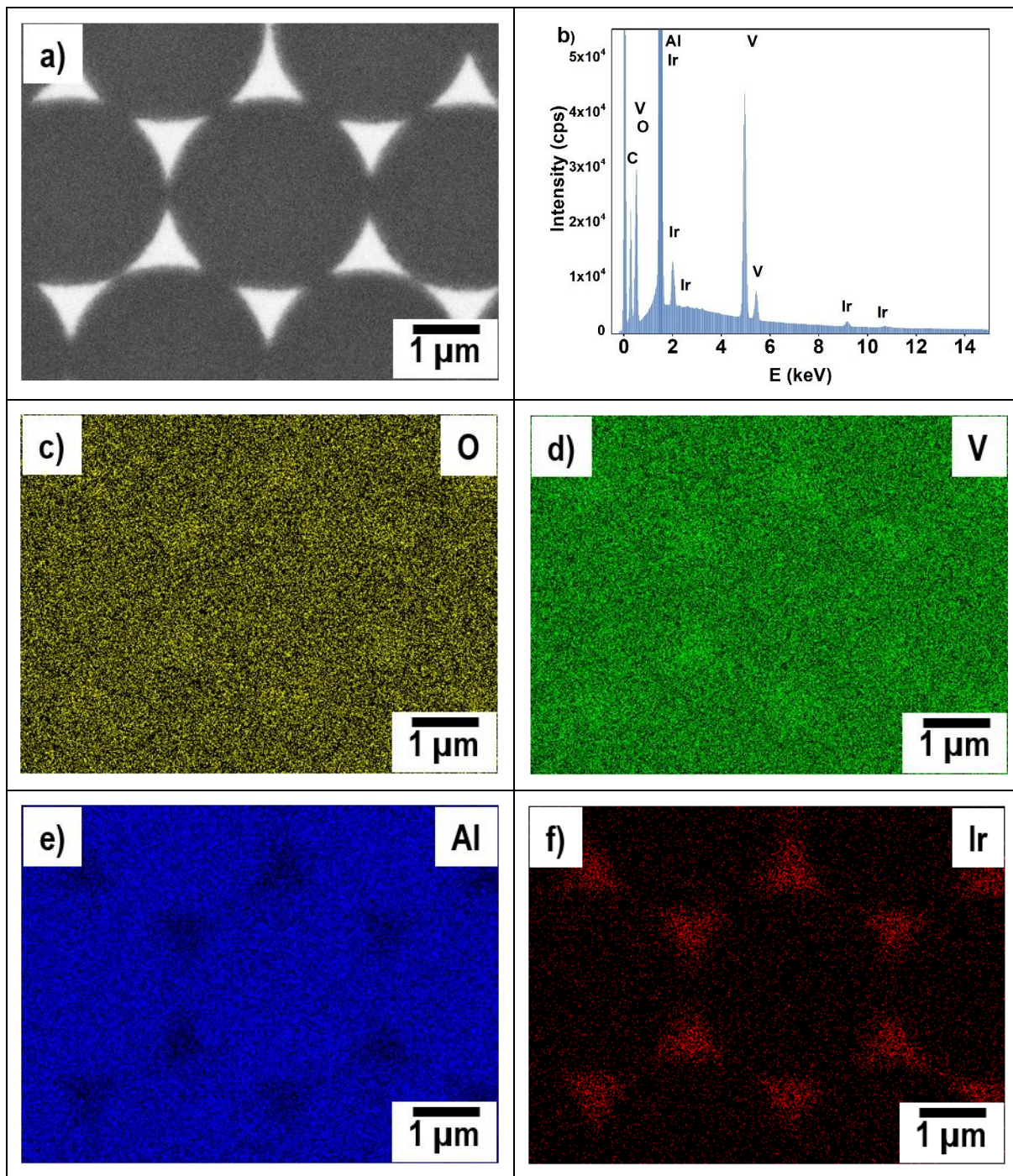


Figure V-3: Energy Dispersive X-Ray Spectroscopy results and Elemental mapping of a sample consisting of Ir nanoparticle arrays made with 3 μm polystyrene microsphere and embedded into 200 nm of VO_2 . a) SEM image of Ir nanoparticle arrays made with 3 μm polystyrene microsphere and embedded into 200 nm of VO_2 . b) EDS elemental analyses of Ir nanoparticle arrays made with 3 μm polystyrene microsphere and embedded into 200 nm of VO_2 . c) Elemental map of Oxygen. d) Elemental map of Vanadium. e) Elemental map of Aluminum. f) Elemental map of Iridium.

The EDS investigations in Figure V-3, reveal that the sample contains only the elements we have expected to be present: Ir, V, O, and Al. The SEM image from Figure V-3 a) can be correlated with the elemental maps in Figure V-3 c-e, revealing that the Ir metal is concentrated into Ir nanoparticles.

The shape of Au nanoparticle's changes during VO₂ deposition while Ir nanoparticles maintain their room temperature shape. The Au nanoparticles are influenced by solid-state dewetting while Ir nanoparticles are not (Figure V-2 vs. Figure V-3).

V.2. Influence of metallic nanoparticle arrays on Vanadium dioxide optical; transmittance, optical hysteresis, transmission contrast, and optically determined temperature of transition.

As we have presented in *Chapter I*, optical characteristics (n , k , ϵ_i , ϵ_r , etc.) that influence the optical transmission of VO₂ are dependent on the wavelength at which those properties are determined and, on the thickness of the VO₂ thin film. The optical transmission dependence on wavelength and thickness of VO₂ thin films are shown in Figure V-4.

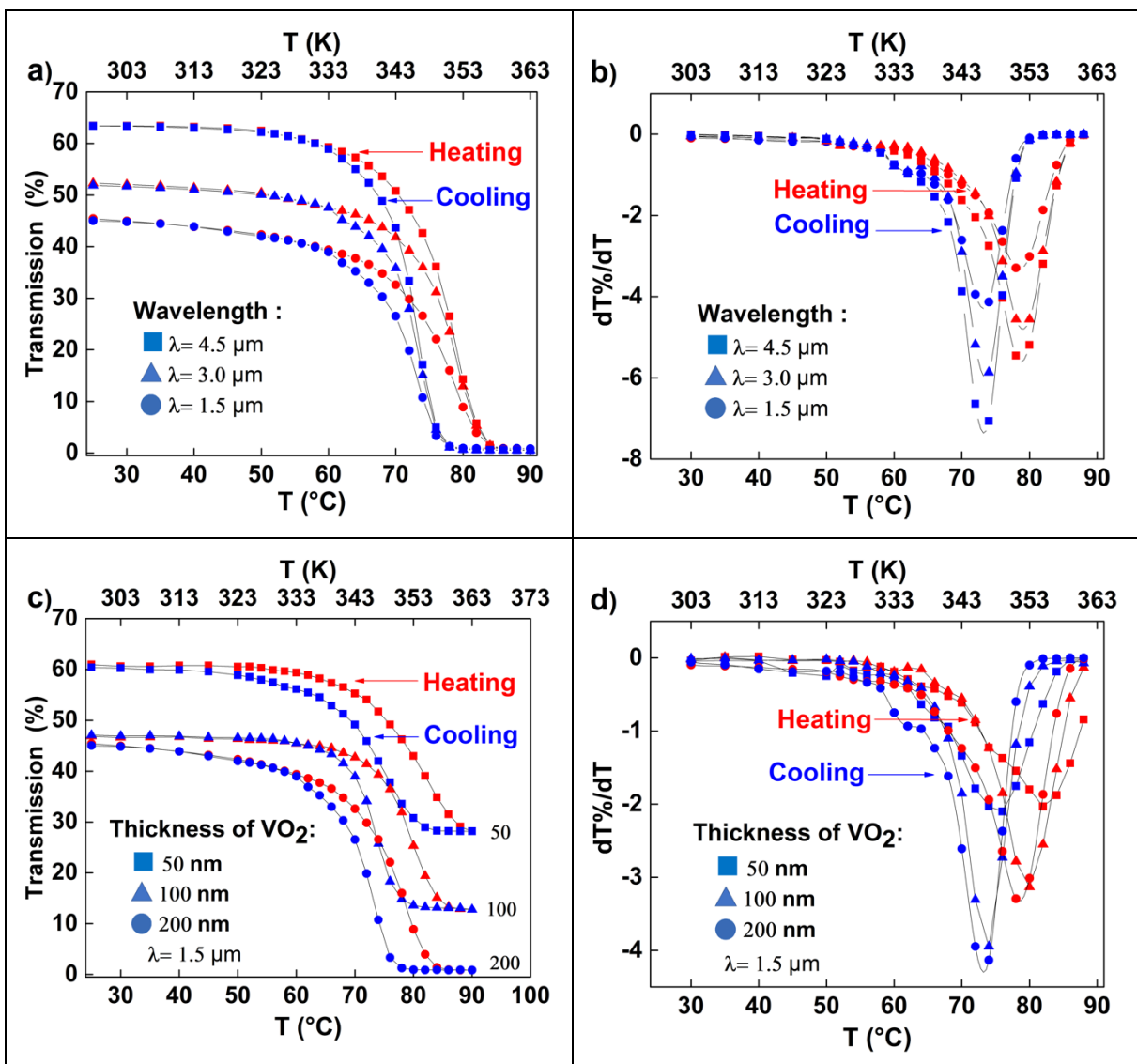


Figure V-4: Optical transmission of VO₂ deposited on the Al₂O₃-c substrate. a) Wavelength dependence of the optical transmission of a 200 nm VO₂ thin film. b) Wavelength dependence of transition temperatures for a 200 nm VO₂ thin film. c) The influence of thickness VO₂ on the optical transmission at a wavelength $\lambda = 1.5 \mu\text{m}$. d) The influence of thickness VO₂ on transition temperature (semiconductor to metal (heating) and metal to semiconductor (cooling)).

The optical transmission of a 200 nm VO₂ thin film for three wavelengths (1.5, 3, and 4.5 μm) and as a function of temperature (heating vs. cooling) is presented in Figure V-4 a). Furthermore, it is visible that as a function of wavelength, the transmission contrast (defined as $T_{VO_2 \text{ insulator}}\% - T_{VO_2 \text{ metallic}}\%$) drops from 65 % measured at 4.5 μm to 45 % at a wavelength of 1.5 μm. From optical measurements, it is possible to determine the transition temperature of VO₂, by making the derivatives of the temperature dependence of transmission for a particular wavelength. The temperature difference between the minimum of the derivatives (heating and cooling) of transmission measurements represents the transition hysteresis, which for Figure V-4 b) is 6 °C. The amplitude of the derivative is linked to the quality of the transition. The greater the difference between the value of the derivative at room temperature and the value at the transition temperature the greater the quality of the sample (see Figure V-4 a)). The influence of thinness on the transmission contrast is also present for the VO₂ thin films with metallic nanoparticles inside, Figure V-5.

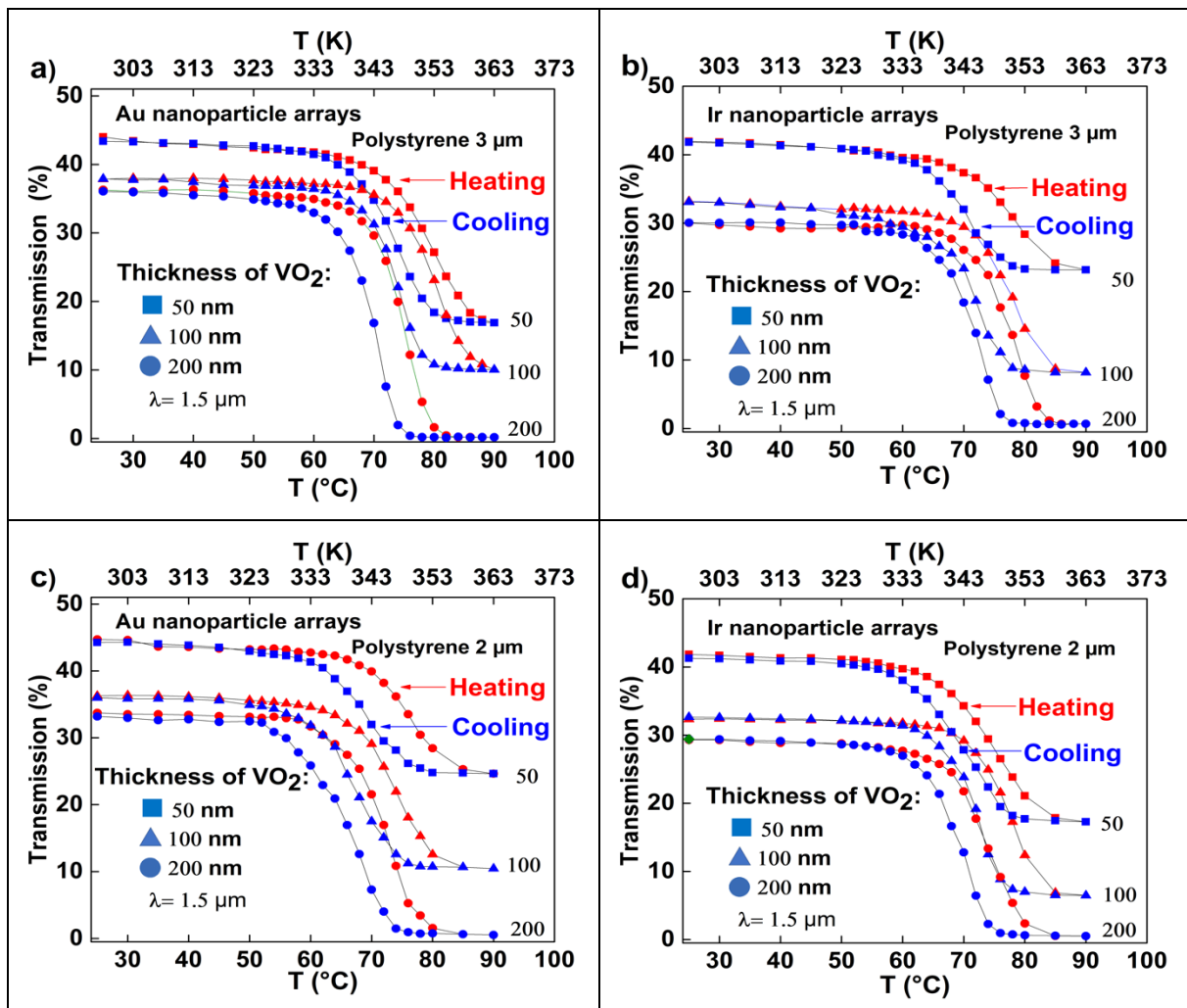


Figure V-5: Optical transmission of 50, 100, and 200 nm VO₂ with metallic nanoparticle arrays inside, measured at a wavelength of 1.5 μm, during heating up (colored in red) and cooling down (blue points), for: a) Gold arrays made with 3 μm polystyrene microsphere, b) Iridium arrays made with 3 μm polystyrene microsphere, c) Gold arrays made with 2 μm polystyrene microsphere, d) Iridium arrays made with 2 μm polystyrene microsphere. The thickness of the metallic nanoparticles is 50 nm.

The shape of the transmission curves (when heating up and cooling down) for VO₂ that contains metallic nanoparticles (Au or Ir) made with 3, or 2 μm polystyrene microsphere are similar to those of the VO₂ samples that do not contain metallic nanoparticles (Figure V-5 and Figure V-4 c). What is clear from Figure V-5 is that the transmission contrast of samples containing metallic nanoparticles is lower than that of pure VO₂ samples, for the same thickness of VO₂. The transmission contrast difference between Au and Ir samples is due to Au's dewetting during VO₂ deposition. As for the transition temperature, there are differences between the samples, differences also found for the metal from which the nanoparticles are made (Au or Ir), see Figure V-6.

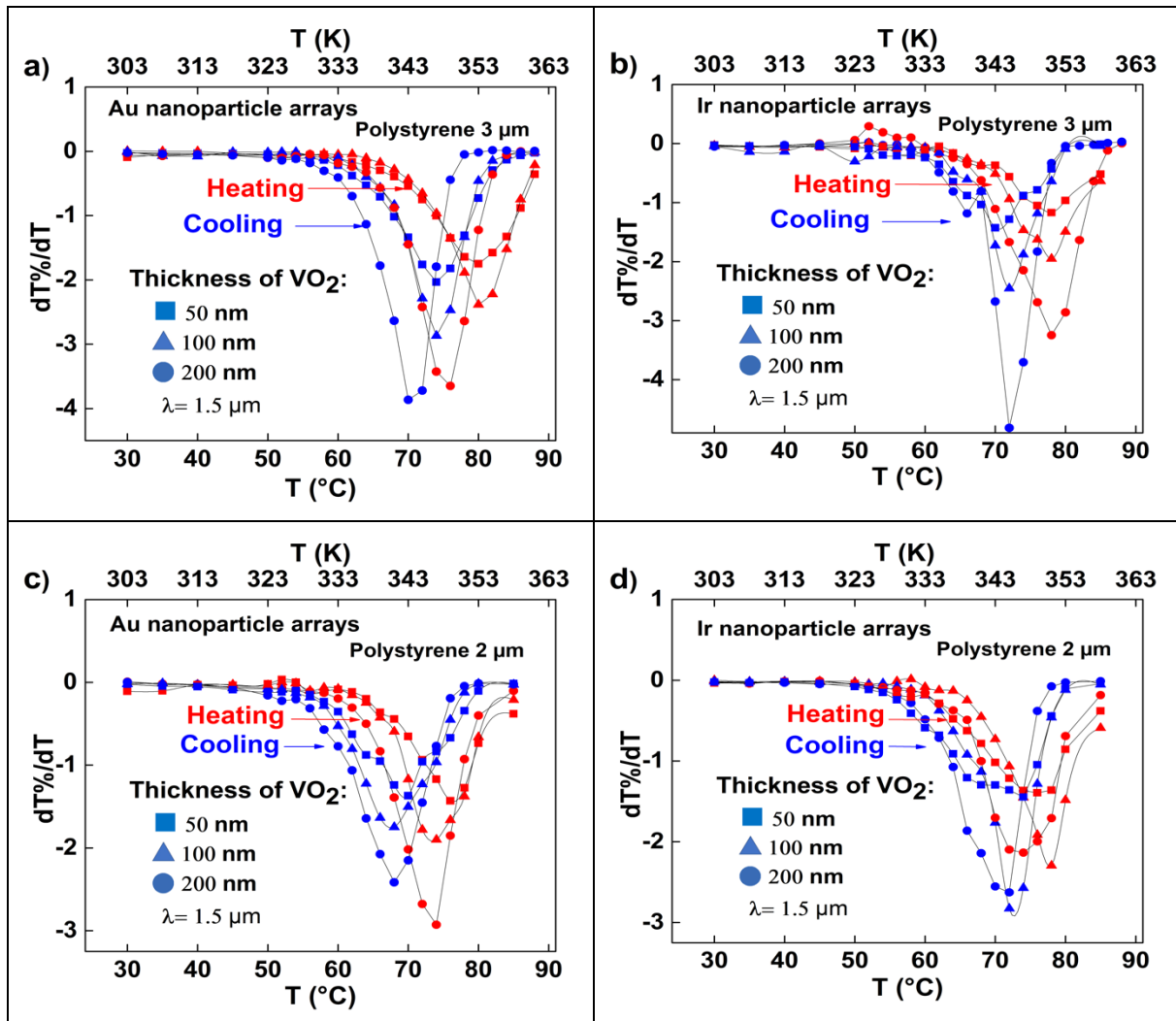


Figure V-6: Derivatives of the temperature dependence of transmission of 50, 100, and 200 nm VO₂ with metallic nanoparticle arrays inside, measured at a wavelength of 1.5 μm, during heating up (colored in red) and cooling down (blue points), for a) Gold arrays made with 3 μm polystyrene microsphere, b) Iridium arrays made with 3 μm polystyrene microsphere, c) Gold arrays made with 2 μm polystyrene microsphere, d) Iridium arrays made with 2 μm polystyrene microsphere. The thickness of the metallic nanoparticles is 50 nm.

For a 50 nm VO₂ thin film, the insulator-metal transition is at 82 °C and the metal-insulator transition is at 76 °C, while for a 200 nm VO₂ thin film, the insulator-metal transition is at 78 °C and the metal-insulator transition is at 72 °C. This is also the case for VO₂ thin films with Au nanoparticle arrays made with 3 μm polystyrene microspheres inside them (Figure V-6 a), but both transition temperatures are lower than pristine VO₂. For the 50

nm VO₂ thin film that contains Au nanoparticles, Figure V-6 a), the insulator-metal transition is at 80 °C, and the metal-insulator transition is at 74 °C, while for a 200 nm VO₂ thin film, the insulator-metal transition is at 76 °C and the metal-insulator transition is at 70 °C. Similar behavior is also present for VO₂ thin films that contain Au nanoparticles made with 2 μm polystyrene microspheres (Figure V-6 c). For the samples made with Ir nanoparticles, Figure V-6 b) and Figure V-6 d), the influence of VO₂ thickness seems to be less present, but the transition temperatures are at a lower temperature compared to a simple VO₂ thin film (with the same thickness).

Further than this, a similar dependence of the optical transmission is found for samples made with Au nanoparticle arrays that were, before VO₂ deposition, thermally treated at 532 °C. For both samples, Au nanoparticles made with 2 and 3 μm polystyrene microspheres, the transmission contrast is approximately 26 % (see Figure V-7 a), comparable to samples of the same 100 nm VO₂ thickness but made with metallic nanoparticle with no thermal treatment before VO₂ deposition (see also Figure V-5).

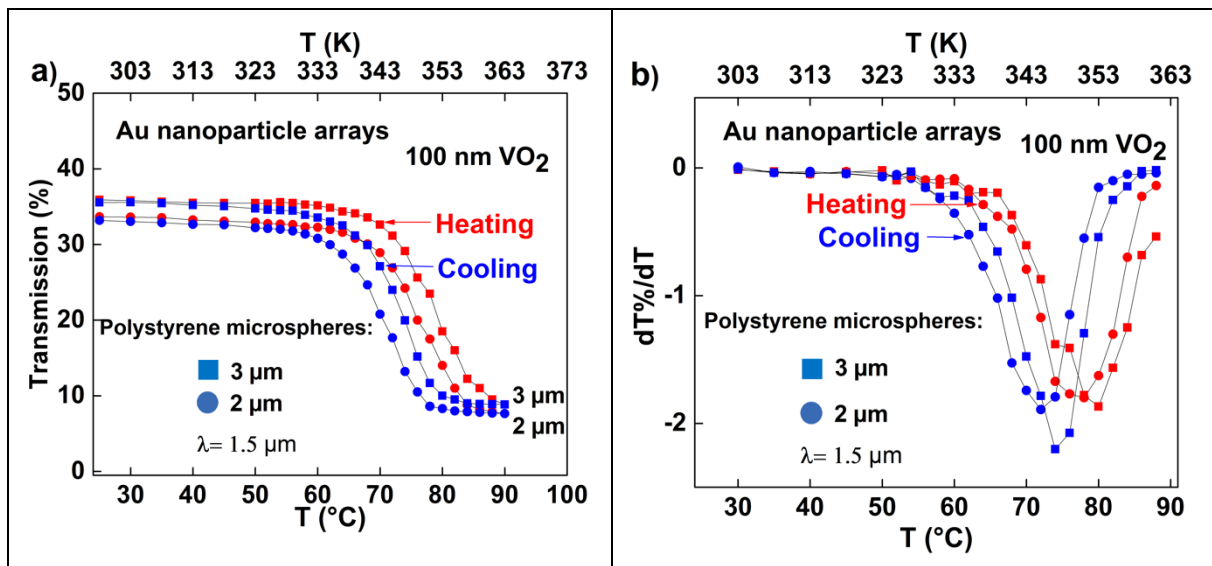


Figure V-7: a) Optical transmission of 100 nm VO₂ thin films that contain Au nanoparticle arrays made with 2 and 3 μm polystyrene microspheres and thermally treated at 532 °C before VO₂ deposition. b) Derivatives of the temperature dependence of optical transmission of 100 nm VO₂ thin films that contain Au nanoparticle arrays made with 2 and 3 μm polystyrene microspheres and thermally treated at 532 °C before VO₂ deposition.

VO₂ thin films' transition temperatures in which Au nanoparticle arrays thermally treated at 532 °C before VO₂ deposition are presented in Figure V-7 b). There is a 2°C difference between the VO₂ thin films containing Au nanoparticles made with 2 and 3 μm polystyrene microsphere (2°C higher for the Au nanoparticle made with 3 μm polystyrene microspheres) (see Figure V-7 b).

For better tracing all temperatures of transition, transition width, transmission contrast of each sample (from Figure V-4 to Figure V-7), we have summarized the data in Table V-1.

Table V-1: Influence of metallic nanoparticle array on the optical transmission contrast, the temperature of transition, and transition hysteresis width of VO₂.

	Metal nanoparticle arrays	VO ₂ thickness (nm)	Transition temperature (°C)		Transition hysteresis width (ΔT_c) (°C)	Transmission contrast (%T _{25°C} -%T _{90°C}) (%)
			T _{up}	T _{down}		
VO ₂	-	50	82	76	6	32
	-	100	80	74	6	35
	-	200	78	72	6	45
3 μ m polystyrene microspheres	Au	50	80	74	6	26
	Au	100	80	74	6	28
	Au	200	76	70	6	36
	Ir	50	78	70	8	18
	Ir	100	78	72	6	25
	Ir	200	78	72	6	30
2 μ m polystyrene microspheres	Au	50	76	70	6	20
	Au	100	74	68	6	26
	Au	200	74	68	6	34
	Ir	50	76	72	4	24
	Ir	100	78	72	6	26
	Ir	200	74	70	6	30
Au+532 °C	Au/ polystyrene 3 μ m	100	80	74	6	27
	Au /polystyrene 2 μ m	100	78	72	6	26

In Table V-1, all the data are deduced from optical transmission measurements performed at a wavelength of 1.5 μ m (by FTIR spectroscopy), with the purpose of showing that the metallic nanoparticles have a direct influence on the VO₂ thin films. It is important to emphasize that this particular wavelength was selected for two main reasons. First, in the case of VO₂ thin films containing metallic nanoparticles, the presence of a localized plasmonic resonance of the sample (at the wavelength for which we plot the transmission curves) can influence the shape of the curves. At 1.5 μ m, none of the samples have an LSPR (see Table IV-2). The second reason (also

an example of application) is that 1.5 μm is a widely used wavelength in optical communication systems, systems for which our samples can also be used [166].

The optical light transmission has the same characteristics for samples that contain metallic nanoparticles and the pristine VO_2 samples (Figure V-4 to Figure V-7). The transition's hysteresis is on average close to 6 $^\circ\text{C}$. As a general remark, the transition temperature is lower for samples that contain metallic nanoparticles (Table V-1).

The lower transition temperature in the case of VO_2 thin films containing metallic nanoparticles may be due to electron injection into VO_2 through metal nanoparticles VO_2 semiconductor junction, or due to strain development between the Au nanoparticles and VO_2 , or even oxygen vacancies and symmetry breaking at the Au- VO_2 interface.

The lower electronic work function in Au (4.8 eV) compared to in monoclinic VO_2 (5.4 eV) can induce an electron flow from Au into VO_2 , an electron flow destabilizes the semiconducting phase and decrease the transition temperature. In the Mott insulator description, the transition occurs when the insulator's electron carrier density reaches a critical value. Indeed, Xu et al. [167] observed a reduction in VO_2 thin film's critical temperature containing Au nanoparticles of 10 $^\circ\text{C}$ (10 K) for a Au to VO_2 mass proportion of 14.4%. Previously, Orlianges et al. [168] observed a reduction of transition temperature by 3.3 $^\circ\text{C}$ by embedding 10 nm Au nanoparticles into VO_2 thin films with a Au mass proportion of 10.4%.

The Au mass proportion can be estimated by taking as a reference "a hexagonal unit cell" (i.e., the unit cell of the polystyrene microsphere deposited by the Langmuir-Blodgett process) with a side length of 3 μm . For each such unit cell, there are six Au nanoparticles inside of it. The thickness of the VO_2 is assumed to be constant at 200 nm. The Au nanoparticles can cover 9.3 % of the hexagonal unit cell's surface from the polystyrene microspheres' packing. Assuming that the Au nanoparticles have no curvature, i.e., the area of the nanoparticle's side that is in contact with the substrate is equal to the area of the top of the Au nanoparticles, then the maximum Au mass proportion can reach no more than 10.09 %. This is an overestimation since Au nanoparticles have curvature. From experimental measurements (AFM), the Au mass proportion reaches $\sim 4.8 \pm 0.5$ %. The effect of the electron injection depends on the effective contact area [169].

An increase in the effective contact area between Au and VO_2 results in an enhancement of electron injection, leading to a lower transition temperature. It is reasonable for our samples to consider that the effective contact area between Au nanoparticles and VO_2 is lower than in previous studies [168] [167]. Combining the lower Au to VO_2 mass proportion together with the lower contact area, the reduction in the transition temperature, although possible, may not be linked just to electron injection. It is worth mentioning that Orlianges et al. [168] observed the reduction of transition temperature without any change of XRD peak position of VO_2 when embedding the Au nanoparticles. Strain can play a role in shifting the transition temperature [170]. The influence and presence of strain in our samples is discussed in the next section.

V.3. Influence of metallic nanoparticle arrays on Vanadium dioxide crystalline structure

V.3.1. Assessment of crystalline structure of Vanadium dioxide by XRD

To assess the crystallinity in samples the x-ray patterns of a 200 nm pristine sample of VO₂ and metallic (Au and Ir) nanoparticle arrays embedded in VO₂ are recorded and presented in Figure V-8. All the samples are made using Al₂O₃-c substrates, and the peak at $2\theta = 41.68^\circ$ corresponds to (0006) reflection of the substrate. The small peak at $2\theta \approx 65^\circ$ is associated also with the Al₂O₃-c substrate and is present in the XRD patterns due to the rotation of the samples during measurements. Here, the metal (Au and Ir) nanoparticles were deposited at room temperature by PLD, and the VO₂ is deposited on the nanoparticle arrays at 500 °C.

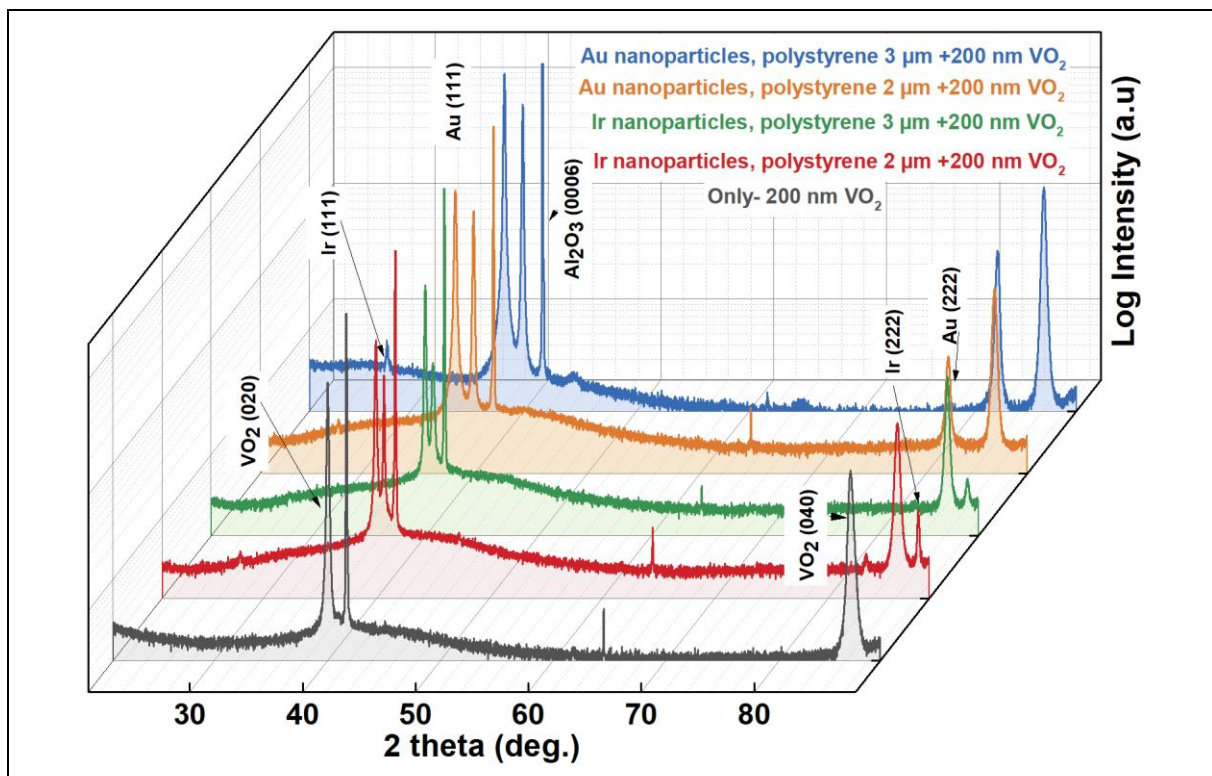


Figure V-8: The θ - 2θ XRD pattern of 200 nm VO₂ thin films, with and without metallic nanoparticles embedded. The black pattern corresponds to a pristine sample of 200 nm VO₂. The red line corresponds to the XRD pattern of Iridium nanoparticle arrays made with 2 μm polystyrene microsphere and embedded into 200 nm VO₂. The green line corresponds to the XRD pattern of Iridium nanoparticle arrays made with a 3 μm polystyrene microsphere and embedded into 200 nm VO₂. The orange line corresponds to the XRD pattern of Gold nanoparticle arrays made with 2 μm polystyrene microsphere and embedded into 200 nm VO₂. The blue line corresponds to the XRD pattern of Gold nanoparticle arrays made with 2 μm polystyrene microsphere and embedded into 200 nm VO₂.

The presence of the (111) reflection from Au at theoretical $2\theta = 38.17^\circ$ position reveals that the Au nanoparticles are crystalline, with a face-centered cubic (fcc) structure that does not change by embedding them in 200 nm of VO₂. This is true for Au nanoparticles made with 2 or 3 μm polystyrene microspheres. The Au nanoparticles are crystallized when they are made by PLD deposition (see also *Chapter III*). For the case of Ir nanoparticles, Figure V-8 confirms the presence of (111) reflection from Ir at theoretical $2\theta = 40.76^\circ$ position, proving that the Ir nanoparticles are also crystalline. The x-ray patterns in Figure V-8 show that the VO₂ is

mono-orientated, having a monoclinic structure with a (020) reflection at a theoretical $2\theta = 39.76^\circ$ position regardless or not if VO_2 has metallic nanoparticles inside. Both the metallic nanoparticles and VO_2 show a single crystallographic orientation on the theta-2theta XRD measurements from 20° up to 90° and to see the subtle differences between our samples; we will focus on a smaller 2θ interval, as is presented in Figure V-10.

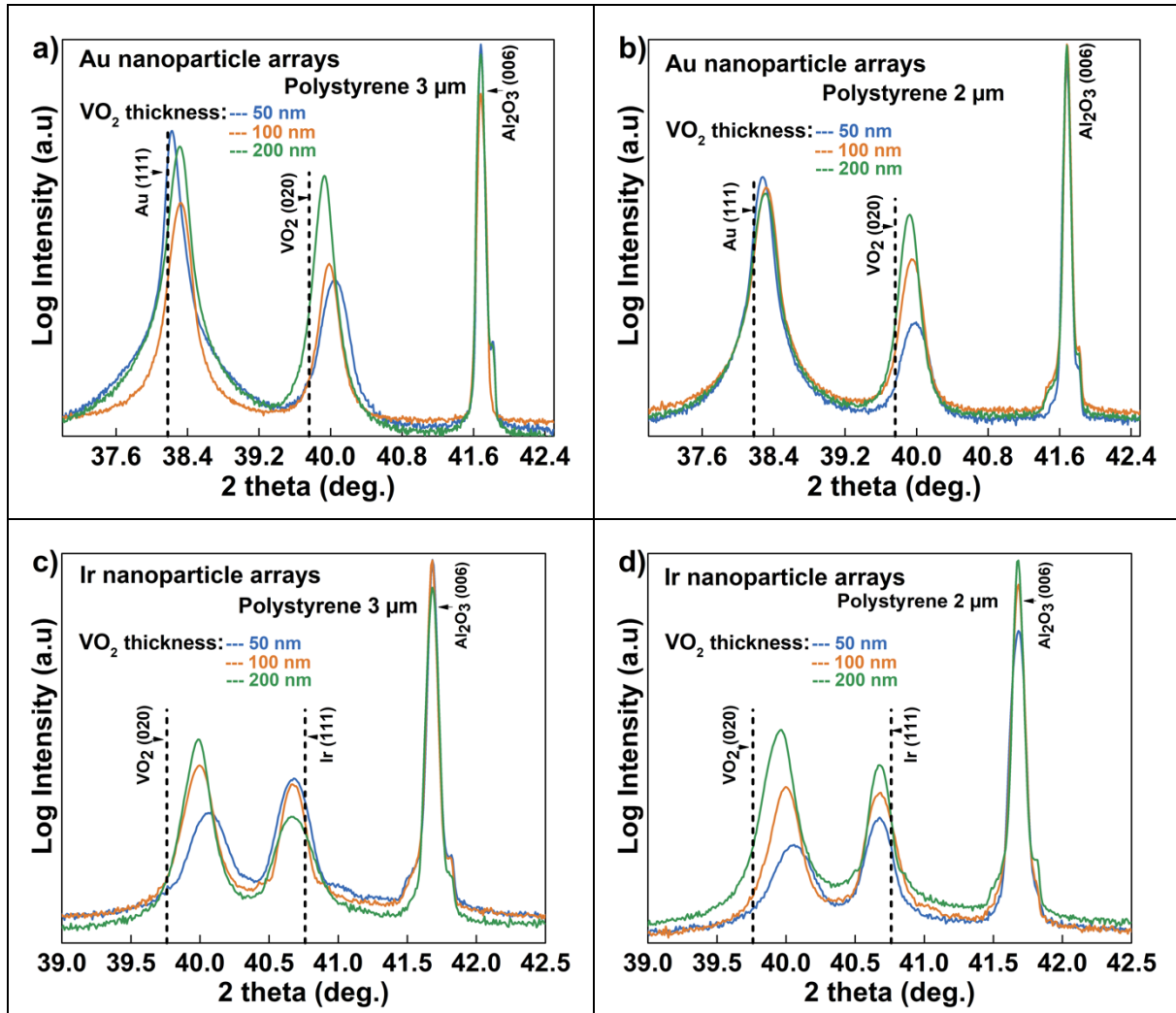


Figure V-9: The theta-2theta XRD pattern of metallic nanoparticles arrays embedded into 50, 100, and 200 nm of VO_2 , respectively. a) Au nanoparticle arrays made with $3\ \mu\text{m}$ polystyrene. b) Au nanoparticle arrays made with $2\ \mu\text{m}$ polystyrene microspheres. c) Ir nanoparticle arrays made with $3\ \mu\text{m}$ polystyrene microspheres. d) Ir nanoparticle arrays made with $2\ \mu\text{m}$ polystyrene microspheres. The thickness of the metallic nanoparticles is 50 nm. The dotted vertical lines correspond to the theoretical 2θ position of strain-free, Au, Ir, and VO_2 .

The XRD patterns of 50 nm metallic (Au and Ir) nanoparticle arrays, made with 2 or $3\ \mu\text{m}$ polystyrene microspheres and embedded into 50, 100, and 200 nm of VO_2 are given in Figure V-9. The 2θ interval that we selected for presenting the structural interaction between Au nanoparticles and VO_2 is $37^\circ - 42.5^\circ$, while for Ir nanoparticles and VO_2 , the interval is $39^\circ - 42.5^\circ$. This peak position of the Al_2O_3 -c substrate is set to the theoretical one and allows us to see the exact differences between samples and not the differences due to experimental measurements. It is visible that the metallic nanoparticles' 2θ peak position and as well the 2θ position of the (020) VO_2 differ from the theoretical one (the black dotted vertical lines in Figure V-9). The peaks Au and VO_2

are shifted to a higher 2theta position than the theoretical one indicated the presence of compression in the a parameter of Au unit cell and b parameter of VO_2 unit cell. While for Ir the shift is to a higher 2theta value, showing and enlargement of a . The value of the shift in the 2theta position is dependent on the thickness of the VO_2 . This 2theta thickness dependent shift is also present for VO_2 pristine (see Figure V-10 a).

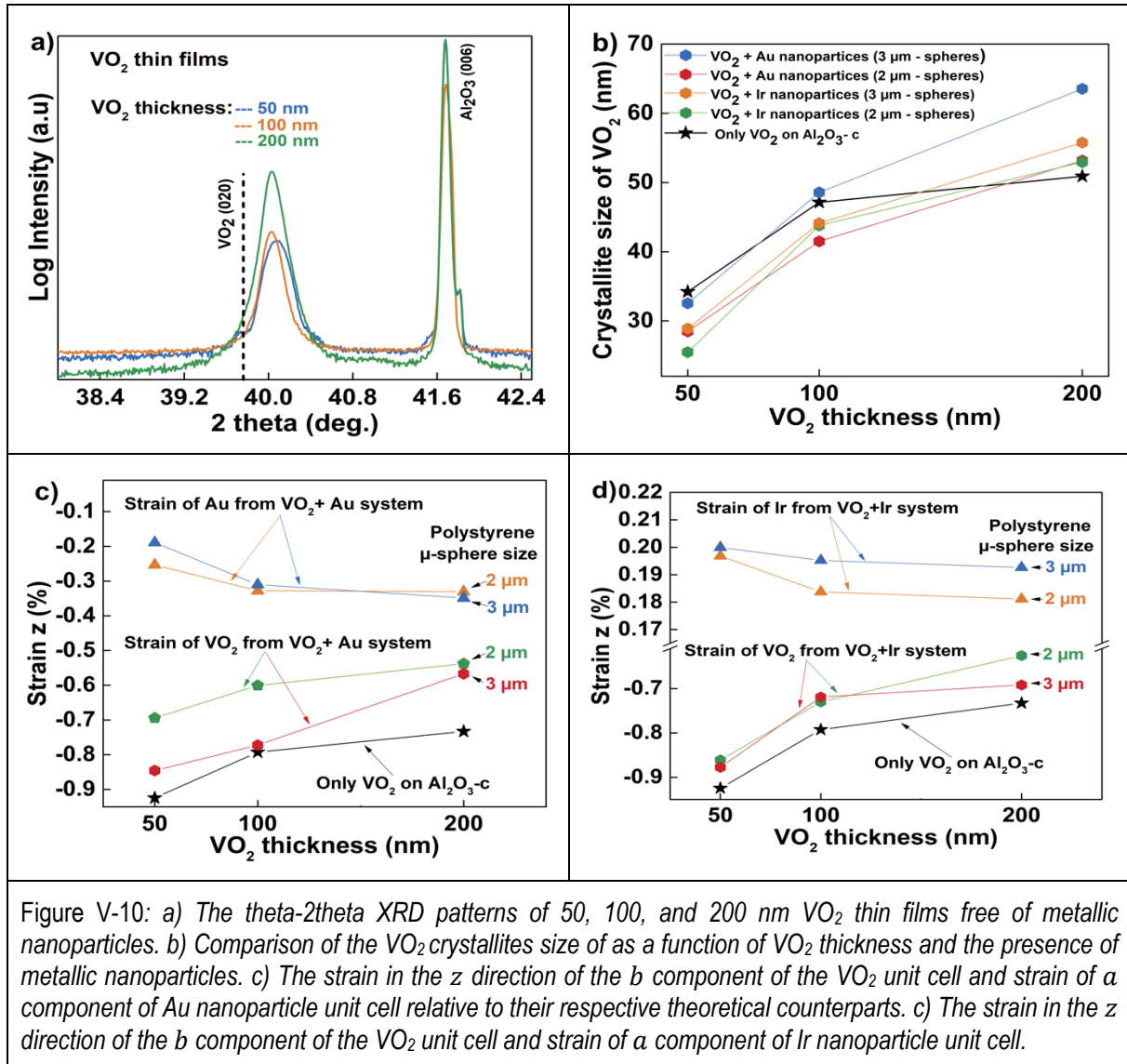


Figure V-10: a) The theta-2theta XRD patterns of 50, 100, and 200 nm VO_2 thin films free of metallic nanoparticles. b) Comparison of the VO_2 crystallites size of as a function of VO_2 thickness and the presence of metallic nanoparticles. c) The strain in the z direction of the b component of the VO_2 unit cell and strain of a component of Au nanoparticle unit cell relative to their respective theoretical counterparts. c) The strain in the z direction of the b component of the VO_2 unit cell and strain of a component of Ir nanoparticle unit cell.

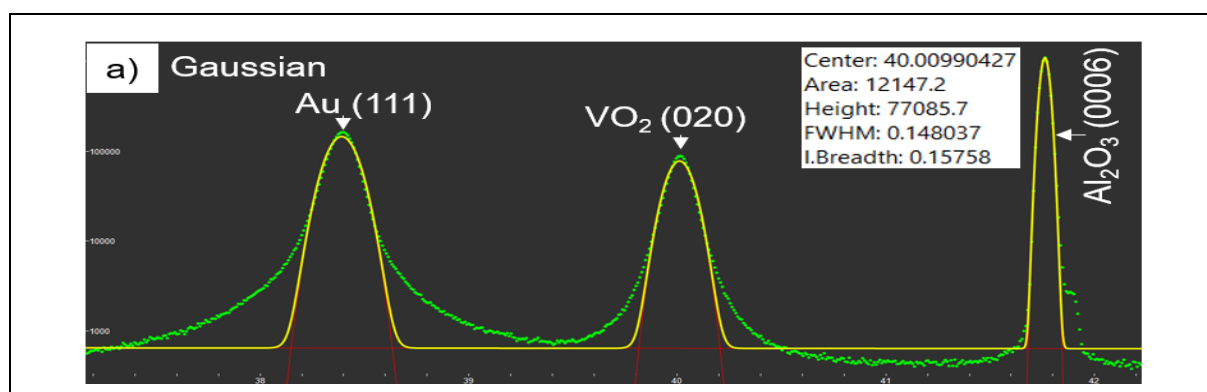
The thinner the VO_2 is, the higher the corresponding 2theta position of the (020) reflection is (Figure V-10 a). This is to be expected since there is a thermal expansion mismatch between VO_2 and Al_2O_3 -c substrate [171]. The thickness of the metallic nanoparticles is 50 nm for all the samples; therefore, the change in their 2theta peak position originates from the influence of VO_2 . An increase in VO_2 thickness shifts the Au peak position to a higher value and Ir to a lower value. From the XRD data, we were able to calculate the crystallite size of VO_2 thin films as a function of (VO_2) thickness and the relation between the size of the VO_2 crystallites with the presence of metallic nanoparticles. We deduced also the strain (%) in the b component of the VO_2 unit cell and strain of a metallic nanoparticle unit cell component compared to their respective theoretical equivalents. The VO_2 crystallite size and the strain calculations are presented in Figure V-10 b-d. When the VO_2 pristine has a thickness equal to 50 nm, the

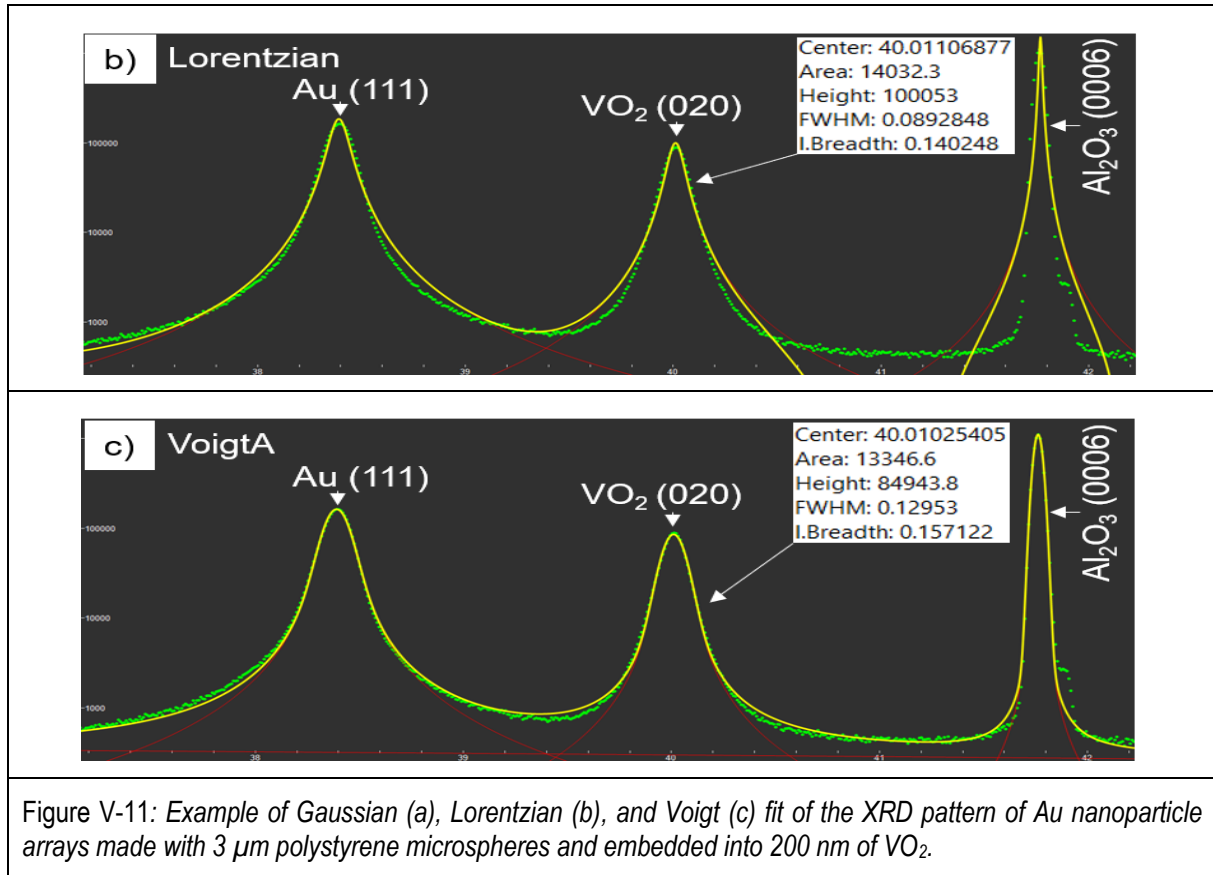
crystallites' size is around 35 nm. If the VO₂ thickness increases to 200 nm, then the crystallite size also increases to 50 nm. As is visible in Figure V-10 d), for a VO₂ thickness of 50 nm, the crystallites' size is smaller when VO₂ contains metallic nanoparticles (28 nm for Ir and 32 for Au). When the thickness of VO₂ is 200 nm, the opposite happens, and the crystallite size of VO₂ containing metallic nanoparticles is higher (56 nm for Ir nanoparticle and 64 nm for Au nanoparticle). As presented in Figure V-10 c-d, the strain of the *b* parameter of VO₂ unit cell reaches almost 1% when the pristine VO₂. The VO₂ containing metallic nanoparticles has a lower value of strain than pristine VO₂. When Au and Ir are inside VO₂, the VO₂ matrix compresses the Au and Ir nanoparticles in the out-of-plane direction. The value of metallic nanoparticle compression is dependent on the VO₂ thickness (the thicker the VO₂, the higher the compression). In VO₂, the strain alters the orbital occupancy near the Fermi energy level E_F. The higher compressive strain along the out-of-plane direction of the VO₂ thin films pristine makes the d_{||} and π* orbitals to shift upward and the d*_{||} orbital downward in rapport to the VO₂ thin films containing metallic nanoparticles [170] (see also *Chapter I*). Consequently, the higher out-of-plane compressive strain along the *b* direction in the VO₂ thin films pristine increases the size of the band-gap of the insulator state, leading to a higher energy barrier and a higher transition temperature. The strain explains the higher transition temperature of VO₂ thin films pristine found from optical transmission measurements in Table I-1. In general, there is a small confusion in thin films on how to extract the crystallite size and strain from theta-2theta XRD measurements. In light of this, we will briefly present the actual procedure that we employed to extract the information displayed in Figure V-10 b-d.

The crystallite size can be determined by using the Williamson–Hall method, Scherrer's formula, or Stokes and Wilson formula [172]–[175]. For the Williamson–Hall method, we need at least 3 diffraction peaks for each material, not our case (see Figure V-8) [173]. The Scherrer's formula can be expressed as:

$$D = \frac{k\lambda}{\beta(\cos\theta)} \quad \text{Equation (5.1)}$$

,here *D* is the size of the crystallites, *k* = 0.9, λ = 1.504 Å and β is the integral Breadth [176]. The integral Breadth β is the width of a rectangle with the same height as the peak area. In Scherrer's formula, β is deduced by using a Gaussian fit of the experimental data. However, as presented in Figure V-11 a), a Gaussian fit and or a Lorentzian fit (Figure V-11b) is not perfectly adapted for our experimental data. The experimental data's best fit is obtained when using a Voigt function, which is a convolution of a Lorentzian and Gaussian line shapes, Figure V-11c).





In Scherrer's formula, the k parameter is linked to the function used in fitting the data and is equal to 0.9 for a Gaussian fit, 0.64 for a Lorentzian fit. However, when using a Voigt fit, we must use the Stokes and Wilson formula [177]:

$$D = \lambda/\beta(\cos\theta) \quad \text{Equation (5.2)}$$

We include the instrumental influence on the crystallite size by expressing β [173] as:

$$\beta = \sqrt{(\beta_{VO_2}^2 - \beta_{Al_2O_3}^2)} \quad \text{Equation (5.3)}$$

, and we fix the substrate peak position to the theoretical one. Using Stokes and Wilson formula, we have extracted the data presented in Figure V-10 b).

The strain of Au nanoparticles, Figure V-10 c-d, is expressed as:

$$\text{Strain } z \text{ (\%)} = \frac{a_{exp} - a_{theoretic}}{a_{theoretic}} \quad \text{Equation (5.4)}$$

Equation (5.4) is also used for determining the strain in Ir and VO₂. The a_{exp} of Au and Ir nanoparticles and the b_{exp} of VO₂ are extracted through the planar spacing d_{hkl} using Bragg law ($2 d_{hkl} \sin\theta = n\lambda$), for Au and Ir $d_{1411} = a \sqrt{3}$ and for VO₂ $d_{020} = \frac{b}{2}$ [178].

V.3.2. HR-XRD on Au nanoparticle arrays embedded VO₂, assessing the structural quality of Au nanoparticles and VO₂.

The HR-XRD measurement results obtained on Au nanoparticle arrays embedded into different samples of different VO₂ thicknesses are given in Figure V-12.

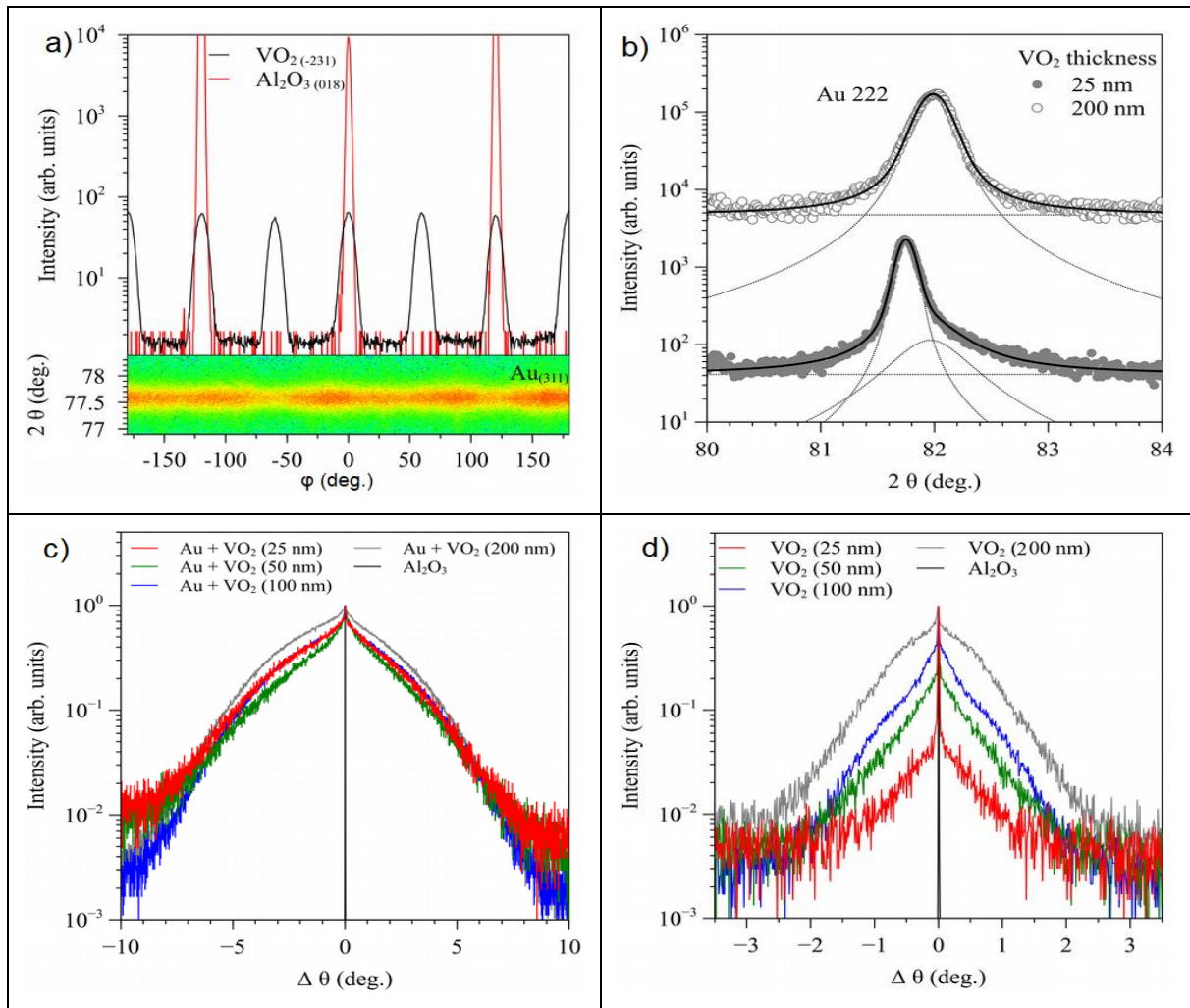


Figure V-12: HR-XRD measurement performed on Au nanoparticle arrays embedded into different samples of different VO₂ thicknesses. a) ϕ -scan recorded from the (220) planes of VO₂, the red lines indicate the positions of the (104) peaks of the Al₂O₃-c substrate, the thickness of VO₂ is 200 nm. b) The theta-2 theta scan of Au nanoparticles embedded into 25 and 200 nm of VO₂, respectively. c) ω -theta measurements showing the rocking curves of Au nanoparticles for different VO₂ thicknesses. d) ω -theta measurements showing the rocking curves VO₂ as a function of VO₂ thickness.

Figure V-12 a) reveals a six-fold symmetry instead of the two-fold symmetry expected for the (220) planes, that is due to the existence of three structurally equivalent orientations of the (010) planes with respect to the (001) plane of Al₂O₃-c substrate, inducing three in-plane epitaxial variants [178].

The corresponding epitaxial relations between VO₂ and the Al₂O₃-c substrate are: (010)_{VO₂} \parallel (001)_{Al₂O₃}; [100]_{VO₂} \parallel [210]_{Al₂O₃}, [100]_{VO₂} \parallel [-110]_{Al₂O₃} and [100]_{VO₂} \parallel [120]_{Al₂O₃}. On the other

hand, Figure 4.12 a confirms that the Au nanoparticles are not epitaxial; they have a (111) preferred orientation (with rocking curve width of roughly $\sim 6^\circ$), but there is no in-plane orientation.

A higher thickness of VO₂ shifts the 2theta peak position of Au nanoparticles towards large angles, indicating the development of compressive strain into Au (Figure V-12 b). Conversely, the (020) peak of VO₂ is shifted towards smaller angles indicating the reduction of compressive strain, i.e., the thermal strain is relaxed with increasing thickness.

The XRD data show an asymmetry in the (222) Au peak. This hints towards the possibility that Au nanoparticles may experience different levels of strain, with the higher one most likely concentrated at the interface between Au-VO₂-Al₂O₃-c substrate and a lower level of strain induced directly by VO₂. Besides strain, the nanoparticles are all equivalent, whatever the thickness of VO₂ is, 25 nm or 200 nm (Figure V-12 c).

Concerning VO₂ structural quality, the evolution of the rocking curve in Figure V-12 d) is well explained by the increasing thickness, which results in higher diffuse scattering intensity.

The VO₂ has the same structure and experiences nearly the same level of strain relaxation when Au or Ir nanoparticles are present in VO₂. Therefore, we expect that the result obtained for Au by HR-XRD to be fully applicable for Ir nanoparticles' case.

V.3.3. Temperature induced structural transition of VO₂ containing metallic (Au or Ir) nanoparticles revealed by HR-XRD measurements.

Temperature induced structural transition of VO₂ containing metallic (Au or Ir) nanoparticles is studied by HR-XRD. When VO₂ is heated up, the insulator to metal transition is accompanied by a structural transition from the monoclinic (M₁) structure to the rutile (R) structure (for more details, see Chapter I).

There is a debate on which transition comes first, the metal to insulator/insulator to metal transition (i.e., the electronic transition) or the structural transition.

The precision with which we control the temperature is approximately 2°C for the Peltier plate in the optical transmission measurements and close to 2°C for the heater in HR-XRD.

The structure evolution of HR-XRD diagrams of 200 nm VO₂ containing Au or Ir nanoparticles made with 3 μm polystyrene microspheres, during heating up from a temperature close to room temperature up to 100 °C is presented in Figure V-13.

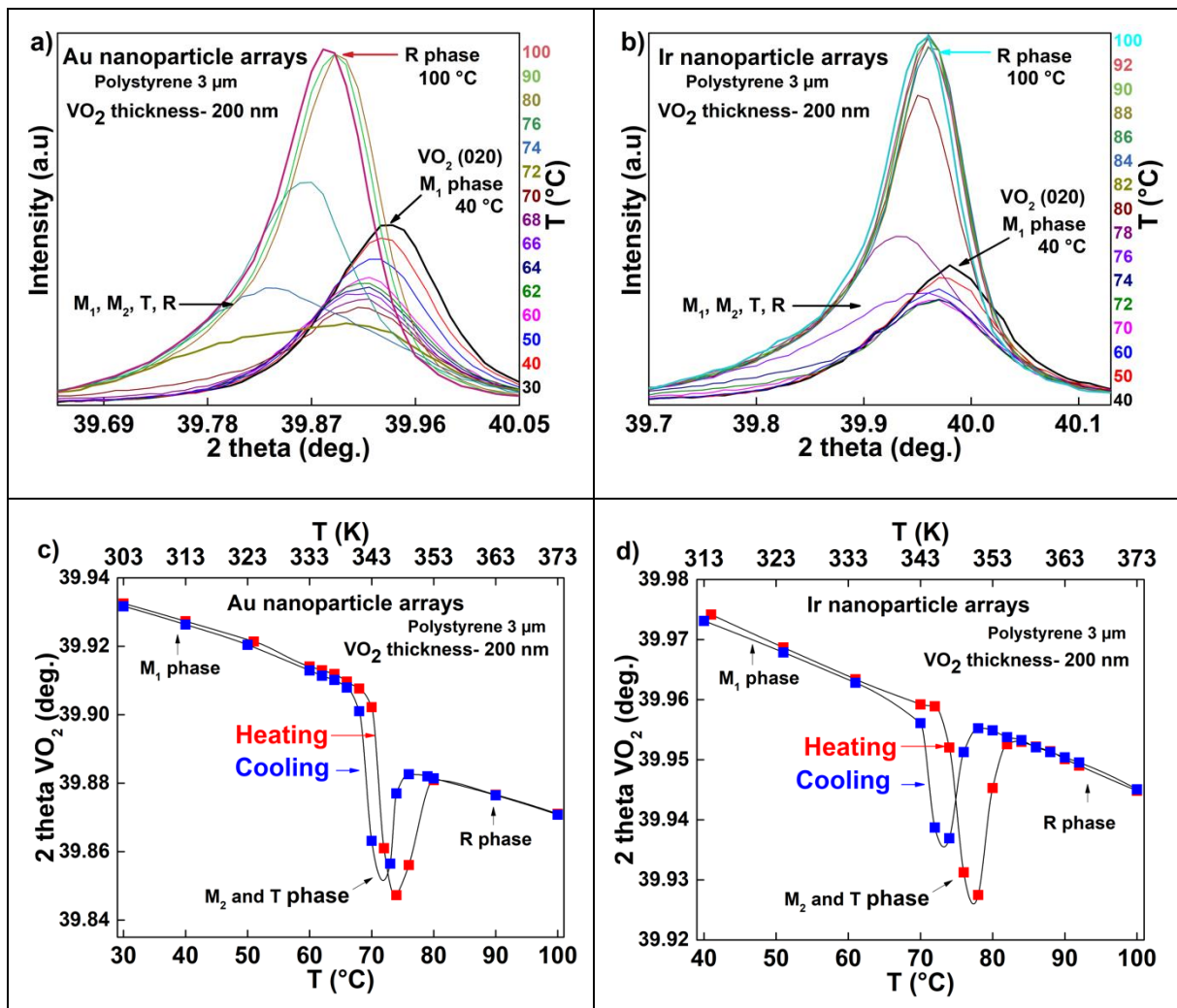


Figure V-13: HR-XRD temperature θ - 2θ measurement performed during heating up of 200 nm VO₂ containing Au nanoparticle arrays (a) and Ir nanoparticle arrays (b). c) 2θ temperature evolution, heating up and cooling down, of 200 nm VO₂ containing Au nanoparticle arrays. d) 2θ temperature evolution, heating up and cooling down, of 200 nm VO₂ containing Ir nanoparticle arrays. The metallic nanoparticles have a 50 nm thickness and are made using 3 μ m polystyrene microspheres.

At room temperature in both VO₂ containing Au and Ir has a monoclinic structure (M₁), with a small asymmetry of the peaks (Figure V-13). This asymmetry may be due to different levels of strain in monoclinic structure, or our samples may contain small traces of VO₂ with a triclinic structure. The triclinic structure is associated with high levels of strain and has an XRD peak almost indistinguishable from that of the M₁ structure. As the temperature goes up, the samples' structure starts to change, and the peak starts shift to lower 2θ values. The 2θ shift is due to a combination of thermal dilatation of the M₁ structure and the apparition of M₂, born from the M₁ structure and T. When the R structure appears, the VO₂ starts moving back to higher 2θ values. Since these measurements are difficult to distinguish between each intermediate phase's position and percentage, we have assigned a global Voigt function to each measurement and deduced a global 2θ position for a given temperature. In the initial stages of the heating process, the 2θ position of VO₂ shifts linearly towards lower values suggesting that the shift is most likely due to the thermal expansion of the M₁ phase. Then at 68 °C for Au nanoparticles and 72 °C for Ir nanoparticles, the peak moves rapidly to a lower 2θ value, indicating the presence

of intermediate M_2 phase. The peaks' rapid evolution stops at 80 °C for Au nanoparticles and at 84 °C for Ir nanoparticles. After this temperature, the peak moves, again, linearly to lower 2θ values showing that now the VO_2 is in the R phase, and the peak shifts on the bases of thermal expansion. During cooling down, the peak returns to the original position. As was the case of optical transmission measurements, the structural transition also has a hysteresis, with a width of 2 °C for Au nanoparticles and 4 °C for Ir. Note that the hysteresis's value may be affected by experiential conditions. However, our samples also have structural hysteresis.

The intensity of the VO_2 peak also evolves with temperature (Figure V-13). The peak intensity evolution with the temperature of metallic nanoparticles and VO_2 are presented in Figure V-14.

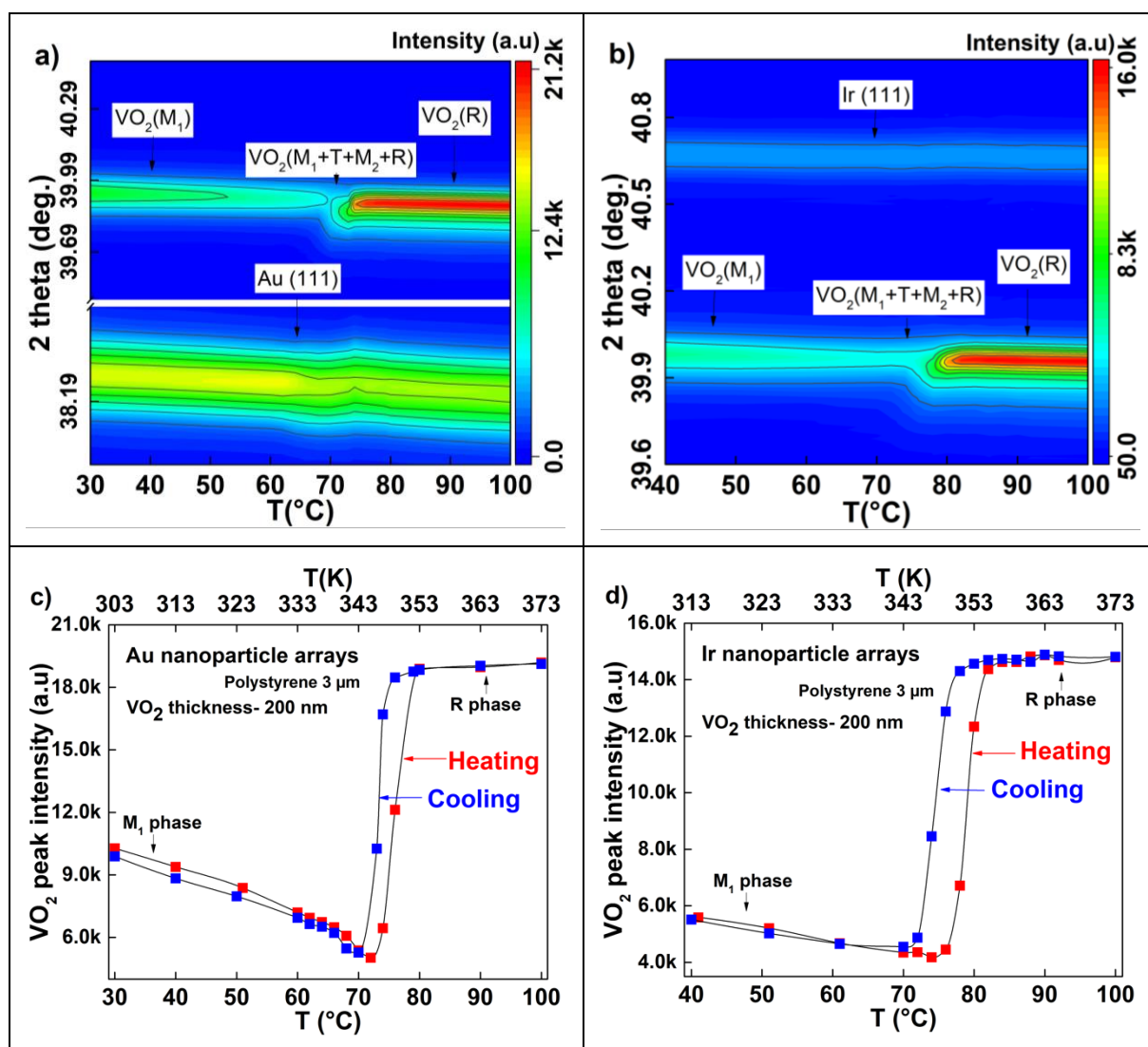


Figure V-14: HR-XRD temperature θ - 2θ measurements used for peak intensity assessment and performed during heating up of 200 nm VO_2 containing Au nanoparticle arrays (a) and Ir nanoparticle arrays (b). c) Peak intensity evolution of VO_2 containing Au nanoparticle arrays, extracted using a Voigt fit of the experimental data. d) Peak intensity evolution of VO_2 containing Au nanoparticle arrays, extracted using a Voigt fit of the experimental data.

The 2D representation of the peak intensity of the Au- VO_2 (Figure V-14 a) and Ir- VO_2 (Figure V-14 b) shows that the intensity of Au and Ir remains constant during the VO_2 structural transition. During the structural

transition, the VO_2 peak intensity changes (see Figure V-14 c-d). In XRD, the diffracted beam's intensity in a given direction is proportional to the modulus of the square of geometrical structure factor $F(hkl)$, which is connected to the occupancy of atoms in different Wyckoff positions of a unit cell [179]. Multiple factors influence the intensity, such as thermal vibration of atoms in the lattice point, polarization, multiplicity factor, Lorentz factor, and absorption factor [179], [180]. Therefore, the intensity of a diffracted beam depends on both the crystalline nature and the occupancy of the individual Wyckoff position in a crystal [179]. For our case, the crystalline nature does not change during heating up from room temperature to 100°C , so that the number of planes orientated in a particular direction can increase and induce an increase in peak intensity. When the required number of atoms occupies all the Wyckoff positions in a crystal, the structure factor will give a different value, that in our case, for the transition from monoclinic to rutile structure leads to high intensity of the VO_2 peak. During HR-XRD, the metallic nanoparticles act as probes and can give information's about the crystallographic structure of VO_2 (work in progress)

V.4. Raman spectroscopy measurements were performed on VO_2 thin films and VO_2 thin films with embedded metallic nanoparticle arrays.

V.4.1. Raman spectroscopy point measurements.

Raman spectroscopy point measurements made on pristine VO_2 and VO_2 with inclusion of metallic (Au or Ir) nanoparticle arrays are presented in Figure V-15.

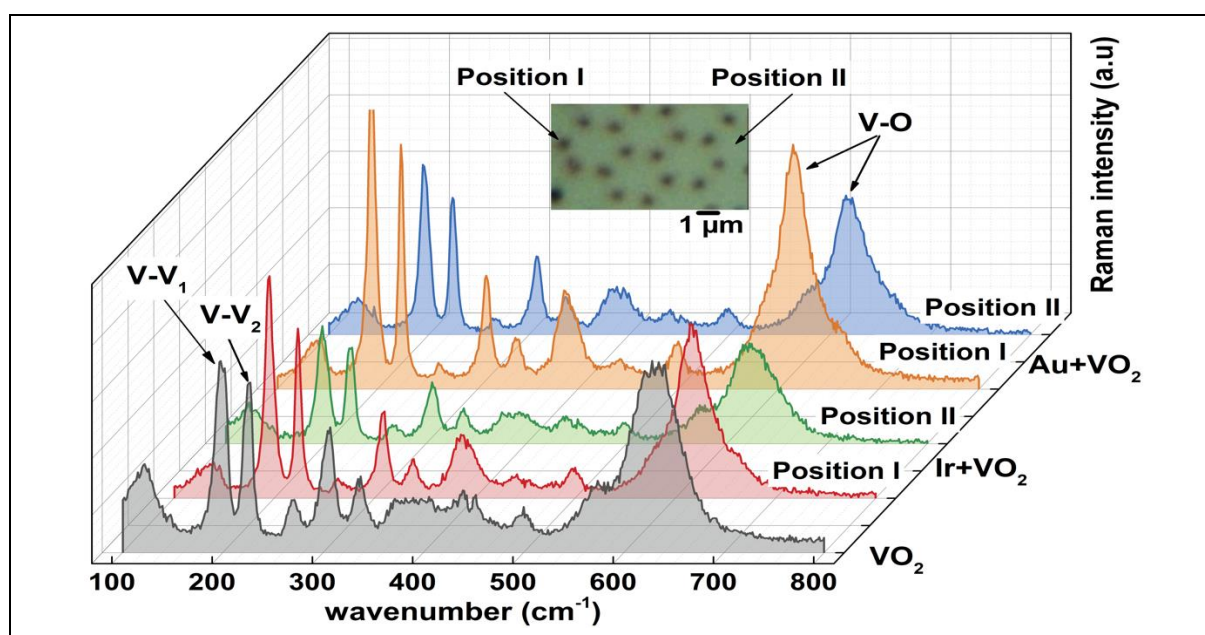


Figure V-15: Raman spectra of a 200 nm VO_2 thin film (the black line), Raman spectra of a 200 nm VO_2 containing metallic nanoparticle arrays made with $3\ \mu\text{m}$ polystyrene microspheres; the red and green lines are for VO_2 with Ir nanoparticle inside, the orange and blue lines are for VO_2 with Au nanoparticle inside. "Position I" represents the Raman measurement made directly on top of the nanoparticles, while "Position II" corresponds to Raman measurements made in the free space between the metallic nanoparticles.

For the Raman measurements, the laser spot has a diameter of $1\ \mu\text{m}^2$, the laser wavelength is $532\ \text{nm}$, and the power is $0.4\ \text{mW}$. In Figure V-15, the acquisition time is 300 seconds for each Raman spectra. For the case

of samples that contain metallic nanoparticle arrays, we have measured two positions on the same sample. Position “I” represents the Raman measurements made on the VO₂ that is directly on top of the metallic nanoparticle arrays, and Position “II” is associated with the measurements made in the free VO₂ space between the metallic nanoparticles. It is interesting that in Figure V-15, the Raman spectra for the samples that contain metallic nanoparticle arrays are position dependent. The Raman spectra acquired from Position “II” are similar to the Raman spectra taken from pristine VO₂ samples. The main difference between the Raman spectra measured from Position “I” and “II” seems to be the presence of a shoulder (or an additional peak) at 575 cm⁻¹. To understand this difference in greater detail, we have performed Raman measurements in temperature for both the sample of pristine VO₂ and on the samples of VO₂ containing metallic nanoparticles. The results of Raman measurements in temperature are presented in Figure V-16.

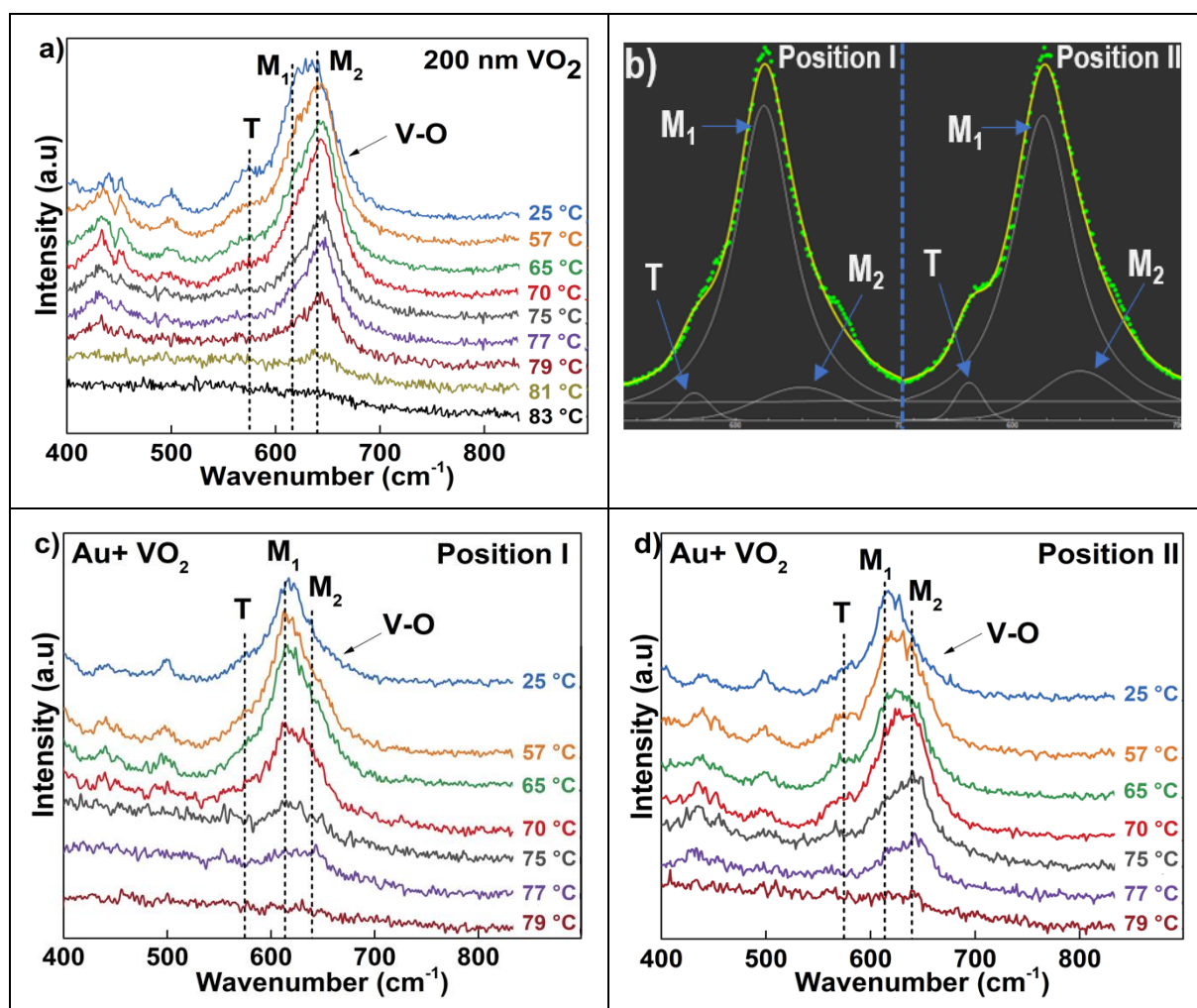


Figure V-16: The evolution of Raman spectra as a function of temperature. a) Temperature dependence of Raman spectra of 200 nm VO₂ thin films. b) Example of a fit used to extract the VO₂ phases from Raman measurements. c) Temperature dependence of Raman spectra from Position “I” of 200 nm of VO₂ containing Au nanoparticle arrays. d) Temperature dependence of Raman spectra from Position “II” of 200 nm of VO₂ containing Au nanoparticle arrays. The Raman data are acquired during heating up.

A fit of the Raman bands using a mix of Lorentz and Gaussian functions (Figure V-16 b) is used to identify and assign the Raman modes to their corresponding VO₂ phases. Special attention is paid to the V—O vibrations

to identify the VO₂ phases present in our sample by assigning the vibration at 575 cm⁻¹, 614 cm⁻¹, and 640 cm⁻¹ respectively for VO₂ (T, M₁, M₂) (Figure V-16) [181]–[183], [184, p. 2], [185]. The monoclinic M₁ and M₂ have a set of strong well-resolved bands, whereas T demonstrates similar spectral features. This is explained by the similarity of their crystal structures, all representing distorted rutile. In Figure V-15, the M₁ structure, the vibration at 197 cm⁻¹ corresponds to vanadium atoms' motion along the c-axis of the VO₂ crystal (stretching motion of V–V dimers). The mode at 220 cm⁻¹ of M₁ is associated with the perpendicular motion of metal ions (V–V dimers' tilting motion). Raman scattering in rutile (R) consists of weak and broad lines associated only with the motion of oxygen atoms [181]. We deduced the intensity of the VO₂ phases from the mix function fit as a function of temperature (see Figure V-17).

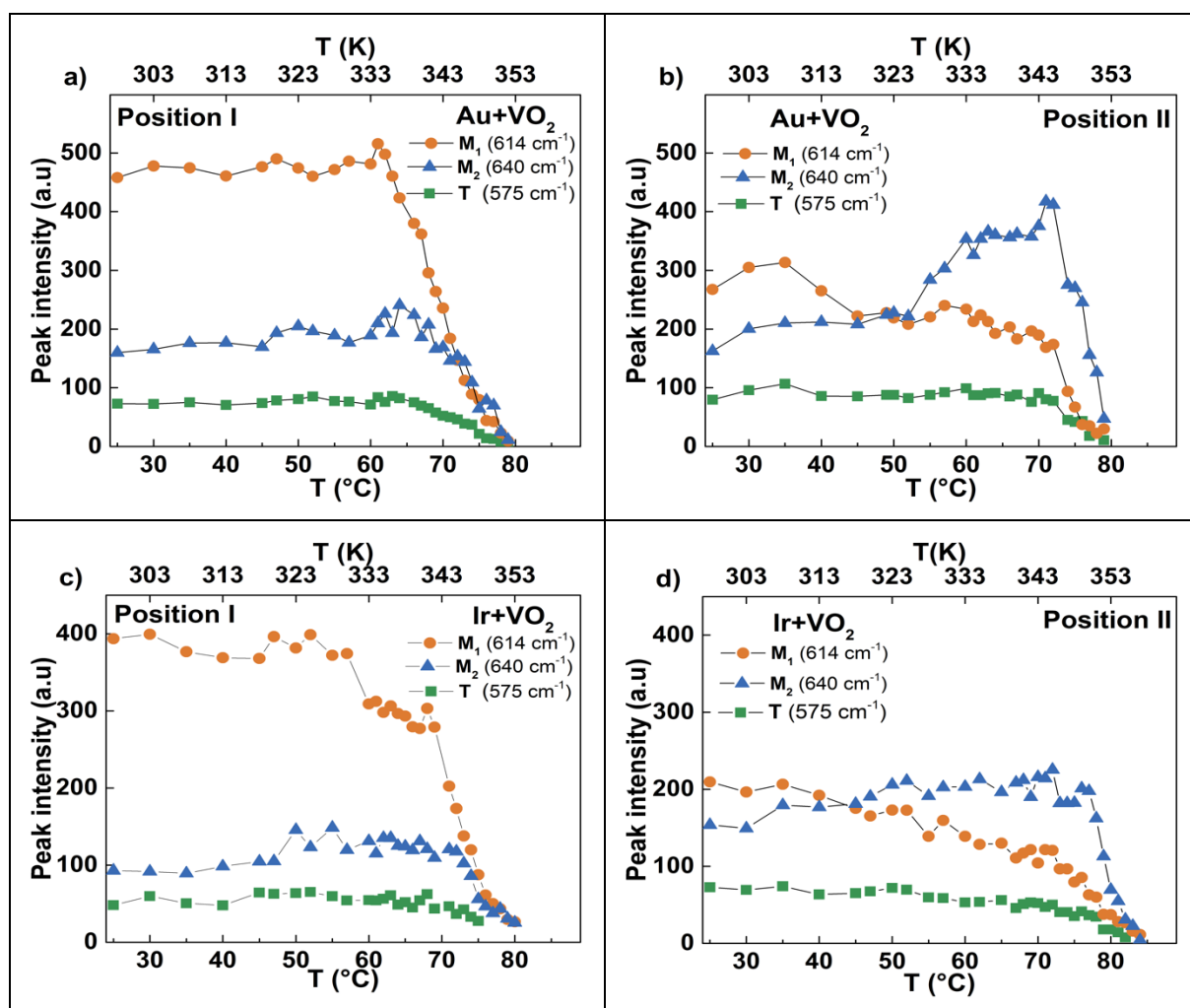


Figure V-17: The evolution of Raman peak vibrations intensity of VO₂ M₁, M₂, and T phases, extracted using a mix function (Gauss and Lorentz), as a function of temperature. a-b) The intensity of VO₂ phases containing Au nanoparticle arrays (Position “I” and “II”). c-d) The intensity of VO₂ phases containing Ir nanoparticle arrays (Position “I” and “II”). The data are collected during heating.

As the temperature increases from room temperature to the transition temperature, the signatures of monoclinic M₁, M₂ and triclinic T disappear, and broad lines are associated with rutile-VO₂ start to appear (Figure V-16). This is true for VO₂ pristine and VO₂ containing Au nanoparticles (for both Position “I” and “II”). The Raman results obtained for VO₂ with Ir nanoparticle inside are similar to that of VO₂ containing Au nanoparticle. The

similarity between the results for Ir and Au are visible in Figure V-17. The VO₂ follows different transition pathways from M₁ to R in relation to Position “I” and “II”. In Position “I,” the intensity of the M₁ phase remains higher than the intensity of the M₂ phase as the temperature goes up. In Position “II,” at room temperature, the intensity of the M₁ is greater than that of the M₂, but as the temperature increases, the M₂ intensity becomes more significant than that of the M₁. The evolution of the intensities as a function of temperature in Position “II” is similar to that of a pristine VO₂ sample and is expected to be for the usual transition pathway M₁-M₂-R of VO₂ thin films. The T phase's temperature evolution, as the temperature goes up, the T phase's intensity remains constant, but then suddenly it goes to zero.

V.4.2. Raman spectroscopy mapping

The Raman spectroscopy point measurement showed a clear distinction between the Raman spectra regarding the position on the sample on which that measurement is performed.

For the samples of VO₂ containing metallic nanoparticles position on which the Raman measurement is made is essential. Therefore, we have performed Raman spectroscopy mapping in temperature to see the precise evolution of M₁, M₂, and T in rapport to the metallic nanoparticles' location/position.

Each Raman map contains a sequence of successive point measurements. Each point's area is one μm², with a 20 second acquisition time per point, and the step between point measurements is 300 nm. Each Raman map's total area is approximately 5x5 μm². All the Raman maps are made in the same heating cycle (i.e., we make the map at room temperature, we heat the sample at 60 °C, make a new map, then heat to 65°C make another map and so on, without cooling the sample between maps). The VO₂ MIT can also be induced by laser of the Raman system (data not shown here). Thus, the Raman laser's power was set to the lowest possible settings, 0.4 mW, so the maps reflect just the temperature's influence on the VO₂ phases and not of the Raman laser. The VO₂ MIT can also be induced by

Raman surface mapping's raw data are processed by cosmic ray removal, and then a noise filter to the 5th component is added to compensate for the low VO₂ signal to noise ratio. The Raman vibrations are assigned respectively to 575 cm⁻¹, 614 cm⁻¹ and 640 cm⁻¹ for (T, M₁, M₂) and fit the experimental data with a mix function (Lorentzian and Gaussian) and a baseline (polynomial of order 1) and then the maps are extracted. Then, each frequency's intensities are plotted as a function of position on the sample in Figure V-18 and Figure V-19. The Raman maps made on a 200 nm VO₂ sample that contains Au nanoparticle arrays inside are given in Figure V-18. The data is collected at four temperatures (R_T, 65 °C, 70°C, and 75 °C), and then data is decomposed into maps showing the intensity of the M₁, M₂, and T in relation to the position of the Au nanoparticles.

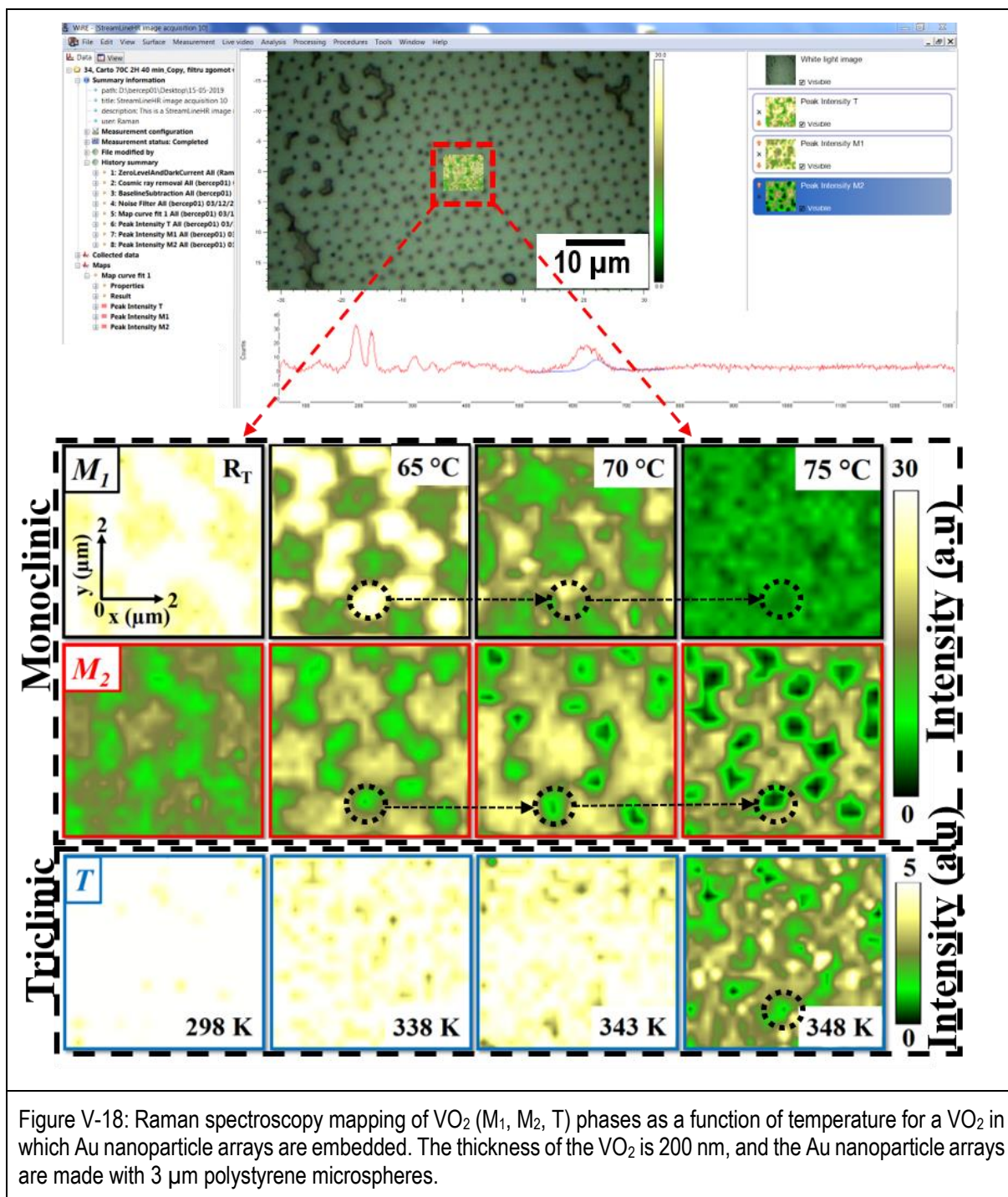


Figure V-18: Raman spectroscopy mapping of VO₂ (M₁, M₂, T) phases as a function of temperature for a VO₂ in which Au nanoparticle arrays are embedded. The thickness of the VO₂ is 200 nm, and the Au nanoparticle arrays are made with 3 μm polystyrene microspheres.

The reconstructed Raman maps shown in Figure V-18 where the contrast of colors is linked to the variation of the intensities of each fitted mode, give a spatial repartition of the phases. The vibrations are assigned at the same frequency as for the Raman point measurements. Of course, A_g mode at 575 cm⁻¹ of T is less intense than A_g of M₁ and M₂[181], [186]. Indeed, the Z-scale bar is from 0 to 30 (a.u) for the M₁ and M₂ and from 0 to 5 (a.u) for T. Moreover, the intensity of the M₁ phase at R_T is higher in the Position “I” than in Position “II” and as the temperature rises the M₁ phase is consumed by the R phase. The transition from M₁ to R is associated with a decrease in intensity of the M₁ phase. Contrarily, the intensity of the M₂ phase is higher in the Position “II” than in Position “I”. As the temperature rises the M₂ intensity in Position “II” grows while on Position “I” decreases even

more. This increase of the M_2 intensity is associated with the transition of VO_2 from M_1 to M_2 phase. The intensity of the T phase is almost constant until 343K and then at 348 K is higher in Position "II" than in Position "I". Finally, when corroborating the intensities of the M_1 , M_2 and T with spatial repartition, the existence of a core-shell structure within the sample is confirmed. At 348 K, all the VO_2 in Position "I" is in the metallic phase(R), while the VO_2 in Position "II" is in semiconductor phase (M_2 , T). The Raman maps made on a 200 nm VO_2 sample that contains Ir nanoparticle arrays inside is presented in Figure V-19.

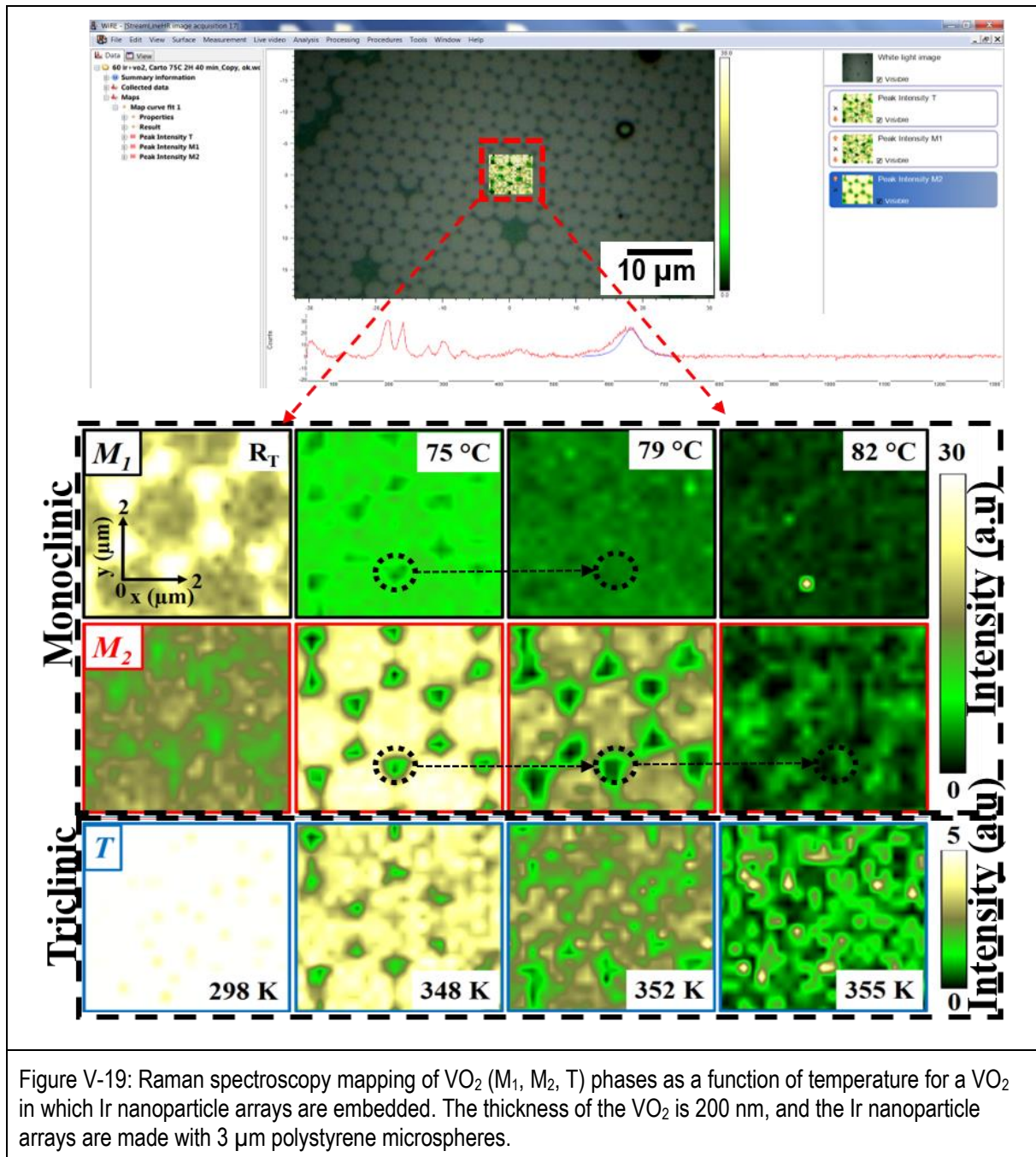


Figure V-19 shows that the Raman mapping result obtained for VO_2 containing Ir nanoparticles is similar to that of VO_2 with Au nanoparticles inside. The Raman mapping's proves that the VO_2 in the immediate vicinity of

the metallic nanoparticles goes to the rutile (metallic) phase at a lower temperature than the rest of the VO₂ that makes up the sample.

V.5. Conclusions

Chapter V proved an interaction, beyond plasmonic effects, between the metallic nanoparticle arrays and the VO₂ matrix. At the beginning of Chapter V, optical transmission measurements showed that metallic nanoparticle arrays decrease the insulator to the metal transition temperature of VO₂. This decrease of temperature was later correlated to a decrease in the stress of the *b* unit cell parameter of VO₂ that contains metallic nanoparticles compared to the VO₂ free of metallic nanoparticles. Further than that, XRD measurements showed that metallic nanoparticles promote an increase in the size of VO₂ crystallites. By HR-XRD, the crystalline quality of VO₂ and that VO₂ grows epitaxially onto the underlying Al₂O₃-c substrate. The HR-XRD theta/2theta measurements in temperature showed that, indeed, VO₂ has a phase transition, from monoclinic to rutile during heating and from rutile to monoclinic during cooling. Through Raman measurements, we could better discriminate between the different insulator phases (M₁, M₂, and T) of VO₂. Raman measurements showed that there is a clear distinction between the Raman spectra collected on top of the metallic nanoparticles and those collected on the pristine VO₂. By Raman spectroscopy mapping it is visible that a VO₂ (R) shell starts to grow on the metallic nanoparticles surface as the temperature increases. The pristine VO₂ follows normal transition pathways. The VO₂ rutile shell “increases the volume” of the metallic nanoparticles. Thereby we assume and is the origin of the red shifts the wavelength position of the LSPR peaks is a consequence of the formation of this metallic VO₂ shell. The Raman spectroscopy findings fully support the theoretical FDTD approach presented in Chapter IV. The VO₂ metallic shell causes the system to behave like an adaptive periodic metal architecture, with temperature dependent plasmonic properties.

General conclusions and perspectives:

The presented work concerns the development of composite materials elaborated by combination of two processes, i.e., Pulsed Laser Deposition (PLD) and Langmuir-Blodgett (LB). The thin film materials obtained, present specific optimized architecture forming by isolated and organized metallic (Au and Ir) nanoparticle embedded (or not) in an oxide matrix (Al_2O_3 , VO_2). These composite materials, developed on chosen substrates, reveal characteristic strong optical absorption in the visible and the near infra-red (NIR) regime.

The Langmuir-Blodgett process consists of depositing a microsphere (polystyrene or SiO_2) monolayer arranged in a 2D hexagonal close-packed structure on a substrate. Polystyrene microsphere monolayers are subsequently used as masks or templates through which metals (Au or Ir) are deposited. The deposition of metals is carried out using Pulsed Laser Deposition. After the metal deposition process, the polystyrene microspheres are removed with acetone, revealing, a characteristic array of nanoparticles with a specific triangular shape (for each nanoparticle). The resulting metallic nanoparticle arrays exhibit particular properties and especially localized surface plasmon resonances (LSPR), characterized by selective absorption of light with a specific wavelength.

An optimization work was firstly achieved on LB process to well control and define the ordered microspheres. The quality of the organization obtained respectively with 2, 3 or 5 μm microspheres were quantified exploiting direct optical images and associated Fast Fourier Transform (see Chapter II). After gold or iridium deposition, the pristine metallic sketches presented a fractal character. Surface substrate covering (about 9.3% of the total surface) was constant and independent from the sphere diameter.

LSPR of gold and iridium metallic organized nanoparticles were located essentially in the NIR regime. As an example, Au (resp. Ir) metallic nanoparticles made with 3 μm polystyrene microspheres, revealed a LSPR peak located at $\lambda \approx 4.45 \mu\text{m}$ (resp. $\lambda \approx 4.39 \mu\text{m}$). The size of metallic nanoparticles generated with 2 μm polystyrene microspheres were reduced and consecutively LSPR peak position were blue shifted ($\lambda \approx 2.85 \mu\text{m}$ for Au and $\lambda \approx 2.95 \mu\text{m}$ for Ir). We proved that nature and size of the elementary nanoparticles were then essential to define a specific value for the wavelength LSPR. The shape of the nanoparticles was also a key point to fix a LSPR value (confirmed experimentally and by FDTD).

A rigorous study on the evolution (vs. temperature) of the size and shape of the Au/Ir nanoparticles and consequently the Au/Ir sketch was presented. During a thermal treatment from room temperature up to 1000°C, Au nanoparticles were strongly modified. Solid state dewetting and coalescence phenomena were pointing out for big (200nm) and small (15nm) nanoparticles, respectively. At the opposite, for the same temperature range, modifications in shape and size for Ir nanoparticles were minors. At the same time, atomic phases and crystallographic evolution were systematically controlled and checked using in-situ observation (SEM and HR-

XRD). The Au nanoparticle shape modifications is exploited by making an active and controllable LSPR tunable system. By selecting the suitable thermal treatment temperature, for Au nanoparticles made with 3 μm polystyrene microspheres, the metallic sketch can be made to resonate at any wavelength within MidIR 4.45 μm to NIR 1.54 μm , a huge interval of around 3 μm .

To modulate the metallic nanoparticle arrays' LSPR peak position, a good option can be exploiting the surrounding dielectric environments. For that, we developed two matrices. The Au nanoparticle arrays was embedded first into an alumina matrix. As a function of the alumina's thickness, we obtained a redshift in the metallic nanoparticles array's LSPR peak position. An increase in alumina thickness induced an increase in the wavelength position of the LSPR peak. Furthermore, to create a smart LSPR adaptive sensor, the metallic nanoparticle arrays were embedded into an "active" matrix of vanadium dioxide. VO_2 material undergoes a first-order semiconductor to metal transition at 68 °C, accompanied by a dielectric function tunable with temperature or other physical stimuli. Consequently, depending on the temperature, each identified LSPR peak should reveal a significant wavelength shift and modulation.

A good quality of VO_2 PLD thin films imposes a synthesis temperature around 500°C. This relatively high temperature makes the study on the temperature effects on Au/Ir nanoparticles useful. For Ir nanoparticle arrays, the effects of temperature are minimal.

As for alumina matrix, deposition of VO_2 on an array of Au nanoparticles induced a redshift in the LSPR peak position. The redshift seemed to increase if the thickness layer of the matrix increased. If the VO_2 thickness on top of the Au nanoparticle arrays was 100 nm or greater than that, two LSPR peaks appeared. We concluded that these two peaks' apparition is linked to a coupling effect between VO_2 and the metallic sketch. As an example, for an array of Au nanoparticles embedded into 200 nm of VO_2 , two LSPR peaks are identified at $\lambda \approx 3.49 \mu\text{m}$ and $\lambda \approx 4.78 \mu\text{m}$. Removing chemically the VO_2 matrix leads to the presence of a single LSPR peak at $\lambda \approx 2.8 \mu\text{m}$.

Surprisingly, during semiconductor to metal transition (SMT), the two LSPR peaks of the nanocomposite both changed their position to a higher wavelength, i.e., a redshift ... as if the nanoparticles were increasing in volume. These observations, validated for the two metals, were different from anything that we could find in the literature, and a significant amount of time was spent trying to find an explanation for this behavior of the LSPR nanocomposite peaks temperature dependence. A particular attention was paid to the composite using local Raman spectroscopy phase mapping during the transition. We proved that several phases co-exist inside the matrix (T, M_1 , M_2 , R), and the structural heterogeneity, VO_2 matrix+metal nanoparticle, generated interfaces, which were the 2D zone where the VO_2 transition was initiated. At a given temperature, lower than the SMT temperature, the metallic nanoparticles were composed by the original metallic core (Au or Ir) and a metallic VO_2 shell within a VO_2 semiconductor surrounding matrix. This artificially increase of the metallic volume is responsible of the LSPR

redshift observed. The rest of the VO₂ follows normal transition pathways (M₁- M₂- R). All the experimental data linked to LSPR resonances and the effect of this core-shell structure on the LSPR peaks were supported by a simplified theoretical approach via the finite difference time domain (FDTD) method. A method that rigorously solved Maxwell's equations and allowed one to obtain the LSPR peak position in different nanoparticle configurations.

Prospects

The LSPR tunability based on the formation of a core-shell structure and the actual proof of its existence, by Raman spectroscopy constitute a major result of this thesis and shows a “measurable” interaction between the metallic nanoparticle (Au or Ir) arrays and the surrounding VO₂ environment. Based on this interaction, the metallic nanoparticles can act as flooded probes useful for characterizing and understanding the matrix properties. Following the strain applied on metallic particles and the unit cell modification (using HR-XRD), we think that it is possible to follow the transition characteristic of the VO₂ matrix. When the unit cell of Au (or Ir) nanoparticles embedded in VO₂ is extracted from HR-XRD measurements performed at different temperatures, the unit cell variations reveal the phase transition of the VO₂. First results obtained are very encouraging.

There are scientific aspects as the true origin of the double resonance peak of the metal nanoparticle array-VO₂ nanocomposite that needs further investigations. It is a truth that the FDTD simulation of the nanocomposite also revealed the presence of a double resonance peak, but some questions still remain. More than this, as we have presented in Chapter I, the LSPR resonances can be successfully implemented in applications such as a Surface-enhanced Raman scattering or Surface-Enhanced Infrared Absorption. For us, this is still a work in progress; we obtained few promising results, but there are still practical steps that need further improvement.

. Table V-2 presents a list of keywords summarizing the most important results obtained in this Ph.D. thesis.

Table V-2: Conclusion keywords.

Keywords	Procedures and concept used to explain the result	Degree of success
Development of Colloidal lithography process (polystyrene microsphere deposition)	Optical microscopy, SEM observation/ measurements	Successful
Thin films synthesis using Pulsed Laser Deposition (gold, iridium, alumina, vanadium dioxide)	AFM, SEM, XRD, HR-XRD, Raman spectroscopy	Successful
LSPR measurements on gold and iridium nanoparticle arrays	UV-VIS, FTIR spectroscopy + FDTD simulation	Successful
LSPR tunability by:	AFM, SEM, UV-VIS, FTIR, <i>in-situ</i> SEM, <i>in-situ</i> HR-XRD	Successful

-Polystyrene microsphere size -Thermal treatments	+ FDTD simulation	
Nanocomposite development for LSPR tunability	AFM, SEM- FIB, UV-VIS, FTIR, <i>in-situ</i> SEM, <i>in-situ</i> HR-XRD, Raman spectroscopy + FDTD simulation	Successful
Origin of the double LSPR peaks of the nanocomposite	Metal (Au, Ir)-VO ₂ coupling FDTD simulation	Work in progress
Origin of the LSPR redshift of the nanocomposite	Adaptive nanoparticle array core-shell structure formation, Raman spectroscopy FDTD simulation	Successful
LSPR based sensor	UV-VIS, FTIR spectroscopy	Work in progress

PUBLICATIONS / COMMUNICATIONS

3 Papers (2 submitted), 7 (4+3) Congress

P1. *Vanadium dioxide – Iridium composite development: specific near infrared surface plasmon resonance*
A.I. BERCEA*, C. CHAMPEAUX, C.D. CONSTANTINESCU, F. DUMAS-BOUCHIAT*,
Journal of Composite Science **submitted** (2021)
*Corresponding author

P2. *Adaptive metal-semiconductor periodic arrays for infrared optical modulation*
A.I. BERCEA*, C. CHAMPEAUX, A. BOULLE, C. CONSTANTINESCU, J. CORNETTE, M. COLAS, S.
VEDRAINE, F. DUMAS-BOUCHIAT*,
Acta Materialia **submitted** (2021)
*Corresponding author

P3. *Packed colloidal spheres for thin film structuration; towards modulation and tunability of surface plasmon resonance*
A. BERCEA*, C. CONSTANTINESCU, F. DUMAS-BOUCHIAT, C. CHAMPEAUX,
PLUMEE 9 (1) (2019)
<http://pubs.ub.ro/?pg=revues&rev=plumee&num=201901&vol=9&aid=4970>
*Corresponding author

4 International Congress (3 talks, 1 poster)

C1. *Pulsed Laser Deposition for the fabrication of Gold nanoparticle arrays and Gold nanoparticles-Vanadium dioxide nanocomposites*
A. BERCEA, C. CHAMPEAUX, C. CONSTANTINESCU, F. DUMAS-BOUCHIAT,
Oral Presentation, Plasma Thin Film International Union Meeting, **PLATHINIUM** 2021, Virtual Meeting -
conference by visio-conference, 13 – 17 septembre 2021

C2. *Pulsed Laser Deposition; towards fabrication of metallic nanoparticle arrays with localized surface plasmon resonances properties*
A. BERCEA, C. CHAMPEAUX, C. CONSTANTINESCU, F. DUMAS-BOUCHIAT,
Oral Presentation, **E-MRS 2021**, symposium I: advanced functional films grown by pulsed laser deposition
method, Virtual Meeting – conference by visio-conference, 31 mai – 04 juin 2021

C3. *Vanadium dioxide thin films tuning the localized surface plasmon resonances*
A. BERCEA, C. CONSTANTINESCU, M. COLA, A. BOULLE, C. CHAMPEAUX, F. DUMAS-BOUCHIAT,
Poster Presentation, **PLATHINIUM** - Plasma Thin Film International Union Meeting 23 - 27 septembre 2019,
Antibes, France

C4. *Packed colloidal spheres for thin film structuration towards modulation and tunability of surface plasmon resonance*
A. BERCEA, C. CONSTANTINESCU, C. CHAMPEAUX, F. DUMAS-BOUCHIAT,

Oral Presentation, **PLUMEE** - Plasma Thin Film International Union Meeting 10 - 12 avril 2019, Limoges, France

3 National Congress (2 talks, 1 poster)

C5. *Periodic multi-scale structuring of surfaces by self-assembly of colloidal masks: shape-size coupling effects, electronics and optics applications*

A. BERCEA, F. DUMAS-BOUCHIAT, C. CONSTANTINESCU, C. CHAMPEAUX,

Poster Presentation, **journée des doctorants de l'institut IRCER**, 06 juin 2019, Limoges

C6. *Localized surface plasmon resonance (LSPR) properties of micropatterned thin films defined by pulsed laser deposition (PLD) and Langmuir-Blodgett (LB)*

A. BERCEA, C. CONSTANTINESCU, F. DUMAS-BOUCHIAT, C. CHAMPEAUX,

Oral Presentation, **MATV2L-Milieux 2D**, 24-25 janvier 2019, Blois

C7. *Surface plasmon resonance properties of nano-/micro-structures fabricated by colloidal lithography and laser-assisted processes*

A. BERCEA, C. CONSTANTINESCU, F. DUMAS-BOUCHIAT, C. CHAMPEAUX,

Oral Presentation, **Matériaux** 2018, 19-23 novembre 2018, Strasbourg

Bibliography

General works

Particular works

- [1] M. S. Zubairy, "A Very Brief History of Light," in *Optics in Our Time*, M. D. Al-Amri, M. El-Gomati, and M. S. Zubairy, Eds. Cham: Springer International Publishing, 2016, pp. 3–24. doi: 10.1007/978-3-319-31903-2_1.
- [2] S. Kasani, K. Curtin, and N. Wu, "A review of 2D and 3D plasmonic nanostructure array patterns: fabrication, light management and sensing applications," *Nanophotonics*, vol. 8, no. 12, pp. 2065–2089, Oct. 2019, doi: 10.1515/nanoph-2019-0158.
- [3] S. A. Maier, *Plasmonics: Fundamentals and Applications*. Springer US, 2007. doi: 10.1007/0-387-37825-1.
- [4] W. A. Murray, S. Astilean, and W. L. Barnes, "Transition from localized surface plasmon resonance to extended surface plasmon-polariton as metallic nanoparticles merge to form a periodic hole array," *Phys. Rev. B*, vol. 69, no. 16, p. 165407, Apr. 2004, doi: 10.1103/PhysRevB.69.165407.
- [5] K. Kneipp *et al.*, "Extremely Large Enhancement Factors in Surface-Enhanced Raman Scattering for Molecules on Colloidal Gold Clusters:," *Appl. Spectrosc.*, Aug. 2016, doi: 10.1366/0003702981943059.
- [6] K. L. Kelly, E. Coronado, L. L. Zhao, and G. C. Schatz, "The Optical Properties of Metal Nanoparticles: The Influence of Size, Shape, and Dielectric Environment," *J. Phys. Chem. B*, vol. 107, no. 3, Art. no. 3, Jan. 2003, doi: 10.1021/jp026731y.
- [7] X. Z. Wei and P. Mulvaney, "Chapter 3 - Optical Properties of Strongly Coupled Plasmonic Nanoparticle Clusters," in *Handbook of Surface Science*, vol. 4, N. V. Richardson and S. Holloway, Eds. North-Holland, 2014, pp. 75–108. doi: 10.1016/B978-0-444-59526-3.00003-3.
- [8] M. Faraday, "X. The Bakerian Lecture. —Experimental relations of gold (and other metals) to light," *Philos. Trans. R. Soc. Lond.*, vol. 147, pp. 145–181, Jan. 1857, doi: 10.1098/rstl.1857.0011.
- [9] J. G. Smith, J. A. Fauchaux, and P. K. Jain, "Plasmon resonances for solar energy harvesting: A mechanistic outlook," *Nano Today*, vol. 10, no. 1, pp. 67–80, Feb. 2015, doi: 10.1016/j.nantod.2014.12.004.
- [10] A. Gellé and A. Moores, "Plasmonic nanoparticles: Photocatalysts with a bright future," *Curr. Opin. Green Sustain. Chem.*, vol. 15, pp. 60–66, Feb. 2019, doi: 10.1016/j.cogsc.2018.10.002.
- [11] "Present and Future of Surface-Enhanced Raman Scattering | ACS Nano." <https://pubs.acs.org/doi/10.1021/acsnano.9b04224> (accessed Nov. 22, 2020).
- [12] S. Lee and I. Choi, "Fabrication Strategies of 3D Plasmonic Structures for SERS," *BioChip J.*, vol. 13, no. 1, pp. 30–42, Mar. 2019, doi: 10.1007/s13206-019-3105-y.
- [13] A. Mahigir, T.-W. Chang, A. Behnam, G. L. Liu, M. R. Gartia, and G. Veronis, "Plasmonic nanohole array for enhancing the SERS signal of a single layer of graphene in water," *Sci. Rep.*, vol. 7, no. 1, Art. no. 1, Oct. 2017, doi: 10.1038/s41598-017-14369-x.
- [14] M. Kim *et al.*, "Accordion-like plasmonic silver nanorod array exhibiting multiple electromagnetic responses," *NPG Asia Mater.*, vol. 10, no. 4, Art. no. 4, Apr. 2018, doi: 10.1038/s41427-018-0033-6.

- [15] L. Zhang *et al.*, “Reproducible Plasmonic Nanopyramid Array of Various Metals for Highly Sensitive Refractometric and Surface-Enhanced Raman Biosensing,” *ACS Omega*, vol. 3, no. 10, pp. 14181–14187, Oct. 2018, doi: 10.1021/acsomega.7b02016.
- [16] H. Liu, X. Zhang, and T. Zhai, “Plasmonic nano-ring arrays through patterning gold nanoparticles into interferograms,” *Opt. Express*, vol. 21, no. 13, pp. 15314–15322, Jul. 2013, doi: 10.1364/OE.21.015314.
- [17] P. A. Ledin *et al.*, “Light-Responsive Plasmonic Arrays Consisting of Silver Nanocubes and a Photoisomerizable Matrix,” *ACS Appl. Mater. Interfaces*, vol. 7, no. 8, pp. 4902–4912, Mar. 2015, doi: 10.1021/am508993z.
- [18] S. Zou and G. C. Schatz, “Silver nanoparticle array structures that produce giant enhancements in electromagnetic fields,” *Chem. Phys. Lett.*, vol. 403, no. 1–3, pp. 62–67, Feb. 2005, doi: 10.1016/j.cplett.2004.12.107.
- [19] LIGO Scientific Collaboration and Virgo Collaboration *et al.*, “Observation of Gravitational Waves from a Binary Black Hole Merger,” *Phys. Rev. Lett.*, vol. 116, no. 6, p. 061102, Feb. 2016, doi: 10.1103/PhysRevLett.116.061102.
- [20] R. L. Thomas, L. D. Favro, X. Han, and Z. Ouyang, “5.18 - Thermal Methods Used in Composite Inspection,” in *Comprehensive Composite Materials*, A. Kelly and C. Zweben, Eds. Oxford: Pergamon, 2000, pp. 427–446. doi: 10.1016/B0-08-042993-9/00082-6.
- [21] V. L. Ginzburg, “Chapter VII - CHERENKOV EFFECT, DOPPLER EFFECT, TRANSITION RADIATION,” in *Theoretical Physics and Astrophysics*, V. L. Ginzburg, Ed. Amsterdam: Pergamon, 1979, pp. 125–169. doi: 10.1016/B978-0-08-023066-5.50012-2.
- [22] A. Einstein, “The Advent of the Quantum Theory,” *Science*, vol. 113, no. 2926, pp. 82–84, Jan. 1951, doi: 10.1126/science.113.2926.82.
- [23] H. Günther and V. Müller, *The Special Theory of Relativity: Einstein’s World in New Axiomatics*. Springer Nature, 2019.
- [24] “Energy Transfer from Electromagnetic Fields to Materials | IntechOpen.” <https://www.intechopen.com/books/electromagnetic-fields-and-waves/energy-transfer-from-electromagnetic-fields-to-materials> (accessed Jun. 01, 2020).
- [25] H. K. Gupta, *Geothermal Resources: An Energy Alternative*. Elsevier, 2014.
- [26] C. Elachi and J. J. van Zyl, *Introduction To The Physics and Techniques of Remote Sensing*. John Wiley & Sons, 2006.
- [27] J. W. Haus, “Electrodynamics for nanophotonics,” in *Fundamentals and Applications of Nanophotonics*, 2016, pp. 13–43. doi: 10.1016/B978-1-78242-464-2.00002-6.
- [28] J. J. Jongen, “Interaction of Lasers with Plasmon Resonance (LSPR) coatings: manipulation of Au nanoparticles,” 2011. /paper/Interaction-of-Lasers-with-Plasmon-Resonance-(LSPR)-Jongen/2a9d88e57779241f24afac4cfe22ecbfd3ec3203 (accessed Jun. 01, 2020).
- [29] D. De Ceglia and M. A. Vincenti, “Plasmonics,” in *Fundamentals and Applications of Nanophotonics*, 2016, pp. 233–252. doi: 10.1016/B978-1-78242-464-2.00008-7.
- [30] Z. Vardeny and O. Brafman, “Phonon-polaritons in Cu halides: Anomalies and their temperature dependence,” *Phys. Rev. B*, vol. 21, no. 6, pp. 2585–2595, Mar. 1980, doi: 10.1103/PhysRevB.21.2585.
- [31] Steudle, “Elements of Nanophotonics — Nanooptik, Chapter 7: Plasmonics.” <https://www.physik.hu-berlin.de/de/nano/lehre/Gastvorlesung%20Wien> (accessed Jun. 01, 2020).
- [32] W. L. Barnes, A. Dereux, and T. W. Ebbesen, “Surface plasmon subwavelength optics,” *Nature*, vol. 424, no. 6950, pp. 824–830, Aug. 2003, doi: 10.1038/nature01937.

- [33]W. L. Barnes, A. Dereux, and T. W. Ebbesen, "Surface plasmon subwavelength optics," *Nature*, vol. 424, no. 6950, Art. no. 6950, Aug. 2003, doi: 10.1038/nature01937.
- [34]F. Ye, J. Merlo, M. Burns, and M. Naughton, "Optical and electrical mappings of surface plasmon cavity modes," *Nanophotonics*, vol. 3, Mar. 2014, doi: 10.1515/nanoph-2013-0038.
- [35]A. Norrman, T. Setälä, and A. T. Friberg, "Long-range higher-order surface-plasmon polaritons," *Phys. Rev. A*, vol. 90, no. 5, p. 053849, Nov. 2014, doi: 10.1103/PhysRevA.90.053849.
- [36]E. Petryayeva and U. J. Krull, "Localized surface plasmon resonance: Nanostructures, bioassays and biosensing—A review," *Anal. Chim. Acta*, vol. 706, no. 1, pp. 8–24, Nov. 2011, doi: 10.1016/j.aca.2011.08.020.
- [37]S. A. Maier, *Plasmonics: Fundamentals and Applications*. Springer US, 2007. doi: 10.1007/0-387-37825-1.
- [38]M. Hu *et al.*, "Gold nanostructures: engineering their plasmonic properties for biomedical applications," *Chem. Soc. Rev.*, vol. 35, no. 11, pp. 1084–1094, Oct. 2006, doi: 10.1039/B517615H.
- [39]K. L. Kelly, E. Coronado, L. L. Zhao, and G. C. Schatz, "The Optical Properties of Metal Nanoparticles: The Influence of Size, Shape, and Dielectric Environment," *J. Phys. Chem. B*, vol. 107, no. 3, pp. 668–677, Jan. 2003, doi: 10.1021/jp026731y.
- [40]K. A. Willets and R. P. Van Duyne, "Localized Surface Plasmon Resonance Spectroscopy and Sensing," *Annu. Rev. Phys. Chem.*, vol. 58, no. 1, pp. 267–297, 2007, doi: 10.1146/annurev.physchem.58.032806.104607.
- [41]S. A. Maier and H. A. Atwater, "Plasmonics: Localization and guiding of electromagnetic energy in metal/dielectric structures," *J. Appl. Phys.*, vol. 98, no. 1, p. 011101, Jul. 2005, doi: 10.1063/1.1951057.
- [42]S. Link and M. A. El-Sayed, "Shape and size dependence of radiative, non-radiative and photothermal properties of gold nanocrystals," *Int. Rev. Phys. Chem.*, vol. 19, no. 3, pp. 409–453, Jul. 2000, doi: 10.1080/01442350050034180.
- [43]"A comparison of techniques used to simulate the scattering of electromagnetic radiation by metallic nanostructures: Journal of Modern Optics: Vol 57, No 5." <https://www.tandfonline.com/doi/abs/10.1080/09500341003628702> (accessed Jun. 01, 2020).
- [44]J. Ozhikandathil and M. Packirisamy, "Simulation and Implementation of a Morphology-Tuned Gold Nano-Islands Integrated Plasmonic Sensor," *Sensors*, vol. 14, no. 6, pp. 10497–10513, Jun. 2014, doi: 10.3390/s140610497.
- [45]Kane Yee, "Numerical solution of initial boundary value problems involving maxwell's equations in isotropic media," *IEEE Trans. Antennas Propag.*, vol. 14, no. 3, pp. 302–307, May 1966, doi: 10.1109/TAP.1966.1138693.
- [46]"Numerical methods for nanophotonics: standard problems and future challenges - Gallinet - 2015 - Laser & Photonics Reviews - Wiley Online Library." <https://onlinelibrary.wiley.com/doi/full/10.1002/lpor.201500122> (accessed Jun. 02, 2020).
- [47]Y. Zhao and Y. Hao, "Finite-Difference Time-Domain Study of Guided Modes in Nano-Plasmonic Waveguides," *IEEE Trans. Antennas Propag.*, vol. 55, no. 11, pp. 3070–3077, Nov. 2007, doi: 10.1109/TAP.2007.908370.
- [48]J.-P. Berenger, "A perfectly matched layer for the absorption of electromagnetic waves," *J. Comput. Phys.*, vol. 114, no. 2, pp. 185–200, Oct. 1994, doi: 10.1006/jcph.1994.1159.

- [49]X. Lu, M. Rycenga, S. E. Skrabalak, B. Wiley, and Y. Xia, "Chemical synthesis of novel plasmonic nanoparticles," *Annu. Rev. Phys. Chem.*, vol. 60, pp. 167–192, 2009, doi: 10.1146/annurev.physchem.040808.090434.
- [50]B. J. Wiley, S. H. Im, Z.-Y. Li, J. McLellan, A. Siekkinen, and Y. Xia, "Maneuvering the surface plasmon resonance of silver nanostructures through shape-controlled synthesis," *J. Phys. Chem. B*, vol. 110, no. 32, pp. 15666–15675, Aug. 2006, doi: 10.1021/jp0608628.
- [51]B. J. Wiley *et al.*, "Synthesis and Optical Properties of Silver Nanobars and Nanorice," *Nano Lett.*, vol. 7, no. 4, pp. 1032–1036, Apr. 2007, doi: 10.1021/nl070214f.
- [52]J. Aizpurua, G. W. Bryant, L. J. Richter, F. J. García de Abajo, B. K. Kelley, and T. Mallouk, "Optical properties of coupled metallic nanorods for field-enhanced spectroscopy," *Phys. Rev. B*, vol. 71, no. 23, p. 235420, Jun. 2005, doi: 10.1103/PhysRevB.71.235420.
- [53]K. Schraml *et al.*, "Linear and non-linear response of lithographically defined plasmonic nanoantennas," in *Photonic and Phononic Properties of Engineered Nanostructures V*, Feb. 2015, vol. 9371, p. 93711D. doi: 10.1117/12.2079104.
- [54]"A Review on Surface-Enhanced Raman Scattering." <https://www.ncbi.nlm.nih.gov/pmc/articles/PMC6627380/> (accessed Jun. 02, 2020).
- [55]H. Wei, S. M. H. Abtahi, and P. J. Vikesland, "Plasmonic colorimetric and SERS sensors for environmental analysis," *Environ. Sci. Nano*, vol. 2, no. 2, pp. 120–135, Apr. 2015, doi: 10.1039/C4EN00211C.
- [56]S. Abalde-Cela, S. Carregal-Romero, J. P. Coelho, and A. Guerrero-Martínez, "Recent progress on colloidal metal nanoparticles as signal enhancers in nanosensing," *Adv. Colloid Interface Sci.*, vol. 233, pp. 255–270, Jul. 2016, doi: 10.1016/j.cis.2015.05.002.
- [57]X. Yang *et al.*, "Nanomaterial-Based Plasmon-Enhanced Infrared Spectroscopy," *Adv. Mater.*, vol. 30, no. 20, p. 1704896, 2018, doi: 10.1002/adma.201704896.
- [58]Z. Hu, M. Straßburg, N. Dietz, A. Asghar, and I. Ferguson, "Composition dependence of the infrared dielectric functions in Si-doped hexagonal Al_xGa_{1-x}N films on c -plane sapphire substrates," *Phys. Rev. B - PHYS REV B*, vol. 72, Dec. 2005, doi: 10.1103/PhysRevB.72.245326.
- [59]P. Pandey, M. Sui, M.-Y. Li, Q. Zhang, E.-S. Kim, and J. Lee, "Shape transformation of self-assembled Au nanoparticles by the systematic control of deposition amount on sapphire (0001)," *RSC Adv.*, vol. 5, no. 81, pp. 66212–66220, Jul. 2015, doi: 10.1039/C5RA07631E.
- [60]P. Kim, A. Anderko, A. Navrotsky, and R. Riman, "Trends in Structure and Thermodynamic Properties of Normal Rare Earth Carbonates and Rare Earth Hydroxycarbonates," *Minerals*, vol. 8, p. 106, Mar. 2018, doi: 10.3390/min8030106.
- [61]Y. Gong, C. Wang, Q. Shen, and L. Zhang, "Low-temperature deposition of iridium thin films by pulsed laser deposition," *Vacuum*, vol. 82, no. 6, pp. 594–598, Feb. 2008, doi: 10.1016/j.vacuum.2007.09.003.
- [62]"Synthesis and Characterization of Nanoscale Colloidal Iridium Metal Clusters by Chemical Reduction Method using Monohydric and Dihydric Alcohols | Semantic Scholar." <https://www.semanticscholar.org/paper/Synthesis-and-Characterization-of-Nanoscale-Iridium-Goel-Bhatt/de19dcc567715c82bd89a08902a8a475d49b51d0> (accessed Jun. 02, 2020).
- [63]R. Zhang *et al.*, "A Simple and Fast Method to Synthesize Cubic Iridium Nanoparticles with Clean Surface Free from Surfactants," *Nanomaterials*, vol. 9, no. 1, Jan. 2019, doi: 10.3390/nano9010076.
- [64]"(PDF) Atomic Layer Deposition of Iridium Thin Films and their Application in Gold Electrodeposition."

https://www.researchgate.net/publication/230743670_Atomic_Layer_Deposition_of_Iridium_Thin_Films_and_their_Application_in_Gold_Electrodeposition (accessed Jun. 02, 2020).

- [65] A. Lehmuskero, M. Kuittinen, and P. Vahimaa, "Refractive index and extinction coefficient dependence of thin Al and Ir films on deposition technique and thickness," *Opt. Express*, vol. 15, no. 17, pp. 10744–10752, Aug. 2007, doi: 10.1364/OE.15.010744.
- [66] J. Greene, "Review Article: Tracing the recorded history of thin-film sputter deposition: From the 1800s to 2017," *J. Vac. Sci. Technol. Vac. Surf. Films*, vol. 35, p. 05C204, Sep. 2017, doi: 10.1116/1.4998940.
- [67] D. K. T. Ng, B. S. Bholra, R. M. Bakker, and S.-T. Ho, "Ultrasoother Gold Films via Pulsed Laser Deposition," *Adv. Funct. Mater.*, vol. 21, no. 13, pp. 2587–2592, 2011, doi: 10.1002/adfm.201002303.
- [68] J. Elias *et al.*, "Electrodeposition of gold thin films with controlled morphologies and their applications in electrocatalysis and SERS," *Nanotechnology*, vol. 23, no. 25, p. 255705, May 2012, doi: 10.1088/0957-4484/23/25/255705.
- [69] R. Herizchi, E. Abbasi, M. Milani, and A. Akbarzadeh, "Current methods for synthesis of gold nanoparticles," *Artif. Cells Nanomedicine Biotechnol.*, vol. 44, no. 2, pp. 596–602, Feb. 2016, doi: 10.3109/21691401.2014.971807.
- [70] "Nanosphere Lithography: A Powerful Method for the Controlled Manufacturing of Nanomaterials." <https://www.hindawi.com/journals/jnm/2013/948510/> (accessed Jun. 02, 2020).
- [71] "Infrared Dielectric Function of Gold Films in Relation to Their Morphology | The Journal of Physical Chemistry C." <https://pubs.acs.org/doi/abs/10.1021/jp5027465> (accessed Jun. 02, 2020).
- [72] R. L. Olmon *et al.*, "Optical dielectric function of gold," *Phys. Rev. B*, vol. 86, no. 23, p. 235147, Dec. 2012, doi: 10.1103/PhysRevB.86.235147.
- [73] F. J. Morin, "Oxides Which Show a Metal-to-Insulator Transition at the Neel Temperature," *Phys. Rev. Lett.*, vol. 3, no. 1, pp. 34–36, Jul. 1959, doi: 10.1103/PhysRevLett.3.34.
- [74] K. Liu, S. Lee, S. Yang, O. Delaire, and J. Wu, "Recent progresses on physics and applications of vanadium dioxide," *Mater. Today*, vol. 21, no. 8, pp. 875–896, Oct. 2018, doi: 10.1016/j.mattod.2018.03.029.
- [75] T. J. Huffman *et al.*, "Insulating phases of vanadium dioxide are Mott-Hubbard insulators," *Phys. Rev. B*, vol. 95, no. 7, p. 075125, Feb. 2017, doi: 10.1103/PhysRevB.95.075125.
- [76] P. Shvets, O. Dikaya, K. Maksimova, and A. Goikhman, "A review of Raman spectroscopy of vanadium oxides," *J. Raman Spectrosc.*, vol. 50, no. 8, pp. 1226–1244, 2019, doi: 10.1002/jrs.5616.
- [77] "Recent progress in the phase-transition mechanism and modulation of vanadium dioxide materials | NPG Asia Materials." <https://www.nature.com/articles/s41427-018-0061-2> (accessed Jun. 02, 2020).
- [78] A. Moatti, R. Sachan, S. Gupta, and J. Narayan, "Vacancy-Driven Robust Metallicity of Structurally Pinned Monoclinic Epitaxial VO₂ Thin Films," *ACS Appl. Mater. Interfaces*, vol. 11, no. 3, pp. 3547–3554, Jan. 2019, doi: 10.1021/acsami.8b17879.
- [79] M. Li, S. Magdassi, Y. Gao, and Y. Long, "Hydrothermal Synthesis of VO₂ Polymorphs: Advantages, Challenges and Prospects for the Application of Energy Efficient Smart Windows," *Small*, vol. 13, no. 36, p. 1701147, 2017, doi: 10.1002/smll.201701147.
- [80] J. B. Goodenough, "The two components of the crystallographic transition in VO₂," *J. Solid State Chem.*, vol. 3, no. 4, pp. 490–500, Nov. 1971, doi: 10.1016/0022-4596(71)90091-0.

- [81]C. Wan *et al.*, “On the Optical Properties of Thin-Film Vanadium Dioxide from the Visible to the Far Infrared,” *Ann. Phys.*, vol. 531, no. 10, p. 1900188, 2019, doi: 10.1002/andp.201900188.
- [82]A. Sohn, T. Kanki, K. Sakai, H. Tanaka, and D.-W. Kim, “Fractal Nature of Metallic and Insulating Domain Configurations in a VO₂ Thin Film Revealed by Kelvin Probe Force Microscopy,” *Sci. Rep.*, vol. 5, no. 1, p. 10417, May 2015, doi: 10.1038/srep10417.
- [83]J. A. Ramirez-Rincon *et al.*, “Thermal hysteresis measurement of the VO₂ dielectric function for its metal-insulator transition by visible-IR ellipsometry,” *J. Appl. Phys.*, vol. 124, no. 19, p. 195102, Nov. 2018, doi: 10.1063/1.5049747.
- [84]Y.-L. Huang, H.-J. Liu, C.-H. Ma, P. Yu, Y.-H. Chu, and J.-C. Yang, “Pulsed laser deposition of complex oxide heteroepitaxy,” *Chin. J. Phys.*, vol. 60, pp. 481–501, Aug. 2019, doi: 10.1016/j.cjph.2019.05.030.
- [85]J. (陈吉堃) Chen *et al.*, “Plasma interactions determine the composition in pulsed laser deposited thin films,” *Appl. Phys. Lett.*, vol. 105, no. 11, p. 114104, Sep. 2014, doi: 10.1063/1.4895788.
- [86]C. Yu, A. S. Sokolov, P. Kulik, and V. G. Harris, “Stoichiometry, phase, and texture evolution in PLD-Grown hexagonal barium ferrite films as a function of laser process parameters,” *J. Alloys Compd.*, vol. 814, p. 152301, Jan. 2020, doi: 10.1016/j.jallcom.2019.152301.
- [87]J. Lapano, M. Brahlek, L. Zhang, J. Roth, A. Pogrebnyakov, and R. Engel-Herbert, “Scaling growth rates for perovskite oxide virtual substrates on silicon,” *Nat. Commun.*, vol. 10, no. 1, p. 2464, Jun. 2019, doi: 10.1038/s41467-019-10273-2.
- [88]R. Dietsch, T. Holz, D. Weißbach, and R. Scholz, “Large area PLD of nanometer-multilayers,” *Appl. Surf. Sci.*, vol. 197–198, pp. 169–174, Sep. 2002, doi: 10.1016/S0169-4332(02)00320-3.
- [89]D. Dijkkamp *et al.*, “Preparation of Y-Ba-Cu oxide superconductor thin films using pulsed laser evaporation from high T_c bulk material,” *Appl. Phys. Lett.*, vol. 51, no. 8, pp. 619–621, Aug. 1987, doi: 10.1063/1.98366.
- [90]O. Loebich, “The optical properties of gold,” *Gold Bull.*, vol. 5, no. 1, pp. 2–10, Mar. 1972, doi: 10.1007/BF03215148.
- [91]R. Delmdahl and R. Pätzelt, “Pulsed laser deposition with excimer lasers,” *Phys. Status Solidi C*, vol. 5, no. 10, pp. 3276–3279, 2008, doi: 10.1002/pssc.200779515.
- [92]A. H. Hamad, “Effects of Different Laser Pulse Regimes (Nanosecond, Picosecond and Femtosecond) on the Ablation of Materials for Production of Nanoparticles in Liquid Solution,” *High Energy Short Pulse Lasers*, Sep. 2016, doi: 10.5772/63892.
- [93]F. Garrelie, C. Champeaux, and A. Catherinot, “Expansion dynamics of the plasma plume created by laser ablation in a background gas,” *Appl. Phys. A*, vol. 69, no. 1, pp. S55–S58, Dec. 1999, doi: 10.1007/s003399900198.
- [94]A. Ojeda-G-P, C. W. Schneider, M. Döbeli, T. Lippert, and A. Wokaun, “Plasma plume dynamics, rebound, and recoating of the ablation target in pulsed laser deposition,” *J. Appl. Phys.*, vol. 121, no. 13, p. 135306, Apr. 2017, doi: 10.1063/1.4979780.
- [95]L. W. Martin, Y.-H. Chu, and R. Ramesh, “Advances in the growth and characterization of magnetic, ferroelectric, and multiferroic oxide thin films,” *Mater. Sci. Eng. R Rep.*, vol. 68, no. 4, pp. 89–133, May 2010, doi: 10.1016/j.mser.2010.03.001.
- [96]A. Barbier, “23 - Single and heterostructure multiferroic thin films,” in *Magnetic, Ferroelectric, and Multiferroic Metal Oxides*, B. D. Stojanovic, Ed. Elsevier, 2018, pp. 487–514. doi: 10.1016/B978-0-12-8111180-2.00023-2.

- [97] M. Yang *et al.*, “Surface-growth-mode-induced Strain Effects on the Metal-Insulator Transition in Epitaxial Vanadium Dioxide Thin Films,” *RSC Adv.*, vol. 5, pp. 80122–80128, Sep. 2015, doi: 10.1039/c5ra13490k.
- [98] T. G. Andersson, “The initial growth of vapour deposited gold films,” *Gold Bull.*, vol. 15, no. 1, pp. 7–18, Mar. 1982, doi: 10.1007/BF03216565.
- [99] F. Ndeye Rokhaya, I. Gammoudi, F. Moroté, C. Grauby-Heywang, and T. Cohen-Bouhacina, “Phase Behavior and Structure Properties of Supported Lipid Monolayers and Bilayers in Interaction with Silica Nanoparticles,” Jun. 2013.
- [100] D. Grojo *et al.*, “Bessel-like photonic nanojets from core-shell sub-wavelength spheres,” *Opt. Lett.*, vol. 39, no. 13, pp. 3989–3992, Jul. 2014, doi: 10.1364/OL.39.003989.
- [101] O. Oliveira, A. Riul Jr, and V. Leite, “Water at interfaces and its influence on the electrical properties of adsorbed films,” *Braz. J. Phys.*, vol. 34, Mar. 2004, doi: 10.1590/S0103-97332004000100011.
- [102] A. Deák, I. Székely, E. Kálmán, Zs. Keresztes, A. L. Kovács, and Z. Hórvölgyi, “Nanostructured silica Langmuir–Blodgett films with antireflective properties prepared on glass substrates,” *Thin Solid Films*, vol. 484, no. 1, pp. 310–317, Jul. 2005, doi: 10.1016/j.tsf.2005.01.096.
- [103] M. Parchine, T. Kohoutek, M. Bardosova, and M. E. Pemble, “Large area colloidal photonic crystals for light trapping in flexible organic photovoltaic modules applied using a roll-to-roll Langmuir-Blodgett method,” *Sol. Energy Mater. Sol. Cells*, vol. 185, pp. 158–165, Oct. 2018, doi: 10.1016/j.solmat.2018.05.026.
- [104] K. Li *et al.*, “Free-standing Ag triangle arrays a configurable vertical gap for surface enhanced Raman spectroscopy,” *Nanotechnology*, vol. 28, no. 38, p. 385401, Sep. 2017, doi: 10.1088/1361-6528/aa7a4d.
- [105] M. Ardini *et al.*, “Live Intracellular Biorthogonal Imaging by Surface Enhanced Raman Spectroscopy using Alkyne-Silver Nanoparticles Clusters,” *Sci. Rep.*, vol. 8, no. 1, p. 12652, Aug. 2018, doi: 10.1038/s41598-018-31165-3.
- [106] L. N. D. Kallepalli, C. Constantinescu, P. Delaporte, O. Utéza, and D. Grojo, “Ultra-high ordered, centimeter scale preparation of microsphere Langmuir films,” *J. Colloid Interface Sci.*, vol. 446, pp. 237–243, May 2015, doi: 10.1016/j.jcis.2015.01.047.
- [107] V. K. Sikka, A. K. Jones, and R. Ross, “Spill resistant surfaces having hydrophobic and oleophobic borders,” WO2010042668A1, Apr. 15, 2010 Accessed: Jun. 02, 2020. [Online]. Available: <https://patents.google.com/patent/WO2010042668A1/en>
- [108] S.-Y. Zhang, M. D. Regulacio, and M.-Y. Han, “Self-assembly of colloidal one-dimensional nanocrystals,” *Chem. Soc. Rev.*, vol. 43, no. 7, pp. 2301–2323, Mar. 2014, doi: 10.1039/C3CS60397K.
- [109] R. van Dommelen, P. Fanzio, and L. Sasso, “Surface self-assembly of colloidal crystals for micro- and nano-patterning,” *Adv. Colloid Interface Sci.*, vol. 251, pp. 97–114, Jan. 2018, doi: 10.1016/j.cis.2017.10.007.
- [110] L. V. Woodcock, “Entropy difference between the face-centred cubic and hexagonal close-packed crystal structures,” *Nature*, vol. 385, no. 6612, pp. 141–143, Jan. 1997, doi: 10.1038/385141a0.
- [111] X. Li, O. Niitsoo, and A. Couzis, “Electrostatically driven adsorption of silica nanoparticles on functionalized surfaces,” *J. Colloid Interface Sci.*, vol. 394, pp. 26–35, Mar. 2013, doi: 10.1016/j.jcis.2012.11.042.
- [112] “Crystal Perfection of Particle Monolayer at the Air–Water Interface | Langmuir.” <https://pubs.acs.org/doi/abs/10.1021/acs.langmuir.5b03151> (accessed Jun. 02, 2020).

- [113] O. S. Deshmukh, D. van den Ende, M. C. Stuart, F. Mugele, and M. H. G. Duits, “Hard and soft colloids at fluid interfaces: Adsorption, interactions, assembly & rheology,” *Adv. Colloid Interface Sci.*, vol. 222, pp. 215–227, Aug. 2015, doi: 10.1016/j.cis.2014.09.003.
- [114] V. Lotito and T. Zambelli, “Approaches to self-assembly of colloidal monolayers: A guide for nanotechnologists,” *Adv. Colloid Interface Sci.*, vol. 246, pp. 217–274, Aug. 2017, doi: 10.1016/j.cis.2017.04.003.
- [115] Y. Min, M. Akbulut, K. Kristiansen, Y. Golan, and J. Israelachvili, “The role of interparticle and external forces in nanoparticle assembly,” *Nat. Mater.*, vol. 7, no. 7, pp. 527–538, Jul. 2008, doi: 10.1038/nmat2206.
- [116] S. Atiganyanun, M. Zhou, O. K. Abudayyeh, S. M. Han, and S. E. Han, “Control of Randomness in Microsphere-Based Photonic Crystals Assembled by Langmuir–Blodgett Process,” *Langmuir*, vol. 33, no. 48, pp. 13783–13789, Dec. 2017, doi: 10.1021/acs.langmuir.7b03060.
- [117] P. Stavroulakis, S. Boden, T. Johnson, and D. M. Bagnall, “Suppression of backscattered diffraction from sub-wavelength ‘moth-eye’ arrays,” *Opt. Express*, vol. 21, pp. 1–11, Jan. 2013, doi: 10.1364/OE.21.000001.
- [118] “Atomic Force Microscopy - an overview | ScienceDirect Topics.” <https://www.sciencedirect.com/topics/physics-and-astronomy/atomic-force-microscopy> (accessed Jul. 02, 2020).
- [119] K. Akhtar, S. A. Khan, S. B. Khan, and A. M. Asiri, “Scanning Electron Microscopy: Principle and Applications in Nanomaterials Characterization,” in *Handbook of Materials Characterization*, S. K. Sharma, Ed. Cham: Springer International Publishing, 2018, pp. 113–145. doi: 10.1007/978-3-319-92955-2_4.
- [120] M. Sezen, “Focused Ion Beams (FIB) — Novel Methodologies and Recent Applications for Multidisciplinary Sciences,” *Mod. Electron Microsc. Phys. Life Sci.*, Feb. 2016, doi: 10.5772/61634.
- [121] “UV/VIS Spectroscopy - an overview | ScienceDirect Topics.” <https://www.sciencedirect.com/topics/chemistry/uv-vis-spectroscopy> (accessed Nov. 14, 2020).
- [122] A. A. Ismail, F. R. van de Voort, and J. Sedman, “Chapter 4 Fourier transform infrared spectroscopy: Principles and applications,” in *Techniques and Instrumentation in Analytical Chemistry*, vol. 18, J. R. J. Paré and J. M. R. Bélanger, Eds. Elsevier, 1997, pp. 93–139. doi: 10.1016/S0167-9244(97)80013-3.
- [123] “X Ray Diffraction - an overview | ScienceDirect Topics.” <https://www.sciencedirect.com/topics/medicine-and-dentistry/x-ray-diffraction> (accessed Nov. 14, 2020).
- [124] H. Fitouri, M. M. Habchi, and A. Rebey, “High-Resolution X-Ray Diffraction of III–V Semiconductor Thin Films,” *X-Ray Scatt.*, Jan. 2017, doi: 10.5772/65404.
- [125] D. W. Shipp, F. Sinjab, and I. Notingher, “Raman spectroscopy: techniques and applications in the life sciences,” *Adv. Opt. Photonics*, vol. 9, no. 2, pp. 315–428, Jun. 2017, doi: 10.1364/AOP.9.000315.
- [126] M. Wojdyr, “Fityk: a general-purpose peak fitting program,” *J. Appl. Crystallogr.*, vol. 43, no. 5, Art. no. ARRAY(0xacefa08), Oct. 2010, doi: 10.1107/S0021889810030499.
- [127] P. Patoka and M. Giersig, “Self-assembly of latex particles for the creation of nanostructures with tunable plasmonic properties,” *J. Mater. Chem.*, vol. 21, no. 42, pp. 16783–16796, Oct. 2011, doi: 10.1039/C1JM11936B.
- [128] Ph. Buffat and J.-P. Borel, “Size effect on the melting temperature of gold particles,” *Phys. Rev. A*, vol. 13, no. 6, pp. 2287–2298, Jun. 1976, doi: 10.1103/PhysRevA.13.2287.

- [129] C. Zhao *et al.*, “Tailoring Plasmon Resonances in Aluminium Nanoparticle Arrays Fabricated Using Anodic Aluminium Oxide,” *Adv. Opt. Mater.*, vol. 3, no. 2, pp. 248–256, 2015, doi: 10.1002/adom.201400325.
- [130] A. Kosinova *et al.*, “Tuning the nanoscale morphology and optical properties of porous gold nanoparticles by surface passivation and annealing,” *Acta Mater.*, vol. 127, pp. 108–116, Apr. 2017, doi: 10.1016/j.actamat.2017.01.014.
- [131] F. Font and T. G. Myers, “Spherically symmetric nanoparticle melting with a variable phase change temperature,” *J. Nanoparticle Res.*, vol. 15, no. 12, p. 2086, Nov. 2013, doi: 10.1007/s11051-013-2086-3.
- [132] G. L. Allen, R. A. Bayles, W. W. Gile, and W. A. Jesser, “Small particle melting of pure metals,” *Thin Solid Films*, vol. 144, no. 2, pp. 297–308, Nov. 1986, doi: 10.1016/0040-6090(86)90422-0.
- [133] S. K. Gupta, M. Talati, and P. K. Jha, “Shape and Size Dependent Melting Point Temperature of Nanoparticles,” *Materials Science Forum*, 2008. <https://www.scientific.net/MSF.570.132> (accessed Jul. 27, 2020).
- [134] C. M. Müller, F. C. F. Mornaghini, and R. Spolenak, “Ordered arrays of faceted gold nanoparticles obtained by dewetting and nanosphere lithography,” *Nanotechnology*, vol. 19, no. 48, p. 485306, Nov. 2008, doi: 10.1088/0957-4484/19/48/485306.
- [135] F. Gao and Z. Gu, “Melting Temperature of Metallic Nanoparticles,” in *Handbook of Nanoparticles*, M. Aliofkhazraei, Ed. Cham: Springer International Publishing, 2016, pp. 661–690. doi: 10.1007/978-3-319-15338-4_6.
- [136] P. Antoniammal and D. Arivuoli, “Size and Shape Dependence on Melting Temperature of Gallium Nitride Nanoparticles,” *Journal of Nanomaterials*, Jun. 03, 2012. <https://www.hindawi.com/journals/jnm/2012/415797/> (accessed Jul. 27, 2020).
- [137] C. V. Thompson, “Solid-State Dewetting of Thin Films,” *Annu. Rev. Mater. Res.*, vol. 42, no. 1, pp. 399–434, Jul. 2012, doi: 10.1146/annurev-matsci-070511-155048.
- [138] P. Farzinpour, A. Sundar, K. D. Gilroy, Z. E. Eskin, R. A. Hughes, and S. Neretina, “Altering the dewetting characteristics of ultrathin gold and silver films using a sacrificial antimony layer,” *Nanotechnology*, vol. 23, no. 49, p. 495604, Nov. 2012, doi: 10.1088/0957-4484/23/49/495604.
- [139] A. Kosinova *et al.*, “Tuning the nanoscale morphology and optical properties of porous gold nanoparticles by surface passivation and annealing,” *Acta Mater.*, vol. 127, pp. 108–116, Apr. 2017, doi: 10.1016/j.actamat.2017.01.014.
- [140] A. H. Tavakoli *et al.*, “Amorphous Alumina Nanoparticles: Structure, Surface Energy, and Thermodynamic Phase Stability,” *J. Phys. Chem. C*, vol. 117, no. 33, pp. 17123–17130, Aug. 2013, doi: 10.1021/jp405820g.
- [141] J. M. McHale, A. Auroux, A. J. Perrotta, and A. Navrotsky, “Surface Energies and Thermodynamic Phase Stability in Nanocrystalline Aluminas,” *Science*, vol. 277, no. 5327, pp. 788–791, Aug. 1997, doi: 10.1126/science.277.5327.788.
- [142] L. Vitos, A. V. Ruban, H. L. Skriver, and J. Kollár, “The surface energy of metals,” *Surf. Sci.*, vol. 411, no. 1, pp. 186–202, Aug. 1998, doi: 10.1016/S0039-6028(98)00363-X.
- [143] R. M. Pilliar and J. Nutting, “Solid-solid interfacial energy determinations in metal-ceramic systems,” *Philos. Mag. J. Theor. Exp. Appl. Phys.*, vol. 16, no. 139, pp. 181–188, Jul. 1967, doi: 10.1080/14786436708229267.
- [144] D. Holec, P. Dumitraschkewitz, F. D. Fischer, and D. Vollath, “Size-dependent surface energies of Au nanoparticles,” *ArXiv14127195 Cond-Mat*, Mar. 2018, Accessed: Jul. 27, 2020. [Online]. Available: <http://arxiv.org/abs/1412.7195>

- [145] N. Masoud, T. Partsch, K. P. de Jong, and P. E. de Jongh, "Thermal stability of oxide-supported gold nanoparticles," *GOLD BULLETIN*, Jun. 2019. <http://localhost/handle/1874/389801> (accessed Jul. 28, 2020).
- [146] D. Chatterjee, A. R. K. Kamalnath, R. Ahmad, A. K. Singh, and N. Ravishankar, "Orientation Selection during Heterogeneous Nucleation: Implications for Heterogeneous Catalysis," *J. Phys. Chem. C*, vol. 121, no. 18, pp. 10027–10037, May 2017, doi: 10.1021/acs.jpcc.7b02237.
- [147] E. J. Siem, W. C. Carter ‡, and D. Chatain §, "The equilibrium shape of anisotropic interfacial particles," *Philos. Mag.*, vol. 84, no. 10, pp. 991–1010, Apr. 2004, doi: 10.1080/14786430310001639897.
- [148] W. W. Mullins and G. S. Rohrer, "Nucleation Barrier for Volume-Conserving Shape Changes of Faceted Crystals," *J. Am. Ceram. Soc.*, vol. 83, no. 1, pp. 214–16, 2000, doi: 10.1111/j.1151-2916.2000.tb01173.x.
- [149] G. S. Rohrer, C. L. Rohrer, and W. W. Mullins, "Coarsening of Faceted Crystals," *J. Am. Ceram. Soc.*, vol. 85, no. 3, pp. 675–682, 2002, doi: 10.1111/j.1151-2916.2002.tb00149.x.
- [150] J. Lu, Y. Hong, Q. Li, Y. Xu, W. Fang, and M. Qiu, "Light-induced reversible expansion of individual gold nanoplates," *AIP Adv.*, vol. 7, no. 10, p. 105025, Oct. 2017, doi: 10.1063/1.4998703.
- [151] D. R. Lide, *CRC handbook of chemistry and physics: a ready-reference book of chemical and physical data*. Boca Raton, FL: CRC Press, 1992.
- [152] S. Shi, S. Qian, X. Hou, J. Mu, J. He, and X. Chou, "Structural and Optical Properties of Amorphous Al₂O₃ Thin Film Deposited by Atomic Layer Deposition," *Advances in Condensed Matter Physics*, Mar. 06, 2018. <https://www.hindawi.com/journals/acmp/2018/7598978/> (accessed Oct. 01, 2020).
- [153] J. Kischkat *et al.*, "Mid-infrared optical properties of thin films of aluminum oxide, titanium dioxide, silicon dioxide, aluminum nitride, and silicon nitride," *Appl. Opt.*, vol. 51, no. 28, pp. 6789–6798, Oct. 2012, doi: 10.1364/AO.51.006789.
- [154] R. J. Wells, "Rapid approximation to the Voigt/Faddeeva function and its derivatives," *J. Quant. Spectrosc. Radiat. Transf.*, vol. 62, no. 1, pp. 29–48, May 1999, doi: 10.1016/S0022-4073(97)00231-8.
- [155] J. Y. Suh, E. U. Donev, D. W. Ferrara, K. A. Tetz, L. C. Feldman, and R. F. H. Jr, "Modulation of the gold particle–plasmon resonance by the metal–semiconductor transition of vanadium dioxide," *J. Opt. Pure Appl. Opt.*, vol. 10, no. 5, p. 055202, Mar. 2008, doi: 10.1088/1464-4258/10/5/055202.
- [156] G. Xu, C.-M. Huang, M. Tazawa, P. Jin, and L.-H. Chen, "Tunable optical properties of nano-Au on vanadium dioxide," *Opt. Commun.*, vol. 282, no. 5, pp. 896–902, Mar. 2009, doi: 10.1016/j.optcom.2008.11.045.
- [157] Y. Li *et al.*, "Active macroscale visible plasmonic nanorod self-assembled monolayer," *Photonics Res.*, vol. 6, no. 5, pp. 409–416, May 2018, doi: 10.1364/PRJ.6.000409.
- [158] "Plasmonic Probe of the Semiconductor to Metal Phase Transition in Vanadium Dioxide | Nano Letters." <https://pubs.acs.org/doi/abs/10.1021/nl401823r> (accessed Oct. 14, 2020).
- [159] H. Matsui, Y.-L. Ho, T. Kanki, H. Tanaka, J.-J. Delaunay, and H. Tabata, "Mid-infrared Plasmonic Resonances in 2D VO₂ Nanosquare Arrays," *Adv. Opt. Mater.*, vol. 3, no. 12, pp. 1759–1767, 2015, doi: <https://doi.org/10.1002/adom.201500322>.
- [160] D. W. Ferrara, J. Nag, E. R. MacQuarrie, A. B. Kaye, and R. F. Haglund, "Plasmonic Probe of the Semiconductor to Metal Phase Transition in Vanadium Dioxide," *Nano Lett.*, vol. 13, no. 9, pp. 4169–4175, Sep. 2013, doi: 10.1021/nl401823r.

- [161] L. Zhao, K. L. Kelly, and G. C. Schatz, "The Extinction Spectra of Silver Nanoparticle Arrays: Influence of Array Structure on Plasmon Resonance Wavelength and Width," *J. Phys. Chem. B*, vol. 107, no. 30, pp. 7343–7350, Jul. 2003, doi: 10.1021/jp034235j.
- [162] K. Appavoo *et al.*, "Role of Defects in the Phase Transition of VO₂ Nanoparticles Probed by Plasmon Resonance Spectroscopy," *Nano Lett.*, vol. 12, no. 2, pp. 780–786, Feb. 2012, doi: 10.1021/nl203782y.
- [163] P. Zhang *et al.*, "Manipulations from oxygen partial pressure on the higher energy electronic transition and dielectric function of VO₂ films during a metal–insulator transition process," *J. Mater. Chem. C*, vol. 3, no. 19, pp. 5033–5040, May 2015, doi: 10.1039/C5TC00002E.
- [164] "Surface Plasmons and Optical Dynamics on Vanadium Dioxide | IntechOpen." https://www.intechopen.com/books/novel-imaging-and-spectroscopy/surface-plasmons-and-optical-dynamics-on-vanadium-dioxide?fbclid=IwAR1U-TPBSD_FTDn3B43gvj9WRXrje1Yl-kvaB4bv6THFVHFITjRM67eR5Ik (accessed Mar. 01, 2021).
- [165] "Energy Dispersive X-Ray Spectroscopy - an overview | ScienceDirect Topics." <https://www.sciencedirect.com/topics/engineering/energy-dispersive-x-ray-spectroscopy> (accessed Oct. 20, 2020).
- [166] E. Leitgeb *et al.*, "Analysis and evaluation of optimum wavelengths for free-space optical transceivers," in *2010 12th International Conference on Transparent Optical Networks*, Jun. 2010, pp. 1–7. doi: 10.1109/ICTON.2010.5549009.
- [167] G. Xu, C.-M. Huang, M. Tazawa, P. Jin, D.-M. Chen, and L. Miao, "Electron injection assisted phase transition in a nano-Au-VO₂ junction," *Appl. Phys. Lett.*, vol. 93, no. 6, p. 061911, Aug. 2008, doi: 10.1063/1.2972106.
- [168] J.-C. Orlianges, J. Leroy, A. Crunteanu, R. Mayet, P. Carles, and C. Champeaux, "Electrical and optical properties of vanadium dioxide containing gold nanoparticles deposited by pulsed laser deposition," *Appl. Phys. Lett.*, vol. 101, no. 13, p. 133102, Sep. 2012, doi: 10.1063/1.4754708.
- [169] J. Lowell and A. C. Rose-Innes, "Contact electrification," *Adv. Phys.*, vol. 29, no. 6, pp. 947–1023, Dec. 1980, doi: 10.1080/00018738000101466.
- [170] M. Yang *et al.*, "Surface-growth-mode-induced strain effects on the metal–insulator transition in epitaxial vanadium dioxide thin films," *RSC Adv.*, vol. 5, no. 98, pp. 80122–80128, Sep. 2015, doi: 10.1039/C5RA13490K.
- [171] V. Théry *et al.*, "Role of thermal strain in the metal-insulator and structural phase transition of epitaxial $\{\mathrm{VO}\}_2$ films," *Phys. Rev. B*, vol. 93, no. 18, p. 184106, May 2016, doi: 10.1103/PhysRevB.93.184106.
- [172] D. Balzar, "X-Ray Diffraction Line Broadening: Modeling and Applications to High-Tc Superconductors," *J. Res. Natl. Inst. Stand. Technol.*, vol. 98, no. 3, pp. 321–353, 1993, doi: 10.6028/jres.098.026.
- [173] E. R. Shaaban *et al.*, "Structural, linear and nonlinear optical properties of co-doped ZnO thin films," *Appl. Phys. A*, vol. 122, no. 1, p. 20, Dec. 2015, doi: 10.1007/s00339-015-9551-z.
- [174] J. I. Langford and D. Louër, "Powder diffraction," *Rep. Prog. Phys.*, vol. 59, no. 2, pp. 131–234, Feb. 1996, doi: 10.1088/0034-4885/59/2/002.
- [175] "X-ray Diffraction Methods to Study Crystallite Size and Lattice Constants of Carbon Materials - ScienceDirect." <https://www.sciencedirect.com/science/article/pii/B9780080441634500103> (accessed Nov. 09, 2020).

- [176] M. Shiraishi and M. Inagaki, "Chapter 10 - X-ray Diffraction Methods to Study Crystallite Size and Lattice Constants of Carbon Materials," in *Carbon Alloys*, E. Yasuda, M. Inagaki, K. Kaneko, M. Endo, A. Oya, and Y. Tanabe, Eds. Oxford: Elsevier Science, 2003, pp. 161–173. doi: 10.1016/B978-008044163-4/50010-3.
- [177] A. R. Stokes and A. J. C. Wilson, "The diffraction of X rays by distorted crystal aggregates - I," *Proc. Phys. Soc.*, vol. 56, no. 3, pp. 174–181, May 1944, doi: 10.1088/0959-5309/56/3/303.
- [178] V. Théry *et al.*, "Structural and electrical properties of large area epitaxial VO₂ films grown by electron beam evaporation," *J. Appl. Phys.*, vol. 121, no. 5, p. 055303, Feb. 2017, doi: 10.1063/1.4975117.
- [179] A. Authier, *Dynamical Theory of X-ray Diffraction*. Oxford University Press, 2001.
- [180] P. P. EWALD, "Crystal Optics for Visible Light and X Rays," *Rev. Mod. Phys.*, vol. 37, no. 1, pp. 46–56, Jan. 1965, doi: 10.1103/RevModPhys.37.46.
- [181] P. Shvets, O. Dikaya, K. Maksimova, and A. Goikhman, "A review of Raman spectroscopy of vanadium oxides," *J. Raman Spectrosc.*, vol. 50, no. 8, Art. no. 8, 2019, doi: 10.1002/jrs.5616.
- [182] A. M. Makarevich *et al.*, "Chemical synthesis of high quality epitaxial vanadium dioxide films with sharp electrical and optical switch properties," *J. Mater. Chem. C*, vol. 3, no. 35, pp. 9197–9205, Aug. 2015, doi: 10.1039/C5TC01811K.
- [183] S. S. Majid *et al.*, "Insulator-metal transitions in the T phase Cr-doped and $M1$ phase undoped VO_2 thin films," *Phys. Rev. B*, vol. 98, no. 7, p. 075152, Aug. 2018, doi: 10.1103/PhysRevB.98.075152.
- [184] B. T. O'Callahan, A. C. Jones, J. Hyung Park, D. H. Cobden, J. M. Atkin, and M. B. Raschke, "Inhomogeneity of the ultrafast insulator-to-metal transition dynamics of VO₂," *Nat. Commun.*, vol. 6, p. 6849, Apr. 2015, doi: 10.1038/ncomms7849.
- [185] H. Zhang *et al.*, "The structural phase transition process of free-standing monoclinic vanadium dioxide micron-sized rods: temperature-dependent Raman study," *RSC Adv.*, vol. 5, no. 101, pp. 83139–83143, Sep. 2015, doi: 10.1039/C5RA15947D.
- [186] D. H. Jung *et al.*, "Electrical and optical properties of VO₂ thin films grown on various sapphire substrates by using RF sputtering deposition," *J. KOREAN Phys. Soc.*, vol. 69, no. 12, p. 1787, 2016.
- [187] P. Arora, E. Talker, N. Mazurski, and U. Levy, "Dispersion engineering with plasmonic nano structures for enhanced surface plasmon resonance sensing," *Sci. Rep.*, vol. 8, no. 1, p. 9060, Jun. 2018, doi: 10.1038/s41598-018-27023-x.
- [188] K. Diest, V. Liberman, D. Lennon, P. Welander, and M. Rothschild, "Aluminum plasmonics: Optimization of plasmonic properties using liquid-prism-coupled ellipsometry," *Opt. Express*, vol. 21, pp. 28638–50, Nov. 2013, doi: 10.1364/OE.21.028638.
- [189] C. Zhao, J. Zhang, and Y. Liu, "Light Manipulation with Encoded Plasmonic Nanostructures," *EPJ Appl. Metamaterials*, vol. 1, p. 6, Dec. 2014, doi: 10.1051/epjam/2014006.
- [190] X. Fan, W. Zheng, and D. J. Singh, "Light scattering and surface plasmons on small spherical particles," *Light Sci. Appl.*, vol. 3, no. 6, pp. e179–e179, Jun. 2014, doi: 10.1038/lsa.2014.60.
- [191] C. Forestiere, G. Iadarola, L. Dal Negro, and G. Miano, "Near-field calculation based on the T-matrix method with discrete sources," *J. Quant. Spectrosc. Radiat. Transf.*, vol. 112, no. 14, pp. 2384–2394, Sep. 2011, doi: 10.1016/j.jqsrt.2011.05.009.

- [192] N. G. Khlebtsov, “T-matrix method in plasmonics: An overview,” *J. Quant. Spectrosc. Radiat. Transf.*, vol. 123, pp. 184–217, Jul. 2013, doi: 10.1016/j.jqsrt.2012.12.027.
- [193] M. A. Yurkin and A. G. Hoekstra, “The discrete dipole approximation: An overview and recent developments,” *J. Quant. Spectrosc. Radiat. Transf.*, vol. 106, no. 1, pp. 558–589, Jul. 2007, doi: 10.1016/j.jqsrt.2007.01.034.
- [194] “Interaction of Localized Surface Plasmons of a Silver Nanosphere Dimer Embedded in a Uniform Medium: Scanning Transmission Electron Microscopy Electron Energy-Loss Spectroscopy and Discrete Dipole Approximation Simulation | The Journal of Physical Chemistry C.” <https://pubs.acs.org/doi/10.1021/acs.jpcc.8b11434> (accessed Jun. 01, 2020).
- [195] X. Xu *et al.*, “Discrete Dipole Approximation Simulation of the Surface Plasmon Resonance of Core/Shell Nanostructure and the Study of Resonance Cavity Effect,” *J. Phys. Chem. C*, vol. 116, no. 45, pp. 24046–24053, Nov. 2012, doi: 10.1021/jp306238x.
- [196] K.-H. Kim and M. A. Yurkin, “Time-domain discrete-dipole approximation for simulation of temporal response of plasmonic nanoparticles,” *Opt. Express*, vol. 23, no. 12, pp. 15555–15564, Jun. 2015, doi: 10.1364/OE.23.015555.
- [197] M. Osawa, “Surface-Enhanced Infrared Absorption,” *Top. Appl. Phys.*, vol. 81, pp. 163–187, Jan. 2001.
- [198] L. Wu and X. Jiang, “Infrared Spectroscopy for Studying Plasma Membranes,” in *Membrane Biophysics: New Insights and Methods*, 2018, pp. 319–354. doi: 10.1007/978-981-10-6823-2_11.
- [199] Á. I. López-Lorente, P. Wang, and B. Mizaikoff, “Towards label-free mid-infrared protein assays: in-situ formation of bare gold nanoparticles for surface enhanced infrared absorption spectroscopy of bovine serum albumin,” *Microchim. Acta*, vol. 184, no. 2, pp. 453–462, Feb. 2017, doi: 10.1007/s00604-016-2031-0.
- [200] “Phys. Rev. Lett. 94, 026404 (2005) - Dynamical Singlets and Correlation-Assisted Peierls Transition in V_2O_3 .” <https://journals.aps.org/prl/abstract/10.1103/PhysRevLett.94.026404> (accessed Jun. 02, 2020).
- [201] H. Zheng and L. K. Wagner, “Computation of the Correlated Metal-Insulator Transition in Vanadium Dioxide from First Principles,” *Phys. Rev. Lett.*, vol. 114, no. 17, p. 176401, Apr. 2015, doi: 10.1103/PhysRevLett.114.176401.
- [202] O. Nájera, M. Civelli, V. Dobrosavljević, and M. Rozenberg, “Resolving the VO₂ controversy: Mott mechanism dominates the insulator-to-metal transition,” *Phys. Rev. B*, vol. 95, Jan. 2017, doi: 10.1103/PhysRevB.95.035113.
- [203] MC. Rao, “A Brief Introduction to Excimer Lasers: Fundamental Study, IJAPBC – Vol. 2(3), Jul-Sep, 2013 ISSN: 2277 - 4688.” <http://www.ijapbc.com/archives7.html> (accessed Sep. 02, 2013).
- [204] H. Abramczyk, *Introduction to Laser Spectroscopy*. Elsevier, 2005.
- [205] R. Paetzel, “Comparison excimer laser – Solid state laser,” *Int. Congr. Appl. Lasers Electro-Opt.*, vol. 2002, no. 1, p. 163015, Oct. 2002, doi: 10.2351/1.5066151.
- [206] C. Ma *et al.*, “Longitudinally diode-pumped planar waveguide YAG/Yb:LuAG/YAG ceramic laser at 1030.7 nm,” *Opt. Lett.*, vol. 41, no. 14, pp. 3317–3319, Jul. 2016, doi: 10.1364/OL.41.003317.
- [207] “Colloid Science: Principles, Methods and Applications, 2nd Edition , p. 36–49, Chapter 3 | Wiley,” <https://www.wiley.com/en-us/Colloid+Science%3A+Principles%2C+Methods+and+Applications%2C+2nd+Edition-p-9781444320206> (accessed Jun. 02, 2020).

- [208] J. N. Israelachvili, Ed., “Units, Symbols, Useful Quantities and Relations,” in *Intermolecular and Surface Forces (Third Edition)*, San Diego: Academic Press, 2011, pp. xxiii–xxviii. doi: 10.1016/B978-0-12-375182-9.10030-2.
- [209] “Colloid Science: Principles, Methods and Applications, 2nd Edition, p. 14–35 Chapter 2, | Wiley,” *Wiley.com*. <https://www.wiley.com/en-us/Colloid+Science%3A+Principles%2C+Methods+and+Applications%2C+2nd+Edition-p-9781444320206> (accessed Jun. 02, 2020).
- [210] J. van Duijneveldt, “Effect of Polymers on Colloid Stability, Chapter 8,” in *Colloid Science*, John Wiley & Sons, Ltd, 2009, pp. 143–158. doi: 10.1002/9781444305395.ch8.

Appendix 1. Appendix for Chapter I

Appendix 1.1. Coupling of light to a surface plasmon using a prism

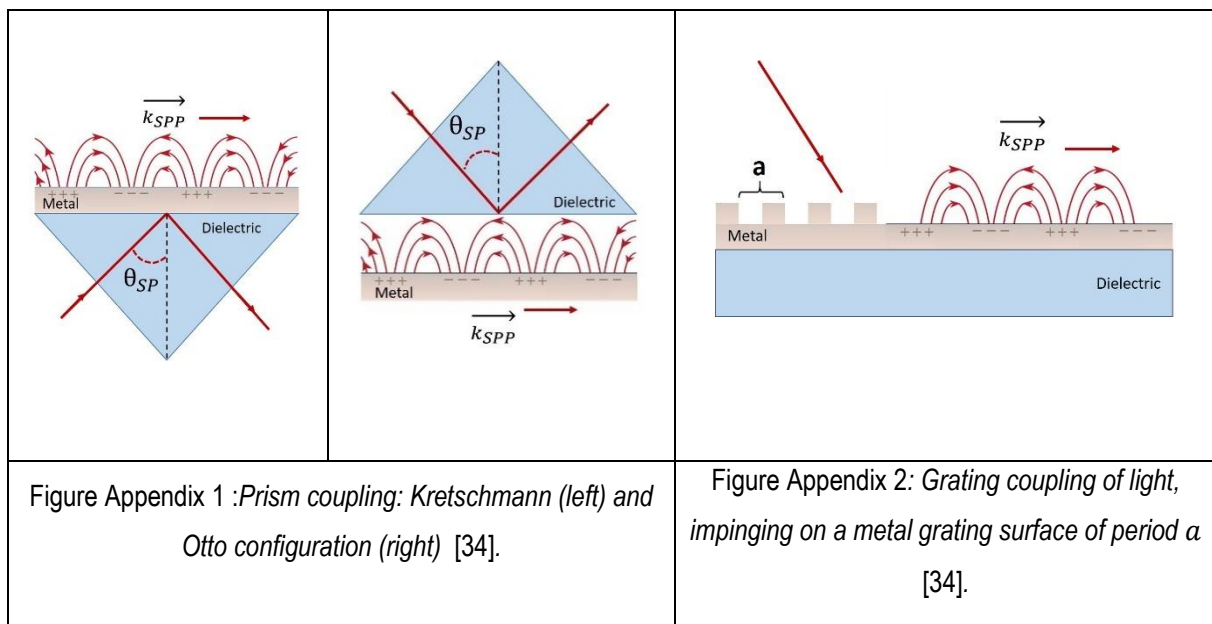
The coupling of light to a surface plasmon using a prism is known as an attenuated total internal reflection (TIR). Prism coupling is possible in two configurations referred to as the Kretschmann-configuration [187] and Otto configuration [188] (see Figure Appendix 1). Both configurations involve the coupling of the SPPs to the evanescent electromagnetic field formed upon total internal reflection of a light beam at a surface in an optically dense medium.

By using the diffraction effects of a grating pattern on the metal surface is possible to overcome the mismatch in the wavevector between the in-plane momentum $k_x = k \sin \theta$ of impinging photons and β [189]. If we consider a system (see Figure Appendix 2) based on a one-dimensional grating of grooves, with a lattice constant a , then the phase matching will take place when the condition expressed in Equation (A.1) is fulfilled.

$$\beta = k \sin \theta_{SP} \pm n \frac{2\pi}{a} \quad \text{Equation (A.1)}$$

where $\frac{2\pi}{a}$ is the reciprocal vector of the grating and $n = 1, 2, 3, \dots$

The grating coupling method allows us to define a better-confined region as the SPP source, compared to prism coupling [34].



Excitation of SPP using highly focused optical beams is based on the prism coupling technique, where a microscope objective that has high numerical aperture (NA) is used for SPP excitation [31], [34], [189]. In this case, the objective is immersed in oil, index-matched to the metal surface, and the high NA of the objective ensures a large angular spread of the focused excitation beam. The angular spread is sufficiently large to overcome the critical angle of the total internal reflection. Therefore, wave vectors $k_x = \beta$ are available for phase matching to SPPs at the metal-air interface. This method is particularly useful for the excitation of SPPs at a variety of frequencies.

Excitation of SPP by prism coupling, grating coupling, or using highly focused optical beams is subjected to limitation induced by the diffraction limit of light. In principle, near-field excitation provides the possibility to excite SPP locally with sub-wavelength resolution.

By squeezing photons through a metal tip or an aperture smaller than the SPP wavelength, photons acquire enough lateral momentum to couple to SPP [34].

Appendix 1.2. Techniques used to simulate the scattering of electromagnetic radiation by metallic nanoparticles

Mie theory [43], [190] is a solution of the Maxwell equations that can be applied to deduce the scattering of an incident plane wave by a spherical, isotropic, and non-magnetic nanoparticle, placed in a non-absorbing isotropic medium and working under the assumption that in the region of interest there are no sources (charges or currents). Mie theory is most of the time used for simulating the optical response of metallic nanoparticles because, in principle, it offers an exact solution for the scattering of electromagnetic radiation by spherical geometries that is limited only by the truncation order of the solution. The Mie theory can be adapted to simulate the optical response of other spherically symmetric geometries such as systems of dielectric particles with metallic coatings.

The linearity of the Maxwell equations certifies a direct relationship between the coefficients of the vector spherical harmonics of the incident and scattered electric and magnetic fields. In the matrix representation, an operator called Transition Matrix (T-Matrix) links the coefficients of the incident and scattered electric and magnetic fields.

$$\begin{bmatrix} a_n^{scattered} \\ b_n^{scattered} \end{bmatrix} = \begin{bmatrix} T_{11} & T_{12} \\ T_{21} & T_{22} \end{bmatrix} \begin{bmatrix} a_n^{incident} \\ b_n^{incident} \end{bmatrix} \quad \text{Equation (A.2)}$$

where T terms correspond to the elements of the T-Matrix, $a_n^{scattered}$, $b_n^{scattered}$, $a_n^{incident}$, $b_n^{incident}$ are the coefficients of the scattered and incident field, respectively.

The elements of the T-matrix are linked only to the relative refractive index of the nanoparticle $m = \frac{n_1}{n_2}$ (n_1 is the complex refractive index of the nanoparticle and n_2 is the refractive index of the surrounding environment), the orientation of the nanoparticle concerning the coordinate system and the size parameter $\chi = \frac{2\pi n_2 a}{\lambda}$ (a is the radius of the nanoparticle and λ is the wavelength in vacuum). The essential advantage of this method is that T-matrix is the property of a nanoparticle. Therefore, once it has been determined, the scattered fields can be computed for any nanoparticle orientation without starting everything from scratch. This technique can also be used for determining the optical response of an array of symmetrical nanoparticles. For more information about the T-matrix technique, see also [191], [192].

In the discrete-dipole approximation (DDA), each nanoparticle is modeled as an array of N finite cubic elements or cells. In DDA, each cell is taken sufficiently small so that only dipole interactions with the incident electric field and induced fields in the neighboring cells have to be considered. This method of taking small cells reduces the solution of Maxwell equations to an algebraic problem of many coupled dipoles [43]. In this way, every dipole in the array acquires a dipole moment in response to the external electric field and at the same time in response to the electric fields from the neighboring dipoles. The radiated electric field of an individual dipole in the array can be approximated by the following expression:

$$\mathbf{E}_{dipole} = \frac{e \frac{i\omega d}{c}}{4\pi\epsilon_0} \left[\frac{\omega^2}{c^2 d} \hat{\mathbf{r}} \cdot \mathbf{p} \hat{\mathbf{r}} + \left(\frac{1}{d^3} - \frac{i\omega}{cd^2} \right) [3(\hat{\mathbf{r}} \cdot \mathbf{p})\hat{\mathbf{r}} - \mathbf{p}] \right] \quad \text{Equation (A.3)}$$

where $\hat{\mathbf{r}}$ is the unit vector associated with a vector \mathbf{r} that is taken from the dipole to the location at which the electric field is analyzed, d is the distance to the sampling point, \mathbf{p} is the vector associated with the induced dipole moment, ω is the angular frequency of the scattered radiation and ϵ_0 is the permittivity of free space [43].

In the calculation of the scattering characteristics of the continuous array, every dipole in the cubic assembly has an induced dipole moment given by: $P_i = \alpha_i \mathbf{E}_{local}$, where α_i is the polarizability of the material associated with the dipole moment. Polarizability is the way by which the material parameters are introduced into the simulation.

The electric field \mathbf{E}_{local} at \mathbf{r}_i is given by the contribution of the incident wave, $\mathbf{E}_{inc,i}$, plus the contribution of all the other dipoles, \mathbf{E}_j , and can be express as:

$$\mathbf{E}_{local} = \mathbf{E}_{inc,i} + \sum_{\substack{j=1 \\ i \neq j}}^N \mathbf{E}_j = \mathbf{E}_{inc,i} - \sum_{\substack{j=1 \\ i \neq j}}^N \mathbf{A}_{ij} \mathbf{p}_j \quad \text{Equation (A.4)}$$

$$\text{where: } \mathbf{A}_{ij} \mathbf{p}_j = k^2 e^{ir_{ij}} \left(\frac{\hat{\mathbf{p}}_j \left(r_{ij} \frac{(\mathbf{r}_{ij} \cdot \mathbf{p}_j)}{r_{ij}^3} \right)}{r_{ij}^3} \right) + e^{ikr_{ij}(1-ikr_{ij})} \left(\frac{r_{ij}^2 \mathbf{p}_j - 3\hat{\mathbf{p}}_j (r_{ij} (\mathbf{r}_{ij} \cdot \mathbf{p}_j))}{r_{ij}^5} \right) \quad \text{Equation (A.5)}$$

where: $i = 1, 2, \dots, N, j = 1, 2, \dots, N$ and $i \neq j$.

The interaction matrix \mathbf{A}_{ij} describes the sum of the retarded fields from all other dipoles, except for $i \neq j$. In Equation (A.5), \mathbf{r}_{ij} and \mathbf{p}_j represent the position and induced dipole moments of every cell within the array. $\hat{\mathbf{p}}_j$ represents the projection along the unit vector of the dipole moment \mathbf{p}_j [43].

Once the position, polarizability, and the scattered electric field associated with all the dipoles have been determined, the scattering efficiency (Q_{sca}) can be calculated by using Equation (A.6).

$$Q_{sca} = \frac{C_{sca}}{\pi a^2} \quad \text{Equation (A.6)}$$

i.e., the Q_{sca} is equal to the scattering cross-section C_{sca} normalized by the geometrical cross-section area of the scatter.

The C_{sca} (see Equation (A.7)) can be defined as the integral of the scattered electric field squared across a spherical surface in the far-field and later normalized by the incident irradiance $|\mathbf{E}_i|^2$.

$$C_{sca} = \frac{k}{|\mathbf{E}_i|^2} \int_{dS} |\mathbf{E}_{scattered}(\mathbf{r}'). \hat{\mathbf{r}}|^2 dS \quad \text{Equation (A.7)}$$

A critical advantage of the DDA simulation technique is that it can be utilized to evaluate the scattering properties of isotropic non-spherical nanoparticles that are axially-symmetric or can possess other planes of symmetry [43]. In some cases, DDA can be costly in computation time since the simulation is heavily dependent on the inter-dipole spacing and the total number of dipoles that are used to recreate the original scattering object. For a more in-depth description of the DDA technique, see also [193]–[196].

Appendix 1.3. Surface-Enhanced Raman Scattering and Surface-Enhanced Infrared Absorption

One important application of surface plasmons is based on enhancing the scattering process of emitters (e.g., a molecule) near metal nanostructures. Surface-Enhanced Raman Scattering (**SERS**) is such an application [31], [54], [55]. Raman scattering is the inelastic scattering of photons that can occur when photons interact with matter. In the interaction, photons can lose energy to a molecule that gets excited from the ground state to its first excited vibrational state (known as Stokes Raman scattering) or, photons can gain energy from a molecule that undergoes the opposite process (anti-Stokes Raman scattering). By this way, inelastically scattered photons contain information on the vibrational modes of the materials through which they interact [54].

Stokes bands have a stronger intensity than the anti-Stokes bands; therefore, they are normally considered when the Raman spectra are reported. The Raman signal generated by a sample can be written as [54]:

$$P_{Raman} = KN\sigma_k I \quad \text{Equation (A.8)}$$

where P_{Raman} is the Raman power measured by the detector (in [photons/s]). K accounts for a fraction of photons that, once emitted from the molecules, are collected and converted into electrons by the detector. N is the number of illuminated molecules, σ_k is the Raman cross-section of the k -th mode integrated over the bandwidth and overall the emission directions (measured in [$\text{cm}^2/\text{molecule}$]) and I is the laser intensity impinging on the sample [(measured in [$\text{photons}/\text{cm}^2 \cdot \text{s}$])].

Raman is intrinsically a very weak phenomenon. However, the Raman scattering generated by molecules can be strongly amplified by placing them near the surface of a suitable substrate (e.g., nanostructured substrates, nanoparticles, etc.), facilitating its apparition of the SERS effect [54]. The Raman and SERS scattered powers (P_{Raman} and P_{SERS}) are related through the following expression:

$$P_{SERS} = G_{SERS} P_{Raman} = G_{SERS}^{Em} G_{SERS}^{Chem} P_{Raman} \quad \text{Equation (A.9)}$$

where: G_{SERS} is the total SERS enhancement factor and accounts for the amplification induced by the suitable substrate

The total SERS enhancement envelops the total contribution of electromagnetic G_{SERS}^{Em} and chemical G_{SERS}^{Chem} contributions to the enhancement factor.

Origin of Electromagnetic Enhancement G_{SERS}^{Em} [54]:

- It arises from the localization of light at the surface of the substrate.
- It is a characteristic of the substrate, and it is independent of the type of molecule.
- It is the strongest contribution to the SERS enhancement and can reach 10^{10} .
- It is a long-range effect, compared to the length of a typical chemical bond; therefore, molecules can be placed up to 10 nm away from the substrate.

Origin of Chemical Enhancement G_{SERS}^{Chem} [54]:

- The chemical enhancement emerges from a modification of a molecule's polarizability and is usually a consequence of physicochemical interaction between the molecule and the substrate.
- Is dependent on the type of molecule.

- The chemical enhancement contribution is smaller than that of the electromagnetic one and may reach magnitude 10^2 - 10^4 .
- It is considered a short-range effect; usually, the separation distance between the molecule and the substrate must be in the range of few Angstroms.

The electromagnetic enhancement has two distinct contributions: one comes from the **local field enhancement** and the second one from the **re-radiation enhancement**. In the local field (or near field) enhancement, the excitation of surface plasmons induces a strong spatial localization and, therefore, an amplification of the laser light in a small spatial region, known as **hot spots** [54]. At the same time, the re-radiation enhancement comes from the presence of metallic structures nearby the molecule.

The metallic structures modify the efficiency with which the molecule radiates Raman power. Since the power radiated by a molecule oscillating at the Raman frequency depends on the environment surrounding it.

The electromagnetic and chemical enhancements are presented in Figure Appendix 3.

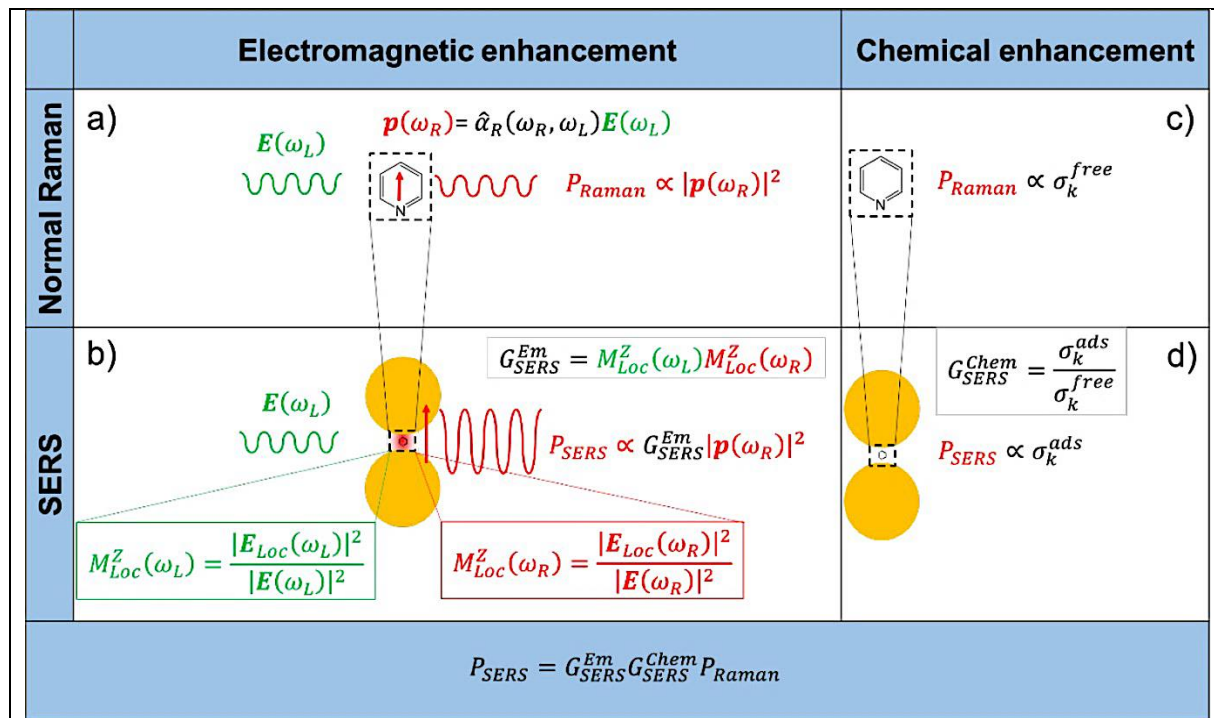


Figure Appendix 3 :Electromagnetic and chemical enhancement mechanisms: a) Normal Raman, b) SERS electromagnetic enhancement. Chemical enhancement: c) Normal Raman, d) SERS chemical enhancement. The figure is taken from reference [54].

In the classical framework of the Raman scattering, the local field enhancement can be understood starting from the following expression [54]:

$$\mathbf{p}(\omega_R) = \hat{\alpha}_R(\omega_R, \omega_L) \mathbf{E}(\omega_L) \quad \text{Equation (A.10)}$$

where $\mathbf{E}(\omega_L)$ is the external electric field, oscillating at a laser frequency ω_L , induces in the molecule a dipole ($\mathbf{p}(\omega_R)$) oscillating at the Raman frequency ω_R . And, $\hat{\alpha}_R(\omega_R, \omega_L)$ is the Raman polarizability tensor of the molecule.

The radiated power P_{Raman} is proportional to the square modulus of the dipole [54]:

$$P_{Raman} = \frac{\omega_R^4}{12\pi\epsilon_0 c^3} |\mathbf{p}(\omega_R)|^2 = \frac{\omega_R^4}{12\pi\epsilon_0 c^3} |\hat{\alpha}_R(\omega_R, \omega_L) \mathbf{E}(\omega_L)|^2 \quad \text{Equation (A.11)}$$

It is worth mentioning that in this case, P_{Raman} is derived from classical physics and is expressed as: $P_{Raman} [W] (\text{Equation (A.9)}) = \hbar\omega P_{Raman} \left[\frac{\text{photons}}{s} \right]$ (from Equation (A.8)); the angular frequency ω is measured in [radians/s] and is related to the wavenumber used in spectroscopy by $\omega = 2\pi c\tilde{\nu}$. The presence of the specific substrate (used for SERS), close to the molecule of interest, can be taken into consideration through the local electric field ($E_{LOC}(\omega_L)$) stronger than the input one, experienced by the molecule. Equation (A.11) highlights one important fact: the higher the electric field, the higher the radiated power will be. The **local field enhancement** (note: that the incident laser is linearly polarized, along the axis Z perpendicular to the propagation direction) can be expressed as:

$$M_{LOC}^Z(\omega_L) = \frac{|E_{LOC}(\omega_L)|^2}{|E(\omega_L)|^2} \quad \text{Equation (A.12)}$$

The second component of the electromagnetic enhancement, re-radiation enhancement, has a physical origin in quantum mechanics; however, it can be explained in a classical framework by making use of the self-reaction field [54]. Let us consider a dipole placed in a vacuum or embedded in a homogenous environment. In this case, the radiated power diffuses into space following the usual emission pattern of a dipole. Usually, interfaces are present around the molecules. Therefore, the electromagnetic field irradiated by the dipole is scattered at these interfaces and will be to a certain degree reflected backward at the dipole position. This back-scattered radiation or self-reaction field influences how the dipole radiates power and makes it dependent on the environment [54]. The ratio between the power radiated by a dipole placed in an inhomogeneous environment (P_{Rad}) with respect to the vacuum (P_0) can be expressed as [54]:

$$M_{Rad} = \frac{P_{Rad}}{P_0} = 1 + \frac{6\pi\epsilon_0}{|p_0|^2 k^3} \text{Im}\{p_0^* \cdot E_{SR-0}\} \quad \text{Equation (A.13)}$$

where p_0 is the complex amplitude of the dipole, E_{SR-0} represents the self-reaction field and k is the wavevector of the emitted radiation.

Even if the origin of the two electromagnetic enhancement mechanisms is different, the spectra dependence of M_{LOC}^Z and M_{Rad} is very similar [54]. The radiation emitted by the dipole can also excite surface plasmons in the substrate. This means that (for a more detailed explanation, see [54]) the re-radiation enhancement can be recast as a local field enhancement problem with an exciting laser frequency ω_R instead of ω_L . Therefore, it is possible to express G_{SERS}^{Em} containing only the local field enhancement, at the laser, and the Raman frequency, without the re-radiation problem.

The electromagnetic SERS enhancement of a single molecule can be expressed under the $|E|^4$ approximation, as [54]:

$$G_{SERS}^{Em}(E^4) = M_{LOC}^Z(\omega_L) M_{LOC}^Z(\omega_R) = \left[\frac{E_{LOC}(\omega_L)}{E(\omega_L)} \right]^2 \left[\frac{E_{LOC}(\omega_R)}{E(\omega_R)} \right]^2 \quad \text{Equation (A.14)}$$

Although beyond this thesis's scope, for scientific consistency, we will also briefly discuss chemical enhancement. In terms of magnitude, chemical enhancement is way less powerful than the electromagnetic one;

however, it is essential because it determines the SERS spectra's spectral pattern (i.e., the Raman shifts and the band intensity ratios) [54].

The adsorption of a molecule on the substrate can be classified based on the strength of the interaction between that molecule and the substrate. In this case, there are two types of adsorption: physisorption and chemisorption. Physisorption or physical adsorption is the adsorption process in which the interaction enthalpy is less negative than -25kJ/mol , while chemisorption (chemical adsorption) is the adsorption process in which the enthalpy is more negative than -40kJ/mol [54]. Van der Waals forces drive physisorption; therefore, the structure of the molecule is not significantly modified.

However, in chemisorption, a chemical bond between the molecule and the substrate is formed and, so, a stronger perturbation of the molecule structure is to be expected. Although to different degrees, both interaction mechanisms change the molecule's electronic and geometrical structure, and consequently, the Raman cross-section of vibrational modes of the molecule will change compared to those of a free molecule. The chemical enhancement is defined as [54]:

$$G_{SERS}^{Ghem} = \frac{\sigma_k^{ads}}{\sigma_k^{free}} \quad \text{Equation (A.15)}$$

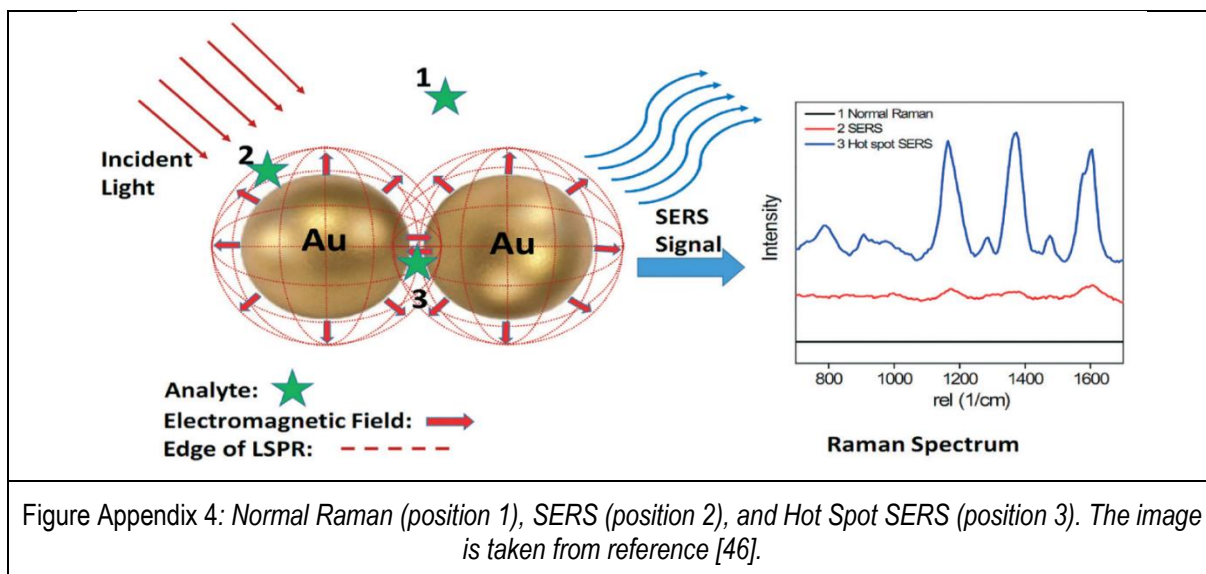
where σ_k^{ads} and σ_k^{free} are the Raman cross-sections of the k -th vibrational mode of the adsorbed and the free molecule, correspondingly.

The chemical enhancement is influenced by other mechanisms such as non-resonant chemical effect, resonant charge transfer chemical effect, and *transient* charge transfer mechanisms [54]. In a non-resonant chemical effect, the interaction between molecule and substrate does not lead to the formation of a new electronic state, and the Raman vibrational modes will just slightly change.

In resonant charge transfer chemical effect, the interaction leads to the formation of a metal-molecule charge transfer state, and by this, some of the Raman modes can be enhanced. The *transient* charge transfer mechanisms can bring the formation of a temporary electron transfer between the metal and the molecule, thus changing some Raman modes temporarily.

Role of hot spots in SERS

Figure Appendix 4 shows the schematics of a SERS process; and compares how the Raman signal looks like a function of the position in which a molecule is placed in rapport to the nanoparticles.



The electric field distribution at a surface of a plasmonic element (substrate, nanoparticle) is highly inhomogeneous, and in the case of nanoparticles, the field can be localized in the small spatial regions called “**hot spots**”.

As mentioned before, the electric field around a nanoparticle is influenced by the charge distribution of the neighboring nanoparticles and vice versa, with the higher value of electric field enhancement being between nanoparticles (see *Figure I-11*).

Therefore, the enhancement factor G_{SERS} will also be inhomogeneous and will follow the spatial distribution of the electric field enhancement. If we compare the G_{SERS} with the gap size g between neighboring nanoparticles, is possible to deduce the following expression $G_{SERS} \sim \frac{1}{g^2}$ [54]. This expression is just an approximation for a precise value of G_{SERS} the polarization of the incident light has to be taken into consideration (see *Figure I-8*). Furthermore, if $g < 1 \text{ nm}$ the quantum mechanical phenomena (like electron tunneling) can limit the increase of field enhancement and of G_{SERS} .

Surface-Enhanced Infrared Absorption (SEIRA)

To a certain degree, it is possible to consider that SEIRA and SERS phenomena have a similar mechanism behind their generation. The techniques are complementary, and both the electromagnetic and chemical effects play a crucial role. Nevertheless, there are significant differences.

The primary difference between SEIRA and SERS is that SERS happens when there is a change in the molecule's polarizability close to the substrate/surface, and SEIRA, there is a need for a change in the dipole moment perpendicular to the substrate surface [56].

In SEIRA, the incident photons are inelastically absorbed with a probability that is proportional to the product of incident light intensity and the enhancement at the plasmonic hot spot in which the absorbing material (molecule) is placed [57]. Whereas, in a Stokes (or anti-Stokes) SERS process, there is first an inelastic absorption of the incident photons (like in SEIRA) followed by an inelastic reemission process of the photons at a lower frequency with a probability proportional to the intensity enhancement [57].

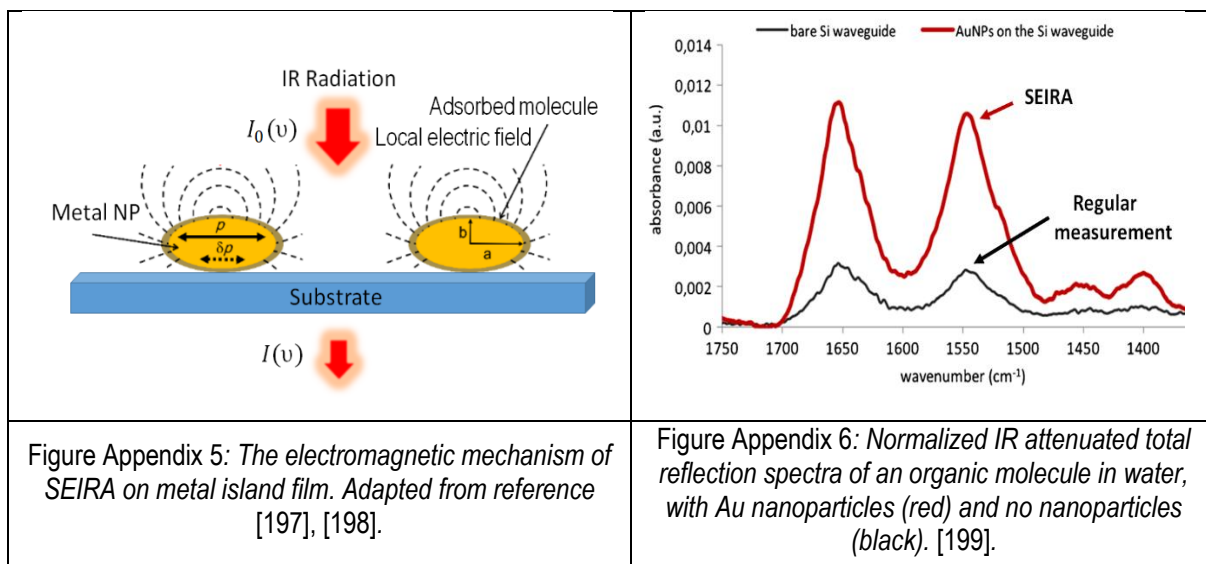


Figure Appendix 5 shows metal nanoparticles that are polarized by the incident photon field through the excitation of collective electron resonance (localized plasmon modes) and the dipole p induced in a nanoparticle generates a local electromagnetic field stronger than the incident photon field around the metal nanoparticles.

The presence of nanoparticles greatly enhances the intensity and quality of SEIRA (Surface-enhanced infrared absorption spectroscopy) signal of an organic molecule compared to the signal of the same molecule's measurements in the same conditions, but without nanoparticles inside (see Figure Appendix 5).

As in the case of SERS, in SEIRA, two different mechanisms contribute to the total enhancement of the signal: first the electromagnetic enhancement and the chemical enhancement mechanism.

The infrared absorption (A) can be expressed as [197]:

$$A \propto \left| \frac{\partial \mu}{\partial Q} \mathbf{E} \right|^2 = \left| \frac{\partial \mu}{\partial Q} \right|^2 |\mathbf{E}|^2 \cos^2 \theta \quad \text{Equation (A.16)}$$

where $\frac{\partial \mu}{\partial Q}$ is the derivative of the dipole moment to a normal coordinate Q and θ is the angle between $\frac{\partial \mu}{\partial Q}$ and \mathbf{E} .

The intensity of the electric field $|\mathbf{E}|^2$ at the surface of nanoparticles is different from that of the incident photon field. The coupling of the incident photon field to the metal surface can enhance the field; therefore, the electromagnetic mechanism assumes an increase of the total electric field at the surface [197].

The intensity of the enhanced electromagnetic field decays abruptly as the distance from the surface (d) of the nanoparticle increases, as expressed by the following relation:

$$|E_{local}|^2 \propto \left(\frac{a}{a+b} \right)^6 \quad \text{Equation (A.16)}$$

where: a is the local radius of curvature of the nanoparticles.

The E_{local} is polarized along the surface normal at every point on the surface of the nanoparticles (see Figure Appendix 5) which makes this model well adapted for expanding the relative short-range enhancement [197].

If we take the case of a system consisting of metal nanoparticles, adsorbed molecules, and a host medium, the system's transmittance or reflectance can be deduced using the Fresnel equations [49]. Moreover, by using

the effective medium approximation, it is possible to link the effective dielectric function of the system with the polarization susceptibility (α) of the nanoparticles.

The best-known models of the effective medium theory are those proposed Maxwell-Garnett and Bruggemann [197]. In the Maxwell-Garnett, model polarization susceptibility (α) is linked to the effective dielectric function ε_{MG} by the following expression:

$$\varepsilon_{MG} = \varepsilon_{env} \left(\frac{3+2F\alpha}{3-F\alpha} \right) \quad \text{Equation (A.17)}$$

where F is the filling factor of the metal within the considered system and ε_{env} is the dielectric constant of the surrounding medium.

It is worth mentioning the Maxwell-Garnett model only includes weak interaction between nanoparticles, through the Lorentz field and is useful when the nanoparticles are well separated from each other. When the nanoparticles are sufficiently close to each other, the Bruggemann model provides a better description of the effective dielectric function since it considers the dipole interaction between nanoparticles [197]. Based on the Bruggemann model, the effective dielectric function is:

$$\varepsilon_{BR} = \varepsilon_{env} \frac{3(1-F)+F\alpha'}{3(1-F)-2F\alpha'} \quad \text{Equation (A.18)}$$

This model assumes that the nanoparticles are embedded in an effective medium and so, α and ε_{env} are replaced by α' and ε_{BR} respectively [197].

In the SEIRA case, the electromagnetic field enhancement is estimated, theoretically, to be close to ten-fold or less [197]. This is because, in the mid-infrared region, metals have relatively large values of the imaginary part of the dielectric function that promotes strong damping of the localized plasmon modes. Therefore, up to 1000 times, the high enhancement cannot be explained just by this field enhancement [197]. The adsorbed molecules can induce additional dipoles in the nanoparticle and perturb the metallic nanoparticles' optical properties.

The perturbation is larger at vibrational frequencies of the molecule than other frequencies; hence, the spectrum of the nanoparticles should be identical to the spectrum of the molecule [197].

Besides this, due to the interaction between the molecule and the metal surface, the chemical mechanism ensures an increase of $\left| \frac{\partial \mu}{\partial Q} \right|^2$ (through the absorption coefficient) of the enhancement factor. In general, adsorbed molecules are orientated with a specific direction with respect to the surface [197]. For randomly orientated molecules, the space average of $\cos^2 \theta$ is 1/3 and the orientation effect gives an additional enhancement to the factor three, at maximum, to the dipole modes that have dipole charges parallel to \mathbf{E} [197].

In conclusion, the SEIRA effect can be characterized as follows [197]:

- The enhanced spectra can be analyzed working in transmission, attenuated total-reflection (ATR), external-reflection and diffuse-reflection modes,
- The enhancement depends on the morphology of the metal nanoparticles,
- The enhancement is higher for the molecules attached directly to the surface of nanoparticles and decays rapidly from the surface,

- nanoparticles that exhibit SEIRA have a broad absorption range, extending from the visible to infrared,
- Vibrational modes that have the dipole moment derivative components perpendicular to the surface a predominantly enhanced,
- Both physisorbed (based on van der Waals attraction between surfaces) and chemisorbed (in which the electronic structure molecules is changed and covalent or ionic bonds form) molecules exhibit enhancement. In general, the chemisorbed molecules show a larger enhancement.

In general, molecules have relatively low absorption coefficients of molecules in the infrared region of the spectrum. These limits, to a certain degree, the field of applications based on infrared spectroscopy. Therefore, SEIRA spectroscopy (SEIRAS) is now appealing to a wide range of applications since it can improve and lower the detection limit of molecules in the infrared.

Appendix 1.4. VO₂ metal to insulator transition debate.

Modern theories and simulation of the electronic structure of VO₂ have added some corrections to the Goodenough description. This was done to reduce the controversy between the theories based on effective single-particle and the correlated electronic state description in the Mott-Hubbard theory [74]. Goodenough based his model on the theoretical model suggested by Rudolf Peierls in 1930.

Rudolf Peierls proposed a theoretical model in which he assumed that a 1D conductor is made of equally spaced atoms with a constant lattice a , each atom having a conduction electron [77]. The interaction between the electrons and the lattice makes the 1D system quite unstable, and at low temperatures, the lattice distortion will occur at pairs of atoms. If the modulation vector $q = 2k$ (k is the Fermi wave vector) the Fermi surface and the boundary of the Brillouin zone are totally "nested" [77]. If the energy dissipated by the opening of the gap is more significant than the elasticity of the lattice distortion, the energy of the total electronic lattice system is lowered, giving rise to a transition from a conductor to an insulating system [77]. The strong point of the Peierls phase transition mechanism is that it can quantitatively explain that the opening of the bandgap is induced by $V - V$ dimerization. Peierls theory fails to explain the band gap of 0.6 eV of the M₁ phase, the presence of the metastable M₂ phase, etc. [77].

Besides the Goodenough model, Mott and Zylbersztein (later developed as the Mott-Hubbard model) proposed that electronic correlations might be the principal effect leading to the opening of the bandgap in the M₁ phase [74]. The Hubbard model defines a Mott insulator by two characteristics; the first one is the relative electron interaction strength $\frac{U}{t}$, where U is the Coulombic repulsion and t is the orbital bandwidth, and the second one is the electron density n [78]. If we take the case of a single electron model, $n = 1$ is defined as a half-filled band condition, and in a multiorbital system, this rule can be defined for each orbital [78]. To decrease the bandgap of the insulating phase U has to decrease and/or t must increase. If then U becomes sufficiently small the two Hubbard bands will meet and the insulating phase will become metallic. The decrease of U can be done by changing the charge state and effective spin state, while increasing t can be made by elongating the lattice parameters [78]. In the case of VO₂, when calculating the energy states, an additional U energy can come from the

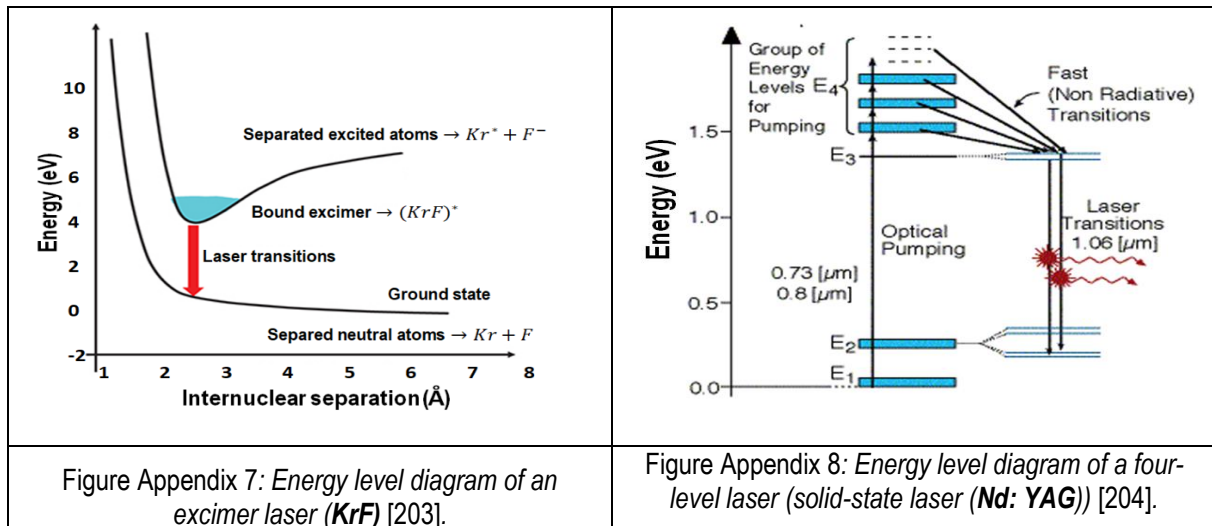
repulsion of d electrons [77]. The VO_2 is a two-band multiorbital system where U and t can be adjusted with relative ease. In VO_2 , U can also be decreased by the introduction of free carriers and the presence of V^{3+} ; one of the electrons might be trapped locally by V^{4+} and create V^{3+} [77]. The presence of V^{3+} weakens the electron correlation and the Coulombic interaction and together with an enhanced number of free carriers given by other non-trapped electrons, drive the system toward a metallic state by lowering U [77].

The significant controversies that remain with the Peierls perspective (a broad bandgap, etc.) seem to be settled to a certain degree by introducing the additional Hubbard energy U . Experimental evidence shows that both electron-electron interactions and $V - V$ dimerization distortions contribute to the transition from the insulating M_1 phase to the metallic R phase. Therefore, MIT results from the interactions and competition among electrons, orbitals, and lattices [77]. Recent theoretical approaches try to bridge the gap between the purely Mott-like and purely Peierls-like mechanisms of MIT [74]. S. Biermann et al. [200] has introduced the concept of “correlation assisted Peierls transition” using Cluster-DMFT simulations and concluded that electronic correlations are required in starting the bandgap opening process. H. Zheng et al. [201], by performing first-principles quantum Monte Carlo (QMC) calculations, has proposed that the metal to an insulator phase transition to be a “spin Peierls-like transition.” While, O. Nájera et al. [202] has shown that “Mott mechanism dominates the insulator-to-metal transition” by making simulations based on the dimer Hubbard model (DHM). The changes induced in VO_2 by the MIT's presence have a direct effect on its physical properties. Starting from the isolator phase to the metallic one, the interactions and competition among electrons, orbitals, and lattices change continuously, and at the end of MIT quite dramatically the optical properties of VO_2 .

Appendix 2. Appendix to Chapter II.

Appendix 2.1. Energy level diagram of an excimer laser vs. a solid-state laser and their beam profiles

The energy level diagram of an excimer laser is presented in Figure Appendix 7, and Figure Appendix 8 shows the energy level diagram of a solid-state laser (Nd: YAG).



Albert Einstein introduced the laser and maser's theoretical foundations in 1917 in a paper called "On the Quantum Theory of Radiation". In this paper, he deduced the theoretical framework for a laser by a re-derivation of Max Planck's law of radiation, theoretically built upon probability coefficients (Einstein coefficients) for the absorption, spontaneous emission, and stimulated emission of electromagnetic radiation. In 1955, Prokhorov and Basov introduced the concept that by optical pumping of a multi-level system, it is possible to obtain a population inversion, which was later established as the primary laser pumping method. However, the first operating solid-state laser device was made by Theodore Maiman in 1960. A solid-state laser consists of the following main components: a gain medium (a medium that can have a population inversion), a system that can provide energy to sustain the population inversion (flash lamp), and a resonant cavity (a pair of mirrors on either end of the gain medium). The gain medium is a material with properties that allow it to have a population inversion and amplify light by stimulated emission. The gain medium absorbs some of the pumped energy, and in this process, some of its electrons are raised into a higher-energy quantum state (an excited state). When the number of particles in an excited state is greater than the number of particles in a lower energy state, the so-called population inversion is accomplished. If population inversion is achieved, the stimulated emission rate is greater than the absorption rate of light in the medium (i.e., light is amplified). When this system is placed inside an optical resonant cavity, the laser effect can take place. For inversion of the population to occur, the gain medium has to have at least two higher energy states available, but the system is more efficient if there are three available higher energy states (see **Error! Reference source not found.**). An excimer laser has an entirely different working principle (see Figure Appendix 7) compared to Theodore Maiman's discovery. The term excimer is an abbreviation of the expression excited dimer, which describes a molecule that exists only in an excited state (e.g. (KrF)^{*}) [204]. An excimer laser is a gas laser

used as a gain medium, a mixture made from a noble gas (Kr, etc.) and a halogen (F₂, etc.). The gas molecules are separated in the ground state, but when a fast-electric field discharge (lasting few tens of ns) is applied, the halogen and the noble gas will bond together, forming the excited dimer. In the ground state, the gas reverts to the original separate constituents leading simultaneously to a reduction in the lower level's population and an increasing population inversion between the state's excited and ground states, inducing the laser transitions with a near field beam profile presented in Figure Appendix 9.

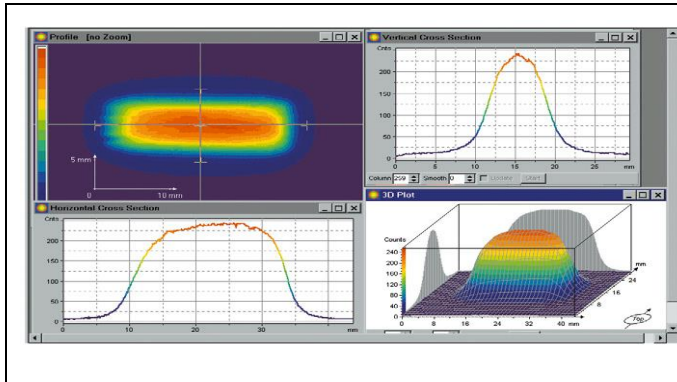


Figure Appendix 9 : Near field beam profile of an excimer laser [205].

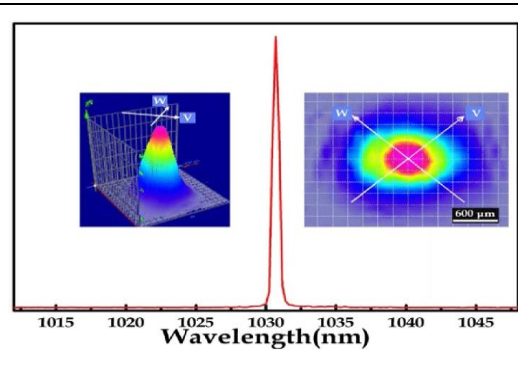


Figure Appendix 10: Near field beam profile of a solid-state laser [206].

The beam profile of an excimer laser is very different from a solid-state laser (see Figure Appendix 9 and Figure Appendix 10). An excimer laser has a flat-top (top-hat) beam profile, whereas a solid-state laser has a Gaussian-shaped beam profile. This difference in beam profile makes the excimer laser a better choice for PLD since the Gaussian-shaped beam profile of solid-state laser makes it prone to uncontrolled material splashing due to shallow energy density gradients. Besides that, the excimer lasers work at low wavelengths (at photon energies between 5 eV to 7.9 eV), have a high energy per pulse (100 to 1000 mJ), show a homogenous spatial distribution of energy within the laser spot, and have great energy stability from shot-to-shot, at a low repetition rate [91].

Appendix 2.2. Nanosecond laser ablation vs femtosecond laser ablation

The fact that the laser has a pulse duration of few nanoseconds (as is the case of our laser), picoseconds, or femtoseconds changes the ablation mechanisms (see Figure Appendix 11).

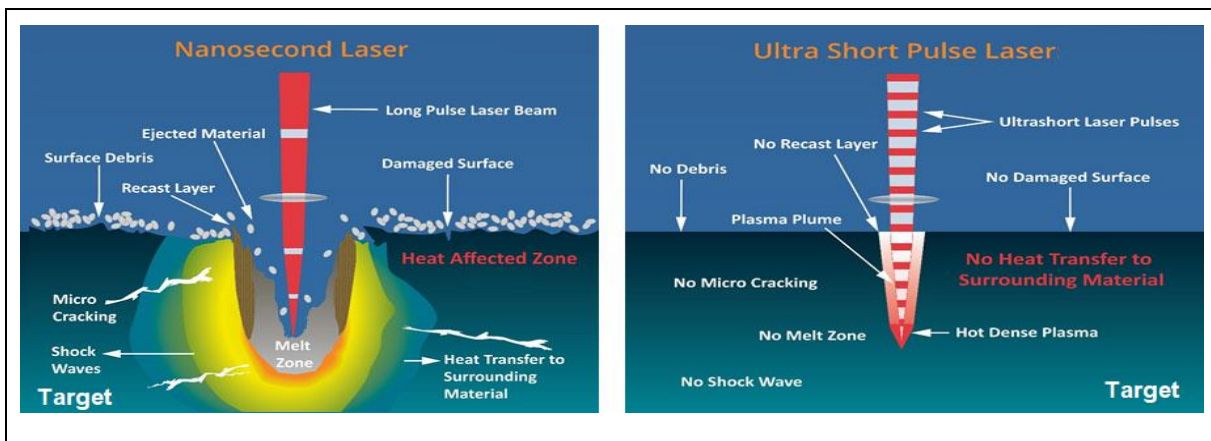


Figure Appendix 11: *Nanosecond laser ablation vs femtosecond laser ablation.* Source: [https://www.ipgphotonics.com/en/products/lasers/pico-femtosecond-fiber-lasers/1-03-1-06-micron/ylpp-r-series#\[nanosecond-vs-ultra-short-pulse\]](https://www.ipgphotonics.com/en/products/lasers/pico-femtosecond-fiber-lasers/1-03-1-06-micron/ylpp-r-series#[nanosecond-vs-ultra-short-pulse]).

The ablation process starts with photon absorption, followed by heating and photoionization of the area directly impacted by the laser beam. After this, the ablated material is released from the target as a stream of solid fragments, vapor, liquid drops, and/or as an expanding plasma plume. The material is ablated in the nanosecond regime due to melt expulsion driven by the vapor pressure and the recoil pressure of light [92]. The melted material will then solidify again around the laser's impact area, which is not the case for femtosecond lasers (see Figure Appendix 11). For femtosecond lasers, the pulse duration is shorter than the electron cooling time and electron-lattice coupling can be neglected. Hence electron heat conduction inside the target material can be ignored during the pulse. Yet, for a complete description of the process, the thermal aspects have to be considered. This is beyond the scope of this thesis.

Laser pulse duration also impacts the ablation threshold and penetration depth; when the pulses are in the nanosecond regime the ablation threshold increases.

Appendix 2.3. Interaction forces between microspheres

Van der Waals's interaction between microspheres

Van der Waals's interactions originate from the interaction present between the microspheres' individual constituent [113]. In Table Appendix 1 are given some examples of expressions of the interaction energy computed for two microspheres of radii R_1 and R_2 with inter-microspheres surface separation h and between a microsphere of radius R and a plane and of the interaction energy per unit area between two flat surfaces separated by a distance h [114].

Table Appendix 1: Expression of the van der Waals interaction for different geometries [114]

Geometry	Expression of Van der Waals interaction	
Two spheres or microspheres	$E_{vdW} = -\frac{A_H}{6} \left[\frac{2R_1R_2}{h(h+2R_1+2R_2)} + \frac{2R_1R_2}{(h+2R_1)(h+2R_2)} + \ln \frac{h(h+2R_1+2R_2)}{(h+2R_1)(h+2R_2)} \right]$	
	for large separation ($h \gg R_1 + R_2$)	$E_{vdW} \propto -\frac{1}{h^6}$
	for short separation ($h \ll R_1 + R_2$)	$E_{vdW} = -\frac{A_H}{6} \frac{R_1R_2}{R_1+R_2} \propto -\frac{1}{h}$
	if $R_1 = R_2 = R$	$E_{vdW} = -\frac{A_H R}{12h}$
microsphere-plane	$E_{vdW} = -\frac{A_H}{6} \left[\frac{R}{h} + \frac{R}{(h+2R)} + \ln \frac{h}{(h+2R)} \right]$	
Two flat surfaces	$E_{vdW} = -\frac{A_H}{12\pi h^2}$	

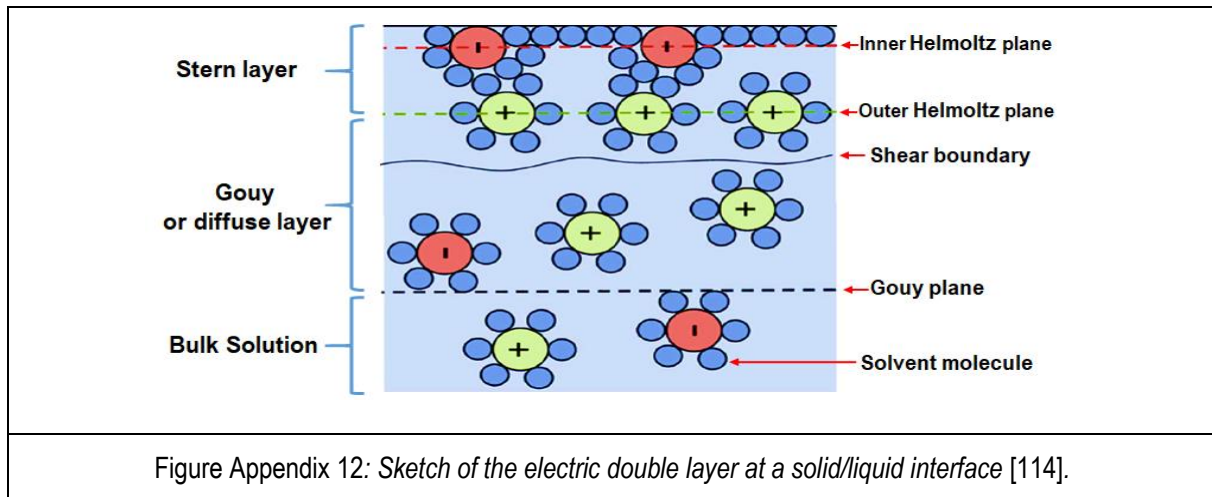
A_H is the combined effective Hamaker constant and can be computed starting from the Hamaker constants of the individual media; it typically has values around 10–20 J [207]. The effective Hamaker constant depends on the fractional volume of the microspheres immersed in each phase, leading to the observed enhancement of the Van der Waals interaction of microspheres at air/liquid interface to a microsphere in water [114]. The Van der Waals forces are attractive if the Hamaker constant is positive or repulsive if the Hamaker constant is negative. The van der Waals force between two identical bodies in any medium is always attractive, and such interactions are expected to play a role for microspheres at an interface. For spheres with sizes in the nm- μ m range, the corresponding energies typically in the range 0.1–1 $k_B T$ [114].

Electrostatic interaction between microspheres

The electrostatic interactions are given by the microparticle's surface charges and can be either attractive or repulsive (like Van der Waals forces). Surface charges can originate from:

- Ionization or dissociation of surface groups, e.g. dissociation of protons from surface carboxylic groups ($-\text{COOH} \rightarrow -\text{COO}^- + \text{H}^+$) that give rise to a negatively charged surface; PS microspheres are often commercially available with surface functional groups such as carboxylic acid, amine, and sulfate groups; pH can be used to control the degree and nature of ionization by protonation or deprotonation of surface groups [114];
- Adsorption and binding of ions from solution onto a previously uncharged surface; e.g., adsorption of $-\text{OH}^-$ groups to the air/water or hydrocarbon/water interfaces resulting in a negative charge or adsorption of surfactants to the microsphere surface. This process is also sensitive to pH. In the so-called ion exchangeable surfaces, the adsorption of ions from a solution can also take place onto oppositely charged surface sites, e.g., adsorption of cationic Ca^{2+} to anionic $-\text{COO}^-$ sites vacated by H^+ [208].

Despite the charging mechanism or charge regulation mechanism, the electro-neutrality is reached when the final surface charge of co-ions is balanced by an equal but oppositely charged region of counter-ions, with some of the counter-ions bound to the surface while others in rapid thermal motion close to the surface [114]. This is the electric double layer model in which the bound counter-ions are within the Helmholtz or Stern layer, and the free counter-ions are within the Gouy or diffuse layer; the theory has been developed by Gouy, Chapman, Debye, Hückel and later changed by Stern and Grahame [114], [207], [209]. A sketch of the double layer model is presented in Figure Appendix 12.



The inner Helmholtz plane is the place of the centers of specifically adsorbed co-ions, while the outer Helmholtz plane goes through the centers of counter-ions, typically hydrated or solvated, at their closest approach [209]. The inner layer is placed between the surface and the outer Helmholtz plane; the potential drop across this layer is assumed to be linear, while from the outer Helmholtz plane, it starts to obey the Poisson-Boltzmann equation. The total thickness of such layers (usually few Å) is linked to the finite size of the surface groups (co-ions) and transiently bound counter-ions [114], [209]. As in the case of the van der Waals interaction, analytical expressions have been derived for the electrostatic double layer interaction energies for different geometries. As an example, the expressions for some specific cases and geometries are reported in Table Appendix 2. The expressions presented in Table Appendix 2 suggests that the electric double layer interaction between surfaces, particles with different geometries has an exponential decay with distance, while van der Waals interactions exhibit a power-law decay.

Moreover, differently from the van der Waals interaction, the electric double layer interaction is much more sensitive to variations in electrolyte concentration and pH [114], [208]. Electrostatic double layer interaction between identically charged planes is repulsive. The interaction between non-identically charged planes can be attractive or repulsive depending on the separation; however, at extensive separations, the double layer interaction can become weakly attractive even for identical particles [114], [208].

Table Appendix 2: Expressions of the electrostatic double layer interaction for a variety geometries [114]

Geometry	Expression of the electrostatic double layer interaction	
Two spheres or microspheres	In case of a thin electric double layer ($k^{-1} \ll R_1, R_2$), small separation ($hk^{-1} \ll R_1, R_2$) for any surface potential $k^{-1} \ll R_1, R_2$ and ψ_{S2} only if $e^{kh} \gg 1$ $E_{edl} = \frac{128\pi R_1 R_2}{k^2 (R_1 + R_2)} n_0 k_B T Z_1 Z_2 e^{-kh}$	
	For small constant surface potentials and any $h \ll R_1, R_2$ $E_{edl} = \frac{\pi \epsilon \epsilon_0 R_1 R_2}{R_1 + R_2} (\) \psi_{S1} + \psi_{S2} 2 \ln(1 + e^{-kh}) + (\) \psi_{S1} - \psi_{S2} 2 \ln(1 - e^{-kh})$	
	For constant surface charges and any $h \ll R_1, R_2$ $E_{edl} = \frac{-\pi R_1 R_2}{\epsilon \epsilon_0 k^2 (R_1 + R_2)} (\) \sigma_{S1} + \sigma_{S2} 2 \ln(1 + e^{-kh}) + (\) \sigma_{S1} - \sigma_{S2} 2 \ln(1 - e^{-kh})$	
	If $R_1 = R_2 = R$ for any $h \geq R$	$E_{edl} = \frac{4\pi \epsilon \epsilon_0 R^2 \psi_S^2}{(2R + h)} e^{-kh}$
	If $R_1 = R_2 = R$ for any h	$E_{edl} = 4\pi \epsilon \epsilon_0 R^2 \psi_S^2 \frac{R + h}{(2R + h)} \ln \left(1 + \frac{R e^{-kh}}{R + h} \right)$
Sphere-flat surface	For similar constant potential surfaces and $h \ll R$, $E_{edl} = \frac{64\pi \epsilon \epsilon_0 (k_B T)^2 Z^2 R}{(zq)^2} e^{-kh}$	
Two flat surfaces	For similar constant potential surfaces $E_{edl} = \frac{32k \epsilon \epsilon_0 (k_B T)^2 Z^2}{(zq)^2} e^{-kh}$	

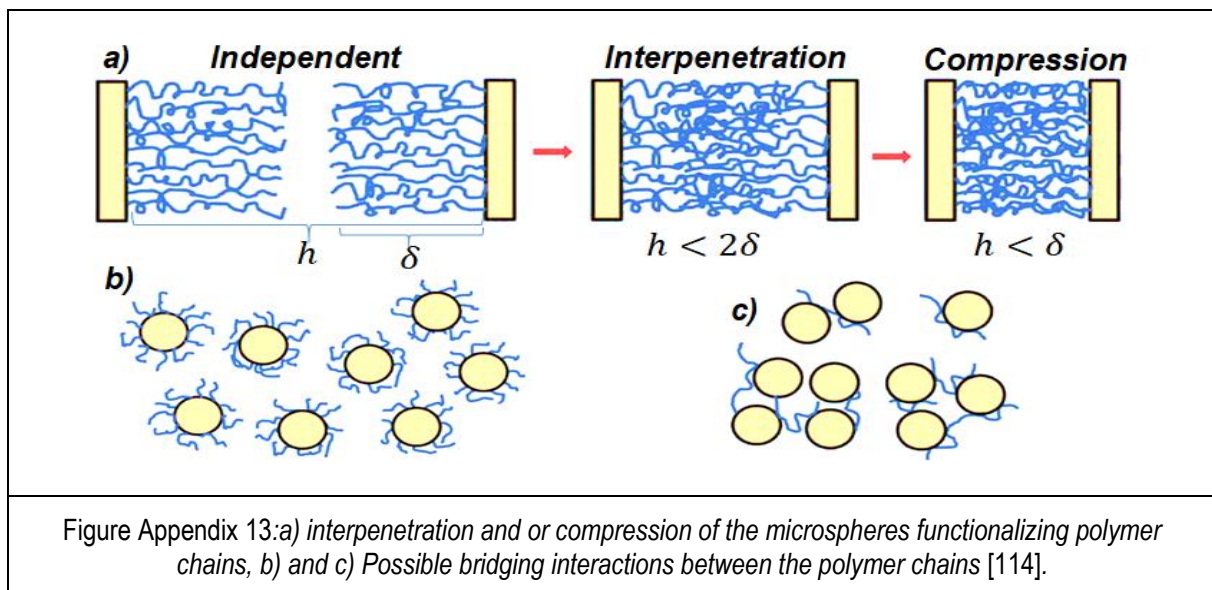
were ϵ_0 is the permittivity of free space, ϵ is the relative permittivity, q is the elementary charge; ψ_S is called Stern potential and is the potential at the outer Helmholtz and Stern plane. The quantity $\frac{1}{k}$, known as Debye length, gives an estimate of the double-layer thickness. In the Derjaguin-Landau-Verwey-Overbeek (DLVO theory), the overall interaction energy is expressed as the sum of the van der Waals and electrostatic contributions as [114]:

$$E_{DLVO} = E_{vdW} + E_{edl} \quad \text{Equation (A.19)}$$

As a result, the colloidal stability is linked to the balance between attractive van der Waals forces and electrostatic repulsion. The DLVO theory is a useful tool, although it does have its limitations, namely due to electrostatic decay, because of screening [109]. However, other types of surface forces often come into play in colloidal stability and can be monotonically repulsive, monotonically attractive, or oscillatory [208]. Amongst the non-DLVO surface forces, there are the steric forces, capillary forces, structural forces, fluctuation wave forces, hydrophobic attraction, and solvation forces [114].

Steric effect.

Colloidal microspheres (functionalized with C_{18}) in highly concentrated media are subject to steric effects, where the presence of other microspheres in the liquid physically blocks further ordering or material deformation [115]. When two microspheres approach each other, as soon as the inter-particle distance is below twice the unperturbed layer thickness δ , the polymer functionalization layers (C_{18} molecules) will touch each other leading to interpenetration and or compression (see **Error! Reference source not found.** a)). In case of a suitable solvent for the polymer used to functionalize the microspheres, the local increase in polymer concentration carries a free energy penalty, and this gives rise to steric or overlap repulsion between microspheres, noticeable as soon as $h < 2\delta$ and growing quickly for $h < \delta$ as compression [114].



Furthermore, bridging interactions can be present when the same adsorbing polymer chain attaches to two distinct microspheres, making the microspheres attract one another (see Figure Appendix 13c)). This can happen when, for example, the surface of the microspheres is not covered by the polymeric species (C_{18}). When the polymer covers the surface, bridging can still occur if some portions of the initial polymer are detached and provide new sites for attachment of polymer fractions adsorbed on the microspheres or polymer-polymer bonding (see Figure Appendix 13 b)). The steric repulsion is a useful tool to compensate Van der Waals attraction by generating an energy barrier that inhibits the microspheres' approach. For example, copolymers and surfactants (with the head group adsorbed to the particles and the tail groups used for stabilization) can be used to stabilize microspheres in the water sub-phase [114]. The solubility in a given solvent of most of the polymers is directly linked with temperature. In a suitable solvent, the polymer chains are extended in a relatively open, random-coil configuration, thus ensuring an optimum protective layer thickness [114], [210]. If the solvent is poor (or if the temperature variation makes the solvent poor), the polymer chains shrink and collapse into a compact configuration due to the attraction between segments of the chains; the temperature at which the transition occurs is called θ (or theta) temperature [114].

Capillary forces

The attractive capillary forces appear as a consequence of the formation of liquid bridges, typically observed in meniscus effects, forming between microspheres (microparticles) due to surface tension [109]. Capillary interactions for sub-micrometer and micrometer-sized floating microspheres can become non-negligible if there is an irregular contact line between microspheres, microspheres, and sub-phase. In other words, when the deformation around a single microsphere is non-axisymmetric, and the three-phase line of contact is no more circular. This can happen if the microsphere surface is rough, angular, or heterogeneous, such as alternating hydrophilic and hydrophobic surfaces at the liquid-fluid interface [114]. In our case, the polystyrene microspheres do not have a rough surface, and they are almost perfect spheres, just their size can vary a bit. Therefore, the capillary interaction can be neglected.

Appendix 3. Appendix to Chapter IV

Appendix 3.1. Evolution of position and intensity of the resonance peaks of the Au nanoparticle arrays (2 μm polystyrene microspheres) and Ir Au nanoparticle arrays embedded in VO_2

Figure Appendix 14 shows the evolution of position and intensity of the resonance peaks of the Au nanoparticle arrays, made with 2 μm polystyrene microspheres and embedded into 200 nm, 100 nm and 50 nm of VO_2 as a function of temperature.

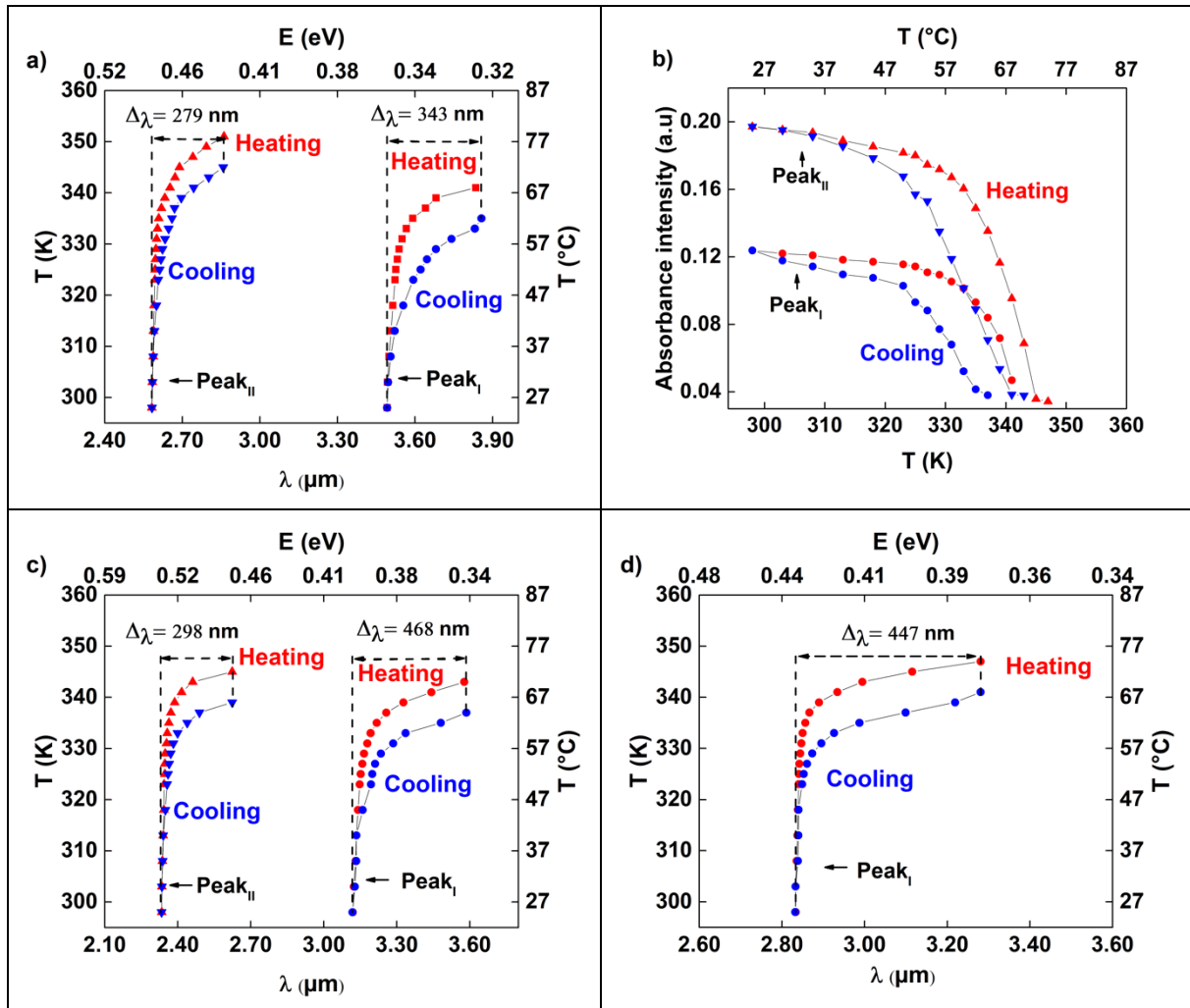


Figure Appendix 14: a) Temperature evolution of resonance peaks wavelength of Au nanoparticle arrays made with 2 μm polystyrene microspheres and embedded into 200 nm VO_2 matrix. b) Temperature evolution of resonance peaks intensity of Au nanoparticle arrays made with 3 μm polystyrene microspheres and embedded into 100 nm VO_2 matrix. c) Temperature evolution of resonance peaks wavelength of Au nanoparticle arrays made with 2 μm polystyrene microspheres and embedded into 200 nm VO_2 matrix. d) Temperature evolution of resonance peaks wavelength of Au nanoparticle arrays made with 2 μm polystyrene microspheres and embedded into 50 nm VO_2 matrix. The thickness of the Au nanoparticles is 50 nm.

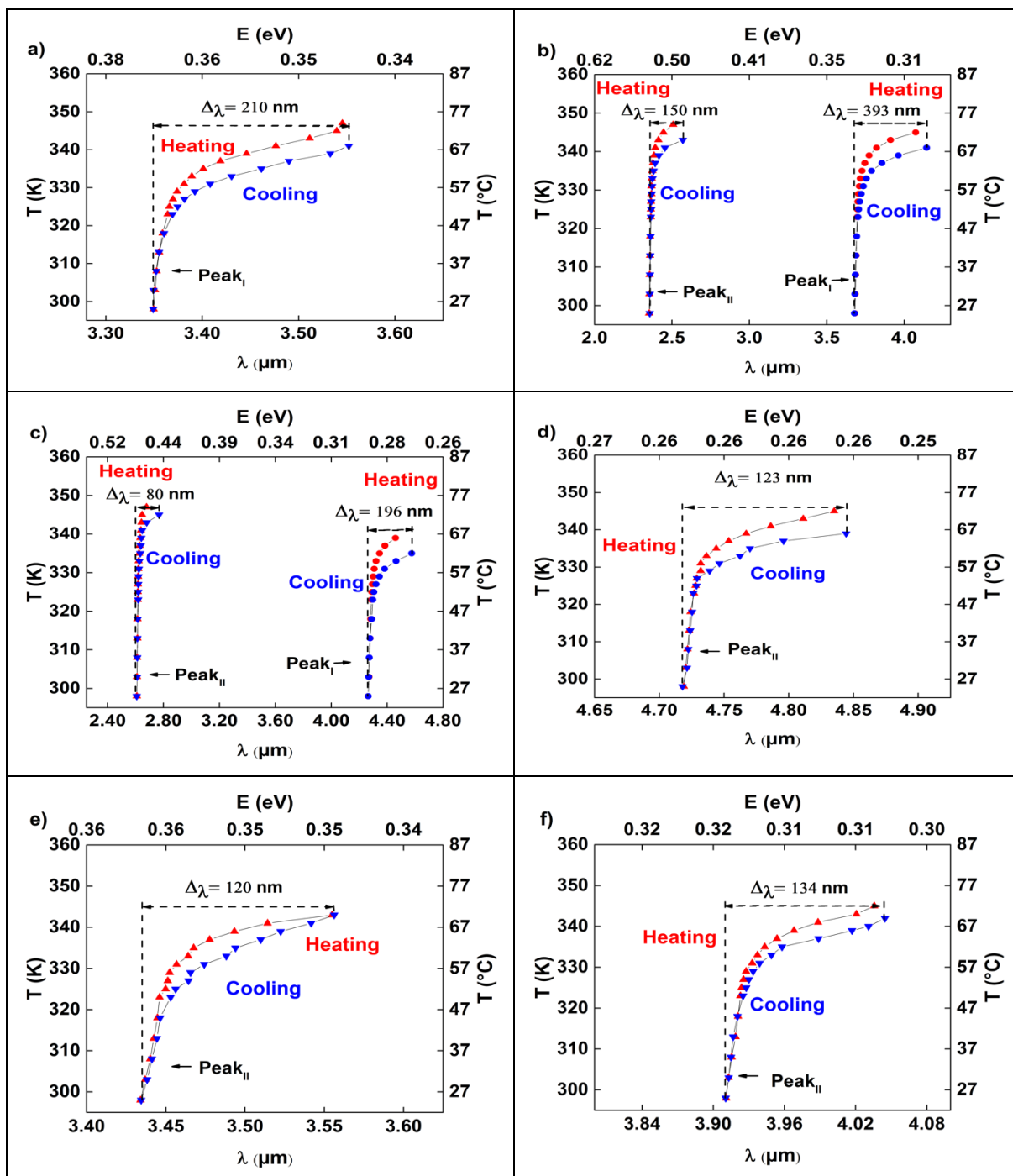


Figure Appendix 15: a) Temperature evolution of resonance peak of Ir nanoparticle arrays made with 2 μm polystyrene microspheres, placed in 50 nm of VO_2 . b) Temperature evolution of resonance peaks of Ir nanoparticle arrays made with 2 μm polystyrene microspheres, placed in 100 nm of VO_2 . c) Temperature evolution of resonance peaks of Ir nanoparticle arrays made with 2 μm polystyrene microspheres, placed in 200 nm of VO_2 . d) Temperature evolution of resonance peak of Ir nanoparticle arrays made with 3 μm polystyrene microspheres, placed in 50 nm of VO_2 . e) Temperature evolution of resonance peak of Ir nanoparticle arrays made with 3 μm polystyrene microspheres, placed in 100 nm of VO_2 . f) Temperature evolution of resonance peaks of Ir nanoparticle arrays made with 2 μm polystyrene microspheres, placed in 200 nm of VO_2 .

Figure Appendix 14 shows evolution as a function of the temperature of the Ir nanoparticle arrays' resonance peaks, made with 2 and 3 μm polystyrene microspheres and embedded into different thicknesses of VO_2 .

Figure Appendix 14 and Figure Appendix 15 shows a direct connection between the temperature of the VO₂ matrix and the wavelength peak position of the metallic nanoparticle arrays resonances. When the VO₂ matrix's temperature is increased from 25 °C towards 90 °C, the resonance peaks' position starts to redshift, moving from a lower wavelength value to a higher one as VO₂ transits from an insulator to a metallic state. If the VO₂ is cooled down, the metallic nanoparticle resonance position will blue shift back to its initial position. The absorbance intensity of the metallic nanoparticle arrays' resonance peaks decreases as the temperature increases. When the sample is cooled down, the metallic nanoparticle arrays' absorbance intensity goes back to the previous value. In general, for both resonance peak position and peak intensity, there is a visible difference between the value at the same temperature if the measurement is made when heating up compared to when the measurement is made during cooling down. This is because the VO₂ transition from the insulator state to the metallic state is controlled by the transition of individual crystalline grains of the VO₂, and this transition has a hysteresis (i.e., at a temperature close to 68 °C there is a mixture of VO₂ crystalline grains in the insulator state and metallic state which depends on the fact that the transition is insulator to metal or metal to insulator).

Structuration périodique multi-échelle de surface par auto assemblage de masques colloïdaux : couplage forme-taille-propriétés, applications électroniques et optiques

Cette thèse s'inscrit dans le cadre de développement de procédés et de matériaux composites en films minces pour des applications optiques et électriques.

Un procédé de Langmuir-Blodgett (LB), récemment acquis à l'institut IRCER, associé à un procédé de dépôt par ablation laser permet la synthèse de composites - films minces d'architectures contrôlées. Sur un substrat monocristallin de silicium ou de saphir, une monocouche de sphères de polystyrène de taille rigoureusement identique (d'environ 2-5 μm de diamètre), auto-organisées, est déposée en structure compacte par procédé LB et est utilisée comme masque colloïdal autorisant des photolithographies. Ce masque, couplé à des dépôts métalliques par ablation par laser impulsif, permet de générer des structures 2D (quasi-triangles auto-organisés) dont les dimensions sub-microniques sont fonctions des tailles des sphères initiales. La surface de recouvrement métallique d'environ 9% est indépendante de la taille des sphères utilisées, la géométrie caractéristique est de dimension fractale.

Dans ce document, deux types de métaux différents et complémentaires, sont utilisés afin de générer ces architectures, l'iridium et l'or. A ces échelles, l'or présente des effets de démouillage significatif autour de 500°C contrairement à l'iridium. Une étude rigoureuse sur les modifications des structures métalliques d'or induites par la température entre 20°C et 1000°C est présentée (démouillage à l'état solide). Les architectures métalliques, de géométries fixes ou modifiées par recuit, sont alors noyées dans une matrice de VO₂, synthétisée à 500°C. Le dioxyde de vanadium, est un oxyde dit « intelligent », connu pour sa transition de phase à 68°C accompagnée par un changement drastique de ses propriétés physico-chimiques (transition isolant/métal). Les composites Ir/VO₂ et Au/VO₂ développés dans cette thèse, présentent des propriétés d'absorption optique, dans le visible et surtout dans le proche infra-rouge, fascinantes. Des résonances plasmons de surface locales (LSPR) liées aux architectures métalliques et à la nature des métaux utilisés sont observées et simulées par approche FDTD (Finite Difference Time Domain). Ces LSPRs sont modulables en amplitude et accordables, jusqu'à plus de 600 nm, en fonction de la température de la matrice VO₂ et de la nature des éléments composant l'architecture métallique.

L'apparition de structures singulières cœur-coquilles métalliques en matrice diélectrique, mises en évidence par spectroscopie RAMAN et confirmées par spectroscopie infra-rouge, justifie le décalage des longueurs d'ondes d'absorption observées dans l'infra-rouge. De plus, les inclusions métalliques, noyées au sein du VO₂ permettent de sonder cet oxyde caractéristique et donnent de précieuses informations sur les évolutions des phases et des paramètres de maille durant sa transition.

Mots-clés : Plasmonique, modulation LSPR, réseaux de nanoparticules d'or et d'iridium, démouillage à l'état solide, dioxyde de vanadium ; architecture adaptative métal-semi-conducteur, calculs LSPR FDTD.



Periodic multi-scale structuring of surfaces by self-assembly of colloidal masks: shape-size coupling effects

The Langmuir-Blodgett (LB) process, recently acquired at IRCER, associated with a laser ablation deposition technique allows the synthesis of composites - thin films of controlled architectures. On a monocrystalline silicon or sapphire substrate, a monolayer of polystyrene spheres of strictly identical size (about 2-5 μm in diameter), self-organized, is deposited in a compact structure by the LB process and is used as a colloidal mask allowing photolithography. This mask, coupled with metallic thin films by pulsed laser ablation, makes it possible to generate 2D structures (self-organized quasi-triangles) whose sub-micron dimensions are a function of the sizes of the initial spheres. The metal covering area of approximately 9% is independent of the size of the spheres used, the characteristic geometry is of fractal dimension.

In this document, two different and complementary types of metals are used to generate these architectures, iridium and gold. At these scales, gold exhibits significant dewetting effects around 500 ° C unlike iridium. A rigorous study on the modifications of gold metallic structures induced by the temperature between 20 ° C and 1000 ° C is presented (dewetting in the solid state). The metallic architectures, of fixed geometries or modified by annealing, are then embedded in a matrix of VO₂, synthesized at 500 ° C. Vanadium dioxide is a so-called "intelligent" oxide, known for its phase transition at 68 ° C accompanied by a drastic change in its physicochemical properties (insulating-metal transition). The Ir / VO₂ and Au / VO₂ composites developed in this thesis exhibit fascinating optical absorption properties, in the visible and especially in the near infrared range. Local surface plasmon resonances (LSPR) linked to the metallic architectures and to the nature of the metals used are observed and simulated by the FDTD (Finite Difference Time Domain) approach. These LSPRs are adjustable in amplitude and tunable, up to more than 600 nm, depending on the temperature of the VO₂ matrix and the nature of the elements making up the metallic architecture. The appearance of singular metal core-shell structures in a dielectric matrix, demonstrated by RAMAN spectroscopy and confirmed by infrared spectroscopy, justifies the shift in absorption wavelengths observed in the infrared range. In addition, the metallic inclusions embedded in the VO₂ allow this characteristic oxide to be probed and provide valuable information on the evolutions of the phases and lattice parameters during its transition.

Keywords: Plasmonics, LSPR modulation; Gold and Iridium nanoparticles arrays, solid state dewetting, Vanadium dioxide, adaptive metal-semiconductor architecture, LSPR FDTD calculations.

